O. I. Gerasymov

Structure and Photonics of discrete meso-scaled anisotropic Systems

Monography

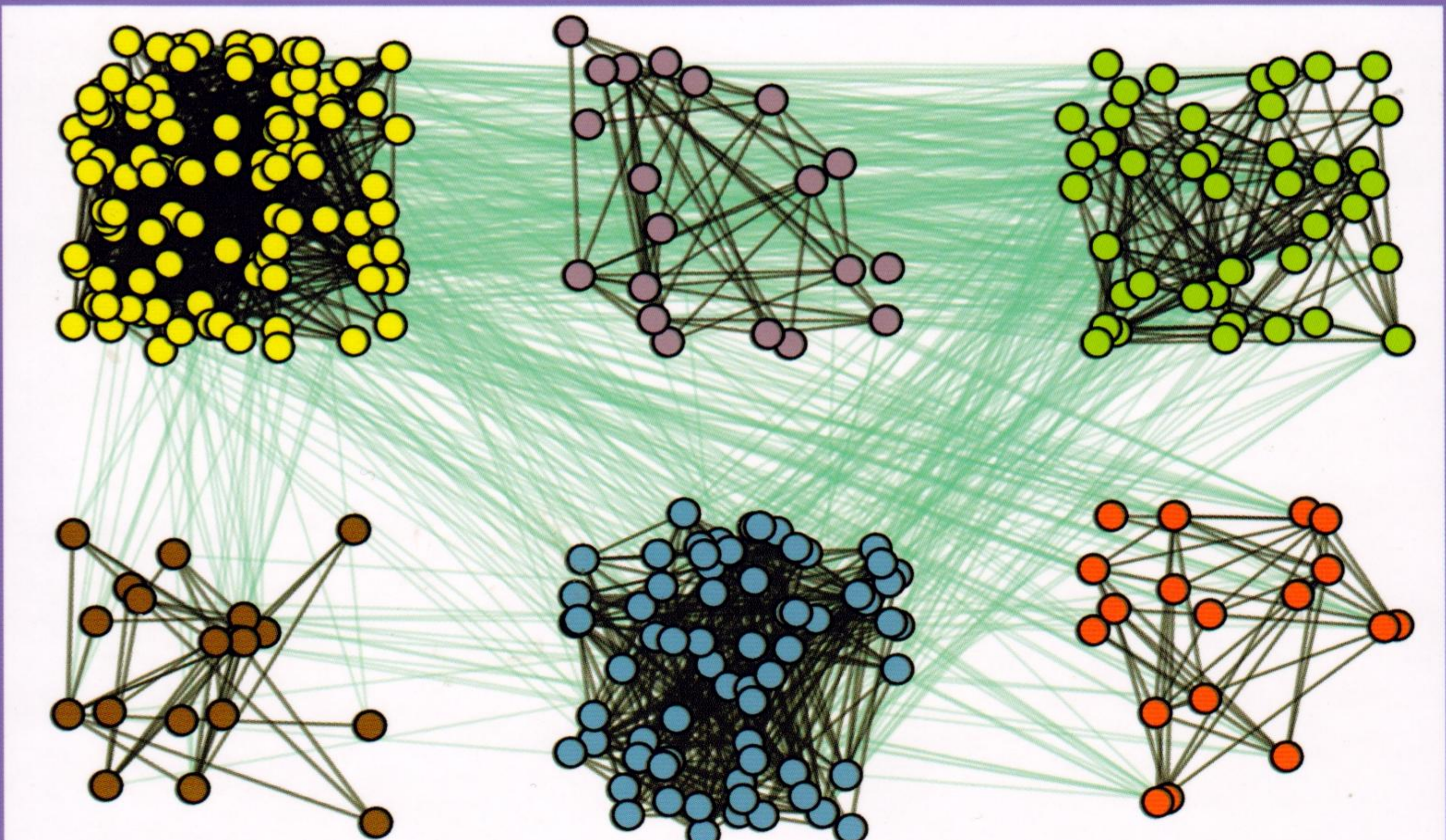

Odessa
TES
2018

Ministry of Higher Education and Science of Ukraine

Odesa State Environmental University

O.I.Gerasymov

Structure and Photonics of discrete meso-scaled anisotropic Systems

Monography

Рекомендовано до друку за рішенням вченої ради ОДЕКУ МОН України (протокол № 9 від 26.10.2017 р.)

Odesa
TES
2018

PACS 42.70.-a

Published by the decisions of the Scientific Council of Odesa State Environmental University (protocol No. 9 from 26.10.2017)

Referees:

Academician **A.G.Zagorodny**, Dr.Sci., Prof., Director of Bogoluybov Institute for Theoretical Physics, NAS of Ukraine, Kiev, Ukraine, Corr. Member of APS of Ukraine

A.V.Chaly, Dr.Sci., Prof., Head of the Department of Physics Bogomolez National Medical University, Kiev, Ukraine

Gerasymov Oleg Ivanovich

Structure and photonics of discrete meso-scaled anisotropic systems : Monography / Gerasymov O.I.; Odesa State Environmental University. Odesa: TES, 2018. - 242 p.

Фотоніка у мезо-масштабі має справу із взаємодією світлових променів (електромагнітних хвиль) у матеріалах, структурованих у масштабі, проміжному між континуальним (макроскопічним) і мікроскопічним. На мезо-масштабах відбуваються чисельні фотонні ефекти, зокрема, має місце відхилення від лінійного сценарію розсіювання світлових хвиль, яке потребує самоузгодженого врахування взаємодії електромагнітних хвиль (фотонів) із середовищем. Специфічні оптичні явища у мезо-масштабі спостерігаються при взаємодії фотонних променів із біологічними об'єктами, зразками м'якої матерії (колоїдами, полімерами, гранульованими матеріалами), штучно синтезованими механічними системами (супергратками). Пропонована монографія знайомить читача із детальним оглядом підходів, методів, моделей, які застосовуються до опису вищезгаданих явищ та їхньої параметризації. Причому, увага приділяється як теоретичним методам, так і опису відповідних експериментальних явищ. Матеріали монографії пропонуються до уваги викладачів, наукових співробітників, студентів і аспірантів, які спеціалізуються в галузі сучасних технологій та їх застосувань в різноманітних галузях, від науково-технічних до убезпечення навколишнього середовища.

Meso-scale photonics involves the interaction of light with material structures of intermediate scale - structures that are too small to be described by traditional continuum methods and too large to be characterized atomistically say as simple dipoles. At such dimensions, photonic phenomena include scale-specific modifications of the structure in response to the light so that a "passive" linear interpretation of the reciprocal action is inadequate, and a nonlinear description including dynamics of the light-structure interaction is necessary. Meso-scale phenomena occur in different circumstances, e.g., biological systems (proteins and DNA), soft materials (colloids and polymers), and fabricated mechanical nanostructures (motors, ratchets and scaffolding. Presented monograph gives a detailed introduction to theoretical approaches , experimental evidences and applications in the field. The book is proposed to attention of lecturers, researchers and students who specialized in modern technologies and their applications including the environmental monitoring and safety technologies.

ISBN 978-617-7337-75-0

CONTENT

Preface

Meso-scale photonics involves the propagation of light in mesoscaled structured materials which are too small to be described by continuum models and contrary, which are too large to be characterized microscopic methods. At such dimensions, photonic phenomena based on particular scale modifications of the structure as a feedback to the electro-magnetic irradiation so that a trivial linear interpretation of the reciprocal action is nonadequate anymore, and a nonlinear description (including dynamics of the light-structure scattering) is required. Meso-scale phenomena occur in different circumstances: biological systems, soft materials (colloids and polymers, granular media), dusty plasmas and fabricated opto-mechanical nanostructures. Presented monograph gives a detailed introduction to theoretical approaches, i.e. models and experimental evidences and applications in the field. The book is proposed to attention of lecturers, researchers and students who specialized in modern technologies and their applications including the environmental monitoring and safety technologies.

1 THE ELECTROMAGNETIC-WAVE PROPAGATION THROUGH A STRATIFIED INHOMOGENEOUS ANISOTROPIC MEDIUM

The electromagnetic-wave propagation through a medium consisting of two dielectric half-spaces with a plate in between, has been investigated. The half-spaces are isotropic with their dielectric permittivity depending only on the z coordinate. The plate is anisotropic, and the components of its dielectric permittivity tensor are also z-dependent. For the first time, the sufficient conditions allowing the transformation of the system of Maxwell's equations into two independent equations, are ascertained. For an arbitrary z-dependence of the dielectric permittivity, the plate's reflectance and transmittance coefficients are obtained, this result being a generalization of the Fresnel formulas. We have considered both determinate and random dependences of the dielectric permittivity on the z-coordinate, and the plate's full-transparency conditions are specified. For a statistically inhomogeneous plate, the conditions of its full opacity are formulated. The Faraday effect in such a medium is studied. The influence of the medium's inhomogeneity on the temporal rotation of the polarization plane of a propagating wave has been demonstrated.

1.1 Introduction

In Ref. [1], it has been shown that the medium's inhomogeneity coupled with its gyrotropy affects substantially the electromagnetic wave propagation through the medium. This results in new effects, and changes — quantitatively and/or qualitatively – "ancient" ones, e.g., the Faraday effect. In this work [1], an electromagnetic wave propagates through a medium consisting of two isotropic homogeneous half-spaces parted with a homogeneous plane-parallel gyrotropic plate. In the present work, the medium includes two isotropic half-spaces with dielectric permittivities depending only on the z-coordinate, these half spaces being divided by an anisotropic plate the dielectric-permittivity tensor of which is also z-dependent. The plate is confined with the $z = 0$ and $z = a$ plates, that is, a is the plate's thickness. The wave propagates along the z-axis and so is incident normally to the plate's surfaces. The paper consists of three sections. In the first one, we consider the propagation of electromagnetic wave through and reflection from an inhomogeneous isotropic plate enclosed between two inhomogeneous isotropic half-spaces. In the second section, requirements are formulated which reduce the problem of wave propagation through anisotropic medium to a problem of propagation of two independent waves in isotropic medium, each of the waves having its own refractive index. And in the third section, the general results obtained in the two previous ones, are applied to a gyrotropic plate. It is to be noted that the medium studied in this work, allows to consider simultaneous influences of the interference, anisotropy and smooth inhomogeneity on the wave propagation.

1.2 Electromagnetic-wave propagation in isotropic inhomogeneous medium

The wave propagation in a medium consisting of two inhomogeneous isotropic half-spaces with an isotropic inhomogeneous plate between them, is described by the following equations

$$\begin{aligned} &\frac{d^2E}{dz^2}+k^2\varepsilon_l(z)E=0, \quad z\le 0\\ &\frac{d^2E}{dz^2}+k^2\varepsilon(z)E=0, \quad 0\le z\le a\\ &\frac{d^2E}{dz^2}+k^2\varepsilon_r(z)E=0, \quad z\ge a \end{aligned} \tag{1.1}$$

Here E is the electrical field, $k=\frac{\omega}{c}$ with ω the frequency of the propagating wave, c is the light velocity in vacuum, and $\varepsilon_l, \varepsilon, \varepsilon_r$ are the dielectric permittivities of, respectively, the left half-space, the plate, and the right half-space. The continuity conditions at the $z = 0$ and $z = a$ planes for the field E and its derivative with respect to z are:

$$\begin{aligned} &E(-0)=E(+0), \quad \frac{\partial E(-0)}{\partial z}=\frac{\partial E(+0)}{\partial z};\\ &E(-a)=E(+a), \quad \frac{\partial E(-a)}{\partial z}=\frac{\partial E(+a)}{\partial z} \end{aligned} \tag{1.2}$$

In addition, at ±∞, the radiation conditions have to be satisfied. We consider first a problem of the wave reflecting and transmitting with no plate between the half-spaces, that is, assuming $a = 0$. The waves in the left half-space are described by the first of equations (1.1) and in the right half-space, by the third one. Let $U_{l1}(z)$ and $U_{l2}(z)$ be the fundamental solution-system of the first of equations (1.1) with the $U_{l1}(0)=U_{l2}(0)=1$ condition. Also, in view of the radiation conditions, $U_{l1}(z)$ is the wave propagating to the right, i.e. the incident wave, and $U_{l2}(z)$ propagates to the left, i. e. the reflected wave. $U_r(z)$ is the wave propagating to the right (transmitted wave), $U_r(z)=1$. Desired solution of the problem has a form

$$E(z)=\begin{cases} U_{l1}(z)+R_0U_{l2}(z) & for \quad z<0 \\ T_0U_r(z) & for \quad z>0 \end{cases} \tag{1.3}$$

where R_0 and T_0 are the coefficients of reflection and transmission, respectively. R_0 and T_0 deduced from boundary conditions (1.2) are resulting in:

$$R_0=\frac{U_r'(0)-U_{l_1}'(0)}{U_{l_2}'(0)-U_r'(0)} \tag{1.4}$$

$$T_0=\frac{U_{l_2}'(0)-U_{l_1}'(0)}{U_{l_2}'(0)-U_r'(0)} \tag{1.5}$$

here and in the following equations, the tag means differentiation by *z*.

Now, consider the same problem, but in the presence of the inhomogeneous plate. Let $U_2(z)$ and $U_2(z)$ form the fundamental solution-system of the second of equations (1) with the $U_1(0)=U_2(0)=1$ condition.

Then, the solution of the system (1.1) we are looking for, has a form

$$E(z)=\begin{cases} U_{l1}(z)+RU_{l2}(z) & for \quad z\le 0 \\ A_1U_1(z)+A_2U_2(z) & for \quad 0\le z\le a \\ TU_r(z) & for \quad z\ge a \end{cases} \tag{1.6}$$

Using boundary conditions (1.2) and solutions (1.6), a system of equations is obtained determining the reflection coefficient *R*, transmission coefficient *T*, A_1 and A_2 the and coefficients. Then, solving this system gives the following expressions for *R* and *T*:

$$R=\frac{[U_1'(a)-U_r(a)U_2'(a)][U_2'(0)-U_{l1}'(0)]+[U_2'(a)-U_2(a)U_r'(a)][U_{l1}'(0)-U_1'(0)]}{[U_1'(a)-U_1(a)U_r'(a)][U_2'(0)-U_{l1}'(0)]+[U_2'(a)-U_2(a)U_r'(a)][U_{l2}'(0)-U_1'(0)]} \tag{1.7}$$

$$T=\frac{[U_2'(0)-U_{l_1}'(0)][U_{l_2}'(0)-U_1'(0)]-[U_{l_1}'(0)-U_1'(0)][U_2'(0)-U_{l_1}'(0)]}{[U_1'(a)-U_1(a)U_r(a)][U_2'(0)-U_{l_1}'(0)]+[U_2'(a)-U_1(a)U_r'(a)][U_{l_2}'(0)-U_1'(0)]} \times\frac{[U_1(a)U_2'(a)-U_1'(a)U_2(a)]}{U_2'(0)-U_1'(0)} \tag{1.8}$$

From the equations (1.1), the following formulas are derived:

$$U_{l_{1,2}}'=\pm i\sqrt{\varepsilon_l(0)},\quad U_{1,2}'(0)=\pm ik\sqrt{\varepsilon(0)},\quad U_r'(a)=ik\sqrt{\varepsilon(a)} \tag{1.9}$$

Let us dwell on the concept of absolute transparency of a plate. For homogeneous plate, this question has been studied in detail in Ref. [2]. For a uniform isotropic plate, it has been shown in Ref. [2] that for a discrete set of frequencies fixed by:

$$k\sqrt{\varepsilon} = q\pi \tag{1.10}$$

where q is an integer, the wave reflected from the l-half-space/plate/r-half-space system behaves as if the plate is absent. This means that the plate can be referred to as completely transparent. The reflection and transmission coefficients coincide with, respectively, those for the l-half-space/r-half-space system determined by formulas (1.4) and (1.5). With no temporal dispersion and ε ω-independent, one obtains from (1.10)

$$\omega_q = \frac{q\pi c}{\sqrt{\varepsilon} a} \tag{1.11}$$

The presence of temporal dispersion introduces serious difficulties in solving equation (1.10).

In the general case of inhomogeneous plate and half-spaces, the absolute-transparency conditions are apparently as follows:

$$R(a,\omega) = R_0(\omega), \quad T(a,\omega) = T_0(\omega) \tag{1.12}$$

where of one can readily proceed to

$$[1 - U_1(a)][U_2'(a) - U_r'(a)] - [1 - U_2(a)][U_1'(a) - U_r'(a)] = 0$$

and then to

$$U_{1,2}(\omega,a) = U_{1,2}(\omega,0) = 1 \tag{1.13}$$

or to

$$U_{1,2}'(\omega,a) = U_{1,2}'(\omega,0) \tag{1.14}$$

Each of these correlations, (1.13) and (1.14), can be regarded as the equation for determining the frequencies and the plate's thicknesses for which the plate is transparent.

The wave propagation through an inhomogeneous plate with ε specifically depending on z has been considered previously [3, 4], but the question of the plate's transparency was not discussed in this work. As for a homogeneous plate, it is transparent for any thickness at the frequencies determined by (1.10).

For the following, we shall need an explicit form for the $U_{l_{1,2}}$, $U_{1,2}$ and U functions.

Let the distances b_l, b_r and b, at which the $\varepsilon_l(z)$, $\varepsilon_r(z)$ and $\varepsilon(z)$ functions substantially change, far exceed the wave-length, so that the WKB method is applicable. Note that

$$b_l^{-1} \sim \frac{1}{\varepsilon_l}\frac{d\varepsilon_l}{dz},\quad b_r^{-1} \sim \frac{1}{\varepsilon_r}\frac{d\varepsilon_r}{dz},\quad b^{-1} \sim \frac{1}{\varepsilon}\frac{d\varepsilon}{dz}$$

The criteria of applicability of the WKB method and the explicit form of the corresponding solutions are well known [4]:

$$\frac{1}{k\sqrt{\varepsilon_l(z)}}\frac{d\varepsilon_l(z)}{dz} << 1,\quad \frac{1}{k\sqrt{\varepsilon_r(z)}}\frac{d\varepsilon_r(z)}{dz} << 1,\quad \frac{1}{k\sqrt{\varepsilon(z)}}\frac{d\varepsilon(z)}{dz} << 1 \tag{1.15}$$

which is the same as $k\sqrt{\varepsilon_l(z)}b_l,\ k\sqrt{\varepsilon_r(z)}b_r,\ k\sqrt{\varepsilon(z)}b \gg 1$, and

$$\begin{aligned} U_{l1,2}(z) &= \left(\frac{\varepsilon_l(0)}{\varepsilon_l(z)}\right)^{1/4} e^{\pm iS_l(z)} \\ U_r(z) &= \left(\frac{\varepsilon_r(0)}{\varepsilon_r(z)}\right)^{1/4} e^{\pm iS_r(z)} \\ U(z) &= \left(\frac{\varepsilon(0)}{\varepsilon(z)}\right)^{1/4} e^{\pm iS(z)} \end{aligned} \tag{1.16}$$

Here, $S_l(z) = k\int_0^z \varepsilon_l^{1/2}(z)dz,\ S_r(z) = k\int_0^z \varepsilon_r^{1/2}(z)dz$, and $S(z) = k\int_0^z \varepsilon^{1/2}(z)dz$. Substituting (1.16) into (1.7) and (1.8) gives for the reflection, R, and transmission, T, coefficients:

$$R = \frac{R_1 + R_2 e^{2iS}}{1 + R_1 R_2 e^{2iS}},\quad T = \left(\frac{\varepsilon(0)}{\varepsilon(a)}\right)^{1/4} \frac{T_1 T_2 e^{2iS}}{1 + R_1 R_2 e^{2iS}} \tag{1.17}$$

where

$$R_1 = \frac{\sqrt{\varepsilon(0)} - \sqrt{\varepsilon_l(0)}}{\sqrt{\varepsilon(0)} + \sqrt{\varepsilon_l(0)}},\quad R_2 = \frac{\sqrt{\varepsilon_r(a)} - \sqrt{\varepsilon(a)}}{\sqrt{\varepsilon_r(a)} + \sqrt{\varepsilon(a)}}$$

$$T_1 = \frac{2\sqrt{\varepsilon_l(0)}}{\sqrt{\varepsilon(0)} + \sqrt{\varepsilon_l(0)}},\quad T_2 = \frac{2\sqrt{\varepsilon(0)}}{\sqrt{\varepsilon_r(0)} + \sqrt{\varepsilon(0)}}$$

Note that in the absence of the plate (a = 0), the reflection R_{lr} and transmission T_{lr} coefficients are:

$$R_{lr} = \frac{\sqrt{\varepsilon_r(0)} - \sqrt{\varepsilon_l(0)}}{\sqrt{\varepsilon(0)} + \sqrt{\varepsilon_l(0)}}, \quad T_1 = \frac{2\sqrt{\varepsilon_l(0)}}{\sqrt{\varepsilon_r(0)} + \sqrt{\varepsilon_l(0)}} \tag{1.18}$$

From (1.13), as well as from (1.14), the following criterions of transparency can be derived:

$$S(a) = \pi q, \quad \varepsilon(a) = \varepsilon(0) \tag{1.19}$$

where q is an integer. We consider some examples of applications for formulas (1.19). Let $\varepsilon(z)$ be a periodical function of z with the period L, that is, $\varepsilon(z + L)=\varepsilon(z)$. Then, from the second equation of (1.19), we obtain

$$a = pL \tag{1.20}$$

where p is an integer. Decomposing $\sqrt{\varepsilon(z)}$ into its Fourier expansion and isolating the zero term, gives

$$\sqrt{\varepsilon(z)} = \sum_{\alpha=-\infty}^{\infty} \eta_\alpha e^{\frac{2\pi i\alpha}{L}z} = \eta_0 + \sum_{\substack{\alpha=-\infty \\ \alpha\neq 0}}^{\infty} \eta_\alpha e^{\frac{2\pi i\alpha}{L}z} \tag{1.21}$$

Substituting this expansion into the first formula of (1.19), the transparency condition for the plate's thickness is

$$k\eta_0 a = \pi q \tag{1.22}$$

With no temporal dispersion, i. e., η_0 being non-dependent of ω, the result is given by

$$\omega_q = \frac{q\pi c}{\eta_0 a} \tag{1.23}$$

And, with account of (1.20):

$$\omega_q = \omega_{qp} = \frac{\pi c}{\eta_0 L}\frac{q}{p} \tag{1.24}$$

It is seen that all the plates with thickness according to (1.20) and at frequencies defined by (1.24), are absolutely transparent. The cases of such a kind are infinite in number. Now, let the function $\sqrt{\varepsilon(z)}$ be polynomial of *N*th power, which represents a general enough and interesting case because, on finite interval $[0,a]$, $\sqrt{\varepsilon(z)}$ can be approximated by a polynomial with any degree of accuracy. It is obvious that this polynomial can be written as

$$\sqrt{\varepsilon(z)} = \sqrt{\varepsilon(0)} + \frac{z}{b}\sum_{\zeta=1}^{N}\eta_\zeta\left(\frac{z}{b}\right)^{\zeta-1} \tag{1.25}$$

here *b* is the distance at which the $\varepsilon(z)$ function substantially changes. It follows from the second condition of (1.19) that the possible values of thickness a are defined by the equation

$$\sum_{\zeta=1}^{N}\eta_\zeta\left(\frac{z}{b}\right)^{\zeta-1} = 0 \tag{1.26}$$

and the number of these values is equal to that of positive solutions of (1.25). It is evident that the possible number of these thicknesses is not more than $N-1$.

Consider some special cases.

a) $N = 1$. Equation (1.24) has no roots, which means that a plate whose $\sqrt{\varepsilon(z)}$ function changes linearly along the z axis, is always nontransparent.

b) $N = 2$. $a = -b\frac{\eta_2}{\eta_1}$, the plate is transparent if $-\frac{\eta_2}{\eta_1} > 0$.

c) $N > 2$. These cases can be considered by analytically or numerically solving Eq. (1.25). In the absence of temporal dispersion, from Eq. (1.25) an expression for the transparency frequencies is obtained:

$$\omega_{q\alpha} = \frac{q\pi c}{\sqrt{\varepsilon(0)}a_\alpha\left[1 + \frac{1}{\sqrt{\varepsilon(0)}}\sum_{\zeta=1}^{N'}\frac{\eta_\zeta}{\zeta+1}\left(\frac{a_\alpha}{b}\right)^{\zeta}\right]} \tag{1.27}$$

Here α denotes positive-root's number of equation (1.25) and N' the number of these roots. If the medium's dielectric permittivity changes at distances much shorter than the wavelength, then electrodynamic properties of the medium, as it was shown in Ref. [5], are described by a dielectric tensor with components non-dependent on *z*, that is the plate is homogeneous.

Note that all results obtained in this section hold also for the scalar field ψ described by the Helmgoltz equation. The case of oblique incidence can also be considered with a solution in the following form:

$$\psi(x,z) = U(z)e^{ik\cos\theta x}$$

where θ is the incident angle and $U(z)$ is described, as before, by Eqs. (1.1), where the following substitutions have to be performed: $\varepsilon_l(z) \to \varepsilon_l(z) - \cos^2\theta$, $\varepsilon(z) \to \varepsilon(z) - \cos^2\theta$, and $\varepsilon_r(z) \to \varepsilon_r(z) - \cos^2\theta$. We end this section by considering an inhomogeneous plate with an inhomogeneous half-space at each side of the plate, the dielectric permittivity of the latter being a random function of the z-coordinate:

$$\varepsilon(z) = \overline{\varepsilon(z)} + \delta\varepsilon(z) \tag{1.28}$$

the upper bar denotes ensemble averaging. Thus, $\varepsilon(z)$ is the average value of the dielectric permittivity and $\delta\varepsilon(z)$ is the fluctuation of the latter. By definition, $\delta\varepsilon(z) = 0$. Suppose as usual that R_1 and R_2 in formulas (1.17) for R and T can be regarded as determinate values, and the only random value here is the phase S:

$$S = k\int_0^a n(z)dz \tag{1.29}$$

where $n(z) = \sqrt{\varepsilon(z)}$. Writing the phase as

$$S = \overline{S} + \delta S \tag{1.30}$$

with $\overline{S}$ being the average value of the phase and δS its fluctuation,

$$\overline{S} = k\int_0^a \overline{n(z)}dz \quad and \quad \delta S = k\int_0^a \overline{\delta n^2(z)}l_n(z)dz, \quad \left(\overline{\delta S} = 0\right) \tag{1.31}$$

Average square of δS is defined by:

$$\overline{\delta S^2} = k^2\int_0^a \overline{\delta n^2(z)}l_n(z)dz \tag{1.32}$$

where

$$\overline{\delta n^2(z)}l_n(z) = \int_0^\infty \overline{\delta n(\xi + z)\delta n(z)}d\xi \tag{1.33}$$

$l_n(z)$ being the mean correlation coefficient of fluctuations of the refractive-index. If the fluctuations of the dielectric permittivity $\delta\varepsilon$ are small compared to its mean value $\bar{\varepsilon}$, then

$$\delta n = \frac{\delta\varepsilon(z)}{2\sqrt{\overline{\varepsilon(z)}}} \tag{1.34}$$

and for $\overline{(\delta S)^2}$, we have

$$\overline{(\delta S)^2} = \frac{k^2}{4}\int_0^a \frac{\overline{\delta\varepsilon^2(z)}l_\varepsilon(z)}{\varepsilon(z)}dz \tag{1.35}$$

Here $l_\varepsilon(z)$ stands for the effective correlation coefficient of fluctuations of the dielectric permittivity. Note that $l_n(z)$ and $l_\varepsilon(z)$ are of the order of *b*.

We are interested in the mean values of the reflection *R* and transmission *T* coefficients, as well as in the average of their modules squared:

$$\begin{aligned} \overline{R}, &= \int R(S)F(S)dS, \quad \overline{|R|^2} = \int |R(S)|^2 F(S)dS \\ \overline{T}, &= \int T(S)F(S)dS, \quad \overline{|T|^2} = \int |T(S)|^2 F(S)dS \end{aligned} \tag{1.36}$$

Consider first a distribution function of the following type:

$$F(S) = \begin{cases} \dfrac{1}{2S_0}, & for \quad \overline{S} - S_0 \le S \le \overline{S} + S_0 \\ 0, & for \quad S \le \overline{S} - S_0; \quad S \ge \overline{S} + S_0 \end{cases} \tag{1.37}$$

where $S_0^2 = 3\overline{|\delta S|^2}$, i. e., the mean-square value, accurate to fixed factor, of the phase incursion. For the sought values, we get

$$\overline{R} = R_1 - \frac{iR_1^2}{4S_0}\ln\frac{1 + R_1R_2e^{2i(\overline{S}+S_0)}}{1 + R_1R_2e^{2i(\overline{S}-S_0)}} \tag{1.38}$$

$$\overline{T} = \frac{\sqrt{\dfrac{\varepsilon(0)}{\varepsilon(a)}}T_1T_2}{2S_0\sqrt{R_1R_2}}\left[\arctan\sqrt{R_1R_2}e^{i(\overline{S}+S_0)} - \arctan\sqrt{R_1R_2}e^{i(\overline{S}-S_0)}\right] \tag{1.39}$$

Note that $S_0 = 2\pi q, \overline{R} = R$, and $\overline{T} = 0$; corresponding expressions for $|R|^2$ and $|T|^2$ are

$$\overline{|R|^2} = 1 - \frac{T_1^2T_2^2}{2S_0\left(1 - R_1^2R_2^2\right)}\left\{arctan\left[\frac{1 - R_1R_2}{(1 + R_1R_2)^2}tan\left(\overline{S} + S_0\right)\right] - arctan\left[\frac{1 - R_1R_2}{(1 + R_1R_2)^2}tan\left(\overline{S} - S_0\right)\right]\right\} \tag{1.40}$$

$$|T|^2 = \frac{\varepsilon(0)}{\varepsilon(a)}\left(1 - |R|^2\right) \tag{1.41}$$

When $S_0 = 2\pi q, \overline{|R|^2} = 1$ and $\overline{|T|^2} = 0$, that is, the plate is completely opaque. This result is analogous to that of obtained in [6] for stochastic localization, but unlike the traditional stochastic localization, for which $|\overline{|R|^2} = 1$ and $\overline{|T|^2} = 0$ only by $a = \infty$ and the correlation coefficient being small compared to the wave length, here the localization takes place by discrete set of the plate's thicknesses. It should be mentioned that in Ref. [7], a problem of the electromagnetic wave propagation through a homogeneous plate confined by statistically rough surfaces, has been considered. In the present work, an analogous problem with Gaussian distribution of the wave phase, has been considered in detail.

1.3. Equations for electromagnetic waves propagating through anisotropic layered media

The Maxwell equation system describing the electromagnetic wave propagation through an anisotropic layered medium is as follows:

$$\begin{aligned} &\frac{d^2E_x}{dz^2} + k_0^2\left[\varepsilon_{xx}(z)E_x + \varepsilon_{xy}(z)E_y + \varepsilon_{xz}(z)E_z\right] = 0 \\ &\frac{d^2E_y}{dz_2} + k_0^2\left[\varepsilon_{yx}(z)E_x + \varepsilon_{yy}(z)E_y + \varepsilon_{yz}(z)E_z\right] = 0 \\ &\varepsilon_{zx}(z)E_x + \varepsilon_{zy}(z)E_y + \varepsilon_{zz}(z)E_z = 0 \end{aligned} \tag{1.42}$$

Here $E_i(z)$ are components of the electric field, $i = x,y,z$, and $\varepsilon_{ik}(k)$ are components of the dielectric permittivity tensor. Eliminating E_z from the equation system (1.42), we get

$$\begin{aligned} &\frac{d^2E_x}{dz^2} + k^2\left[\xi_{xx}(z)E_x + \xi_{xy}(z)E_y\right] = 0 \\ &\frac{d^2E_y}{dz_2} + k^2\left[\xi_{yx}(z)E_x + \xi_{yy}(z)E_y\right] = 0 \end{aligned} \tag{1.43}$$

where

$$\begin{aligned} &\xi_{xx} = \frac{\varepsilon_{xx}\varepsilon_{zz} - \varepsilon_{zx}\varepsilon_{xz}}{\varepsilon_{zz}}, \quad \xi_{xy} = \frac{\varepsilon_{xy}\varepsilon_{zz} - \varepsilon_{zy}\varepsilon_{xz}}{\varepsilon_{zz}} \\ &\xi_{yx} = \frac{\varepsilon_{yx}\varepsilon_{zz} - \varepsilon_{yz}\varepsilon_{zx}}{\varepsilon_{zz}}, \quad \xi_{yy} = \frac{\varepsilon_{yy}\varepsilon_{zz} - \varepsilon_{zy}\varepsilon_{yz}}{\varepsilon_{zz}} \end{aligned} \tag{1.44}$$

Hence, the electromagnetic wave propagation through layered anisotropic medium is described by a system of two second-order equations. The solving of this system is significantly simplified if it can be reduced to two independent equations. For getting the conditions of such a reduction, multiply the second equation of the system (1.43) by a constant $Q_\pm$, sum it up with the first one, factor out the coefficient by Ex, and coefficient by E_y equate with $Q_\pm$, which gives an equation for deriving $Q_\pm$. As a result, we arrive at

$$\frac{d^2E_\pm}{dz^2} + k^2\varepsilon_\pm(z)E_\pm = 0 \tag{1.45}$$

where

$$\begin{aligned} &E_\pm = E_x + Q_\pm E_y \\ &\varepsilon_\pm(z) = \xi_{xx}(z) + Q_\pm \xi_{yx}(z) \\ &\quad = \frac{\xi_{xx}+\xi_{yy}}{2} \pm \sqrt{\frac{(\xi_{xx}+\xi_{yy})^2}{4} + \xi_{yx}\xi_{xy}} \end{aligned} \tag{1.46}$$

and

$$Q_\pm = -\frac{\xi_{xx}-\xi_{yy}}{2\xi_{yx}} \pm \sqrt{\left(\frac{\xi_{xx}-\xi_{yy}}{2\xi_{yx}}\right)^2 + \frac{\xi_{xy}}{\xi_{yx}}} \tag{1.47}$$

For the values $Q_\pm$ to be constant, it is sufficient that the following combinations of the ξ-tensor components would be constant:

$$\frac{\xi_{yy}-\xi_{xx}}{\xi_{yx}} = Q_+ + Q_-, \quad \frac{\xi_{xy}}{\xi_{yx}} = -Q_+Q_- \tag{1.48}$$

Hereinafter we shall assume the conditions (1.48) are satisfied and that the equation system (1.43) can be represented in the form of (1.45). Consider some important special cases. Let the diagonal components ξ_{xx} and ξ_{yy} of the ξ-tensor be equal. Then $Q_+ + Q_- = 0$, from which follows

$$Q_+ = -Q_-, \quad \frac{\xi_{xy}}{\xi_{yx}} = Q_\pm^2 \tag{1.49}$$

If the ξ-tensor is symmetric, $\xi_{xy} = \xi_{yx}$, then $E_\pm = E_x \pm E_y$, $n_\pm^2 = \xi_{xx} \pm \xi_{yx}$, and $Q_\pm = \pm 1$. If this tensor is antisymmetric, $\xi_{xy} = -\xi_{yx}$, then $E_\pm = E_x \pm iE_y$, $n_\pm^2 = \xi_{xx} \pm i\xi_{yx}$, and $Q_\pm = \pm i$, refractive index $n_\pm(z) = \sqrt{\varepsilon_\pm(z)}$ being defined by (1.46). The case of $\xi_{xy} = \xi_{yx} = 0$ is also of importance. Then Eqs. (1.43) can be separated into two independent equations

$$\frac{d^2E_x}{dz^2} + k^2\xi_{xx}E_x = 0 \tag{1.50}$$

and

$$\frac{d^2E_y}{dz^2} + k^2\xi_{yy}E_y = 0 \tag{1.51}$$

Now, substituting the expressions for the components of the tensor ξ from (1.43) into (1.48) gives

$$\frac{(\varepsilon_{yy} - \varepsilon_{xx})\varepsilon_z + \varepsilon_{xz}\varepsilon_{zx} - \varepsilon_{zy}\varepsilon_{yz}}{\varepsilon_{zz}} = Q_+ + Q_-, \quad \frac{\varepsilon_{xy}\varepsilon_{zz} - \varepsilon_{zy}\varepsilon_{xz}}{\varepsilon_{yx}\varepsilon_{zz} - \varepsilon_{zx}\varepsilon_{yz}} = Q_+ + Q_- \tag{1.52}$$

that is, in order the three-equation system (1.42) to be split into two independent equations, the following condition must be fulfilled: two combinations composed from the nine components of the ε_{ik} tensor have to be constants. A wide enough class of the dielectric permittivity tensors meet this requirement. E_x and E_y, as well as D_x and D_y, can be expressed through $E_\pm$:

$$\begin{gathered} E_x = \frac{Q_-E_+ - Q_+E_-}{Q_- - Q_+}, \quad E_y = \frac{E_- - E_+}{Q_- - Q_+} \\ D_x = \xi_{xx}E_x + \xi_{xy}E_y, \quad D_y = \xi_{yx}E_x + \xi_{yy}E_y \end{gathered} \tag{1.53}$$

1.4. Faraday effect in inhomogeneous anisotropic media

To begin with, consider electromagnetic waves propagating through unbounded inhomogeneous anisotropic media. Through this whole section we assume that the electromagnetic field in a medium is described by Eqs. (1.45), that is, the components of the ξ tensor satisfy conditions (1.48). Exact solution of Eqs. (1.45) can be obtained for a wide enough class of the $\varepsilon_\pm(z)$ functions (cf., f.e., [2]). We will not dwell on these solutions and content ourselves with results obtained using the WKB approach. Such a choice is favoured by the fact that by small values of z, that is, when one can assume $\varepsilon_\pm(z) = \varepsilon_\pm(0)$, then $E_\pm = e^{ik\sqrt{\varepsilon_\pm(0)}z}$ is derived from the formulas for the fields obtained by the WKB method, see (1.16). For large values of z, the WKB approach is an asymptotically exact one. Thus, for small and large values of z, the WKB method gives correct results. We expect that also for intermediate values of z, the fields obtained by the WKB method are good approximations. Consider first the Faraday effect in unbounded medium. It is known [5], that this effect is characterized by the relation D_y / D_x describing the rotation of the polarization plane of a wave propagating in an anisotropic medium:

$$\frac{D_y}{D_x} = \frac{\xi_{yx}(Q_-E_+ - Q_+E_-) + \xi_{yy}(E_- - E_+)}{\xi_{xx}(Q_-E_+ - Q_+E_-) + \xi_{xy}(E_- - E_+)} \tag{1.54}$$

$E_{\pm}$ being calculated in the WKB approximation, we obtain

$$E_{\pm} = \sqrt{\frac{\varepsilon_{\pm}(0)}{\varepsilon_{\pm}(z)}}e^{iS_{\pm}}, \quad S_{\pm} = \int_0^z \sqrt{\varepsilon_{\pm}(z)}dz \tag{1.55}$$

and formula (1.54) turns into

$$\frac{D_y}{D_x} = \frac{\left(\xi_{yx}Q_- - \xi_{yy}\right)\sqrt[4]{\frac{\varepsilon_+(0)}{\varepsilon_+(z)}}e^{iS_+} - \left(\xi_{yx}Q_+ - \xi_{yy}\right)\sqrt[4]{\frac{\varepsilon_-(0)}{\varepsilon_-(z)}}e^{iS_-}}{\left(\xi_{xx}Q_- - \xi_{xy}\right)\sqrt[4]{\frac{\varepsilon_+(0)}{\varepsilon_+(z)}}e^{iS_+} - \left(\xi_{xx}Q_+ - \xi_{xy}\right)\sqrt[4]{\frac{\varepsilon_-(0)}{\varepsilon_-(z)}}e^{iS_-}} \tag{1.56}$$

With the aid of expression (1.56), we explore the rotation of the polarization plane of a wave propagating in a gyrotropic medium. A medium is called gyrotropic if the electrical induction vector is related to the electrical field vector by the relation [5]

$$\vec{D} = \varepsilon\vec{E} + i\left[\vec{E},\vec{g}\right] \tag{1.57}$$

where $\vec{g}$ is the gyration vector, ε and $\vec{g}$ being slowly changing functions of z. We will assume the $\vec{g}$-vector lies in the xz-plane, i.e., having only components g_x and g_z. We assume also that the $\vec{g}$-vector is small in the sense that $|g| \ll \varepsilon$ and values of g^2 can be neglected. Using (1.46) and (1.47), and the smallness of g, we get

$$\frac{D_y}{D_x} = \tan\left(\frac{k_0}{2}\int_0^z \frac{g(z)}{\sqrt{\varepsilon(z)}}dz\right) \tag{1.58}$$

With g_x and g_z non-dependent on z, this formula turns into the wellknown expression for the rotation of the polarization plane of the field in gyrotropic homogeneous medium. Now, let the inhomogeneous medium be consisting of an inhomogeneous anisotropic plate with an inhomogeneous half-space on each of sides. Then, the rotation of the polarization plane for the reflected and transmitted fields, respectively are

$$\left(\frac{D_y}{D_x}\right)_R = \frac{\xi_{yx}(0)\left(Q_-R_+ - Q_+R_-\right) + \xi_{yy}(0)\left(R_- - R_+\right)}{\xi_{xx}(0)\left(Q_-R_+ - Q_+R_-\right) + \xi_{xy}(0)\left(R_- - R_+\right)} \tag{1.59}$$

and

$$\left(\frac{D_y}{D_x}\right)_T = \frac{\xi_{yx}(a)\left(Q_-T_+ - Q_+T_-\right) + \xi_{yy}(a)\left(T_- - T_+\right)}{\xi_{xx}(a)\left(Q_-T_+ - Q_+T_-\right) + \xi_{xy}(a)\left(T_- - T_+\right)} \tag{1.60}$$

In the general case, $R_\pm$ and $T_\pm$ are determined by formulas (1.7) and (1.8), respectively, and using the WKB approach, by (1.17). If the inhomogeneous plate is gyrotropic, one has to considerate two cases: a totally transparent plate and a non-transparent plate. The results are presented with components of the ξ_{ik}-tensor expressed in terms of the $\vec{g}$-vector, using Eq. (1.57). For the transparent plate, omitting cumbersome elementary calculations, we get:

$$\left(\frac{D_y}{D_x}\right)_R = \frac{R_2\left(1-R_1^2\right)e^{2iS_a}\sin\sigma}{R_1+\left(1+R_1^2\right)R_2e^{2iS_a}\cos\sigma+R_1R_2^2e^{4iS_a}\sin\sigma} \tag{1.61}$$

$$\left(\frac{D_y}{D_x}\right)_T = \frac{\left(1-R_1R_2\right)e^{2iS_a}\tan\sigma}{1+R_1R_2e^{2iS_a}} \tag{1.62}$$

where $R_{1,2}$ are the same as in (1.17), $S_a = k_0\int_0^a\sqrt{\varepsilon_\pm(z)}dz$, and $\sigma = \frac{k_0}{2}\int_0^z\frac{g(z)}{\sqrt{\varepsilon(z)}}dz$. Analysis and simplification of formulas (1.61) and (1.62) are analogous to the ones carried out in Ref. [1]. The transparency conditions for both waves, as follows from (1.19), are:

$$S_+(a)=\pi q_+,\quad \varepsilon_+(a)=\varepsilon_+(0),\quad S_-(a)=\pi q_-,\quad \varepsilon_-(a)=\varepsilon_-(0) \tag{1.63}$$

where q_+ and q_- are integers, which in general do not coincide. The solutions defining the plate's thicknesses and corresponding frequencies at which the plate is transparent for the reflected wave do not coincide with those for the transmitted wave. However, with small gyrotropy ($g \ll \varepsilon$) and a narrow enough incident wave impulse [1], the plate can be transparent for both waves. The gyrotropy results in a frequency shift that can be determined from Eqs. (1.63), for which aim $q_+ = q_- = q$ has to be put. If the gyrotropy is small (the criterion is given above), then Eqs. (1.63) can be solved using the convergence method, which gives the frequency shift

$$\delta\omega = \delta\omega_{+q} = -\delta\omega_{-q} = k\frac{g(0)-g(a)}{\dfrac{d\varepsilon(a)}{da}} - \frac{\dfrac{k}{2}\displaystyle\int_0^{a_0}\frac{g(z)}{\sqrt{\varepsilon(z)}}dz}{\displaystyle\int_0^{a_0}\frac{dz}{v_g(z)}} \tag{1.64}$$

Here $\frac{1}{v_g(z)} = \frac{d}{d\omega}k\sqrt{\varepsilon(z)}$, k and a_0 are determined from (1.19). Note that for homogeneous plates, the first item in (1.64) is absent. For the fields $E_{R_\pm}$ and $E_{T_\pm}$ we have

$$\begin{aligned} E_{R_\pm} &= R_{lr} e^{-i\left[\omega_q t + S_l\right]} e^{\pm i\delta\omega\left[t + \int_0^z \frac{dz}{v_{gl}(z)}\right]} \\ E_{T_\pm} &= T_{lr} e^{-i\left[\omega_q t + S_r\right]} e^{\pm i\delta\omega\left[t - \int_0^z \frac{dz}{v_{gr}(z)} \pm \varphi\right]} \end{aligned} \tag{1.65}$$

with

$$\varphi = k\frac{g(a) - g(0)}{d\varepsilon / da}$$

And, finally, the rotation of the polarization plane of the reflected and transmitted fields are, respectively,

$$\begin{aligned} \left(\frac{D_y}{D_x}\right)_R &= \tan\delta\omega\left[t + \int_0^z \frac{dz}{v_{gl}(z)}\right] \\ \left(\frac{D_y}{D_x}\right)_T &= \tan\delta\omega\left[t - \int_0^z \frac{dz}{v_{gr}(z)} + \varphi\right] \end{aligned} \tag{1.66}$$

One can see that here, like in the case of homogeneous plate [1], the rotation of the polarization plane has both spatial and temporal components. We will not dwell on the situation when $\xi_{xy} = \xi_{yx}$, because for this case Eqs. (1.50), (1.51) are of the same structure as Eqs. (1.45), which allows to carry out corresponding analysis in an analogous way.

1.5. Conclusions

As asumming up, the Fresnel formulas are generalized for the reflection coefficients of an isotropic plate the dielectric permittivity of which, as well as the dielectric permittivities of enclosing half-spaces, are arbitrary functions of the coordinate, either determinate or stochastic. For the general case, the conditions for the plate's full transparency are formulated. As an example, a case is considered when the plate's dielectric permittivity is a slowly changing function of the coordinate, which justifies application of the WKB method. When the plate's dielectric permittivity is a stochastic function of the coordinate, a new effect appears: the full non-transparency (opacity) for a discrete set of the plate's thicknesses. For an anisotropic plate, sufficient conditions are formulated for the two- equation Maxwell system to be split into two independent equations, which simplifies substantially the calculations. All these results can be applied immediately for working out the needed parameters of the Fabry-Perot interferometers, filters, resonators.

2. WAVES IN INHOMOGENEOUS SOLIDS

The paper aims at presenting a numerical technique used in simulating the propagation of waves in inhomogeneous elastic solids. The basic governing equations are solved by means of a finite-volume scheme that is faithful, accurate, and conservative. Furthermore, this scheme is compatible with thermodynamics through the identification of the notions of numerical fluxes (a notion from numerics) and of excess quantities (a notion from irreversible thermodynamics). A selection of one-dimensional wave propagation problems is presented, the simulation of which exploits the designed numerical scheme. This selection of exemplary problems includes (i) waves in periodic media for weakly nonlinear waves with atypical formation of a wave train, (ii) linear waves in laminates with the competition of different length scales, (iii) nonlinear waves in laminates under an impact loading with a comparison with available experimental data, and (iv) waves in functionally graded materials.

2.1 Introduction

Waves correspond to continuous variations of the states of material points representing a medium. The characteristic feature of waves is their motion. In mechanics the motion of waves is governed by the conservation laws for mass, linear momentum, and energy. These conservation laws, complemented by constitutive relations, are the basis of the theory of thermoelastic waves in solids [8, 10, 16, 26]. Inhomogeneous solids include layered and randomly reinforced composites, multiphase and polycrystalline alloys, functionally graded materials, ceramics and polymers with certain microstructure, etc. Therefore, it is impossible to present a complete theory of linear and nonlinear wave propagation for the full diversity of possible situations, in so far as geometry, contrast of multiphase properties and loading conditions are concerned. From a practical point of view, we need to perform numerical calculations. Many numerical methods have been proposed to compute wave propagation in heterogeneous solids, among them, the stiffness matrix recursive algorithm [40, 45] and the spectral layer element method [17, 18] should be mentioned, in addition to more common finite-element, finite-difference, and finite-volume methods. Here the general idea is the following: division of a body into a finite number of computational cells requires the description of all fields inside the cells as well as the interaction between neighboring cells. Approximation of wanted fields inside the cells leads to discontinuities of the fields at the boundaries between cells. This also leads to the appearance of excess quantities, which represent the difference between the exact and approximate values of the fields. Interaction between neighboring cells is described by means of fluxes at the boundaries of the cells. These fluxes correspond to the excess quantities and, therefore, can be calculated by means of jump relations at the boundaries between cells. In this paper, we demonstrate how the finite-volume wave-propagation algorithm developed in [34] can be reformulated in terms of the excess quantities and then applied to the wave propagation in inhomogeneous solids. Both original and modified algorithms are stable, high-order accurate, thermodynamically consistent, and applicable both to linear and nonlinear waves.

2.1.1 Governing equations

The simplest example of heterogeneous media is a periodic medium composed by materials with different properties. One-dimensional wave propagation in the framework of linear elasticity is governed by the conservation of linear momentum [8]

$$\rho(x)\frac{\partial v}{\partial t}-\frac{\partial \sigma}{\partial x}=0 \tag{2.1}$$

and the kinematic compatibility condition

$$\frac{\partial \varepsilon}{\partial t}=\frac{\partial v}{\partial x} \tag{2.2}$$

Here t is time, x is the space variable, the particle velocity $v = u_t$ is the time derivative of the displacement u, the one-dimensional strain $\varepsilon = u_x$ is the space derivative of the displacement, σ is the Cauchy stress, and ρ is the material density. The compatibility condition (2.2) follows immediately from the definitions of the strain and the particle velocity. The two equations (2.1) and (2.2) contain three unknowns: v, σ and ε. The closure of the system of equations (2.1) and (2.2) is achieved by a constitutive relation, which in the simplest case is Hooke's law

$$\sigma=\rho(x)c^2(x)\varepsilon \tag{2.3}$$

where $c(x)=\sqrt{(\lambda(x)+2\mu(x))/\rho(x)}$ is the corresponding longitudinal wave velocity, and $\lambda(x)$ and $\mu(x)$ are the so-called Lamé coefficients. The indicated explicit dependence on the point x means that the medium is materially inhomogeneous. The system of equations (2.1)–(2.3) can be expressed in the form of a conservation law

$$\frac{\partial}{\partial t}q(x,t)+\frac{\partial}{\partial x}f(q(x,t))=0 \tag{2.4}$$

with

$$q(x,t)=\begin{pmatrix}\varepsilon\\ \rho v\end{pmatrix}\text{ and }f(x,t)=\begin{pmatrix}-v\\ -\rho c^2\varepsilon\end{pmatrix} \tag{2.5}$$

In the linear case, equation (2.4) can be rewritten in the form

$$\frac{\partial}{\partial t}q(x,t)+A\frac{\partial}{\partial x}q(x,t)=0 \tag{2.6}$$

where the matrix A is given by

$$A=\begin{pmatrix}0 & -1/\rho\\ -\rho c^2 & 0\end{pmatrix} \tag{2.7}$$

We will solve the system of equations (2.1)–(2.3) numerically. Although a numerical solution can be difficult with standard methods, high-resolution finite volume methods based on solving Riemann problems have been found to perform very well on linear hyperbolic systems modeling wave propagation in rapidly-varying heterogeneous media [23].

2.2 The wave-propagation algorithm

Standard methods cannot give high accuracy near discontinuities in the material parameters and will often fail completely in problems where the parameters vary drastically on the grid scale. By contrast, solving the Riemann problem at each cell interface properly resolves the solution into waves, taking into account every discontinuity in the parameters, and automatically handling the reflection and transmission of waves at each interface. This is crucial in developing the correct macroscopic behavior. As a result, Riemann-solver methods are quite natural for this application. Moreover, the methods extend easily from linear to nonlinear problems. Expositions of such methods and pointers to the rich literature base can be found in many sources [24. 27, 34, 43, 44].

2.2.1 Averaged quantities

Let us introduce a computational grid of cells $C_n=[x_{n-1/2},x_{n+1/2}]$ with interfaces $x_{n-1/2}=(n-1)/2\Delta x$ and time levels $t_k=k\Delta t$. For simplicity, the grid size

Δx and time step Δt are assumed to be constant. Integrating equation (2.4) over $C_n \times [t_k, t_{k+1}]$ gives

$$\int_{x_{n-1/2}}^{x_{n+1/2}} q(x, t_{k+1})dx = \int_{x_{n-1/2}}^{x_{n+1/2}} q(x, t_k)dx - \left(\int_{t_k}^{t_{k+1}} f(q(x_{n+1/2}, t))dt - \int_{t_k}^{t_{k+1}} f(q(x_{n-1/2}, t))dt \right) \tag{2.8}$$

Introducing the average Q_n of the exact solution on C_n at time $t = t_k$ and the numerical flux F_n that approximates the time average of the exact flux taken at the interface between the cells C_{n-1} and C_n, i. e.

$$Q_n \approx \frac{1}{\Delta x} \int_{x_{n-1/2}}^{x_{n+1/2}} q(x, t_k)dx, \quad F_n \approx \frac{1}{\Delta t} \int_{t_k}^{t_{k+1}} f(q(x_{n-1/2}, t))dt \tag{2.9}$$

we can rewrite equation (2.8) in the form of a numerical method in the flux-differencing form

$$Q_n^{k+1} = Q_n^k - \frac{\Delta t}{\Delta x}\left(F_{n+1}^k - F_n^k\right) \tag{2.10}$$

In general, however, we cannot evaluate the time integrals on the right-hand side of equation (2.8) exactly, since $q(x_{n\pm1/2}, t)$ varies with time along each edge of the cell, and we do not have the exact solution to work with. If we can approximate this average flux based on the values Q^k, then we will have a fully-discrete method.

2.2.2 Numerical fluxes

Numerical fluxes are determined by means of the solution of the Riemann problem at interfaces between cells. The solution of the Riemann problem (at the interface between cells $n - 1$ and n) consists of two waves, which we denote, following [34], W_n^I and W_n^{II}. The left-going wave W_n^I moves into cell $n - 1$, and the right-going wave W_n^{II} moves into cell n. The state between the two waves must be continuous across the interface (Rankine-Hugoniot condition) [34]:

$$W_n^I + W_n^{II} = Q_n - Q_{n-1} \tag{2.11}$$

In the linear case, the considered waves are determined by eigenvectors of the matrix A [34]:

$$W_n^I = \gamma_n^I r_{n-1}^I, \quad W_n^{II} = \gamma_n^{II} r_{n-1}^{II} \tag{2.12}$$

This means that equation (2.11) is represented as

$$W_n^I = \gamma_n^I r_{n-1}^I, \quad W_n^{II} = \gamma_n^{II} r_{n-1}^{II} \tag{2.13}$$

Considering the definition of eigenvectors $Ar = \lambda r$, we see that the eigenvector

$$r^I = \begin{pmatrix} 1 \\ \rho c \end{pmatrix} \tag{2.14}$$

corresponds to the eigenvalue $\lambda^I = -c$ (left-going wave). Similarly, the eigenvector

$$r^{II} = \begin{pmatrix} 1 \\ -\rho c \end{pmatrix} \tag{2.15}$$

corresponds to the eigenvalue $\lambda^{II} = c$ (right-going wave). Substituting the eigenvectors into equation (2.13), we have

$$\gamma_n^I \begin{pmatrix} 1 \\ \rho_{n-1} c_{n-1} \end{pmatrix} + \gamma_n^{II} \begin{pmatrix} 1 \\ -\rho_n c_c \end{pmatrix} = Q_n - Q_{n-1} \tag{2.16}$$

or, more explicitly,

$$\begin{pmatrix} 1 & 1 \\ \rho_{n-1} c_{n-1} & -\rho_n c_c \end{pmatrix} \begin{pmatrix} \gamma_n^I \\ \gamma_n^{II} \end{pmatrix} = \begin{pmatrix} \bar{\varepsilon}_n - \bar{\varepsilon}_{n-1} \\ \rho \bar{v}_n - \rho \bar{v}_{n-1} \end{pmatrix} \tag{2.17}$$

Solving the system of linear equations (2.17), we obtain the amplitudes of the left-going and right-going waves. Then the numerical fluxes in the Godunov-type numerical scheme are determined as follows:

$$F_{n+1}^k = -\lambda_{n+1}^I W_{n+1}^I = -c_{n+1} \gamma_{n+1}^I r_n^I \tag{2.18}$$

$$F_n^k = -\lambda_n^{II} W_n^{II} = -c_n \gamma_n^{II} r_n^{II} \tag{2.19}$$

Finally, the Godunov-type scheme is expressed in the form

$$Q_n^{k+1} = Q_n^k + \frac{\Delta t}{\Delta x}\left(c_{n+1} \gamma_{n+1}^I r_n^I - - c_n \gamma_n^{II} r_n^{II}\right) \tag{2.20}$$

This is the standard form for the wave-propagation algorithm [34]. Within the wave-propagation algorithm, every discontinuity in parameters is taken into account by solving the Riemann problem at each interface between discrete elements. The reflection and transmission of waves at each interface are handled automatically for the considered inhomogeneous media.

2.2.3 Second-order corrections

The scheme considered above is formally first-order accurate only. To increase the order of accuracy, we rewrite the numerical scheme as

$$Q_n^{k+1} = Q_n^k + \Delta_n^{up} - \frac{\Delta t}{\Delta x}\left(\tilde{F}_{n+1}^k - \tilde{F}_n^k\right) \tag{2.21}$$

where Δ_n^{up} equals the upwind flux (or Godunov flux) obtained from equation (2.20). The term $\tilde{F}_n^k$ is used to update the solution so that second order accuracy is achieved. The flux for the second-order Lax-Wendroff scheme may be written as the Godunov flux plus a correction [34],

$$F_n = \frac{1}{2}A(Q_n + Q_{n-1}) - \frac{\Delta t}{2\Delta x}A(Q_n + Q_{n+1}) = F_n^G + \frac{1}{2}|A|\left(1 - \frac{\Delta t}{\Delta x}|A|\right)\Delta Q_n \tag{2.22}$$

where $|A| = A^+ - A^-$. Hence, a natural choice for $\tilde{F}$ is

$$\tilde{F}_n = \frac{1}{2}|A|\left(1 - \frac{\Delta t}{\Delta x}|A|\right)\Delta Q_n = \frac{1}{2}\sum_p \left|\lambda^p\right|\left(1 - \frac{\Delta t}{\Delta x}\left|\lambda^p\right|\right)W_n^p \tag{2.23}$$

The Godunov-type scheme exhibits strong numerical dissipation, and discontinuities in the solution are smeared, causing low accuracy. The Lax-Wendroff scheme, on the other hand, is more accurate in smooth parts of the solution. However, near discontinuities, numerical dispersion generates oscillations, also reducing the accuracy. A successful approach to suppress these oscillations is to apply flux limiters [23, 30, 31, 32].

2.2.4 The conservative wave propagation algorithm

For the conservative wave-propagation algorithm [9], the solution of the generalized Riemann problem is obtained by using the decomposition of the flux difference $f_n(Q_n) - f_{n-1}(Q_{n-1})$ instead of the decomposition (2.11):

$$L_n^I + L_n^{II} = f_n(Q_n) - f_{n-1}(Q_{n-1}) \tag{2.24}$$

The waves L_n^I and L_n^{II} are still proportional to the eigenvectors of the matrix A

$$L_n^I = \beta_n^I r_{n-1}^I, \quad L_n^{II} = \beta_n^{II} r_n^{II} \tag{2.25}$$

and the corresponding numerical scheme has the form

$$Q_n^{l+1} - Q_n^l = -\frac{\Delta t}{\Delta x}\left(L_n^{II} + L_{n+1}^I\right) \tag{2.26}$$

The coefficients β^I and β^{II} are determined from the solution of the system of linear equations

$$\begin{pmatrix} 1 & 1 \\ \rho_{n-1}c_{n-1} & -\rho_n c_c \end{pmatrix}\begin{pmatrix} \beta_n^I \\ \beta_n^{II} \end{pmatrix} = \begin{pmatrix} -\left(\widetilde{v}_n - \widetilde{v}_{n-1}\right) \\ -\left(\rho c^2 \overline{\varepsilon}_n - \rho c^2 \overline{\varepsilon}_{n-1}\right) \end{pmatrix} \tag{2.27}$$

As it is shown in [9], the obtained algorithm is conservative and second-order accurate on smooth solutions.

2.3 Excess quantities and numerical fluxes

We could simply apply the numerical scheme described in the previous sections to simulate the wave propagation in periodic media. However, the splitting of the body into a finite number of computational cells and averaging all the fields over the cell volumes leads to a situation known in thermodynamics as "endoreversible system" [29]. This means that even if the state of each computational cell can be associated with a corresponding local equilibrium state (and, therefore, temperature and entropy can be defined as usual), the state of the whole body is a non-equilibrium one. The computational cells interact with each other, which leads to the appearance of excess quantities. In the admitted non-equilibrium description [39], both stress and velocity are represented as the sum of the averaged (local equilibrium) and excess parts:

$$\sigma = \overline{\sigma} + \Sigma, \quad v = \overline{v} + V \tag{2.28}$$

Here $\overline{\sigma}$ and $\overline{v}$ are averaged fields and Σ and V are the corresponding excess quantities. Therefore, we rewrite a first-order Godunov-type scheme (2.10) in terms of the excess quantities

$$\left(\rho\overline{v}\right)_n^{k+1} - \left(\rho\overline{v}\right)_n^k = \frac{\Delta t}{\Delta x}\left(\Sigma_n^+ - \Sigma_n^-\right) \tag{2.29}$$

$$\bar{\varepsilon}_n^{k+1} - \bar{\varepsilon}_n^k = \frac{\Delta t}{\Delta x}\left(V_n^+ - V_n^-\right) \tag{2.30}$$

Here an overbar denotes averaged quantities, a superscript k denotes a time step, a subscript n denotes the number of the computational cell, while Δt and Δx are time step and space step, respectively. Though excess quantities are determined formally everywhere inside computational cells, we need to know only their values at the boundaries of the cells, where they play the role of numerical fluxes. To determine the values of the excess quantities at the boundaries between computational cells, we apply the jump relation for the linear momentum [13], which is reduced in the isothermal case to

$$[\bar{\sigma} + \Sigma] = 0 \tag{2.31}$$

Similarly, the jump relation following from the kinematic compatibility (2.2) reads

$$[\bar{v} + V] = 0 \tag{2.32}$$

It should be noted that the two last jump conditions can be considered as the continuity of genuine unknown fields at the boundaries between computational cells, which is illustrated in Fig. 2.1.

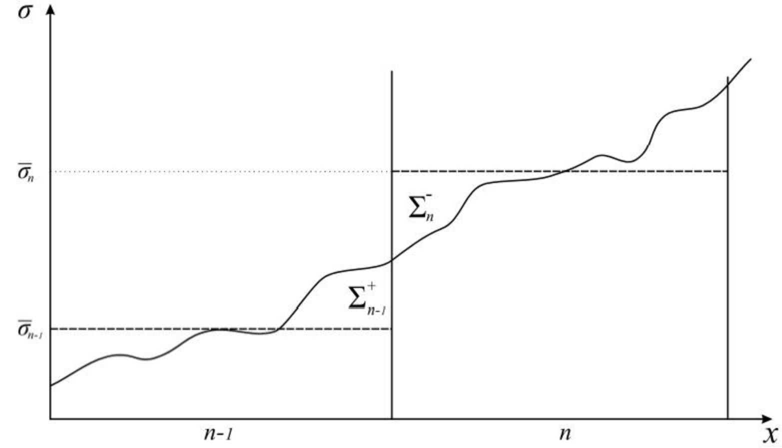

Fig. 2.1 Stresses in the bulk

The values of the excess stresses and excess velocities at the boundaries between computational cells are not independent [15]. Considering Riemann invariants at the interface between computational cells, one can see that

$$\rho_n c_n V_n^- + \Sigma_n^- \equiv 0 \tag{2.33}$$

$$\rho_{n-1} c_{n-1} V_{n-1}^+ - \Sigma_{n-1}^+ \equiv 0 \tag{2.34}$$

i.e., the excess quantities depend on each other at the cell boundary.

2.3.1 Excess quantities at the boundaries between cells

Rewriting the jump relations (2.31), (2.32) in the form

$$\left(\Sigma^{+}\right)_{n-1} - \left(\Sigma^{-}\right)_{n} = \left(\bar{\sigma}\right)_{n} - \left(\bar{\sigma}\right)_{n-1} \tag{2.35}$$

$$\left(V^{+}\right)_{n-1} - \left(V^{-}\right)_{n} = \left(\bar{v}\right)_{n} - \left(\bar{v}\right)_{n-1} \tag{2.36}$$

and using the dependence between excess quantities (equations (2.33) and (2.34)), we obtain then the system of linear equations for the determination of the excess velocities

$$V^{+}_{n-1} - V^{-}_{n} = \bar{v}_{n} - \bar{v}_{n-1} \tag{2.37}$$

$$V^{+}_{n-1}\rho_{n-1}c_{n-1} + V^{-}_{n}\rho_{n}c_{n} = \rho_{n}c^{2}_{n}\bar{\varepsilon}_{n} - \rho_{n-1}c^{2}_{n-1}\bar{\varepsilon}_{n-1} \tag{2.38}$$

In matrix notation the latter system of equations has the form

$$\begin{pmatrix} 1 & 1 \\ \rho_{n-1}c_{n-1} & \rho_{n}c_{n} \end{pmatrix} \begin{pmatrix} -V^{+}_{n-1} \\ V^{-}_{n} \end{pmatrix} = \begin{pmatrix} -\left(\bar{v}_{n} - \bar{v}_{n-1}\right) \\ -\left(\rho c^{2}\bar{\varepsilon}_{n} - \rho c^{2}\bar{\varepsilon}_{n-1}\right) \end{pmatrix} \tag{2.39}$$

Comparing the obtained equation with equation (2.30), we conclude that

$$\beta^{I}_{n} = -V^{+}_{n-1}, \quad \beta^{II}_{n} = V^{-}_{n} \tag{2.40}$$

This means that the excess quantities following from non-equilibrium jump relations at the boundary between computational cells correspond to the numerical fluxes in the conservative wave-propagation algorithm. The representation of the wave-propagation algorithm in terms of the excess quantities given here is formally identical to its conservative form [9]. The advantage of the new representation manifests itself at discontinuities, for which jump relations cannot be reduced to the continuity of true values, e.g., at phase-transition fronts or cracks.

2.4 One-dimensional waves in periodic media

As the first example, we consider the propagation of a pulse in a periodic medium. The initial form of the pulse is given in Fig. 2.2, where the periodic variation in density is also shown by dashed lines. For the test problem, the materials are chosen as polycarbonate ($\rho = 1190\ \text{kg/m}^3$, c = 4000 m/s) and Al 6061 ($\rho = 2703\ \text{kg/m}^3$, c=6149 m/s). We apply the numerical scheme (2.29) and (2.30) for the solution of the system of equations (2.1)–(2.3). The corresponding excess quantities are calculated by means of equations (2.35)–(2.38). As it was noted, we can exploit all the advantages of the wave-propagation algorithm, including second-order corrections and transversal propagation terms [31]. However, no limiters are used in the calculations. Suppressing spurious oscillations is achieved by means of using a first-order Godunov step after each three second order Lax-Wendroff steps. This idea of composition was invented in [36]. Calculations are performed with Courant-Friedrichs-Levy number equal to 1. The simulation result for 4000 time steps is shown in Fig. 2.3. We observe a distortion of the pulse shape and a decrease in the velocity of the pulse propagation in comparison to the maximal longitudinal wave velocity in the materials. These results correspond to the prediction of the effective media theory [41] both qualitatively and quantitatively [23].

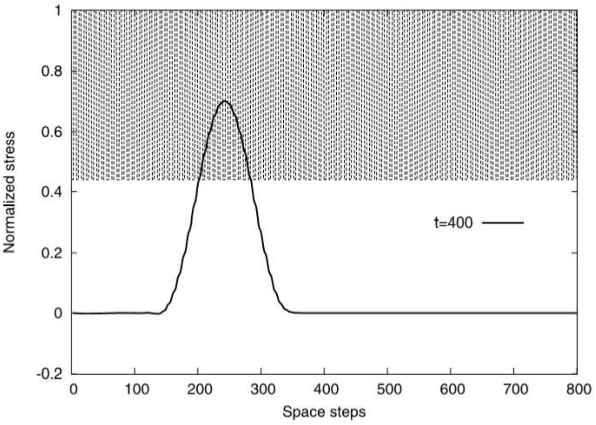

Fig. 2.2 Initial pulse shape. Reproduced from [12].

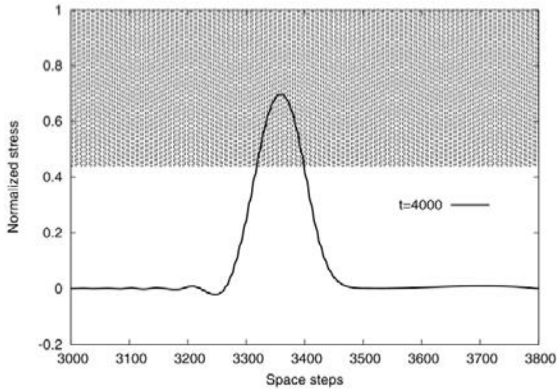

Fig. 2.3 Pulse shape at time step 4000. Reproduced from [12].

It should be noted that the effective media theory [41] leads to the dispersive wave equation

$$\frac{\partial^2 u}{\partial t^2} = \left(c^2 - c_a^2\right)\frac{\partial^2 u}{\partial x^2} + p^2 c_a^2 c_b^2 \frac{\partial^4 u}{\partial x^4} \tag{2.41}$$

where u is the displacement, p is the periodicity parameter, and c_a and c_b are parameters of the effective media [22], instead of the wave equation following from equations (2.1)–(2.3)

$$\frac{\partial^2 u}{\partial t^2} = c^2 \frac{\partial^2 u}{\partial x^2} \tag{2.42}$$

Equation (2.41) exhibits both dispersion (fourth-order space derivative) and the alteration in the longitudinal wave speed.

2.5 One-dimensional weakly nonlinear waves in periodic media

In the next example, we will see the influence of the materials' nonlinearity on the wave propagation. To close the system of equations (2.1) and (2.2) in the case of weakly nonlinear media we apply a simple nonlinear stress-strain relation

$$\sigma = \rho c^2 \varepsilon \left(1 + B\varepsilon\right) \tag{2.43}$$

where B is a parameter of nonlinearity, the values and sign of which are supposed to be different for hard and soft materials.

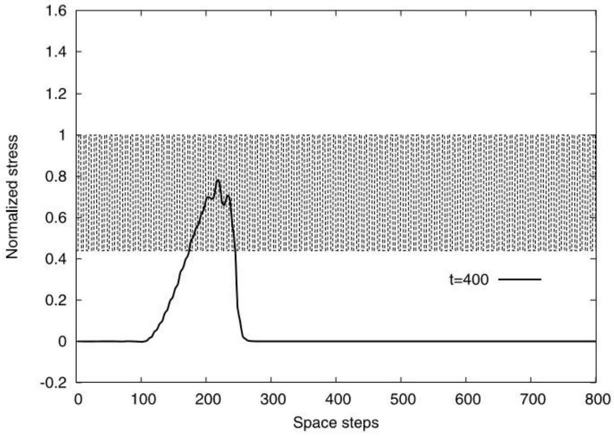

Fig. 2.4 Pulse shape at time step 400. Nonlinear case.

The solution method is almost the same as before. The approximate Riemann solver for the nonlinear elastic media (equation (2.43)) is similar to that used in [33, 35]. A modified longitudinal wave velocity ˆ c, following the nonlinear stress-strain relation (2.43), is applied at each time step in the numerical scheme (2.29) and (2.30):

$$\hat{c} = c\sqrt{1+2B\varepsilon} \tag{2.44}$$

instead of the piecewise constant one corresponding to the linear case. We consider the same pulse shape and the same materials (polycarbonate and Al 6061) as in the case of the linear periodic medium. However, the nonlinear effects appear only for a sufficiently high magnitude of loading. The values of the parameter of nonlinearity B were chosen as 0.24 for Al 6061 and 0.8 for polycarbonate. The results of the simulations corresponding to 400, 1600, and 5200 time steps are shown in Figs. 2.4–2.6.

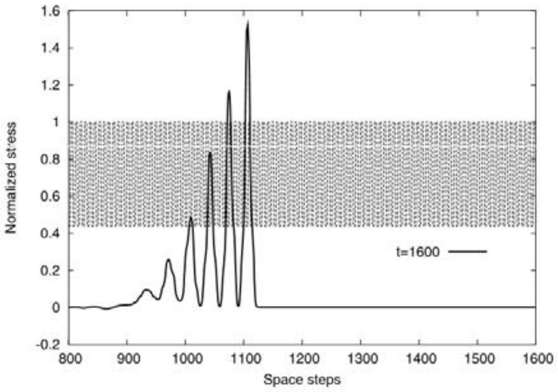

Fig. 2.5 Pulse shape at time step 1600. Nonlinear case.

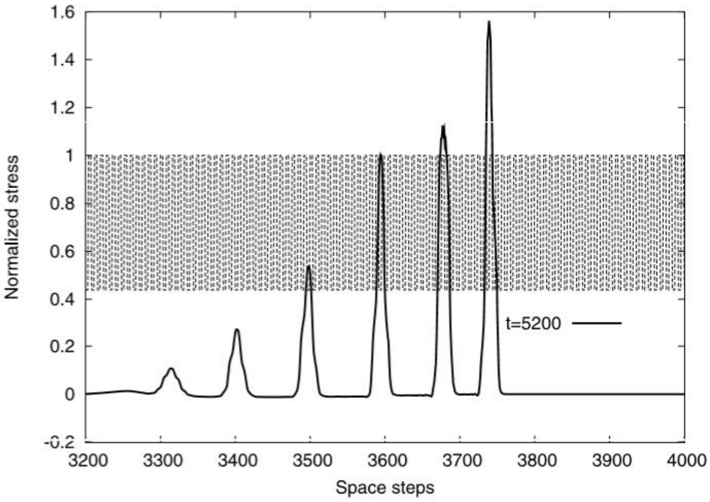

Fig. 2.6 Pulse shape at time step 5200. Nonlinear case. Reproduced from [12].

We observe that an initial bell-shaped pulse is transformed into a train of soliton-like pulses propagating with amplitude-dependent speeds. Such kind of behavior was first reported in [33], where these pulses were called "stegotons" because their shape is influenced by the periodicity. In principle, the soliton-like solution could be expected because if we combine the weak nonlinearity (2.43) with the dispersive wave equation in terms of the effective media theory (2.41), we arrive at the Boussinesq-type equation

$$\frac{\partial^2 u}{\partial t^2} = \left(c^2 - c_a^2\right)\frac{\partial^2 u}{\partial x^2} + \alpha B \frac{\partial u}{\partial x}\frac{\partial^2 u}{\partial x^2} + p^2 c_a^2 c_b^2 \frac{\partial^4 u}{\partial x^4} \tag{2.45}$$

which possesses soliton-like solutions.

2.6 One-dimensional linear waves in laminates

There are three basic length scales in wave propagation phenomena:

– the typical wavelength λ;
– the typical size of the inhomogeneities d;
– the typical size of the whole inhomogeneity domain l.

In the case of infinite periodic media considered above the third length scale was absent. Therefore, it may be instructive to consider wave propagation in a body where the periodic arrangement of layers of different materials is confined within a finite spatial domain.

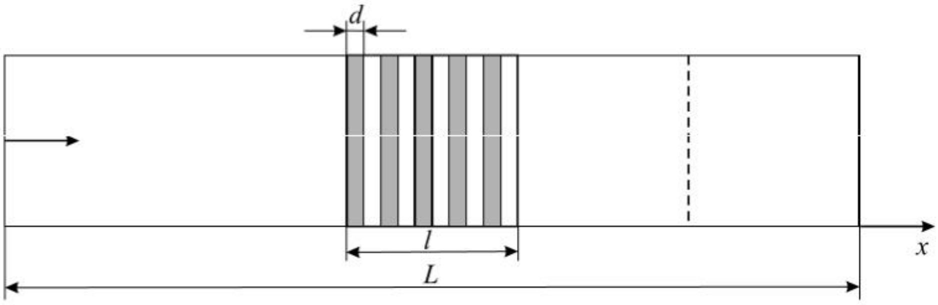

Fig. 2.7 Length scales in laminate.

To investigate the influence of the size of the inhomogeneity domain, we compare the shape of the pulse in the homogeneous medium with the corresponding pulse transmitted through the periodic array with a different number of distinct layers (Fig. 2.7). We use Ti (ρ = 4510 kg/m^3, c = 5020 m/s) and Al (ρ = 2703 kg/m^3, c = 5240 m/s) as materials in the distinct layers in the numerical simulations of linear elastic wave propagation.

We apply a stress pulse, the width λ of which corresponds to 30Δx (Δx is the space step)

$$\sigma(t) = \frac{2}{\cosh^2\left(0.5\left(t - 15\Delta t\right)\right)} \tag{2.46}$$

at the left end of the domain (Fig. 2.7), and record the resulting pulse at $x = 4000\Delta x$. The location is indicated by the dashed line in Fig. 2.7. The results are presented in Figs. 2.8–2.10 (dashed lines). The reference pulse calculated for homogeneous media is drawn with a solid line. As can be observed, if the

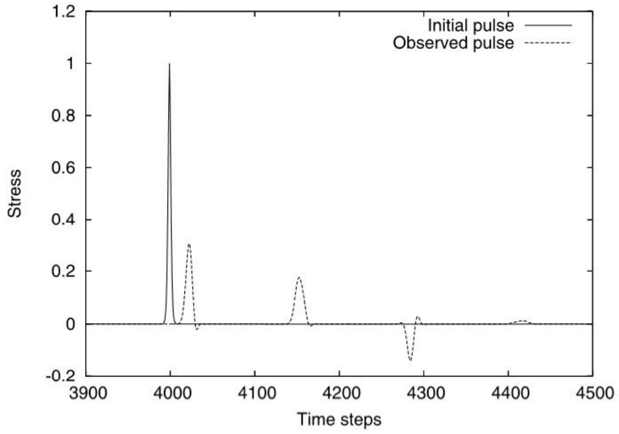

Fig. 2.8 Pulse shape at 4000 time steps ($d = 64\Delta x$, $l = 1000\Delta x$).

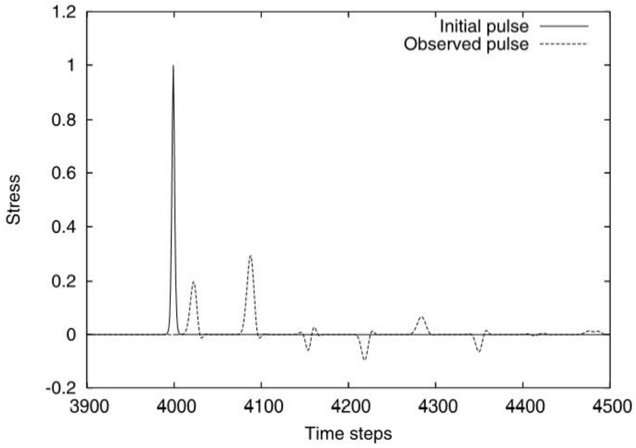

Fig. 2.9 Pulse shape at 4000 time steps ($d = 32\Delta x$, $l = 1000\Delta x$).

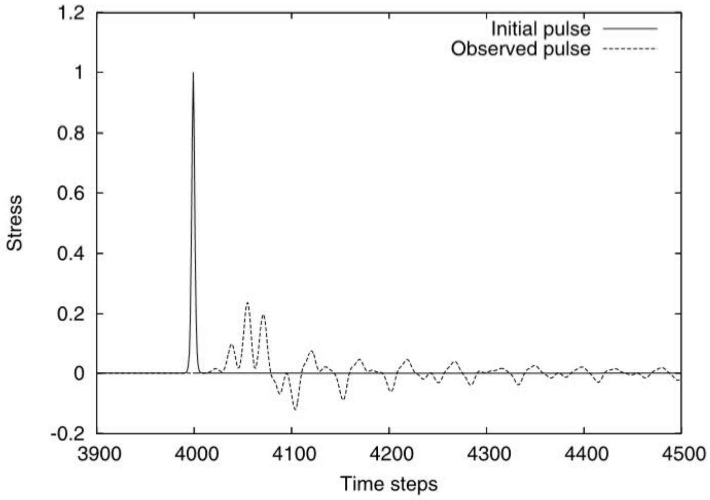

Fig. 2.10 Pulse shape at 4000 time steps ($d = 8\Delta x$, $l = 1000\Delta x$).

wavelength is less then the size of the inhomogeneity ($d \geq \lambda$), we have a strong dispersion of the pulse, i. e., a separation of the wave into components of various frequencies (Figs. 2.8 and 2.9). This dispersion is not so strong if, vice versa, the size of the inhomogeneity d is less then the wavelength λ (Fig. 2.10). Thus, waves in laminates demonstrate dispersive behavior, which is governed by the relations between the characteristic length scales. Taking into account nonlinear effects, we have seen the soliton-like wave propagation. Both nonlinearity and dispersion effects are observed experimentally in laminates under shock loading.

2.7 Nonlinear elastic waves in laminates under impact loading

Though the stress response to an impulsive shock loading has been very well understood for homogeneous materials, the same cannot be said for heterogeneous systems. In heterogeneous media, scattering due to interfaces between dissimilar materials plays an important role for shock wave dissipation and dispersion [25]. Diagnostic experiments for the dynamic behavior of heterogeneous materials under impact loading are usually carried out using a plate impact test configuration under a one-dimensional strain state. These experiments were recently reviewed in [19, 20]. For almost all the experiments, the stress response has shown a sloped rising part followed by an oscillatory behavior with respect to a mean value [19, 20]. Such behavior in the periodically layered systems is consistently exhibited in the systematic experimental work [46]. The specimens used in the shock compression experiments [46] were periodically layered two-component composites prepared by repeating a composite unit as many times as necessary to form a specimen with the desired thickness (see Fig. 2.11). A buffer layer of the same material as the soft component of the specimen was used at the other side of the specimen. A window in contact with the buffer layer was used to prevent the free surface from serious damage due to unloading from shock wave reflection at the free surface. Shock compression experiments were conducted by employing a powder gun loading system, which could accelerate a flat plate flyer to a velocity in the range of 400 m/s to about 2000 m/s. In order to measure the particle velocity history at the specimen window surface, a velocity interferometry system was constructed, and to measure the shock stress history at selected internal interfaces, the manganin stress technique was adopted. Four different materials, polycarbonate, 6061-T6 aluminium alloy, 304 stainless steel, and glass, were chosen as components. The selection of these materials provided a wide range of combinations of shock wave speeds, acoustic impedance and strength levels. The influence of multiple reflections of internal interfaces on shock wave propagation in the layered composites was clearly illustrated by the shock stress profiles measured by manganin gages. The origin of the observed structure of the stress waves was attributed to material heterogeneity at the interfaces. For high velocity impact loading conditions, it was fully realized that material nonlinear effects may play a key role in altering the basic structure of the shock wave. An approximate solution for layered heterogeneous materials subjected to high velocity plate impact has been developed in [19, 20]. For laminated systems under shock loading, shock velocity, density and volume were related to the particle velocity by means of an equation of state. The elastic analysis was extended to shock response by incorporating the nonlinear effects through computing the shock velocities of the wave trains and superimposing them. As pointed out in [46], stress wave propagation through layered media made of isotropic materials provides an ideal model to investigate the effect of heterogeneous materials under shock loading, because the length scales, e.g., the thickness of individual layers, and other measures of heterogeneity, e.g., impedance mismatch, are well defined. Since the impact velocity in shock experiments is sufficiently high, various nonlinear effects may affect the observed behaviour. That is why we apply numerical simulations of finite-amplitude nonlinear wave propagation to the study of scattering, dispersion and attenuation of shock waves in layered heterogeneous materials. The geometry of the problem follows the experimental configuration described in [46] (Fig. 2.12).

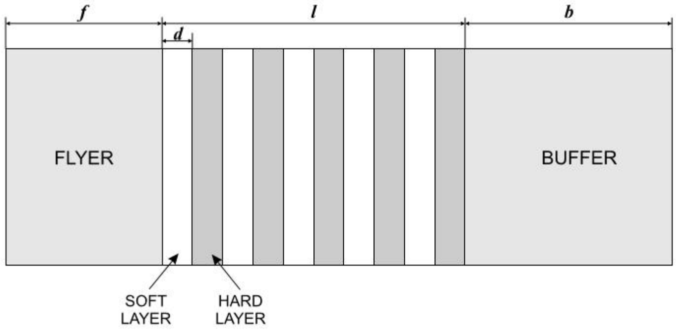

Fig. 2.11 Experimental setting. Reproduced from [46].

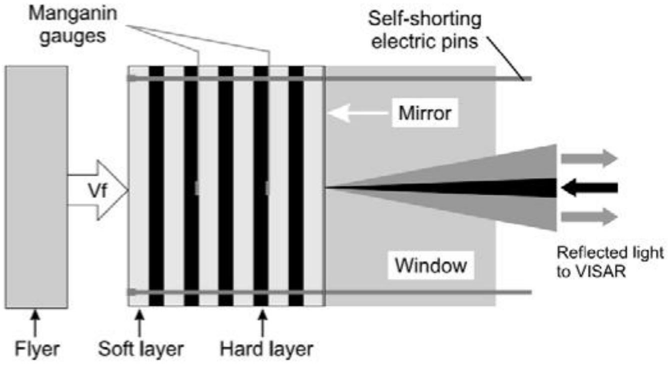

Fig. 2.12 Geometry of the problem.

We consider the initial-boundary value problem of impact loading of a heterogeneous medium composed of alternating layers of two different materials. The impact is provided by a planar flyer of length *L*, which has an initial velocity v_0. A buffer of the same material as the soft component of the specimen is used to eliminate the effect of wave reflection at the stress-free surface. The densities of the two materials are different, and the materials' response to compression is characterized by the distinct stress-strain relations $\sigma(\varepsilon)$. Compressional waves propagating in the direction of the layering are modelled by the one-dimensional hyperbolic system of conservation laws (2.1) – (2.2). Initially, stress and strain are zero inside the flyer, the specimen, and the buffer, but the initial velocity of the flyer is nonzero:

$$v(x,0) = v_0, \quad 0 < x < L \tag{2.47}$$

where L is the size of the flyer. Both left and right boundaries are stress-free. Instead of an equation of state like the one used in [19, 20], we apply a simpler nonlinear stress-strain relation $\sigma(\varepsilon)$ for each material (2.43) (cf. [38]):

$$\sigma = \rho c^2 \varepsilon (1 + B\varepsilon) \tag{2.48}$$

where, as previously, ρ is the density, c is the conventional longitudinal wave speed, and B is a parameter of nonlinearity, the values and signs of which are supposed to be different for hard and soft materials. We apply the same numerical scheme as in the previous example. The results of the numerical simulations compared with experimental data [46] are presented in the next section.

2.7.1 Comparison with experimental data

Figure 2.13 shows the measured and calculated stress time history in the composite, which consists of 8 units of polycarbonate, each 0.74 mm thick, and of 8 units of stainless steel, each 0.37 mm thick. The material properties of the components are extracted from [46]: the density $\rho = 1190$ kg/cm^3 and the sound velocity c=1957 m/s for the polycarbonate; $\rho = 7890$ kg/cm^3 and c=5744 m/s for the stainless steel. The stress time histories correspond to the distance 0.76 mm from the impact face. Calculations are performed for the flyer velocity 561 m/s and the flyer thickness 2.87 mm.

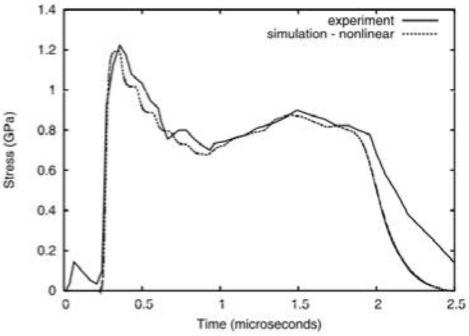

Fig. 2.13 Comparison of shock stress time histories corresponding to the experiment 112501 [46]. Reproduced from [11].

The results of the numerical calculations depend crucially on the choice of the parameter of nonlinearity *B*. We choose this parameter from the condition to match the numerical simulations to the experimental results. Time histories of particle velocity for the same experiment are shown in Fig. 2.14. It should be noted that the particle velocity time histories correspond to the boundary between the specimen and the buffer. As one can see, both stress and particle velocity time histories are well reproduced by the nonlinear model with the same values of the nonlinearity parameter *B*.

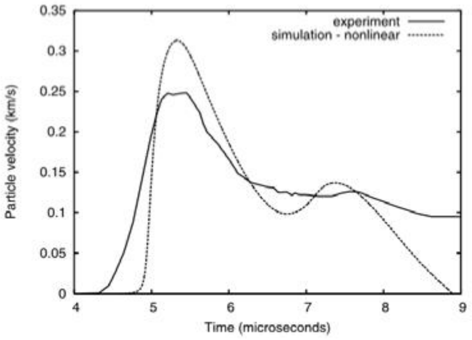

Fig. 2.14 Comparison of particle velocity time histories corresponding to the experiment 112501 [4639]. Reproduced from [11].

As it is pointed out in [46], the influence of multiple reflections of internal interfaces on shock wave propagation in the layered composites is clearly illustrated by the shock stress time histories measured by manganin gages. Therefore, we focus our attention on the comparison of the stress time histories. Figure 2.15 shows the stress time histories in the composite, which consists of 16 units of polycarbonate, each 0.37 mm thick, and of 16 units of stainless steel, each 0.19 mm thick. The stress time histories correspond to the distance 3.44 mm from the impact face. Calculations are performed for the flyer velocity 1043 m/s and the flyer thickness 2.87 mm. The nonlinearity parameter *B* is chosen here to be 2.80 for polycarbonate and zero for stainless steel. Additionally, the stress time history corresponding to the linear elastic solution (i. e., the nonlinearity parameter is zero for both components) is shown. It can be seen that the stress time history computed by means of the considered nonlinear model is very close to the experimental one. It reproduces three main peaks and decreases with distortion, as it is observed in the experiment [46].

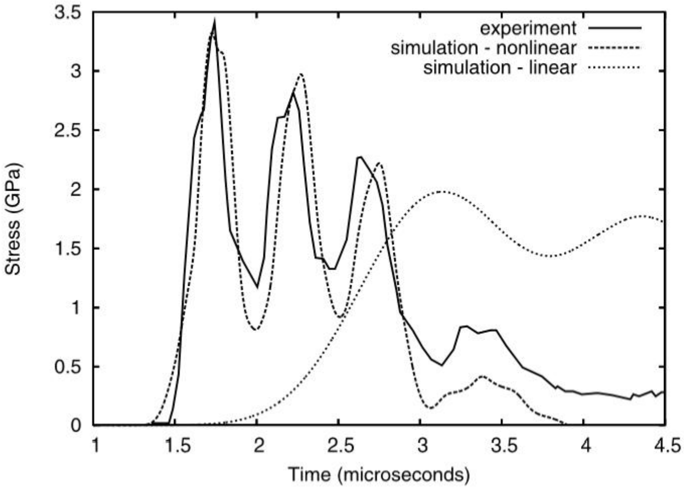

Fig. 2.15 Comparison of shock stress time histories corresponding to the experiment 110501 [46]. Reproduced from [11].

In Fig. 2.16 the same comparison is presented for the same composite as in Figure 2.15, only the flyer thickness is different (5.63mm). This means that the shock energy is approximately twice as high as that in the previous case. The nonlinearity parameter *B* is also increased to 4.03 for polycarbonate and remains zero for stainless steel. As a result all 6 experimentally observed peaks are reproduced well.

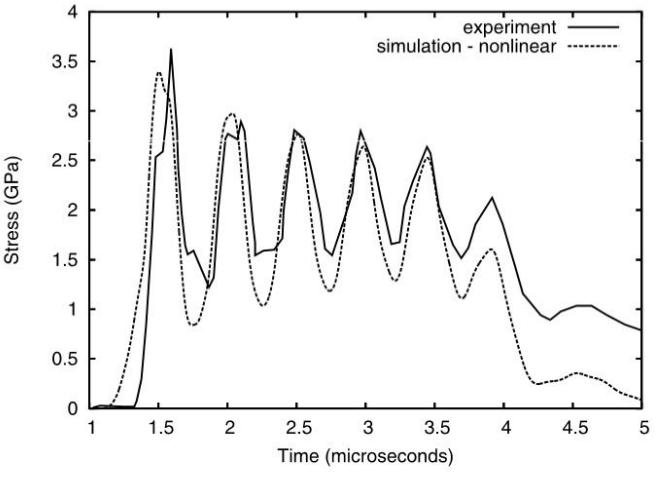

Fig. 2.16 Comparison of shock stress time histories corresponding to the experiment 110502 [46]. Reproduced from [11].

In Fig. 2.17 the comparison of stress time histories is presented for the composite consisting of 160.37 mm thick units of polycarbonate and 160.20 mm thick units of D-263 glass. The material properties of D-263 glass are [46]: the density ρ=2510 kg/cm^3 and the sound velocity c = 5703 m/s. The distance between the measurement point and the impact face is 3.41 mm. Corresponding flyer velocity is 1079 m/s and the flyer thickness is 2.87 mm. The nonlinearity parameter *B* is chosen to be equal 5.025 for polycarbonate and zero for D-263 glass. Again, the stress time history corresponding to the linear elastic solution (i. e., the nonlinearity parameter is zero for both components) is shown. As one can see, the stress time history corresponding to the nonlinear model reproduces all 5 peaks with the same amplitude as observed experimentally.

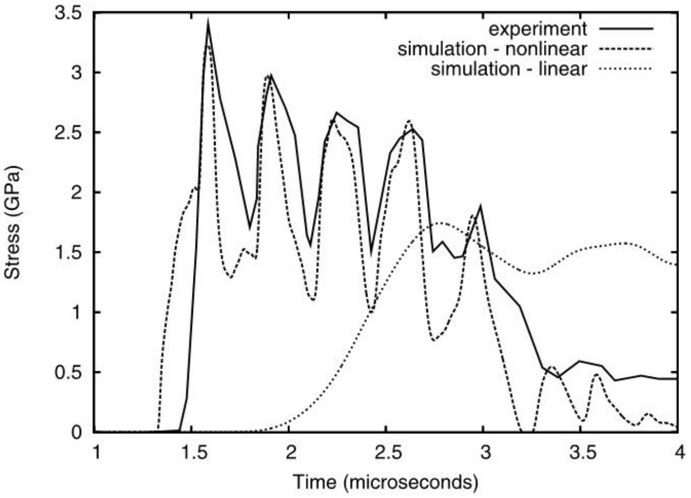

Fig. 2.17 Comparison of shock stress time histories corresponding to the experiment 112301 [46]. Reproduced from [11].

As it can be seen, the agreement between the results of the calculations and the experiments is achieved by the adjustment of the nonlinearity parameter *B*. It follows that the nonlinear behaviour of the soft material is affected not only by the energy of the impact, but also by the scattering induced by internal interfaces. It should be noted that the influence of the nonlinearity is not necessarily small. In the numerical simulations, which match with the experiments, the increase of the actual sound velocity of polycarbonate follows. It may be up to two times higher in comparison to the linear case. This conclusion is really surprising, but supported by the stress time histories. Thus, the application of a nonlinear stress-strain relation for materials in numerical simulations of the plate impact problem of a layered heterogeneous medium shows that a good agreement between computations and experiments can be obtained by adjusting the values of the parameter of nonlinearity [11]. In the numerical simulations of the finite-amplitude shock wave propagation in heterogeneous composites, the flyer size and velocity, the impedance mismatch of hard and soft materials, as well as the number and size of layers in a specimen were the same as in the experiments [46]. Moreover, a nonlinear behaviour of materials was also taken into consideration. This means that combining scattering effects induced by internal interfaces and physical nonlinearity in material behaviour into one nonlinear parameter, provides the possibility to reproduce the shock response in heterogeneous media observed experimentally. In this context, the parameter B is actually influenced by (i) the physical nonlinearity of the soft material and (ii) the mismatch of the elasticity properties of soft and hard materials. The mismatch effect is similar to the type of nonlinearity characteristic to materials with different moduli of elasticity for tension and compression. The mismatch effect manifests itself due to wave scattering at the internal interfaces, and, therefore, depends on the structure of a specimen. The variation of the parameter of nonlinearity confirms the statement that the nonlinear wave propagation is highly affected by the interaction of the wave with the heterogeneous substructure of a solid [46]. It should be noted that layered media do not exhaust all possible substructures of heterogeneous materials. Another example of a heterogeneous substructure is provided by functionally graded materials.

2.8 Waves in functionally graded materials

Functionally graded materials (FGMs) are composed of two or more phases that are fabricated so that their compositions vary more or less continuously in some spatial direction and are characterized by nonlinear gradients that result in graded properties. Traditional composites are homogeneous mixtures, and therefore they involve a compromise between the desirable properties of the component materials. Since significant proportions of an FGM contain the pure form of each component, the need for compromise is eliminated. The properties of both components can be fully utilized. For example, the toughness of a metal can be mated with the refractoriness of a ceramic, without any compromise in the toughness of the metal side or the refractoriness of the ceramic side. Comprehensive reviews of current FGM research may be found in the papers [28] and [37], and in the book [42]. Studies of the evolution of stresses and displacements in FGMs subjected to quasistatic loading [42] show that the utilization of structures and geometry of a graded interface between two dissimilar layers can reduce stresses significantly. Such an effect is also important in the case of dynamical loading, where energy-absorbing applications are of special interest. We consider the one-dimensional problem in elastodynamics for an FGM slab in which material properties vary only in the thickness direction. It is assumed that the slab is isotropic and inhomogeneous with the following fairly general properties [21]:

$$E'(x) = E_0'\left(a\frac{x}{l}+1\right)^m, \quad \rho(x) = \rho_0\left(a\frac{x}{l}+1\right)^n \tag{2.49}$$

where ρ is the mass density, l is the thickness, a, m, and n are arbitrary real constants with $a > -1$, while E_0 and ρ_0 are the elastic constant and density at $x = 0$. The elastic constant E_0 is determined under the assumption that $\sigma_{yy} = \sigma_{zz}$ and the slab is fully constrained at infinity. It can thus be shown that

$$E' = \frac{E(1-v)}{(1+v)(1-2v)} \tag{2.50}$$

with $E(x)$ and $v(x)$ being the Young modulus and the Poisson ratio of the inhomogeneous material. It is assumed that the slab is at rest for $t \leq 0$, therefore, the following initial conditions are valid:

$$v(0,t) = 0, \quad \sigma(x,0) = 0 \tag{2.51}$$

The boundary condition at $x = 0$ is

$$v(x,0) = 0, \quad t > 0 \ \text{(“fixed” boundary)} \tag{2.52}$$

At $x = l$, the slab is subjected to a stress pulse given by

$$\sigma_{xx}(l,t) = \sigma_0 f(t), \quad t > 0 \tag{2.53}$$

where the constant σ_0 is the magnitude of the pulse, the function f describes its time profile, and without any loss in generality, it is assumed that $|f| \leq 1$. Following [21], we consider an FGM slab that consists of nickel and zirconia. The thickness of the slab is l = 5 mm. On one surface the medium is pure nickel and on the other surface pure zirconia, while the material properties $E_0(x)$ and $\rho(x)$ vary smoothly in thickness direction. A pressure pulse defined by

$$\sigma_{xx}(l,t) = \sigma_0 f(t) = -\sigma_0(H(t) - H(t-t_0)) \tag{2.54}$$

is applied to the surface $x = 1$ and the boundary $x = 0$ is “fixed”. Here H is the Heaviside function. The pulse duration is assumed to be $t_0 = 0.2\ \mu s$. The properties of the constituent materials used are given in Table 2.1 [21].

Material	E (GPa)	ν	ρ (kg/m^3)
ZrO	151	0.33	5331
Ni	207	0.31	8900

Table 2.1 Properties of materials

The material parameters for the FGMs used are [21]: $a = -0.12354$, $m = -1.8866$, and $n = -3.8866$. The stress is calculated up to $12\mu s$ (the propagation time of the plane wave through the thickness $l = 5$ mm is approximately 0.77 μs in pure ZrO_2 and 0.88 μs in Ni).

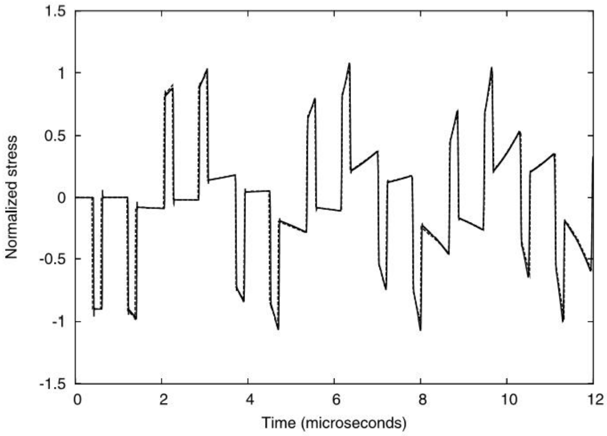

Fig. 2.18 Variation of stress with time in the middle of the slab. Reproduced from [12].

Numerical simulations were performed by means of the same algorithm as above. The comparison of the results of the numerical simulation and of the analytical solution [21] for the time dependence of the normalized stress σ_{xx}/σ_0 at the location $x/l = 1/2$ is shown in Fig. 2.18. As one can see, it is difficult to make a distinction between analytical and numerical results. This means that the applied algorithm is well suited for the simulation of wave propagation in FGM. A nonlinear behaviour for the same materials with the nonlinearity parameter $A = 0.19$ is shown in Figure 2.19. For the comparison, calculations were performed with the value 0.9 of the Courant number both in the linear and nonlinear case. The amplitude amplification and pulse shape distortion in comparison with the linear case is clearly observed. In addition, the velocity of a pulse in the nonlinear material is increased.

2.9 Concluding remarks

As we have seen, linear and non-linear wave propagation in media with rapidly varying properties as well as in functionally graded materials can be successfully simulated by means of the modification of the wave-propagation algorithm based on the non-equilibrium jump relation for true inhomogeneities. It should be emphasized that the used jump relation expresses the continuity of genuine unknown fields at the boundaries between computational cells. The applied algorithm is conservative, stable up to Courant number equal to 1, high-order accurate, and thermodynamically consistent. However, the main advantage of the presented modification of the wave-propagation algorithm is its applicability to the simulation of moving discontinuities. This property is related to the formulation of the algorithm in terms of excess quantities. To apply the algorithm to moving singularities, we simply should change the non-equilibrium jump relation for true inhomogeneities to another nonequilibrium jump relation valid for quasi-inhomogeneities.

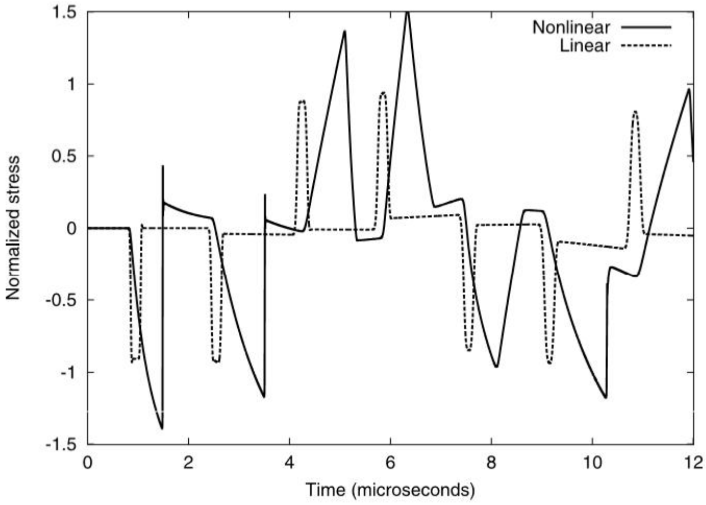

Fig. 2.19 Variation of stress with time in the middle of the slab. Nonlinear case. Reproduced from [12].

3 ELECTROMAGNETIC WAVE PROPAGATION THROUGH INHOMOGENEOUS MATERIAL LAYERS

We use Maxwell’s equations in a sourceless, inhomogeneous medium with continuous permeability $\mu\ (r)$ and permittivity $\epsilon\ (r)$ to study the wave propagation. The general form of the wave equation is derived and by virtue of some physical assumptions, including μ and ϵ as functions of z, the equation has been simplified. Finally by introducing a smooth step dielectric variable we solve the wave equation in the corresponding medium which is in conform with the well known results. Exact double-layer solution in analytic form has been given in terms of the Heun functions.

3.1 Introduction

Having the electric permittivity of a system to be an isotropic and continuous spatial function has numerous applications in chemistry, biophysics and electronics [47–53]. As an example, in heavy doped regions the dielectric constant changes with the density of impurity and so with the position. Such a region can be found in bipolar transistors, $p - n$ junctions and solar cells [48]. It is also common that permittivity is assumed to be an isotropic spatial function that changes continuously in solvent region that allows us to formulate a computational scheme [49]. Other inhomogeneous medium can be seen in a biological membrane, like a lipid bilayer surrounded by water. For this system permittivity changes from a large value in the surrounding water to a lower value in the bilayer [50]. Also in electric double layers (EDL) due to ion accumulation and hydration in the region we face with permittivity variation, with effects on electric potential and interaction pressure between surfaces [51]. The main concern in such studies is the behavior of a non-uniform mixed medium (a chemical solution or a $p - n$ junction) upon an external static electric field using the Poisson-Boltzmann equation. This differential equation (linear or non-linear form) can describe the electrostatic effects extensively, ranging from a bimolecular system [52] to an electrolyte solution [53]. The most regular form of this equation can be written as

$$\nabla \cdot \left[\epsilon(\mathrm{r}) \nabla \psi(r)\right] = -\rho_f(r) - \sum_i c_i^{\infty} z_i q \lambda(r)\, exp\left[\frac{-z_i q \psi(r)}{k_B T}\right] \tag{3.1}$$

In this equation $\epsilon\ (r)$ is the variable dielectric, $\psi\ (r)$ is the electrostatic potential and $\rho_f\ (r)$ represents the charge density of the medium. Further, z_i and c_i^{∞} show the charge and the concentration of ions, T is the temperature, κB is the

Boltzmann constant and $\lambda\ (r)$ is a factor that depends on the accessibility of a position to ions in the medium.

In the present work, we study the wave propagation inside inhomogeneous materials with the electric permittivity $\epsilon(r)$ and the magnetic permeability $\mu\ (r)$ as some isotropic and continuous spatial functions. Without external sources (i.e. $\rho_{free} = 0,\ J_{free} = 0$) the wave equation for the electric component of the electromagnetic wave (EMW) propagating in the medium with $\epsilon = \epsilon(r)$ and $\mu = \mu(r)$ is found to be

$$\nabla^2 E - \epsilon\mu\frac{\partial^2 E}{\partial t^2} = -(\nabla\tilde{\epsilon}.\nabla)E - (E.\nabla)\nabla\tilde{\epsilon} - \nabla(\tilde{\epsilon} - \tilde{\mu})\times(\nabla \times E) \tag{3.2}$$

in which $\tilde{\epsilon} = \ln\epsilon$ and $\tilde{\mu} = \ln\mu$. A similar equation can be written for magnetic component of the EMW but we shall find B using one of the Maxwell's equation. A general approach toward the solution for Eq. (3.2) may not be possible due to the complicated form of the right hand side of the equation but by some simplifications we shall find exact analytical solution for this wave-type equation. There are some attempts to consider propagation of the electromagnetic waves in the context of the general equation given in (3.2). For the case that ϵ and μ are constant our equation reduces to the standard wave-equation which can be found in every electromagnetic book. R Diamant et al have considered this problem in number of papers [54–58]. In their papers, R Diamant et al assume that $\mu = \mu_0$ and the results are mainly numeric. Although having numerical solution has the worth in its own right, herein we are interested to obtain exact analytical solutions for the tangent hyperbolic potential in the azimuthal direction. For single layer our solution is expressed in hypergeometric functions while the double layer case in terms of the rare Heun functions. It is our belief that taking different profiles yield also exact solutions expressible in terms of known mathematical functions. In obtaining exact solutions we abide by the constraint condition $\mu = \mu_0$ =constant, through our inhomogenous layers. We shall assume further that the ϵ and μ vary only in one direction which is also the direction of propagation. This direction throughout the paper will be z–direction.

Organization of the paper is as follows. In Sec. 3.2 we find the form of the wave equation in a general system of coordinates and through some specifications we simplify the wave equation. In Sec. 3.3 we introduce the smooth step dielectric constant and solve the wave equation accordingly. Sec. 3.4 solves the problem of smooth double layers. Our conclusion is presented in Sec. 3.5.

3.2 The wave equation

We start with the sourceless ($\rho_{free} = 0,\ J_{free} = 0$) Maxwell's equations in a medium with variable permittivity ϵ and permeability μ which are given by

$$\nabla.B = 0, \qquad \nabla.D = 0, \qquad \nabla\times E = -\frac{\partial B}{\partial t} \quad \text{and} \quad \nabla\times H = -\frac{\partial D}{\partial t} \tag{3.3}$$

Herein $D = \epsilon E$ is the displacement vector, E is the electric field, $H = \frac{1}{\mu}B$ is the auxiliary magnetic field and B is the magnetic field. To obtain Eq. (3.2) from the Maxwell's equations (3.3) we start from Faraday's law and we act $\nabla\ \times$ from the left i.e., $\nabla\times(\nabla\times E) = -\frac{\partial\nabla\times B}{\partial t}$, which yields

$$\nabla(\nabla.E) - \nabla^2 E = -\frac{\partial}{\partial t}\nabla\times(\mu H) = -\frac{\partial}{\partial t}\left[\mu\nabla\times H - H\times\nabla\mu\right], \tag{3.4}$$

and equivalently

$$\nabla^2 E - \nabla(\nabla.E) = \frac{\partial}{\partial t}\left[\mu\frac{\partial D}{\partial t} - B\times\frac{\nabla\mu}{\mu}\right] = \mu\epsilon\frac{\partial^2 E}{\partial t^2} - \frac{\partial B}{\partial t}\times\nabla\, ln\,\mu. \tag{3.5}$$

Next we rearrange the terms to get

$$\begin{aligned} \nabla^2 E - \mu\epsilon\frac{\partial^2 E}{\partial t^2} &= \nabla(\nabla.E) - \frac{\partial B}{\partial t}\times\nabla\, ln\,\mu = \nabla\left(\nabla.\left(\frac{D}{\epsilon}\right)\right) + (\nabla\times \mathrm{E})\times\nabla\tilde{\mu} \\ &= -\nabla\left(D.\frac{\nabla\epsilon}{\epsilon^2}\right) + (\nabla\times \mathrm{E})\times\nabla\tilde{\mu}. \end{aligned} \tag{3.6}$$

Finally one finds

$$\begin{aligned} \nabla^2 E - \mu\epsilon\frac{\partial^2 E}{\partial t^2} &= -\nabla(E.\nabla\tilde{\epsilon}) - \nabla\tilde{\mu}\times(\nabla\times E) \\ &= -\left[(\nabla\tilde{\epsilon}.\nabla)E + (E.\nabla)\nabla\tilde{\epsilon} + \nabla\tilde{\epsilon}\times(\nabla\times E) + E\times(\nabla\times\nabla\tilde{\epsilon})\right] - \nabla\tilde{\mu}\times(\nabla\times E) \\ &= -(\nabla\tilde{\epsilon}.\nabla)E - (E.\nabla)\nabla\tilde{\epsilon} - \nabla(\tilde{\epsilon}+\tilde{\mu})\times(\nabla\times E), \end{aligned} \tag{3.7}$$

which is nothing but Eq. (3.2). We comment that in finding Eq. (3.7) we have used the mathematical formula: $\nabla\times(\nabla\times A) = \nabla(\nabla.A) - \nabla^2 A$ and $\nabla(A.B) = (B.\nabla)A + (A.\nabla)B + B\times(\nabla\times A) + A\times(\nabla\times B)$ and $\tilde{\epsilon} = ln\,\epsilon$ and $\tilde{\mu} = ln\,\mu$. Upon taking into account that in our study $\epsilon = \epsilon(z)$ and $\mu = \mu(z)$ the general wave equation (3.2) becomes

$$\nabla^2 E - \epsilon\mu \frac{\partial^2 E}{\partial t^2} = -\left(\tilde{\epsilon}' \frac{\partial}{\partial z}\right) E - (E.\nabla)\tilde{\epsilon}'\hat{k} - (\tilde{\epsilon}' + \tilde{\mu}')\hat{k} \times (\nabla \times E), \tag{3.8}$$

in which a prime ‘ denotes $\frac{d}{dz}$. Our further simplification is to consider that the electric and magnetic components of the EMW vary in *z* direction only. This assumption is due to the symmetry of the medium which is physically acceptable. Our latter equation then reduces effectively into the following 1−dimensional three equations for the electric components

$$\left(\frac{\partial^2}{\partial z^2} - \mu\epsilon \frac{\partial^2}{\partial t^2}\right) E_x = \tilde{\mu}' \frac{\partial E_x}{\partial z}, \tag{3.9}$$

$$\left(\frac{\partial^2}{\partial z^2} - \mu\epsilon \frac{\partial^2}{\partial t^2}\right) E_y = \tilde{\mu}' \frac{\partial E_y}{\partial z}, \tag{3.10}$$

$$\left(\frac{\partial^2}{\partial z^2} - \mu\epsilon \frac{\partial^2}{\partial t^2}\right) E_z = -\tilde{\epsilon}' E_z' - E_z \tilde{\epsilon}''. \tag{3.11}$$

Next we consider

$$E(r,t) = \overline{E}(z) e^{i\omega t} \tag{3.12}$$

in which ω is the angular frequency of the wave. A substitution in (3.9) and (3.10) yields:

$$\left(\frac{d^2}{dz^2} + \mu\epsilon\omega^2\right) \overline{E}_i(z) = \frac{\mu'}{\mu} \frac{d\overline{E}_i(z)}{dz} \tag{3.13}$$

for $i = x, y$. To have the third equation (i.e. Eq. (3.11)) satisfied we set $E_z = 0$ (i.e. no longitudinal component) which is equivalent with the propagation of the wave in *z*−direction. Having symmetry with respect to *x* and *y* one can always rotate the system of coordinates in *z* direction such that $\overline{E}(z)$ aligns with one of the coordinates (say *x*). Hence we are left with only one equation in *x*−direction which is expressed as

$$\left(\frac{d^2}{dz^2} + \mu\epsilon\omega^2\right) \overline{E}_x(z) = \frac{\mu'}{\mu} \frac{d\overline{E}_x(z)}{dz} \tag{3.14}$$

and the other two components of the electric field are zero i.e., $E(r,t) = \hat{x}\overline{E}_x(z)e^{i\omega t}$. To do further investigation one must know the form of μ and ϵ in terms of z. For instance, with $\mu = \mu_0 = cont.$ and $\epsilon = \epsilon_0 = cont.$ one finds

$$\left(\frac{d^2}{dz^2} + \frac{\omega^2}{c^2}\right)\overline{E}_x = 0 \tag{3.15}$$

which admits

$$\begin{gathered} \overline{E}_x = \overline{E}_{0x}e^{\mp ikz} \\ \left(\overline{E}_{0x} = const\right) \end{gathered} \tag{3.16}$$

where $k = \frac{\omega}{c}$ and the plane wave is propagating in ±z direction. Our final remark in this section is on the form of the wave equation: if one considers $\mu' = 0$ it reduces to the form of the standard wave equation, but owing to the form of

$\epsilon=\epsilon(z)$ its solution differs from the standard wave equation.

3.3 Smooth step dielectric constant

As an example let's consider $\mu = K_m\mu_0 = cons.$ and $\epsilon = K_e(z)\epsilon_0$, where $K_e(z)$ stands for a smooth function of z given by [57]

$$K_e(z) = K_2 - \frac{\Delta K}{4}(1 - \tanh(az))^2, \tag{3.17}$$

in which a is a positive real constant, $\Delta K = K_2 - K_1$, $K_2 = \lim_{z\to\infty} K_e(z)$ and $K_1 = \lim_{z\to-\infty} K_e(z)$. The wave equation (3.13) becomes

$$\left(\frac{d^2}{dz^2} + \frac{\omega^2}{c^2}K_mK_e(z)\right)\overline{E}_x(z) = 0, \tag{3.18}$$

which after defining the following new parameters

$$k^2 = \frac{\omega^2}{c^2}K_mK_1, \qquad \nu^2 = \frac{\omega^2}{c^2}K_mK_2 \tag{3.19}$$

and considering a new variable

$$\xi = -e^{-2az} \tag{3.20}$$

together with a redefinition of the electric field

$$\overline{E}_x(z) = (-\xi)^{-iv} F(\xi), \tag{3.21}$$

it turns (with $' = \frac{d}{d\xi}$) into

$$\xi F'' + (1-2iv)F' + \frac{1}{4a^2}\left[\frac{(1-4a^2)v^2}{\xi} + \frac{v^2-k^2}{1-\xi} - \frac{v^2-k}{(1-\xi)^2}\right]F = 0. \tag{3.22}$$

Having singularities at $\xi = 0$ and $\xi = 1$ suggests to replace further

$$F(\xi) = \xi^{\sigma}(\xi-1)^{\rho}G(\xi) \tag{3.23}$$

which after some manipulation and choices

$$\sigma = \frac{iv(2a-1)}{2a} \tag{3.24}$$

and

$$\rho = \frac{1}{2}\left(1 - \frac{1}{a}\sqrt{a^2+v^2-k^2}\right) \tag{3.25}$$

it reduces to the following Hypergeometric differential equation (HDE) [59]

$$\begin{aligned}\xi(\xi-1)G'' + \left[\frac{iv-a}{a} - \left(\frac{iv-2a}{a} + \frac{1}{a}\sqrt{a^2+v^2-k^2}\right)\xi\right]G' - \\ -\frac{iv-a}{2a^2}\left(a - \sqrt{a^2+v^2-k^2}\right)G = 0.\end{aligned} \tag{3.26}$$

Comparing with the standard form of the Hypergeometric DE

$$\xi(\xi-1)G'' + [(\alpha+\beta+1)\xi - \gamma]G' + \alpha\beta G = 0 \tag{3.27}$$

one finds

$$\alpha = \frac{1}{2a}\left[a - \sqrt{a^2+v^2-k^2} - i(v+k)\right], \tag{3.28}$$

$$\beta = \frac{1}{2a}\left[a - \sqrt{a^2 + v^2 - k^2} - i(v-k)\right] \tag{3.29}$$

and

$$\gamma = \frac{a - iv}{a} \tag{30}$$

The general solution for the above HDE can be written as

$$G = C_1 F(\alpha,\beta;\gamma;\xi) + C_2\xi^{1-\gamma}F(\alpha-\gamma+1,\beta-+1;2-\gamma;\xi) \tag{3.31}$$

in which C_1 and C_2 are two integration constants. Going to the original variables now, the general solution for the Electric field is given by

$$\begin{aligned}\overline{E}_x(z) = \tilde{C}_1(-\xi)^{-\frac{iv}{2a}}(1-\xi)^{\rho}F(\alpha,\beta;\gamma;\xi)+ \\ \tilde{C}_2(-\xi)^{\frac{iv}{2a}}(1-\xi)^{\rho}F(\alpha-\gamma+1,\beta-\gamma+1;2-\gamma;\xi),\end{aligned} \tag{3.32}$$

where $\overline{C}_1 = C_1(-1)^{\sigma+\rho}$ and $\overline{C}_2 = C_2(-1)^{\sigma+\rho+1-\gamma}$. Let us consider that the wave comes from $z = -\infty$ and goes toward $z = +\infty$. Also we recall that $lim_{z\to\infty}K_e(z)=K_2=cons.$ which implies that $\lim_{z\to\infty}\overline{E}_x(z) \sim e^{i\frac{\omega}{c}\sqrt{K_mK_2z}} = e^{ivz}$. Once $z \to +\infty$ it is clear that $\xi=-e^{-2az} \to 0$, and upon knowing that $F(\alpha, \beta; \gamma; 0) = 1$, makes the limit of the electric field to be

$$\lim_{z\to\infty}\overline{E}_x(z) = \tilde{C}_1 e^{ivz} + \tilde{C}_2 e^{-ivz}. \tag{3.33}$$

This suggests that for this choice we must set $\tilde{C}_2 = 0$, which casts the solution into

$$\overline{E}_x(z) = \tilde{C}_1(-\xi)^{-\frac{iv}{2a}}(1-\xi)^{\rho}F(\alpha,\beta;\gamma;\xi), \tag{3.34}$$

so that

$$\lim_{z\to\infty}\overline{E}_x(z) = \tilde{C}_1 e^{ivz} = E_{02}e^{ivz}. \tag{3.35}$$

Herein we consider the amplitude of the transmitted wave as E_{02}.

The limit of $z \to -\infty$ (and consequently $\xi \to -\infty$) can be found once we apply the following properties for the Hypergeometric functions [60]

$$F(\alpha,\beta;\gamma;\xi)=\frac{\Gamma(\gamma)\Gamma(\beta-\alpha)}{\Gamma(\beta)\Gamma(\gamma-\alpha)}(-1)^{\alpha}\xi^{-\alpha}F\left(\alpha,\alpha+1-\gamma;\alpha+1-\beta;\frac{1}{\xi}\right)+ \\ \frac{\Gamma(\gamma)\Gamma(\alpha-\beta)}{\Gamma(\alpha)\Gamma(\gamma-\alpha)}(-1)^{\beta}\xi^{-\beta}F\left(\beta,\beta+1-\gamma;\beta+1-\alpha;\frac{1}{\xi}\right). \tag{3.36}$$

Hence

$$\lim_{\substack{z\to-\infty\\ \xi\to-\infty}}F(\alpha,\beta;\gamma;\xi)=\lim_{\substack{z\to-\infty\\ \xi\to-\infty}}\frac{\Gamma(\gamma)\Gamma(\beta-\alpha)}{\Gamma(\beta)\Gamma(\gamma-\alpha)}(-1)^{\alpha}\xi^{-\alpha}+\frac{\Gamma(\gamma)\Gamma(\alpha-\beta)}{\Gamma(\alpha)\Gamma(\gamma-\alpha)}(-1)^{\beta}\xi^{-\beta}, \tag{3.37}$$

which upon (3.32), one finds

$$\lim_{\substack{z\to-\infty\\ \xi\to-\infty}}\overline{E}_x(z)=\widetilde{C}_1\left(\frac{\Gamma(\gamma)\Gamma(\beta-\alpha)}{\Gamma(\beta)\Gamma(\gamma-\alpha)}(-\xi)^{-\alpha-\frac{iv}{2a}+\rho}+\frac{\Gamma(\gamma)\Gamma(\alpha-\beta)}{\Gamma(\alpha)\Gamma(\gamma-\alpha)}(-\xi)^{-\beta-\frac{iv}{2a}+\rho}\right) \tag{3.38}$$

Now one can show that

$$-\alpha-\frac{iv}{2a}+\rho=+i\frac{k}{2a} \tag{3.39}$$

$$-\beta-\frac{iv}{2a}+\rho=-i\frac{k}{2a} \tag{3.40}$$

which finally yields

$$\lim_{\substack{z\to-\infty\\ \xi\to-\infty}}\overline{E}_x(z)=\widetilde{C}_1\left(\frac{\Gamma(\gamma)\Gamma(\beta-\alpha)}{\Gamma(\beta)\Gamma(\gamma-\alpha)}e^{-i\mu z}+\frac{\Gamma(\gamma)\Gamma(\alpha-\beta)}{\Gamma(\alpha)\Gamma(\gamma-\alpha)}e^{i\mu z}\right)=E'_{01}e^{-i\mu z}+E_{01}e^{i\mu z}. \tag{3.41}$$

Note that

$$E_{01}=\frac{\Gamma(\gamma)\Gamma(\alpha-\beta)}{\Gamma(\alpha)\Gamma(\gamma-\alpha)}E_{02} \tag{3.42}$$

is the amplitude of the transmitted wave for $z \rightarrow \propto$ and

$$E'_{01}=\frac{\Gamma(\gamma)\Gamma(\beta-\alpha)}{\Gamma(\beta)\Gamma(\gamma-\alpha)}E_{02} \tag{3.43}$$

is the amplitude of the reflected wave for $z \rightarrow -\propto$. Once more we comment that E_{02}, is the amplitude of the transmitted wave while E_{01} and E'_{01} are the amplitudes of the incident and reflected waves, respectively. Having these definitions together with the above equations one obtains the reflection and

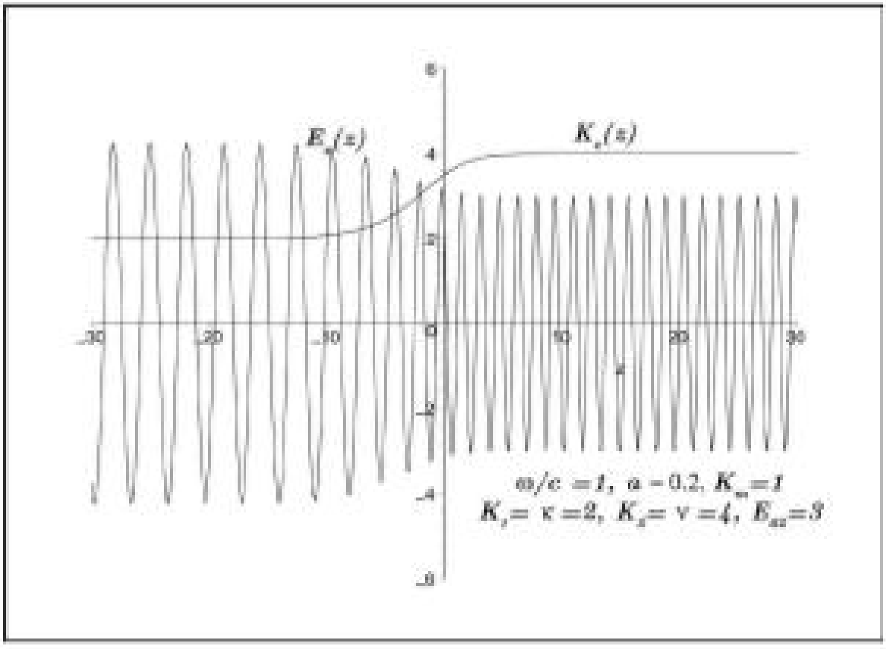

Fig. 3.1: A plot of $\mathrm{Re}\left(\overline{E}_x(z)\right)$ in terms of *z* together with $K_e(z)$ for certain values of the parameters. The smooth changes in the dielectric constant and amplitude of the electric field are clear.

transmission coefficients of the wave as

$$R = \frac{E'_{01}}{E_{01}} = \frac{\Gamma(\alpha)\Gamma(\beta-\alpha)}{\Gamma(\beta)\Gamma(\alpha-\beta)} \tag{3.44}$$

and

$$T = \frac{E_{02}}{E_{01}} = \frac{\Gamma(\alpha)\Gamma(\gamma-\alpha)}{\Gamma(\gamma)\Gamma(\alpha-\beta)}. \tag{3.45}$$

As one observes *R* and *T* depend on *α, β* and *γ* which are complex parameters. This means that *R* and *T* are complex numbers too. In a particular case in which *α, β* and *γ* are given one can calculate the value of the Gamma functions and accordingly *R* and *T* are obtained. Irrespective to the value of the physical parameters, there exist always a complex number assigned to *R* and *T*. In the limit of a sharp step dielectric i.e., $a \to \propto$ one finds

$$\lim_{a\to\infty} R = \lim_{a\to\infty}\frac{\Gamma(\alpha)\Gamma(\beta-\alpha)}{\Gamma(\beta)\Gamma(\alpha-\beta)} = \frac{k-v}{k+v} = \frac{\sqrt{K_m K_1}-\sqrt{K_m K_2}}{\sqrt{K_m K_1}+\sqrt{K_m K_2}} = \frac{n_1-n_2}{n_1+n_2} \tag{3.46}$$

$$\lim_{a\to\infty} T = \lim_{a\to\infty}\frac{\Gamma(\gamma)\Gamma(\alpha-\beta)}{\Gamma(\alpha)\Gamma(\gamma-\alpha)} = \frac{2k}{k+v} = \frac{2\sqrt{K_m K_1}}{\sqrt{K_m K_1}+\sqrt{K_m K_2}} = \frac{2n_1}{n_1+n_2} \tag{3.47}$$

where n_1 and n_2 are the optical indices of the spaces at $z < 0$ and $z > 0$, respectively [61]. In Fig. 3.1 we plot $\mathrm{Re}\left(\overline{E}_x(z)\right)$ in terms of z together with $K_e(z)$ for certain values of parameters. The smooth change in the dielectric constant and amplitude of the electric field are clear.

To complete our solution we rewrite the electric field of a plane wave solution which propagates in positive z direction,

$$E(r,t) = \hat{x}E_{02}(-\xi)^{-\frac{iv}{2a}}(1-\xi)^{\rho}F(\alpha,\beta;\gamma;\xi)e^{i\omega t}, \tag{3.48}$$

together with the magnetic field which can be found by applying the same Maxwell's equation as we started with i.e., $\nabla \times E = -\frac{\partial B}{\partial t}$. Furthermore we need also to use [16]

$$\frac{\partial}{\partial z}F(\alpha,\beta;\gamma;\xi) = \frac{\partial \xi}{\partial z}\frac{\partial}{\partial z}F(\alpha,\beta;\gamma;\xi) = 2a\xi\frac{\alpha\beta}{\gamma}F(\alpha+1,\beta+1;\gamma+1;\xi) \tag{3.49}$$

and in general if we take $E(r,t) = \hat{x}E(z)e^{i\omega t}$ then $B(r,t) = -i\omega\hat{y}\frac{\partial E(z)}{\partial z}e^{i\omega t}$ or finally

$$B(r,t) = \hat{y}\frac{iE_{02}}{2\omega a}(-\xi)^{-\frac{iv}{2a}}(1-\xi)^{\rho}\left[\frac{2a\alpha\beta}{\gamma}F(\beta+1,\alpha+1;\gamma+1;\xi) + \left(\frac{vi}{\xi} - \frac{2a\rho}{(1-\xi)}\right)F(\alpha,\beta;\gamma;\xi)\right]e^{i\omega t} \tag{3.50}$$

3.4 Smooth double layers

Another application of the general equation is to find the EMW passing through a double layer thick shell. For this let us consider $K_m = const.$ with

$$K_e(z) = K_1 + \frac{K_2 - K_1}{2}\left(\tanh az - \tanh a(z-L)\right). \tag{3.51}$$

Here a is a constant which in the limit $a \to \infty$, L becomes the thickness of a flat double layer dielectric of dielectric constant K_2 located inside another medium of dielectric constant K_1. Next, we rewrite the wave equation (3.13) in this matter:

$$\left(\frac{d^2}{dz^2} + \left\{k^2 + \frac{v^2 - k^2}{2}\left(\tanh az - \tanh a(z-L)\right)\right\}\right)\overline{E}_x(z) = 0 \tag{3.52}$$

in which κ and ν are defined in (3.19). We follow a similar change of variable given by (3.21) which modifies the latter equation as

$$\xi^2 E''(\xi) + \xi E'(\xi) + \frac{1}{4a^2}\left(k^2 - \frac{\left(v^2 - k^2\right)(\lambda - 1)}{\lambda(\xi - 1)\left(\xi - \frac{1}{\lambda}\right)}\right)E(\xi) = 0 \tag{3.53}$$

in which $\lambda = exp(2aL)$. Now, we replace $E\ (\xi) = \xi^{\sigma} H\ (\xi)$ with $\sigma = -i\kappa/2a$ to find

$$H''(\xi) + \frac{1 - ik/a}{\xi}H'(\xi) + \frac{\left(k^2 - v^2\right)(\lambda - 1)}{4a^2\lambda\xi(\xi - 1)\left(\xi - \frac{1}{\lambda}\right)}H(\xi) = 0 \tag{3.54}$$

which is a Heun differential equation [63] of the form

$$\omega''(z) + \left(\frac{\gamma}{z} + \frac{\delta}{z-1} + \frac{\epsilon}{z-p}\right)\omega'(z) + \frac{\alpha\beta z - q}{z(z-1)(z-p)}\omega(z) = 0 \tag{3.55}$$

in which $\epsilon = A + \beta - \gamma - \delta + 1$ with a general solution

$$w\ (z) = C_1\ Heun\ G\ (p,\ q,\ \alpha,\ \beta,\ \gamma,\ \delta,\ z) + C_2 z^{1-\gamma}\ HeunG\ (p,\ q - (p\delta + \beta)\ (\gamma - 1),$$
$$\beta - \gamma + 1,\ \alpha - \gamma + 1,\ 2 - \gamma,\ \delta,\ z). \tag{3.56}$$

Herein C_1 and C_2 are two integration constants. Following the general solution we find the final solution of the wave equation as

$$\begin{aligned} E(\xi) = C_1(-\xi)^{\frac{-ik}{2a}}\,HeunG\left(\frac{1}{\lambda e}, \frac{\left(v^2 - k^2\right)(\lambda - 1)}{4a^2\lambda}, 0, \frac{-ik}{a}, \frac{a - ik}{a}, 0, \xi\right) + \\ C_2(-\xi)^{\frac{ik}{2a}}\,HeunG\left(\frac{1}{\lambda}, \frac{\left(v^2 - k^2\right)(\lambda - 1)}{4a^2\lambda}, 0, \frac{ik}{a}, 0, \xi\right). \end{aligned} \tag{3.57}$$

Upon considering $HeunG\ (p,\ q,\ \alpha,\ \beta,\ \gamma,\ \delta,\ 0) = 1$, one easily finds that $\lim_{\substack{z\to\infty \\ \xi\to 0}} E(\xi) = C_1 \exp(ikz) + C_2 \exp(-ikz)$ which after assuming that the wave starts from $z = -\infty$ and propagates toward $z = +\infty$ one must set $C_2 = 0$ and $C_1 = E_{03}$. These, therefore, imply

$$E(\xi) = E_{03}(-\xi)^{\frac{-i\mu}{2a}}\,HeunG\left(\frac{1}{\lambda}, \frac{\left(v^2 - k^2\right)(\lambda - 1)}{4a^2\lambda}, 0, \frac{-i\mu}{a}, \frac{a - ik}{a}, 0, \xi\right), \tag{3.58}$$

where E_{03} is the amplitude of the electric field at the limit $z \rightarrow +\infty$. Fig. 3.2 displays the continuous passage of EMW through medium of the double-layers located at $z = 0$ and $z = 4$.

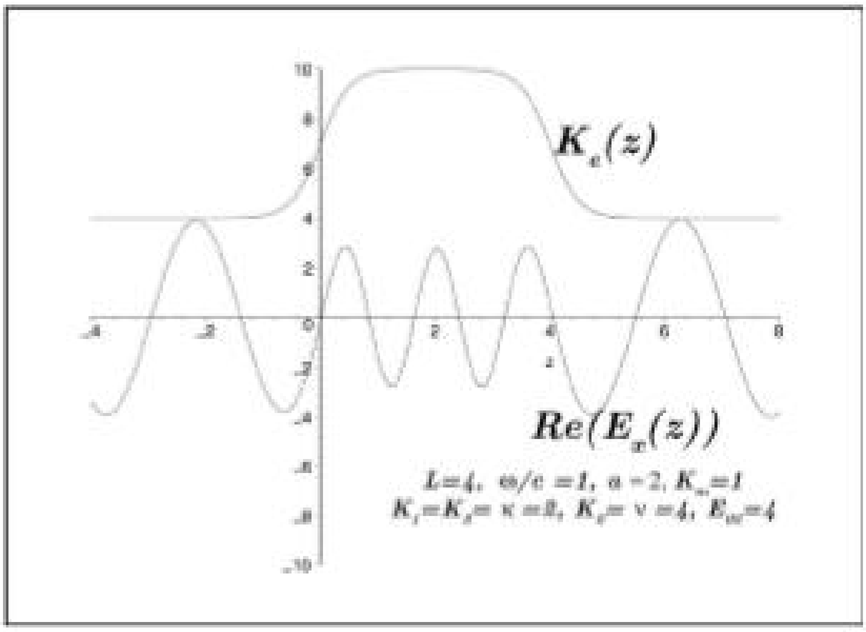

Fig. 3.2: The incoming EMW from $z < 0$ encounters with the first layer at $z = 0$. $Re(E_x(z))$ has similar structure after crossing the second layer at $z = 4$. In between, $0 < z < 4$, the oscillatory behaviour evidently changes.

3.5 Conclusion

In conclusion we have considered media with variable permeability and permittivity varying with z–direction, alone. The general form of the wave equation in such a non-uniform medium is presented. Some simplifications have been considered such as, ϵ and μ are only functions of z which is also the direction of the propagation of the possible EMW. In such a framework we have used the sourceless Maxwell's equations to find a wave equation for the propagation of the EMW. We solved the wave equation for a smooth-step, variable dielectric given the constant permeability. In the limits we obtain the well known reflection and transmission coefficients of the plane waves in normal incidence on the interface plane between two dielectrics. Our results have been presented analytically and schematically. Studying this interesting problem further with more layers is our future plan. The applications of such extremal theories may not be so clear yet but we believe that with the fast developments of the new detecting methods of cancerous cells or organs in biomedical optics, such detailed theories will contribute to have more accurate results. Finally, in the present work we have solved the smooth double layer problem in terms of the Heun's functions.

4. IMPURITY EFFECTS ON THE BAND STRUCTURE OF ONE-DIMENSIONAL PHOTONIC CRYSTALS: EXPERIMENT AND THEORY

We study the effects of single impurities on the transmission in microwave realizations of the photonic Kronig–Penney model, consisting of arrays of Teflon pieces alternating with air spacings in a microwave guide. As only the first propagating mode is considered, the system is essentially one-dimensional (1D) obeying the Helmholtz equation. We derive analytical closed form expressions from which the band structure, frequency of defect modes and band profiles can be determined. These agree very well with experimental data for all types of single defects considered (e.g. interstitial and substitutional) and show that our experimental set-up serves to explore some of the phenomena occurring in more sophisticated experiments. Conversely, based on the understanding provided by our formulae, information about the unknown impurity can be determined by simply observing certain features in the experimental data for the transmission. Further, our results are directly applicable to the closely related quantum 1D Kronig–Penney model.

4.1 Introduction

Research on photonic crystals, theoretical and experimental, has been sustained at a high intensity for several years, ever since the publications of Yablonovitch [64] and John [65] in 1987. One interest for this research is the potentially very high number of applications in optoelectronics (see, e.g., chapter VII of [66]). A substantial part of these studies concerns the study of impurities or defects in one-, two- or three-dimensional (1D, 2D or 3D) photonic crystals.

Impurities or defects in photonic crystals may sometimes be unwanted but may also be extremely useful. For example, impurity states lying in a complete photonic band gap can be used for a waveguide and thus be an essential part of optical devices [67]. By introducing defects periodically in a perfect photonic array, coupled cavity waveguides are formed. The coupling of the cavity modes creates impurity bands which have potential applications for the design of high-efficiency waveguides and waveguide bends [68, 69]. It is important to mention that defects can be introduced in a controlled manner in photonic array experiments, see e.g. [70]. There are promising theoretical results [81] that point defects, in particular a substitutional defect in 3D crystals formed by a lattice of air spheres on a silicon background, may be used as microcavities for localizing light at a given point. Whence we appreciate the technological, as well as academic, importance of understanding the effects of various types of defects or impurities.

There are several calculational methods for the treatment of impurities in photonic crystals. These are based on plane wave expansion of the fields [72]; finite-difference timedomain algorithms [70, 73]; variational methods [71]; R-matrix methods [74]; transfer-matrix methods [75], combined, if necessary, with finite element methods; super-cell [76], Greenfunction, and tight-binding methods (see e.g. [68]). Eigenfrequencies and eigenfunctions of defects can also be calculated via the method of Sakoda [77] based on the numerical simulation of the excitation process of the defect mode by a virtual oscillation dipole moment, in conjunction with the finite-time domain algorithm.

On the other hand, for *electronic* periodic systems the calculation of impurity states dates back to the mid-50s with the introduction of effective mass theory [78, 79] Useful modern methods for the calculation of impurity levels are the super-cell tight-binding methods [80], which are applicable to shallow, deep and intermediate impurity levels [81].

In this work, we investigate experimentally and theoretically the effect of single defects or impurities in the transmission of the electromagnetic field through arrays formed by Teflon pieces alternating with air spacings. A closely related system to ours has been studied by Pradhan and Watson [82] who looked for effects of isolated impurities in a system formed by an array of coaxial connectors.

It is well known that point defects can produce localized states in the gaps [66, 77]. The first experimental observation in photonics was made by McCall *et al* [83]. Can we observe thesein our experiment? How else do impurities manifest themselves in the transmission curves? In this paper, we investigate these questions for various types of single defects. We compare experimental results with those obtained by the transfer matrix calculations, equation (4.13), and point out the most prominent and typical transport features.

One purpose of this paper is to show that our experimental set-up can be used as a testbed to study some of the phenomena occurring in more sophisticated (and expensive) photonic or electronic experimental arrangements. The second purpose is to show that our analytical expressions, derived in section 4 for the photonic Kronig–Penney model with single defects, are very helpful in elucidating the various features in the band structure; in particular, the frequencies of the defect modes and band profiles observed in the experiments.

We remark that since our system is described by the 1D Helmholtz equation our results are directly applicable also to 1D semiconductor (electronic) crystals formed, e.g., by sequences of quantum dots. Effects of irregularities such as an additional scatterer or a quantum dot displaced from its regular position have been the focus of many investigations, especially since these were observed experimentally by Kouwenhoven *et al* [84] in the case of electronic transport in heterostructures and by McCall *et al* [83] in the case of photonic crystals.

4.2. Experimental set-up and the model

The experimental set-up is shown in figure 4.1. It consists of a brass ring where a microwave guide is cut out, in which several Teflon pieces, two carbon absorbers and an antenna are inserted. Another antenna is fixed on the top plate (not shown in the figure) covering the waveguide. The antennas are connected to a network analyzer that allows the measurement of all matrix elements of the scattering matrix. The absorbers are used to eliminate reflection at the ends of the array and hence mimic a 1D scattering system with open ends. This circular waveguide has been used, with metallic screws instead of Teflon pieces, to study the microwave realization of the Hofstadter butterfly [85] and transport properties of 1D on-site correlated disorder potentials [86].

Fig. 4.1. Experimental set-up. Left: overview of the waveguide. Right: enlargement of the part close to the electric dipole antenna and the two carbon absorbers. The top brass plate covering the waveguide is not shown. Thewaveguide has a total diameter of 78 cm, a depth A = 1 cm and a width B = 2 cm. The frequency range of the first propagating mode is from 7.5 to 15 GHz. The length of the Teflon pieces shown is d_0 = 4 cm and their index of refraction is n = p2.08. In this picture, the spacing between all Teflon pieces is d = 4 cm.

In our experiment, the cut-off frequency for the lowest mode is $f_{min}=c/2B\approx 7.5$ GHz and the second mode opens at 15 GHz. All results presented in this paper are restricted to the regime of the first propagating mode. Thus the system is effectively 1D. Since the perimeter of the ring (≈234 cm) is much larger than the maximum wavelength used in our experiments ($2 < \lambda < 4$ cm), our theoretical model assumes, as an approximation, a linear set-up (see figure 4.2).

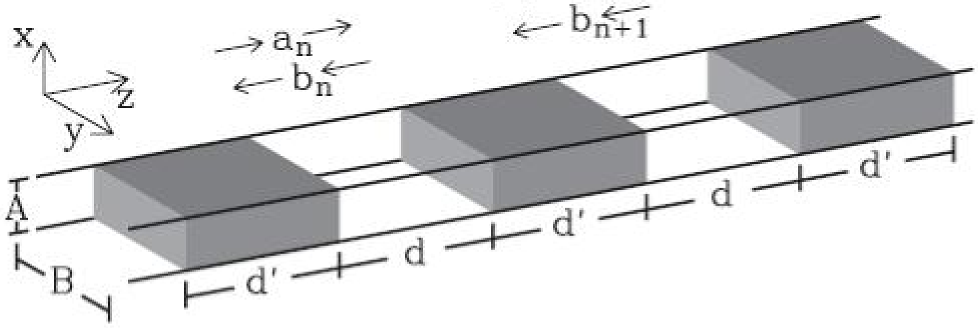

Fig. 4.2. The photonic Kronig–Penney model. The gray blocks are the idealized Teflon pieces of length *d'*, the air spacing is *d*. a_n and b_n are the amplitudes of the wavefunction in the air spacing to the right of the *n*th Teflon piece.

For the lowest TE mode ($E_x = 0$) at $f < 15$ GHz the *y*-component of the electric field $E_y$is also zero and the *x* component is

$$E_x(y,z,t) = E_0 \sin\left(\frac{\pi y}{B}\right)\Phi(z)\exp(i2\pi f t),$$

The wavefunction $\Phi(z)$ obeys the Helmholtz equation

$$\left(\frac{d^2}{dz^2} + k_r^2\right)\Phi(z) = 0, \tag{4.1}$$

where

$$k_r = \sqrt{\frac{(2\pi f)^2}{c^2} n_r^2 - \frac{\pi^2}{B^2}} \tag{4.2}$$

and $n_r = \sqrt{\mu\varepsilon}$ is the position-dependent index of refraction. In the case the Teflon pieces are periodically spaced our system is the electromagnetic counterpart of the quantum 1D Kronig–Penney model.

We use the transfer matrix approach to calculate the transmission. Since both antennas are placed in the air, our transfer matrix should connect the wave function amplitudes from air to air. Referring to figure 4.2, the transfer matrix *Q* for a single cell connects the amplitudes (a_n, b_n) and (a_{n+1}, b_{n+1}):

$$\begin{pmatrix} a_{n+1} \\ b_{n+1} \end{pmatrix} = Q \begin{pmatrix} a_n \\ b_n \end{pmatrix}, \quad \text{with} \quad Q = \begin{pmatrix} Q_{11} & Q_{12} \\ Q_{21} & Q_{22} \end{pmatrix} \tag{4.3}$$

and k (k') denotes the wavevector in air (Teflon pieces) (cf equation (4.2)). The transfer matrix elements for a single cell are

$$Q_{11} = [\cos(k'd') + i\alpha_+ \sin(k'd')]e^{ikd}, \tag{4.4}$$

$$Q_{12} = -i\alpha_- \sin(k'd'), \tag{4.5}$$

where

$$\alpha_\pm = \frac{k^2 \pm k'^2}{2kk'}. \tag{4.6}$$

Due to preservation of flow and time reversibility it yields $Q_{11} = Q_{22}^*$, $Q_{12} = Q_{21}^*$ and $det(Q) = 1$. The elements Q_{ij} are the same as in the quantum 1D model of a square potential well, but with $k = \sqrt{2\mu E}$, $k' = \sqrt{2\mu(E - V_0)}$ and $V_0 > 0$. From (4.2) $k' > k$; thus, the Teflon piece acts as a well ($V_0 < 0$) in quantum mechanics, except that in the photonic array the 'depth' increases with frequency.

The microwave vector network analyzers measure the full scattering matrix S defined by

$$\begin{pmatrix} a_{n+1} \\ b_n \end{pmatrix} = S \begin{pmatrix} a_n \\ b_{n+1} \end{pmatrix} \tag{4.7}$$

In terms of the Q matrix elements, the S matrix reads

$$S = \begin{pmatrix} -\frac{Q_{12}}{Q_{22}} & \frac{1}{Q_{22}} \\ \frac{1}{Q_{22}} & \frac{Q_{12}}{Q_{22}} \end{pmatrix} \tag{4.8}$$

The transmission T through a single cell is given by

$$T = |S_{12}|^2 = \frac{1}{|Q_{22}|^2} = \frac{1}{1 + |Q_{12}|^2}, \tag{4.9}$$

with Q_{12} and Q_{22} given by equations (4.4) and (4.5) for a single cell.

Expression (4.9) together with equation (4.5) shows immediately that a single Teflon piece becomes completely transparent at frequencies obeying the relation

$$k'd' = m\pi, \qquad m = 1,2,3,... \tag{4.10}$$

We shall refer to these frequencies as *1-Teflon resonances*.

For an array of N equally spaced cells without any impurities or defects, we need to evaluate Q to the Nth power; a numerical process that can be easily performed. However, it is more illustrative to use the Cayley–Hamilton theorem of linear algebra to get [87]–[89]

$$T = \frac{1}{1+\left|Q_{12}^{N}\right|^2} = \frac{1}{1+\left|Q_{12}\sin(N\theta)/\sin(\theta)\right|^2}, \tag{4.11}$$

where Θ is the Bloch phase corresponding to the infinitely periodic array:

$$\cos\theta = \Re Q_{11} = \cos(k'd')\cos(kd) - \alpha_+ \sin(k'd')\sin(kd). \tag{4.12}$$

Note that $T = 1$ not only when $Q_{12} = 0$ (i. e. at the 1-Teflon resonances) but also whenever $N\Theta = \pm n\pi$, $n = 1, 2, \ldots, N-1$. The latter gives rise to $N-1$ peaks with $T = 1$ in each transmission band since Θ shifts through π [87]–[90]. According to the above condition, the system of $N = 2$ Teflon pieces separated by air becomes transparent when $\Theta = \pi/2$, which in turn implies $\mathrm{Tr}Q = 0$. We call these the *two cell resonances* emphasizing that it is not just two Teflon pieces next to each other but separated by an air spacing. A little thought reveals that the $N-1$ oscillations are centered around the two cell resonance frequency (see also [89]).

Luna-Acosta *et al* [88] treat the case of the regular Kronig–Penney model (i.e. periodic and no defects) where it is shown that equation (4.11) reproduces most details of the experimental transmission data as a function of frequency for all kinds of periodic arrays considered. Since we are concerned here with the effects of the impurities, we show for comparison the theoretical and experimental results for the transmission amplitude $|S_{12}|$ for an array of 16 equally spaced cells, with Teflon pieces of width $d' = 4.0$ cm and air spacing of width $d = 4.0$ cm, see figure 4.3(a).

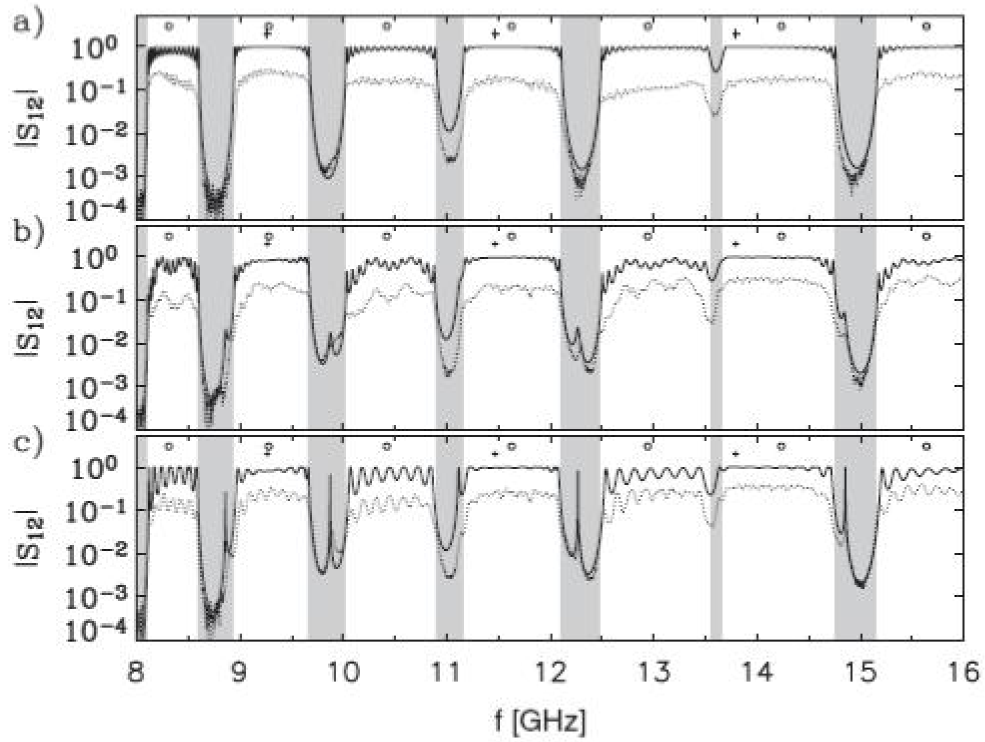

Fig. 4.3. Interstitial impurities for a 16 cell array with $d = d' = 4$ cm. Dotted (solid) lines are the experimental (theoretical) curves. The shaded regions mark the forbidden gaps, given by the condition $\xi^2 < 1$ (a) pure (impurity-free) array; (b) small Teflon piece (3.16 cm) inserted in the center between the 3rd and 4th regular Teflon pieces, (c) small Teflon piece (3.16 cm) inserted in the center between the 8th and 9th regular Teflon pieces. The crosses (circles) mark the frequency values for the 1-Teflon-resonances (two cell resonance), see text.

For the experimental and theoretical curves to agree as well, it was necessary to define some effective length for the length of the Teflon pieces and the air spacings. That is, since the actual waveguide is circular, the Teflon pieces and air spacings are not rectangular pieces but slightly curved with the larger side being exactly 5% larger than the shorter side. (The 4 cm Teflon pieces and the air spacings referred to above actually mean that the shorter side is 4 cm whereas the larger one is 4.2 cm.) It turned out that the best fit could be obtained with an effective length of 4.08 cm, i.e. 2% larger than its shorter side. We emphasize that this is the only fitting parameter in our calculations and moreover it is the same for all calculations presented here. Throughout the paper, whenever we quote the width of a Teflon piece or an air spacing we mean the shorter side of it and in the numerical calculations we use their corresponding effective length.

We remark that our model does not consider the absorption of the signal. However, comparison of the experimental and theoretical data shows that the band structure (gaps and band profiles) is not affected by the absorption except for the attenuation of the transmission, which is about constant throughout the frequency range (the experimental transmission is about five times weaker).

Thus, absorption in our experiment does not destroy coherent phenomena like the band structure (see also [86]).

In figure 4.3 and all subsequent transmission plots the frequency values of the 1-Teflon and two cell resonances are marked by crosses and circles, respectively. Different types of bands are formed depending on the position of the Teflon resonances relative to the two cell resonances [88]. In these and all forthcoming transmission plots we mark with shaded strips the gap regions, defined by the condition that the eigenvalues $\lambda_\pm$ of the transfer matrix Q are real. Since $\lambda_\pm = \xi \pm \sqrt{\xi^2 - 1}$, where $\xi = \Re Q_{11}$, forbidden gaps occur whenever $\xi^2 > 1$.

Given the good agreement between experimental transmission data and the photonic Kronig–Penney model, implied by equation (4.11), we proceed to discuss the effects of impurities in the photonic Kronig–Penney model.

4.3. Impurity effects in the transmission

Different types of defects or impurities can be realized in our experimental set-up with just air and Teflon segments and can be represented by one of the two general sketches shown in figure 4.4. The upper sketch illustrates a general interstitial impurity: an extra piece of Teflon of width *b* placed somewhere in the air spacing between two pieces of Teflon. The rest of the arrangement remains unaltered; the perpendicular dotted lines mark the boundaries of the unit cell along the *pure* crystal. By the definition of a point defect, the interstitial impurity breaks the periodicity only locally. Hence, the length of the extra piece of Teflon should be less than or equal to the air spacing. If the width *b* is larger than this, then the boundaries of the regular cells would be displaced from their original positions and consequently periodicity would be globally broken (it becomes an extended defect, e.g. a topological defect [91, 92]). In this paper, we donot consider topological defects.

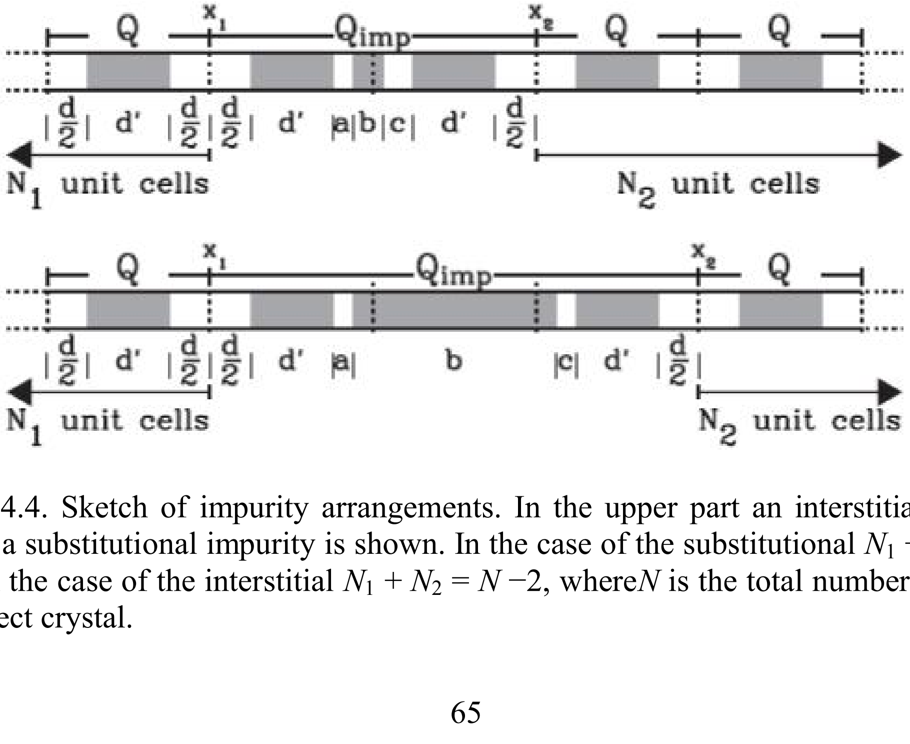

Fig. 4.4. Sketch of impurity arrangements. In the upper part an interstitial and in the lower part a substitutional impurity is shown. In the case of the substitutional $N_1 + N_2 = N - 3$, whereas in the case of the interstitial $N_1 + N_2 = N - 2$, where$N$ is the total number of unit cells of the perfect crystal.

As shown in the upper sketch there are N_1 unit cells periodically arranged to the left of point x_1, each described by the matrix Q, then periodicity is interrupted by the impurity at point x_1 and again recovered at point x_2. To the right of point x_2 there are N_2 cells periodically arranged. The total transfer matrix going from the left end of the array to the right end of the array can bewritten as

$$Q_{tot} = Q^{N_2} Q_{imp} Q^{N_1}, \tag{4.13}$$

where Q_{imp} is the transfer matrix connecting the amplitudes of the wavefunction at x_1 with those at point x_2. Specifically,

$$Q_{imp} = D_{d/2} M D_c M_b D_a M D_{d/2}, \tag{4.14}$$

where D_i ($i = d/2$, a, and c) is the transfer matrix corresponding to an air spacing of length i . M is the transfer matrix for the regular size Teflon piece and M_b that of the Teflon piece of length b. Note that $N_1 + N_2 = N - 2$, where N is the total number of unit cells (and Teflon pieces) of the perfect crystal.

The general case of a single substitutional impurity is shown in the lower sketch of figure 4.4. The substitutional impurity has a length b, shown here longer than the regular size Teflon piece, but it could be of any length and/or of a different dielectric material. Quick inspection shows that the form of the impurity matrix is the same, but the values of the lengths a, b and c are different and now $N_1 + N_2 = N - 3$.

Thus, we have a straightforward *numerical* scheme to calculate the transmission amplitude in the presence of an impurity: for a given impurity arrangement we compute equation (4.13).

In figure 4.3(b), we show the case when an extra Teflon piece of smaller length (than the length of the default Teflon piece) is inserted in the center of the air spacing between the 3rd and 4th regular Teflon pieces, thus $N_1 = 2$, $N_2 = 12$. Figure 4.3(c) shows the case of the same type of impurity but located in the air spacing between the 8th and 9th regular Teflon pieces, thus $N_1 = N_2 = 7$. Note the good agreement between the transfer matrix calculations and the main features of the experimental data.

Inspection of the plots of figure 4.3 reveals that the impurity affects the transmission in two ways: (i) The bands develop different profiles (compared to the pure array, figure 4.3(a)). (ii) Peaks appear in most of the gaps in figure 4.3(b) coinciding in frequency with those of figure 4.3(c). Such a coincidence is expected since the impurity in both arrays occupies the same relative position *within* the cell (in the center of the air spacing) but in a different cell.

In figure 4.3(b) the band profiles look like a superposition of slow and fast oscillations. In figure 4.3(c) the oscillations are larger and only of one type. In both figures 4.3(b) and (c), bands containing 1-Teflon resonances (see the 2nd, 4th and 6th bands) are less affected by the impurity. Note also that the intensity of the peaks is greater when the impurity is placed near the center of the array, figure 4.3(c), than when it is placed near the end of the array, figure 4.3(b). This feature was invariably found in all our experiments.

Figure 4.5 shows the experimental and theoretical curves for three types of substitutional impurities. Figure 4.5(a) pertains to the case when a Teflon is removed from the array, i.e. a vacancy. Specifically, the 8th Teflon is removed. In figure 4.5(b) the 8th regular size Teflon piece is substituted by a smaller, whereas in (c) it is substituted by a larger one. Note that while the defect is in the same numbered cell within the array, the band profiles, the frequencies and intensities of the peaks are different for each case since the defects are different.

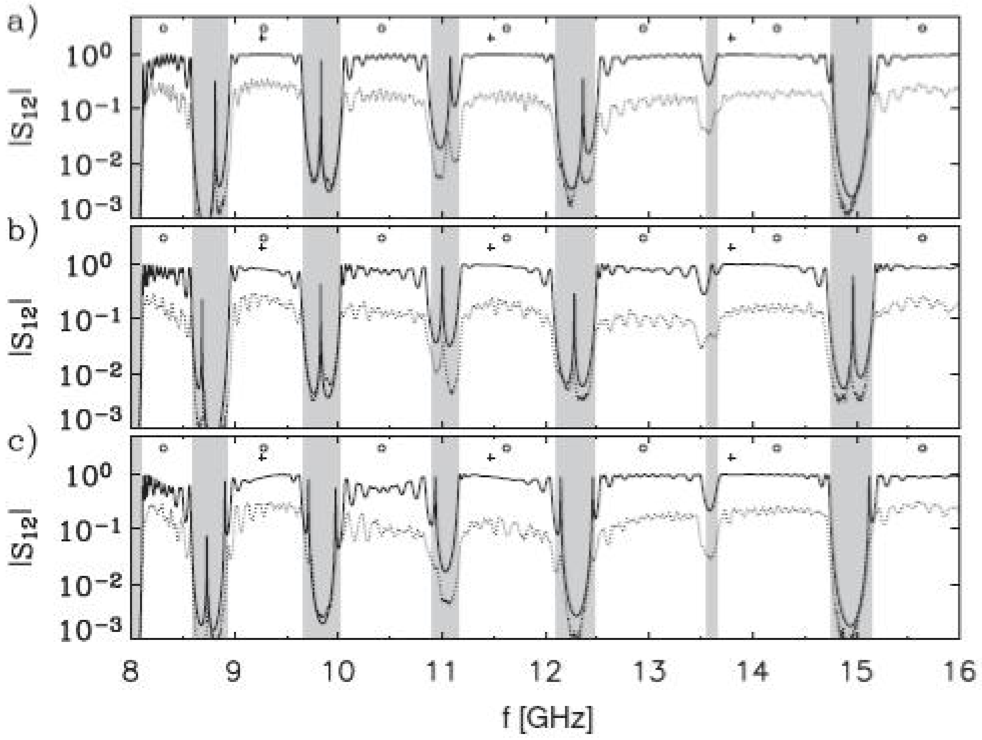

Fig.4.5. Three types of substitutional impurities in an 16 cell array (*d* = *d*0 = 4 cm). Dotted (solid) lines are the experimental (theoretical) curves. In (a) the 8th Teflon piece was removed corresponding to a vacancy. In (b) and (c) it was replaced by a smaller (larger) size Teflon of length *d*0 = 3.16 cm (*d*0 = 6.32 cm), respectively.

A single point defect can produce multiple impurity levels within a band, as has been observed, e.g. by Yablonovitch *et al* [93] in a 3D photonic array with a donor-like impurity. Note that figure 4.5(c) also shows two spikes in most of the gaps.

Shallow impurities in semiconductors, associated with long-range binding, typically show up as spikes near the band edges, whereas deep impurities typically lie near the center of the gap [81]. However, figure 4.5 shows that a single impurity may produce spikes near the center of the gap or near the band edges. Thus we see that the above characterization of the impurity as either deep or shallow is not always applicable.

Although our numerical procedure is seen to reproduce quite well the main features of the experimental data, it does not serve to explain their origin. For this purpose we develop a scheme in the next section which provides us with a general understanding of the direct relation between the number of slow and large or fast and small oscillations and the position of the impurities in the array. We will also show how to determine the frequency position of the impurities.

4.4. Analysis of the effects of the impurities

We express the transfer matrix Q in terms of its diagonal representation Λ. Inserting $Q = P\Lambda P^{-1}$ into equation (4.14) to get

$$Q_{tot} = P\Lambda^{N_2} Q\Lambda^{N_1} P^{-1}, \tag{4.15}$$

Where

$$\widetilde{Q} = P^{-1} Q_{imp} P, \tag{4.16}$$

with

$$P = \begin{pmatrix} \dfrac{Q_{12}}{\lambda_+ - Q_{11}} & \dfrac{Q_{12}}{\lambda_- - Q_{11}} \\ 1 & 1 \end{pmatrix}, \qquad \Lambda = \begin{pmatrix} \lambda_+ & 0 \\ 0 & \lambda_- \end{pmatrix}$$

$$\lambda_\pm = \xi \pm \sqrt{\xi^2 - 1}$$

and $\xi = \mathrm{Tr}Q/2$.

Note that $\widetilde{Q}$ is the impurity matrix in the representation of the diagonal basis of Q. This ‘rotated impurity matrix’ contains information about the coupling of the impurity to the host material through the elements of the transformation matrix P.

From the definition of Q_{tot} and using the representation of P given above we get after some algebra useful expressions for the matrix elements of Qtot:

$$Q_{tot,22} = \lambda_+^{N_1+N_2}\left(f_+\widetilde{Q}_{11} + f_+\widetilde{Q}_{21}\lambda_+^{-2N_1} - f_-\widetilde{Q}_{12}\lambda_+^{-2N_1} - f_-\widetilde{Q}_{22}\lambda_+^{-2(N_1+N_2)}\right), \tag{4.17}$$

where $f_\pm = (\lambda_\pm - Q_{11})/(\lambda_+ - \lambda_-)$,

$$\widetilde{Q}_{21} = Q_{tot,11} f_- + \frac{Q_{imp,12}}{Q_{12}}(\lambda_- Q_{11}) f_+ - \frac{Q_{imp,21} Q_{12}}{\lambda_+ - Q_{11}} f_- - Q_{imp,22} f_- \tag{4.18}$$

and

$$\widetilde{Q}_{22} = Q_{tot,11} f_+ + \frac{Q_{imp,12}}{Q_{12}} (\lambda_- Q_{11}) f_+ - \frac{Q_{imp,21} Q_{12}}{\lambda_+ - Q_{11}} f_+ - Q_{imp,22} f_- . \qquad (4.19)$$

The terms $\widetilde{Q}_{11}$ and $\widetilde{Q}_{12}$ are obtained from $\widetilde{Q}_{22}$ and $\widetilde{Q}_{21}$, respectively, by exchanging λ_+ with λ_- everywhere. As in the case of a single scatterer, it is also true that the complex conjugate of $Q_{\mathrm{tot},11}$ ($Q_{\mathrm{tot},12}$) is $Q_{\mathrm{tot},22}$ ($Q_{\mathrm{tot},21}$). This property is not obeyed by the elements of the rotated impurity matrix. On the other hand, because equation (4.16) is a unitary transformation,

$\mathrm{Tr}(\widetilde{Q}) = \mathrm{Tr}(Q_{\mathrm{imp}})$ and $\det(\widetilde{Q}) = \det(Q_{\mathrm{imp}})$.

Setting $N_1 + N_2 = N$, $\widetilde{Q}_{11} = \widetilde{Q}_{22}$ and $\widetilde{Q}_{12} = \widetilde{Q}_{21} = 0$ in equation (4.16) and using $T = 1/|Q_{\mathrm{tot},22}|$, we recover equation (4.11) that is valid only for the pure array.

4.4.1. Band oscillations

To analyze the effects of the impurity on the band profiles it is convenient, since $T = |Q_{\mathrm{tot},22}|^{-1}$, to study in detail the element $Q_{\mathrm{tot},22}$ given by equation (4.17). In the bands the eigenvalues are complex, $\lambda_- = \lambda_+^*$ and of modulus one, so we can (when considering the absolute value of $Q_{\mathrm{tot},22}$) ignore from our analysis the factor $\lambda_+^{N_1+N_2}$ in front of expression (4.17). We now discuss the quantities $f_\pm$ and $\widetilde{Q}_{ij}$. The functions $f_\pm$ do not contain any information on the impurity: they depend only on $\lambda_\pm$ and Q_{11}, characterizing the periodic array. $f_\pm$ are real and smooth (almost flat) functions within the bands, diverging as $1\big/\sqrt{1-\xi^2}$ at the band edges. More important for our analysis is to note that f_+ and f_- take alternate roles in consecutive bands. Namely, $|f_+|$ is larger than $|f_-|$ in the first and all odd-numbered bands, while the opposite is true in the second and all even-numbered bands.

The quantities $\widetilde{Q}_{ij}$ are also typically very smooth functions within the bands, diverging like $1\big/\sqrt{1-\xi^2}$ at the band edges, and are all roughly of the same magnitude, except for $\widetilde{Q}_{21}$ which diverges at the Teflon resonance (but note that $f_+ = 0$ at Teflon resonances).

With this information about the $f_\pm$ and $\widetilde{Q}_{ij}$ it is expected that in the odd-numbered bands, where terms containing f_- can be ignored to first order, the first two terms in equation (4.17) give the main contribution to $Q_{\mathrm{tot},22}$. Specifically, $T \approx \left| f_+ \left(\widetilde{Q}_{11} + \widetilde{Q}_{21} \lambda_+^{-2N_2} \right) \right|^{-1}$ should yield N_2 oscillations (recall that Θ shifts through π in each band). Figure 4.6(a) shows this term and also $\left| f_+ \widetilde{Q}_{11} \right|^{-1}$ as a function of frequency for the case of an interstitial impurity centered between the third and fourth Teflon pieces (the case corresponding to figure 4.3(b)). For the moment let us concentrate on the first and third transmission bands. The term $|f_+\tilde{Q}_{11}|^{-1}$ (dashed curve in (a)) gives the zero-order approximation to the transmission band. According to the notation of figure 4.4 it follows that $N_1 = 2$ and $N_2 = 12$. The 12 oscillations can be counted in figure 4.4(a) in the plot of $\left|f_+\left(\tilde{Q}_{11}+\tilde{Q}_{21}\lambda_+^{-2N_2}\right)\right|^{-1}$. Moreover, since $\left|f_+\left(\tilde{Q}_{11}+\tilde{Q}_{21}\lambda_+^{-2N_2}\right)\right|^{-1}$ gives the dominant contribution in the odd-numbered bands, the 12 oscillations should also be observed in the total transmission. Indeed this is the case, as is shown by the dashed curve in figure 4.6(b). This plot also shows that the total transmission curve oscillates about a slowly oscillating curve (thick solid line) with two maxima. This slowly oscillating curve is in fact given by $\left|f_+\left(\tilde{Q}_{11}-f_-\tilde{Q}_{12}\lambda_-^{-2N_1}\right)\right|^{-1}$ with $N_1 = 2$ as pointed out above. Finally the last term in equation (4.17) gives an additional $N_1 + N_2$ oscillations of smaller amplitude, which provides small corrections (not readily visible in the plot).

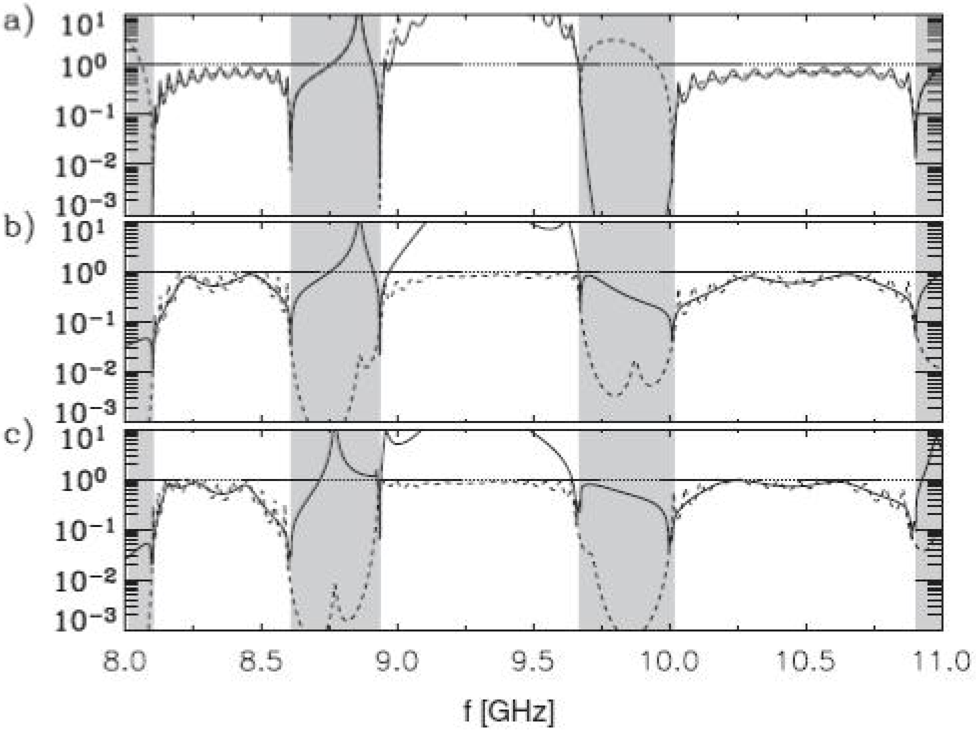

Fig.4.6. Band oscillations due to impurities. (a) and (b) correspond to an interstitial impurity *centered* in the air spacing between the third and the fourth regular size Teflon pieces, whereas in (c) it is *displaced*. $|f_+ \tilde{Q}_{11}|^{-1}$ (dashed) and $\left|f_+\tilde{Q}_{11}+f_+\tilde{Q}_{21}\lambda_+^{-2N_2}\right|^{-1}$ (solid) are shown in (a). In (b) and (c) $|\tilde{Q}_{\text{tot},22}|^{-1}$ (dashed) and $\left|f_+\tilde{Q}_{11}+f_-\tilde{Q}_{12}\lambda_+^{-2N_1}\right|^{-1}$ (solid) are shown.

As figure 4.6(b) shows, the term $\left|f_+\tilde{Q}_{11}+f_-\tilde{Q}_{12}\lambda_+^{-2N_1}\right|^{-1}$ does not agree at all with the average curve of the transmission in the gaps nor in the *even* numbered bands. This is because our discussion has been limited to the bands, where the eigenvalues are complex, and of modulus one, whereas in the gaps the eigenvalues are real, and hence the factor $\lambda_+^{N_1+N_2}$ in (4.17) cannot be ignored (in the next section we shall consider in detail the gap regions). There is no agreement in the *even*-numbered bands either because there the dominant terms are those containing the form factor f_-, namely, the sum $\left|f_-\left(\tilde{Q}_{22}+\tilde{Q}_{12}\lambda_-^{-2N_2}\right)\right|$. This can be readily seen by factoring in equation (4.17) the term $\lambda_-^{N_1+N_2}$ to get $Q_{tot,22}=-\lambda_-^{N_1+N_2}\left(f_-\tilde{Q}_{22}+f_-\tilde{Q}_{12}\lambda_-^{-2N_2}-f_+\tilde{Q}_{21}\lambda_-^{-2N_1}-f_+\tilde{Q}_{11}\lambda_-^{-2(N_1+N_2)}\right)$. Written in this form, it is clear that the same arguments used for the odd-numbered bands work for the even-numbered bands but with f_- and f_+ interchanged. Explicitly, the dominant term in the even-numbered bands is $\left|f_-\left(\tilde{Q}_{22}+\tilde{Q}_{21}\lambda_-^{-2N_2}\right)\right|$, giving rise again to N_2 = 12 oscillations. The second-order term, producing the N_1 = 2 oscillations, is $\left|f_-\tilde{Q}_{22}-f_+\tilde{Q}_{21}\lambda_-^{-2N_1}\right|$.

Thus, *the number of slow and fast oscillations appearing in the profiles of the transmission bands can be read off directly from* equation (4.17). Assuming for the moment that $N_2 > N_1$, the band profiles should show N_2 fast oscillations about a curve with N_1 slow oscillations. This is exactly what we have noticed in our experimental and numerical transmission curves, see e.g. figure 4.3(b), corresponding to an interstitial impurity with (N_1, N_2) = (2, 12), respectively.

On the other hand, if $N_1 = N_2$, then the profile should show only N_1 oscillations of larger amplitude than in the case above ($N_2 \neq N_1$). The experiments confirm this, as is illustrated in figure 4.3(c), where $N_1 = N_2 = 7$. Finally, if N_1 is close but not exactly equal to N_2 then the oscillation pattern becomes more complicated, with irregular (incomplete) oscillations and with no distinctive modulation pattern, as exemplified by the plots of figure 4.5, where $N_1 = 6$ and $N_2 = 8$.

Thus, given some experimental curves for the transmission, one can determine where along the array there is a single impurity by simply observing the pattern and number of oscillations. Note, however, that due to time reversal symmetry it is not possible to deduce on which side of the array to count the N_1 cells. At the very least, the form of the profile indicates the presence of impurity or defect, and whether it is located near the ends or near the center of the array.

It is important to remark that the above conclusions hold as long as the elements $\tilde{Q}_{ij}$ do not have oscillations of their own as is the case of the interstitial impurities discussed above. For certain other types of defects the elements $\tilde{Q}_{ij}$ do have some structure and consequently the type of profiles discussed above becomes somewhat distorted. An extreme example occurs when a smaller Teflon piece is placed off-center between two regular size Teflon pieces, that is, a *displaced* interstitial impurity. Specifically, the $\tilde{Q}_{ij}$ show a strong frequency dependence (e.g. $\tilde{Q}_{11}$ and $\tilde{Q}_{21}$ each have three extrema in their real and imaginary parts in each band). For example, figure 4.6(c) shows the total transmission and $\left|f_+\tilde{Q}_{11} - f_-\tilde{Q}_{12}\lambda_-^{2N_1}\right|^{-1}$ for an interstitial impurity placed off-center between the 3rd and 4th regular size Teflon pieces. This defect is described by the upper sketch of figure 4.4 with N_1 = 2 and N_2 = 12 with N = 16. Note that the term $\left|f_+\tilde{Q}_{11} - f_-\tilde{Q}_{12}\lambda_-^{2N_1}\right|^{-1}$ correctly gives the average curve of the band profile but now there are three slow oscillations and 14 fast oscillations, instead of 2 and 12 oscillations, respectively.

4.4.2. Impurity states

We now analyze the appearance of the peaks in the gaps, the well-known signal for the presence of an impurity. Without limiting in any way the conclusions to be drawn here, let us consider the d = d' = 4 cm array, the example we have been using, and let us label the gaps. Gap one is in the frequency range 7.7–8.1 GHz, see e.g. figure 4.7; gap two in the range 8.6–8.9 GHz, and so on.

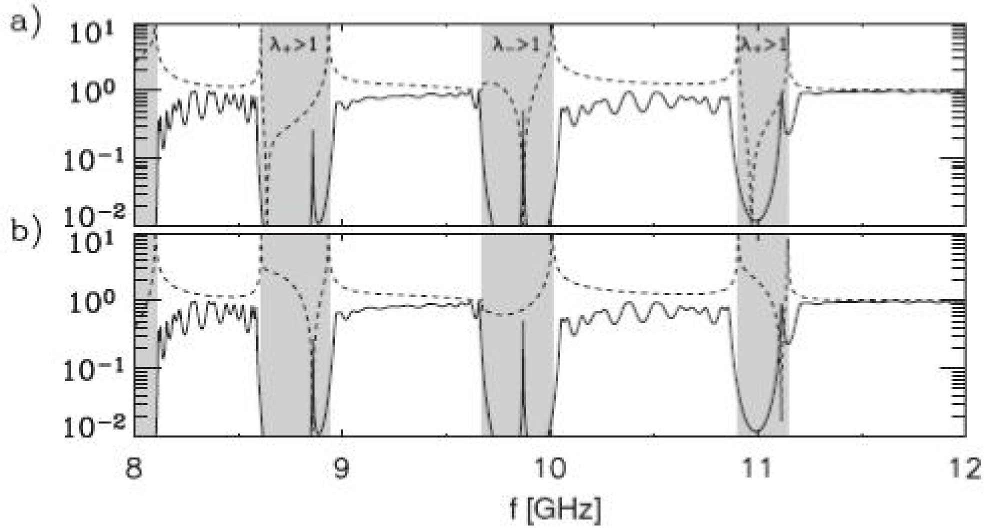

Fig. 4.7. Impurity states. In both plots the transmission amplitude $1/|Q_{\text{tot},22}|$ is shown (solid). In (a) the dashed line corresponds to $\tilde{Q}_{22}$ and in (b) to $\tilde{Q}_{11}$. All parameters are the same as in figure 4.3(c), except that now the impurity is between the 7th and 8th regular size Teflon pieces, thus N_1 = 6 and N_2 = 8.

Recall that in the gaps the eigenvalues are real, therefore, we rewrite equation (4.17) as

$$Q_{tot,22} = f_+\widetilde{Q}_{11}\lambda_+^N + f_+\widetilde{Q}_{21}\lambda_+^{N_1-N_2} - f_-\widetilde{Q}_{12}\lambda_-^{N_1-N_2} - f_-\widetilde{Q}_{22}\lambda_-^N, \qquad (4.20)$$

where $N = N_1 + N_2$. Now, for the transmission to produce a sharp peak in the gaps, $Q_{\text{tot},22}$ must be small in a very narrow range of frequencies. Note that $\lambda_+\lambda_-=1$, with λ_- and λ_+ alternatingly being the larger one in each gap. In the even-numbered gaps (where $\lambda_+ > 1 > \lambda_-$) the dominant term in $Q_{\text{tot},22}$ is the first term in equation (4.20), and it will be large (corresponding to a negligible transmission) unless it happens that $\widetilde{Q}_{11}$ is very small or zero. Similarly, in the odd-numbered gaps (where $\lambda_- > 1 > \lambda_+$), the dominant term is the last one and it will also be a large number unless $\widetilde{Q}_{22}$ happens to be very small. To illustrate this general observation, in figure 4.7 we consider the case of an interstitial impurity placed in the air spacing of the 8th cell in a 16-cell array (thus, $N_1 = 6$, $N_2 = 8$). In figure 4.7(a), we show the transmission amplitude $1/|Q_{\text{tot},22}|$ and also the term $|\widetilde{Q}_{22}|$. In contrast, in (b) the term $|\widetilde{Q}_{11}|$ is shown, together with $1/|Q_{\text{tot},22}|$. Observe in figure 4.7(a) that whenever $\widetilde{Q}_{22}$ goes sharply to zero in the odd-numbered gaps ($\lambda_- > 1$), there is an impurity state at the same frequency. $\widetilde{Q}_{22}$ also goes to zero sharply in the even-numbered gaps ($\lambda_+ > 1$) but here there is no coincidence with the impurity states, in agreement with our argument of the previous paragraph. Similarly, figure 4.7(b) shows that there is an impurity state in the even-numbered gaps at the frequency values where $\widetilde{Q}_{11}$ goes to zero. Thus, our simple argument above really works in determining the position of the impurity states: *an impurity state occurs in odd-numbered gaps at the frequencies where* $\widetilde{Q}_{22}$ *is zero and in the even-numbered gaps where* $\widetilde{Q}_{11}$ *is zero*. A similar case was already shown in figure 4.3(c) except that $N_1 = N_2 = 7$ and thus band profiles are different but peak positions are the same, where we see an excellent agreement with experiment concerning the location of the peaks.

Single impurity states are known to decay exponentially away from the site of the impurity. One then may expect that the intensity of the peak should be stronger the closer the impurity is to either of the ends of the array. However close inspection of formula (4.20) indicates that this is not the case. That is, exactly at the impurity state frequency, say when $\widetilde{Q}_{11}$ is zero in an even-numbered band, the first term in (4.20) is zero and the leading terms are $f_+\widetilde{Q}_{21}\lambda_+^{N_2-N_1} - f_-\widetilde{Q}_{12}\lambda_-^{N_2-N_1}$. The inverse of its absolute value gives to a good approximation the intensity of the peak. For simplicity, let us consider first the case $f_+\widetilde{Q}_{21} = f_-\widetilde{Q}_{12}$ which is valid only for 'symmetric impurities', i.e. when the distance a equals the distance c (see figure 4.4). Note that $\lambda_+^{N_2-N_1} + \lambda_-^{N_2-N_1}$ as a function of $N_2 - N_1$ is symmetric about its minimum $N_2 - N_1 = 0$. Thus, recalling that the transmission is the reciprocal of $|Q_{\text{tot},22}|$, we conclude that *the intensity of the impurity state should be stronger the closer the impurity is to the center of the array*. It is strongest when $N_2 = N_1$, i.e. when the impurity or defect is at the center of the array.

The above argument assumed that the impurity is symmetric. If it is not the case, then it can be shown that the minimum of $\left|f_+\widetilde{Q}_{21}\lambda_+^{N_2-N_1} - f_-\widetilde{Q}_{12}\lambda_+^{N_2-N_1}\right|$ does not occur when the impurity is at the center ($N_1 = N_2$) but at a distance $N_1 - N_2$ that is proportional to the logarithm of $\left|f_-\widetilde{Q}_{12}\right| / \left|f_+\widetilde{Q}_{21}\right|$. Since this ratio is not large, the highest intensity peak still occurs when the impurity is close to the center of the array. This was verified in all our experiments and can be seen clearly by comparing figures 4.3(b) and (c). We emphasize that this effect is independent of the type of the periodic potential and type of impurity in a 1D periodic array. In fact, the same behavior was noted in an experiment with a coaxial connector photonic crystal [82] where, however, no explanation was given.

As we have seen, the intensity of the peaks always decreases as the number N of cells increases. However, an important conclusion, drawn from a detailed examination of equation (4.20) as a function of λ_+, for fixed N, is the following: *the decrement in the peak intensity as N increases is weaker the farther the impurity state is from the center of the transmission band*. This was confirmed by our experimental and theoretical results and it is in agreement with the generally accepted idea that shallow states near the band edges are the shallow levels, associated with long range potentials, in contrast with the deep levels lying near the center of the band (see, e.g., [81]).

4.5. Conclusions

We analyzed the effects on the transmission of single impurities in an array of regularly spaced pieces of Teflon in a microwave guide, described by a 1D photonic Kronig–Penney model. We performed a series of experiments with point defects of various types; namely, interstitial, substitutional and vacancies, and showed that a single impurity affects the transmission in two ways. One is the well-known appearance of localized states in the gaps; the second, to our knowledge not discussed so far in the literature, is the appearance of fast and slow oscillations in the band profiles. Our transfer matrix calculations correctly predicted these features. Experiments with other types of single impurities, e.g. displaced interstitial and displaced substitutional impurities, not reported here, were also found to be equally well described by our model. The transfer matrix calculations (being purely numerical) agree very well with the experimental data, but they provide no insight for the understanding of the various features observed. Thus, as an important contribution, we derived an exact closed form expression for the transmission amplitude that is useful in elucidating the effects of a single impurity on the band profiles, the impurity levels and their intensity. This expression involves elements of the transfer matrix Q of the regular cells in the array and of the transfer matrix $\widetilde{Q}$ of the impurity. Since this matrix is written in the representation that diagonalizes the transfer matrix of the regular cells, $\widetilde{Q}$ contains information about the impurity and its coupling with the host environment.We found that the set of impurity levels is given by the zeroes of the diagonal elements of $\widetilde{Q}$. Further, it was shown that the intensity of the impurity states in the gaps depends on two factors, namely, the off-diagonal elements of $\widetilde{Q}$ and the distance of the impurity from the center of the array. The closer the impurity is to either of the ends of the array, the lower the intensity of its level, and vice versa. It was also shown that the numbers of fast and slow oscillations in the bands give direct information about the position of the impurity, relative to the center of the array.

We note that the agreement between the experimental results and analytical calculations gives us confidence to treat the inverse problem. That is, we can extract information about the unknown defect from the inspection of the band profiles and the localized defect modes. Our method is an alternative approach to the tight-binding and Green's functions methods, for 1D systems, with the advantage that it is simpler and elucidating. Although the experimental realization here is in the microwave regime, the model and the results are equally valid for higher scales of frequency corresponding to light experiments. We remark that we can apply our formalism in a straightforward manner to any kind of regular array with single defects once we have determined the particular transfer matrices for the regular cell and for the impurity.

We emphasize that the formulae (4.17)–(4.20) and the procedure for determining the position and intensity of impurity states and features of the band profiles for the photonic Kronig–Penney model are exactly the same as for the *electronic* Kronig–Penney model (with square barriers) for energies above the barrier. This is so since their transfer matrix elements are identical and the difference is only in the definition of the longitudinal wavevector. Hence our procedure is useful for analyzing the effects of impurities, either in the transport of charged particles in 1D periodic arrays of electronic potentials (e.g. heterostructures) or in the transmission of electromagnetic waves in 1D photonic arrays.

Finally, the fact that our experimental and theoretical results agree very well give us confidence to treat various other types of specific arrangements with the goal of realizing them in other experimental set-ups as photonic devices. We would like to stress that this is by no means self evident. The observed transmission patterns are the result of a complicated interplay of interferences from all structures within the waveguide, and it is well known that interferences are extremely sensitive to perturbations, in particular in the presence of absorption. The present work has shown that we can rely on the experiment in this respect. Thus our experimental setup can be used as a preliminary—and low cost—study of a particular Kronig–Penney model to be implemented later in more sophisticated and expensive microscopic photonic realizations, which might have real applications.

5 ASYMPTOTIC ENERGY PROFILE OF A WAVEPACKET IN DISORDERED CHAINS

We investigate the long time behavior of a wavepacket initially localized at a single site n_0 in translationally invariant harmonic and anharmonic chains with random interactions. In the harmonic case, the energy profile $\overline{\langle e_n(t)\rangle}$ averaged on time and disorder decays for large $|n - n_0|$ as a power law $\overline{\langle e_n(t)\rangle} \approx C|n-n_0|^{-\eta}$ where η = 5/2 and 3/2 for initial displacement and momentum excitations, respectively. The prefactor C depends on the probability distribution of the harmonic coupling constants and diverges in the limit of weak disorder. As a consequence, the moments $\langle m_\nu(t)\rangle$ of the energy distribution averaged with respect to disorder diverge in time as $t^{\beta(\nu)}$ for $\nu \geq 2$, where $\beta = \nu + 1 - \eta$ for $\nu > \eta - 1$. Molecular dynamics simulations yield good agreement with these theoretical predictions. Therefore, in this system, the second moment of the wavepacket diverges as a function of time despite the wavepacket is not spreading. Thus, this only criteria often considered earlier as proving the spreading of a wave packet, cannot be considered as sufficient in any model. The anharmonic case is investigated numerically. It is found for intermediate disorder, that the tail of the energy profile becomes very close to those of the harmonic case. For weak and strong disorder, our results suggest that the crossover to the harmonic behavior occurs at much larger $|n - n_0|$ and larger time.

5.1 Introduction

There has been large activity for many years in the study of the temporal evolution of an initially localized energy excitation in various nonlinear systems, e.g. the discrete, nonlinear Schrödinger equation (DNLS) [94–98], Fermi-Pasta-Ulam (FPU) [99–103] and Klein-Gordon (KG) model [98, 104] with both uniform and random couplings. In the latter case, the main interest is in the interplay of anharmonicity (nonlinearity) and disorder which is not yet fully understood. For harmonic one-dimensional disordered systems, all eigenmodes (called Anderson modes) of the infinite system are known to be localized and form a complete basis. Then a wave packet at time $t = 0$ will remain localized at any time as a linear superposition of Anderson modes of the infinite chain. Whether or not this behavior changes qualitatively by introduction of anharmonicity is highly debated and controversial (see Refs. [96, 97,104] and references therein).

Since an analytical treatment of the time evolution of anharmonic systems with disorder is extremely difficult, most investigations have been done by molecular dynamics simulations. In the numerical studies, one typically follows the wavepacket dynamics by monitoring quantities like the participation ratio *P(t)* (a measure the localization at time *t*), and the time-dependent moments $m_\nu(t)$ of the local energy $e_n(t)$ (see the definitions below). All this measurements are hampered by statistical errors as well as finite size and finite time effects. Even very long calculation times of, say, 10^8 microscopic time units (of order picoseconds) may not be entirely conclusive. Indeed, one can never be sure whether the spreading of a wavepacket is complete or only partial in the infinite-time limit. This issues are intimately related to the spontaneous self-trapping of energy (for example in the form of discrete breathers) which is generic in most nonlinear systems.

Independently on complete or incomplete spreading, one might expect that the evolution of the wavepacket tails should yield relevant information on the spreading process itself. In such regions, the typical displacement becomes small enough such that linear approximation of the forces becomes valid. This motivates the investigation of the harmonic chain, as a first necessary step for an insight of the nonlinear case. Despite the apparent simplicity of such a case there are still issues that have not been fully discussed in the literature. Let us briefly review some of the main results known for this case. Without disorder all eigenstates are extended and it is well-known (see e.g. Ref. [106], and references therein) that

$$m_\nu(t) \sim t^{\beta(\nu)} \tag{5.1}$$

with $\beta(2) = 2$, i.e. the energy spreading is ballistic (note that ν is not necessarily an integer). Introducing disorder and/or anharmonicities, this energy transport is changed and may be superdiffusive $(\beta(2) > 1)$, diffusive $(\beta(2) = 1)$ or subdiffusive $(\beta(2) < 1)$, or it could become logarithmic or disappear $(\beta(2) = 0)$. If the initial excitation is at site zero with amplitude $u_0(0)$, then the disorder averaged propagator $\langle u_n(t)\rangle$ is one of the basic quantities. Although $\langle u_0(t)\rangle$ or $t \rightarrow \propto$ is known analytically for different classes of disorder [108], much less is known for $n \neq 0$. Approximatinghe Anderson modes by plane waves with exponentially decaying amplitudes, it has been shown in Ref. [100] that

$$\langle u_n(t)\rangle \equiv \frac{1}{2(\pi\xi|n|)^{1/2}} exp\left[-\frac{(|n|-ct)^2}{4\xi_0|n|}\right] \tag{5.2}$$

for $|n| \rightarrow \propto$ and $t \rightarrow \propto$. Here, *c* is the sound velocity and ξ_0 a measure of the localization length. Eq. (5.2) shows for $t \rightarrow \propto$ there are two humps which propagate ballistically at the sound velocity *c,* but with an amplitude which decays as $1/\sqrt{t}$. Within its co-moving frame, these humps spread as for normal diffusion. Another approach for calculating $\langle u_n(t)\rangle$ is to use a scaling hypothesis [108]

$$\langle \tilde{u}_n \omega)\rangle = \langle \tilde{u}_0(\omega)\rangle F(n/\xi(\omega)), \qquad \omega \to 0 \tag{5.3}$$

for the Laplace transform of $\langle u_n(\omega)\rangle$ for $\omega \to 0$. A similar Ansatz can be made for $\langle u_n(t)\rangle$ [110–112]. Here, $\xi(\omega)$ denotes a localization length.

In this paper we investigate the energy profile $\overline{\langle e_n(t)\rangle}$ averaged on time and disorder of a wavepacket originating an initially localized excitation. We demonstrate that it asymptotically decays as a power law in space. Thus, the wavepacket remains localized only weakly while its moments appear to diverge in time. This result, which, to the best of our knowledge, has not been reported previously, must be taken into account expecially when attacking more difficult nonlinear case. Indead, some numerical results for the anharmonic chain (a FPU model) will be critically analyzed on the basis of the results on the harmonic one.

The outline of our paper is as follows. In Section 5.2 we will introduce the harmonic model, rephrase some of its well-known properties, define the local energy $e_n(t)$ and give some information on our numerical approach. A virial theorem for the time averaged local kinetic and potential energy will be proven in Section 5.3 It will be applied in this section for the analytical calculation of the time and disorder average of $e_n(t)$. The corresponding analytical result will be compared with the numerical one. Furthermore we will investigate the moments $m_\nu(t)$ of the local energy $\langle e_n(t)\rangle$. The influence of anharmonicity on $e_n(t)$ will be numerically studied in Section 5.4, and the final Section 5.5 contains a summary and some conclusions.

5.2 The disordered harmonic chain

5.2.1 Property of the Anderson modes

As motivated above we investigate the classical dynamics of a disordered harmonic chain with lattice constant a which is invariant under translations. Its classical Hamiltonian reads:

$$H = \sum_n \left[\frac{p_n^2}{2m} + \frac{1}{2} K_n (u_{n+1} - u_n)^2 \right] \tag{5.4}$$

Here, u_n is the displacement of the particle at site n, p_n the corresponding conjugate momentum, m the particle's mass, and K_n the random coupling constants between nearest neighbors. The K_n are independent random variables, identically distributed with some probability distribution $p(K)$. Stability requires all K_n to be positive. In our numerical approach, the system is finite with N particles and with free ends, i.e. $K_{\pm N/2} = 0$. Otherwise, we shall perform analytical calculations in the thermodynamic limit $N \rightarrow \infty$ where the choice of the boundary conditions does not matter. The equations of motions are

$$m\ddot{u}_n = K_n(u_{n+1} - u_n) - K_{n-1}(u_n - u_{n-1}). \tag{5.5}$$

The general solution of Eqs. (5.5) with initial conditions $u_n(0) = u_n$, $u^{\cdot}_n(0) = u^{\cdot}_n$ is given by

$$u_n(t) = U_0 + \dot{U}_0 t + u_n(t) \tag{5.6}$$

where

$$u_n(t) = \sum_{n'}\left[u_{n'}\left(\sum_{v\neq 0} Q_n^{(v)} Q_{n'}^{(v)} \cos\omega_v t\right) + \dot{u}_{n'}\left(\sum_{v\neq 0}\frac{1}{\omega_v} Q_n^{(v)} Q_{n'}^{(v)} \sin\omega_v t\right)\right] \tag{5.7}$$

and $U_0 = \sum_n u_n / N,\ \dot{U}_0 = \sum_n \dot{u}_n / N$ are the position and velocity, respectively, of the center of mass of the whole chain.

The eigenmodes $Q_n^{(v)}$ with eigenfrequency ω_v can be chosen as real with indices v in a countable set. They satisfy

$$K_n\left(Q_n^{(v)} - Q_{n+1}^{(v)}\right) + K_{n-1}\left(Q_n^{(v)} - Q_{n-1}^{(v)}\right) = m\omega_v^2 Q_n^{(v)} \tag{5.8}$$

and the can be normalized, except the unifiorm eigenmode $Q_n^{(0)} \equiv 1$ whith $\omega_0 = 0$ which is extended and cannot be normalized for the infinite system. For any size N of a finite system, the translation invariance of the model implies that $Q_n^{(0)} = \frac{1}{\sqrt{N}}$ is an eigenmode with eigenfrequency $\omega_0 = 0$. In the limit of an infinite system, all eigenmodes are localized, except this single zero-frequency mode which is extended. However, nothing changes in the problem when choosing the center of mass of the whole system immobile at $U_0 = 0$ with $\mathring{U}_0 = 0$. Though the eigenspectrum is discrete for the infinite system, it is dense. The corresponding density of states

$$g(\omega) = \lim_{N\rightarrow\infty}\frac{1}{N}\sum_{v=1}^{N-1}\delta(\omega - \omega_v) \tag{5.9}$$

is a smooth function which is known [108] to be self-averaging, i.e. it is independent on the disorder realization with probability one. Moreover, in the small frequency limit, $\omega \rightarrow 0$, we have [109, 110]

$$g(\omega) \cong \frac{\sqrt{m(K^{-1})}}{\pi} \tag{5.10}$$

The localized eigenmodes, decay exponentially with a localization length [109, 110]

$$\xi_v = \xi(\omega_v) \cong \frac{8(K^{-1})/m}{(K^{-2}) - (K^{-1})^2} \omega_v^{-2} a, \qquad \omega_v \rightarrow 0 \tag{5.11}$$

which diverges at the lower “band” edge at $\omega_0 = 0$.

Then, if the chain is finite with length L, there is a frequency ω_L such that the localization length equals the system size, i.e $\xi(\omega_L) = L = aN$. Consequently, only the eigenmodes with frequency $\omega_v > \omega_L$ can be considered as well localized inside the finite system. while the remaining modes where $\omega_v < \omega_L$ extend over the whole finite system.

Their number which is of order of $\sqrt{N}$ goes to infinity in the limit of an infinite system despite their relative weight for $N \rightarrow \infty$ goes the zero as $1/\sqrt{N}$. As a result, they still play a role for transport quantities, like the energy diffusion constant [99, 103, 111] or the thermal conductivity [112]. Actually, those relatively extended modes behave like acoustic modes whose effective sound velocity is

$$c = \sqrt{\frac{(K^{-1})^{-1}}{m}} a \tag{5.12}$$

Although these results were originally proven for a chain with mass disorder they also hold for our model. Indeed, letting $y_n = (u_{n+1} - u_n)/K_n$, Eq.(5.5) is mapped onto the eigenequation with mass disorder. This property has already been used above since the mass average (m) has been replaced by (K^{-1}).

5.2.2 Local energy and local virial theorem

We define the local energy:

$$e_n(t) = e_n^{(kin)}(t) + e_n^{(pot)}(t)$$

with kinetic and potential parts

$$e_n^{(kin)}(t)=\frac{m}{2}\left(\dot{u}_n(t)\right)^2 \tag{5.13}$$

and

$$e_n^{(pot)}(t)=\frac{1}{2}K_{n-1}\left[u_n(t)-u_{n-1}(t)\right]u_n(t)-\frac{1}{2}K_n\left[u_{n+1}(t)-u_n(t)\right]u_n(t) \tag{5.14}$$

respectively. Then, $\sum_n e_n^{(pot)}$ equals the total potential energy in Eq. (5.4). We will investigate the energy profile for a displacement excitation:

$$u_n(0)=A\delta_{n,n_0}, \qquad p_n(0)\equiv 0 \tag{5.15}$$

and a momentum excitation:

$$u_n(0)\equiv 0, \qquad p_n=B\delta_{n,n_0} \tag{5.16}$$

For calculating numerically $\{u_n(t)\}$ we considered the example of a uniform and uncorrelated distribution of random couplings K_n with probability distribution

$$p(K)=\begin{cases}\dfrac{1}{k(R-1)}, if & k\le K\le Rk\\ 0 & otherwise\end{cases} \tag{5.17}$$

where of course $R\geq 1$.

To explore the role of different disorder strengths we fixed $k = 1$ and took different R. The choice of units is such that $m = 1$ and $a = 1$. Note that with this particular choices the effective sound velocity, Eq. (5.12), is $c=\sqrt{\frac{R-1}{ln R}}$.

Microcanonical simulations were performed for typically N=8192 particles with fourth order symplectic algorithm [113], with typical time step 5×10^{-3} or less. Although the choice of the initial conditions, Eqs. (5.15) and (5.16), implies $U_0 = A/N$, $\overset{\circ}{U}_0 = 0$ and $U_0 = 0$, $\overset{\circ}{U}_0 = B/N$, respectively, these nonzero quantities are rather small, since A and B are of order one and N»1.

In our numerical experiments, we avoid that the wavepacket reaches the chain boundaries which may generate spurious finite-size effects (reflexions etc.). Thus, one should restrict the maximum simulation time tsim to be smaller than $t_{max} \sim N/c$ where c is the sound velocity.

We also fixed $n_0=-N/2+1$ for extending the spatial range of our system, so that one simulates the wavepacket propagation in a semi-infinite medium [101]. Some runs with $n_0=0$ where also performed, yielding similar results. Figure 5.1 shows the numerical profile $e_n(t$ = 2000) for a momentum excitation with B = 2.0. The result for a *single* realization of the disorder exhibits on the log-log-representation strong fluctuations around an average, decaying linearly.

Averaging over a large enough number *[O(10^3)]* disorder realizations strongly reduces these fluctuations and supports the linear dependence on $|n\text{-}n_0|$ on the log-log scale. In the next Section we demonstrate that this is indeed the case and compute analytically the exponents associated with such power-lay decay.

The calculation of the time averaged energy profile will be simplified by means of a local virial theorem, that will be proved below. The well-known virial theorem [114] relates the time average of the *total* kinetic energy to the time average of the virial. The virial [114] involves the gradient of the *total* potential energy. If the potential is harmonic this theorem implies equality between the time averaged *total* kinetic and *total* potential energy. In this subsection we will prove that this relationship also holds for the time averaged *local* kinetic and *local* potential energy, defined by Eqs. (5.13) and (5.14), respectively.

The time average of a function *f(t)* is defined by

$$\bar{f}(t) = \lim_{T\to\infty} \frac{1}{T}\int_0^T dtf(t) \tag{5.18}$$

Substitution of the general solution $u_n(t)$ of Eqs. (5.6), (5.7) into Eq. (5.13) and taking into account

$$\begin{aligned} \overline{cos\,\omega_v t\,cos\,\omega_{v'} t} &= \frac{1}{2}\delta_{vv'} \\ \overline{sin\,\omega_v t\,sin\,\omega_{v'} t} &= \frac{1}{2}\delta_{vv'} \\ \overline{sin\,\omega_v t\,cos\,\omega_{v'} t} &= 0 \end{aligned} \tag{5.19}$$

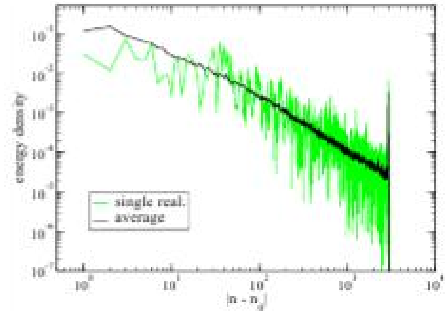

Fig. 5.1: (Color online) Energy profile $e_n(t)$ at $t = 2000$ for a momentum excitation with $B = 2.0$, $N = 8192$ particles, $R = 4$ and for a single realization of disorder (green line) and averaged over 2 x 10^3 realizations (black line).

Yields

$$\bar{e}_n^{(kin)}(\bar{t}) = \frac{m}{2}\dot{U}_0^2 + \frac{m}{4}\sum_{v\neq 0}(Q_n^{(v)})^2\left[\omega_v^2(\sum_{n'} u_{n'}Q_n^{(v)})^2 + (\sum_{n'}\dot{u}_n{}'Q_{n'}^{(v)})^2\right] \tag{5.20}$$

Note that the sum over v remains discrete and cannot be replaced by an integral in the limit of an infinite system.

With our definition Eq. (5.14) of $e_n^{(pot)}$ and using Eq. (5.5), we obtain:

$$e_n^{(pot)}(t) = -\frac{m}{2}\ddot{u}_n(t)u_n(t) \tag{5.21}$$

Substituting $u_n(t)$ from Eqs. (5.6), (5.7), and since $\upsilon_n(t)$ and $\upsilon^{\cdot}n(t)$ has to remain bounded at all times for any initially localized wavepacket (with finite energy), yields

$$\overline{e}_n^{(pot)}(t) = \overline{e}_n^{(kin)}(t) \tag{5.22}$$

for all n and arbitrary initial conditions with finite energy in case that the center of mass has been chosen immobile ($U^{\cdot}_0 = 0$).

5.3 Energy profile: harmonic case

5.3.1 Energy profile

Without restricting generality we choose $m = 1$ and $a = 1$. Let us discuss first the case of a displacement excitation for a given disorder realization. In this case, we obtain from Eqs (5.6) and (5.7) for $A = 1$ and $U_0 = 0$, $U^{\cdot}_0 = 0$

$$\begin{aligned} u_n(t) &= \sum_v Q_n^{(v)} Q_{n_0}^{(v)} \cos\omega_v t \\ \dot{u}_n(t) &= -\sum_{v\neq 0} \omega_v Q_n^{(v)} Q_{n_0}^{(v)} \sin\omega_v t \end{aligned} \tag{5.23}$$

and therefore

$$e_n^{(kin)}(t) = \frac{1}{2}\sum_{v,v'\neq 0} \omega_v \omega_{v'} Q_n^{(v)} Q_{n_0}^{(v)} Q_n^{(v')} Q_{n_0}^{(v')} \sin\omega_v t \sin\omega_{v'} t \tag{5.24}$$

Let us discuss first the qualitative t-dependence of $e_n^{(kin)}(t)$. We will explain how the spectral properties govern its time dependence. Particulary we show that this quantity which is not averaged over time and/or disorder does not decay for $n \to \infty$ and/or $t \to \infty$. Since the eigenspectrum of the infinite random system is discrete with a countable basis of localized eigenstates $\{Q_n^{(v)}\}$, $u_n(t)$ has been expanded in this basis (see Eq. (5.7) and Eq. (5.23)). This expansions is actually an absolutely convergent series of cosine functions of time because

$$\left|\sum_{\mathcal{M}} Q_{n_0}^{(v)} Q_n^{(v)}\right| \le \left(\sum_v Q_{n_0}^{(v)2}\right)^{1/2} \left(\sum_v Q_n^{(v)2}\right)^{1/2} = 1$$

Consequently, $u_n(t)$ is an almost periodic function in the sense of H. Bohr [118]. An equivalent definition for such functions is that for any arbitrarlly small $\epsilon > 0$, there is a monotone sequence of $\tau_\rho(\rho \in \mathrm{Z})$ (called pseudoperiods) which is relatively dense (that is there exists L such that $\tau_{p+1} - \tau_p < L$ for any p) and such that for all p, $f(t)$ is periodic with period τ_p at the accuracy ϵ that is $|f(t+\tau_p) - f(t)| < \in$ for any p and for all t. As a consequence of this recurrence property, an almost periodic function cannot go to zero for $t \to \pm \infty$. The set of almost periodic functions, is an algebra, that is linear combinations and products of almost periodic functions are almost periodic functions, as well.

In our case, the set of eigenfrequencies ω_v is bounded (since the support of the distribution function $p(K)$ is compact) and thus it is straightforward to show that the time derivative $\dot{u}_n(t)$ is also an almost periodic function of time, and the local kinetic energy $e_n^{(kin)}(t)$ defined by Eq. (5.13), as well. $e_n^{(kin)}(t)$ from Eq. (5.24) can be decomposed into a time independent term and remaining time dependent terms :

$$\begin{aligned} e_n^{(kin)}(t) = \frac{1}{4}\sum_{v\neq 0} \omega_v^2 (Q_n^{(v)} Q_{n_0}^{(v)})^2 - \frac{1}{4}\sum_{v\neq 0} \omega_v^2 (Q_n^{(v)} Q_{n_0}^{(v)})^2 \cos 2\omega_v + \\ + \frac{1}{4}\sum_{v\neq v'} \omega_v \omega_{v'} (Q_n^{(v)} Q_{n_0}^{(v)})(Q^{(v')}{}_n Q_{n_0}^{(v')})\left[\cos(\omega_v - \omega_{v'})t + \cos(\omega_v + \omega_{v'})t\right] \end{aligned} \tag{5.25}$$

Note that for a finite chain without disorder, i.e. $K_n \equiv K$, the first and second term on the r.h.s of Eq.(5.25) are of order $1/N$ since the eigenmodes are plane waves where $Q_n^{(v)} \propto 1/\sqrt{N}$. Then $(Q_n^{(v)} Q_{n_0}^{(v)})^2 \propto 1/N^2$, and there are only N such terms. Consequently, they will not contribute to $e_n^{(kin)}(t)$, in the limit $N \to \infty$ when the eigenspectrum of the chain becomes absolutely continuous. In that case $e_n^{(kin)}(t)$ can be represented by an integral which is a Fourier transform of a smooth function and is obviously not an almost periodic function. It decays to zero at infinite time as expected from ballistic diffusion. This is not true in case of disorder, because each term in the series keeps a non vanishing contribution for the infinite system and $e_n^{(kin)}(t)$ does not decay to zero at infinite time because it is almost periodic.

However, in contrast to the ordered chain, $Q_n^{(v)} Q_{n_0}^{(v)}$ is not a smooth function of ων, in case of disorder. The reason is that when the eigenspectrum is discrete, arbitrarily small variations of ω_v may change the location of the corresponding localized eigenstate by arbitrarily large distances. Thus, these eigenstates $\{Q_n^{(v)}\}$ are not continuous functions of ω_v but depend on the disorder realization as well as $e_n^{(kin)}(t)$ and $e_n(t)$ (since they are obtained as discrete series explicitly involving these eigenstates). The consequence is that those quantities are not self-averaging, as clearly demonstrated by Fig. 5.1 for $e_n^{(kin)}(t)$.

5.3.2 Disorder averaged profile

Since $e_n^{(kin)}(t)$ is an almost periodic function of time, it is a stationary solution. Its time average drops all cosine terms in Eq. (5.25) and keeps only the constant term, i.e. we get

$$\overline{e}_n^{(kin)}(t) = \frac{1}{4}\sum_{v\neq 0}\omega_v^2 (Q_n^{(v)} Q_{n_0}^{(v)})^2$$

An attempt to justify the use of the time averaged quantity will be given below. $\overline{e}_n^{(kin)}(t)$ and $e_n(t)$ still depend on the disorder realization. Therefore it is reasonable to calculate the corresponding disorder averaged quantities, as well. Despite they cannot be observed for any single disorder realization, they give information on the general behavior of the profiles. Then we arrive at

$$\overline{(e_n^{(kin)}(t))} = \frac{1}{4}(\sum_{v\neq 0}\omega_v^2 (Q_n^{(v)} Q_{n_0}^{(v)})^2) \tag{5.26}$$

for the infinite system.

Note that, in the infinite system, the set of eigenvalues and eigenvectors are discontinuous functions of the disorder realization. Yet, according to Wegner [22], the disorder average $(F(\{Q_n^{(\omega)}\}))$ of an arbitrary function $F(\{Q_n^{(\omega)}\})$ of the eigenvectors can be well defined as a smooth function of ω as a limit for finite systems with size $N \longrightarrow \infty$.

$$(F(\{Q_n^{(\omega)})\}))q(\omega)\delta\omega = \lim_{N\to+\infty}\int\left(\frac{1}{N}\sum_{\omega<\omega_v<\omega+\delta\omega} F(\{Q_n^{(v)}\}\right)\prod_{n=1}^{N} p(K_n)dK_n$$

The sum in the integral is restricted to eigenvalues ω_v which belong to an interval $[\omega, \omega + \delta\omega]$ of small width $\delta\omega$ and $g(\omega)$ is the density of states defined by Eq. (5.9).

Then, we obtain from Eq. (5.26):

$$\overline{(e_n^{(kin)}(t))} = \frac{1}{4}\int_0^\infty d\omega\omega^2 q(\omega) \lim_{N\to\infty}(N((Q_n^{(\omega)}Q_{n_0}^{(\omega)})^2)) \tag{5.27}$$

Since $e_n^{(pot)}(t) = \overline{e}_n^{(kin)}(t)$, for $N = \infty$ and all realizations of $\{K_n\}$ the time and disorder averaged energy profile is given by

$$\overline{(e_n(t))} = 2\overline{(e_n^{(kin)}(t))} \tag{5.28}$$

i.e. the calculation of $\overline{(e_n(t))}$ is reduced to that of *g(ω)* and the "quadratic" correlation function $((Q_n^{(\omega)}Q_{n_0}^{(\omega)})^2)$ for N→∞. $\{Q_n^{(\omega)}\}$ is the solution of the eigenvalue equation (5.8) with ω_v replaced by *ω*.

Before we come to the Eq.(5.25). Making again use of the self-averaging of the density of states we obtain for the second term on its r.h.s.:

$$-\frac{1}{4}\int_0^\infty d\omega\omega^2 q(\omega) \lim_{N\to\infty}(N((Q_n^{(\omega)}Q_n^{(\omega)})^2))\cos 2\omega t$$

Below, it will be shown that $\lim_{N\to\infty}(N((Q_n^{(\omega)}Q_{n_0}^{(\omega)})^2))$ is a finite and smooth function of *ω*. Therefore, the disorder averaged second term will converge to zero, for $t \to \infty$, due to $g(\omega) \to g_0 = const.$, for $\omega \to 0$. The same property hold for the disorder average of the square bracket term in Eq. (5.25). With the density of states *g(ω,ω')* giving the joint distribution for two eigenfrequencies the disorder averaged square bracket term becomes a double integral over *ω* and *ω'*. Although we do not have a rigorous proof $\lim_{N\to\infty}(N^2((Q_n^{(\omega)}Q_{n_0}^{(\omega)})(Q_n^{(\omega')}Q_{n_0}^{(\omega')})))$ which is part of the integrand should be a finite and smooth function of *ω* and *ω'*. Then, talking the limit $N\to\infty$ first, the square bracket term should converge to zero for $t\to\infty$. If this is true that disorder averaged energy profile converges to an asymptotic profile for $t\to\infty$ which is consistent with our numerical result. Indeed, the disorder averaged profile in Fig. 5.1 depends on t only very weakly, for large *t*. In that case the asymptotic profile equals the time averaged one.

Now we come back to the "quadratic" correlation function. Due to the disorder average it will depend only on $[n-n_0]$. Since the Anderson modes are exponentially localized one expects that this correlation function decays exponentially with $[n-n_0]$. To prove this we first present a crude heuristic approach by assuming

$$Q_n^{(v)} \approx \mathrm{N}_v \exp\left(-\frac{|n-n_v|}{\xi_v}\right) \tag{5.29}$$

where the "center of mass" of the Anderson mode v is at n_v, which is a random variable, depending on $\{K_n\}$. N_v is a normalization constant. It should be remarked, that the envelope of an Anderson mode $Q_n^{(v)}$ decays exponentially, but not $Q_n^{(v)}$ itself. Therefore Eq. (5.29) is a crude approximation neglecting sign changes of $Q_n^{(v)}$ with n. Substituting $Q_n^{(v)}$ from Eq. (5.29) into the "quadratic" correlation function and using :

$$\langle f(n_v)\rangle \approx \frac{1}{N}\sum_{n_v=1}^{N} f(n_v) \tag{5.30}$$

we get :

$$\left\langle \left(Q_n^{(v)}Q_{n_0}^{(v)}\right)^2\right\rangle \approx \frac{1}{N}N_v^4\left[\coth\frac{2}{\xi_v}+|n-n_0|\right]\exp\left[-\frac{2}{\xi_v}|n-n_0|\right] \tag{5.31}$$

i.e. the "quadratic" correlation function decays exponentially.

For an analytical calculation of the "quadratic" correlation function in Eq.(5.27) one can use the approach presented in Refs. [115–117]. These authors prove that the computation of the correlation functions $\left\langle Q_n^{(\omega)}Q_{n_0}^{(\omega)}\right\rangle$ and $\left\langle \left|Q_n^{(\omega)}\right|\left|Q_{n_0}^{(\omega)}\right|\right\rangle$ for $|n - n_0|\to\infty$ is reduced to the solution of an eigenvalue problem for an integral kernel. As a result, these correlation functions decay exponentially for large $|n - n_0|$ with an inverse localization length given by $-\ln|\lambda_{max}(\omega)|$. $|\lambda_{max}(\omega)|$ is the largest absolute value of the eigenvalues of kernel. It is smaller than one. Applying that approach it follows for $|n-n_0|\to\infty$

$$\left\langle \left(Q_n^{(\omega)}Q_{n_0}^{(\omega)}\right)^2\right\rangle \cong \alpha(\omega)\exp\left(-|n-n_0|/\xi_2(\omega)\right) \tag{5.32}$$

with a correlation length $\xi_2(\omega)$. We note that the eigenvalue problem in form of an integral equation can only be used to calculate correlation functions of the Anderson modes and not directly to compute the energy profile itself. But the former is needed (see Eq. (5.27)) for the latter.

The correlation lengths (localization lengths) of the correlation functions calculated in Refs. [115–117] and of the "quadratic" correlation function Eq.(5.32) are different from each other and different from $\xi(\omega)$ (Eq. (5.11)), for finite ω. But for $\omega \to 0$ they exhibit the same divergence, i.e. it is (see Eq.(5.11)):

$$\xi_2(\omega) \cong c_2\omega^{-2}, \qquad \omega \to 0 \tag{5.33}$$

with a positive constant c_2, depending on $p(K)$.

The pre-exponential factor $\alpha(\omega)$ can be determined as follows. Assuming that Eq. (5.32) is valid for all $|n - n_0|$, summation of the l.h.s. and r.h.s. of that equation and accounting for the normalization $\sum_n (Q_n^{(\omega)})^2 = 1$ for $\omega = \omega_v$ (remember that $Q_n^{(v)}$ has been chosen as real) yields for $N \to \infty$:

$$\alpha(\omega) \cong \frac{1}{N \coth(1/\xi_2(\omega))} \cong \frac{\omega^2}{N c_2}, \qquad \omega \to 0 \tag{5.34}$$

In the last line, Eq. (5.33) has been applied. With Eqs. (5.32), (5.34) and (5.27), it follows from Eq. (5.28):

$$\left\langle \overline{e_n(t)} \right\rangle \cong \frac{1}{2} \int_0^\infty d\omega g(\omega) \omega^2 \frac{exp\left(-|n - n_0|/\xi_2(\omega)\right)}{coth(1/\xi_2(\omega))} \tag{5.35}$$

The asymptotic $|n - n_0|$-dependence is governed by the small-ω behavior of the integrand. From Eq. (5.10) we get

$$g(\omega) = dI(\omega)/d\omega \cong \sqrt{\langle K^{-1} \rangle}/\pi, \qquad \omega \to 0. \tag{5.36}$$

Assuming that Egs. (5.33) and (5.36) are valid for all ω will not influence the asymptotic dependence of $\overline{(e_n(t))}$ on $|n - n_0|$. Then we get from Eq. (5.35) for the infinite chain and a *displacement excitation*:

$$\left(e_n(t)\right) \cong \frac{3}{16} \sqrt{c_2^3 (K^{-1}) / \pi} \left| n - n_0{}^{-5/2}, \right| \qquad \left| n - n_0 \to \infty \right|, \tag{5.37}$$

i.e. the time and disorder averaged energy profile decays as a power law in $|n - n_0|$ with an exponent $\eta = 5/2$.

So far we have discussed the energy profile for a displacement excitation. The corresponding calculation for a momentum excitation is similar. With the initial condition Eq. (5.16) and $B = 1$, Eq. (5.7) leads to

$$\dot{u}_n(t) = \sum_{v=1}^{N-1} Q_n^{(v)} Q_{n_0}^{(v)} cos\, \omega_v t \tag{5.38}$$

Besides cos $\omega_v t$ the main difference to $u^{\boldsymbol{\cdot}}_n(t)$ for a displacement excitation (see Eq. (5.23)) is the absence of the prefactor ω_v of $Q_n^{(v)} Q_{n_0}^{(v)}$. As a consequence one obtains

$$\left\langle \overline{e_n(t)} \right\rangle \cong \frac{1}{2}\int_0^\infty d\omega g(\omega)\frac{exp\left(-|n-n_0|/\xi_2(\omega)\right)}{coth\left(1/\xi_2(\omega)\right)} \tag{5.39}$$

where ω^2 in Eq. (5.35) is replaced by one. With the same assumptions as above we obtain for the infinite chain and a *momentum excitation*:

$$\left\langle \overline{e_n(t)} \right\rangle \cong \frac{1}{8}\sqrt{c_2\left\langle K^{-1}\right\rangle/\pi}\,|n-n_0|^{-3/2}, \qquad |n-n_0| \to \infty \tag{5.40}$$

It is not surprising that we find a power law decay again. The corresponding exponent is $\eta = 3/2$.

Figures 5.2 and 5.3 report the numerical result for the disorder averaged energy profile at different large times of a displacement and momentum excitation, respectively. They clearly demonstrate first that, the numerical result of the disorder averaged energy profile becomes independent of t for t large enough, and second, that it converges to a power law for large $|n-n_0|$ with exponents predicted by the analytical calculation. The tree spikes at the t-dependent positions $n(t)$ are the phonon fronts propagating with the effective sound velocity, Eq. (5.12).

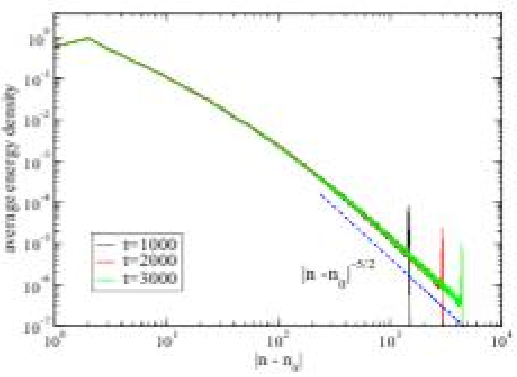

Fig. 5.2: (Color online) Energy profile at three different times averaged over 10^3 realizations of the disorder with $R = 4$ for $N = 8192$ particles and a displacent excitation with $A = 2$. The dashed line is the predicted power law decay, Eq. (5.37). The ballistic peaks propagate at a velocity $c = 1.476$ in agreement with the value $c = 1.471...$ computed from Eq. (5.12).

There is a finite size effect for $N < \infty$, due to the existence of extended states. For $\omega \lesssim \omega_L = \Theta/\sqrt{N}$, (with θ being a suitable constant $O(1)$), it is:

$$\left\langle \left(Q_n^{(\omega)}Q_{n_0}^{(\omega)}\right)^2 \right\rangle \approx \frac{4}{N}sin^2(cqn)sin^2(cqn_0) \tag{5.41}$$

where $\omega \cong cq$. With $g(\omega) \approx g_0$ for the density of extended states it is easy to estimate the contribution of those to $\langle\overline{e_n(t)}\rangle$ in case of a displacement excitation:

$$\langle\overline{e_n(t)}\rangle^{(ext)} \approx \frac{\Theta^3 g_0}{6} N^{-5/2} \tag{5.42}$$

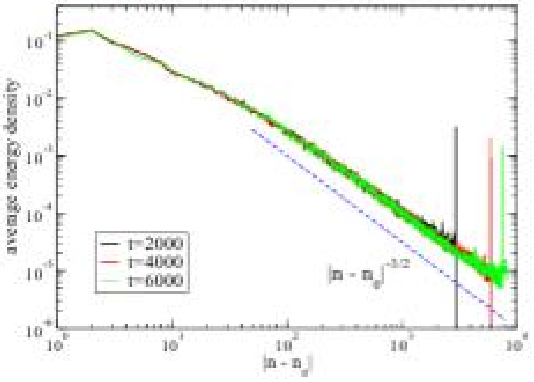

Fig. 5.3: (Color online) Same as Fig. 5.2 but for a momentum excitation with $B = 2$ and averaged over $2\text{x}10^3$ realizations. The dashed line is the predicted power law, Eq. (5.40).

If $1 \ll |n - n_0| \ll N$, then it is $\langle\overline{e_n(t)}\rangle = \langle\overline{e_n(t)}\rangle^{(loc)} + \langle\overline{e_n(t)}\rangle^{(ext)} \cong \langle\overline{e_n(t)}\rangle^{(loc)} \sim |n - n_0|^{-5/2}$. For $|n - n_0| < N$ but $|n - n_0| = O(N)$ there is a crossover value $|n - n_0|_{c.o.}$ depending on θ, g_0 etc. such that

$$\langle\overline{e_n(t)}\rangle^{(loc)} \cong \langle\overline{e_n(t)}\rangle^{(ext)} \sim N^{-5/2} \tag{5.43}$$

For $N = 8192$ this contribution is of order 10^{-10}. The corresponding contribution for a momentum excitation is

$$\langle\overline{e_n(t)}\rangle^{(ext)} \sim N^{-3/2}, \tag{5.44}$$

being of order 10^{-6} for N=8192.

Figure 5.4 compares the energy profiles for different strengths of the disorder, i.e. for various values of the parameter R. We limited ourselves to the case of a displacement excitation. The profiles display the same decay law. The cases with stronger disorder attain the asymptotic profile at smaller distances since in this case the localization lengths are shorter. As seen from Figure 5.4, the data are consistent with the expectation that the asymptotic profile is reached for $|n - n_0| \gg \xi_{min}$. The values of ξ_{min} given in that figure are a rough estimate of the shortest localization length obtained by extrapolating the formula (5.11) at $\omega=\omega_{max}=2c$, i.e. $\xi_{min}=\xi(\omega_{max})$.

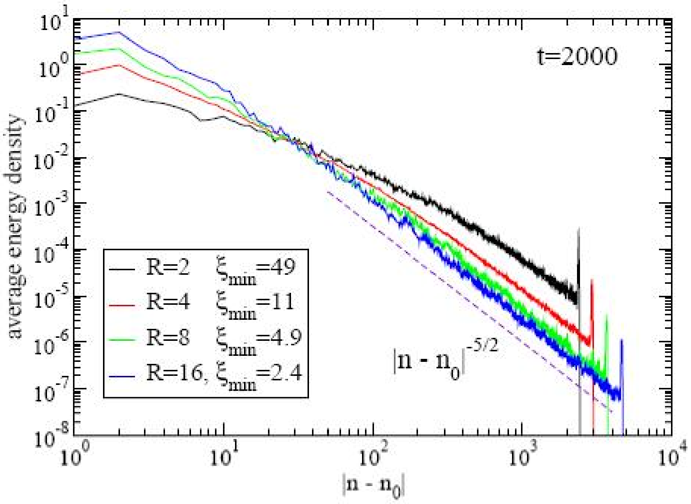

Fig. 5.4: (Color online) Disorder averaged energy profiles at $t = 2000$ for a displacement excitation with $A = 2$ and increasing disorder strengths (top to bottom). Other parameters as in Fig.5.1. The dashed line indicates the predicted power law Eq. (5.37)

The prefactor of both power laws, Eqs. (5.37) and (5.40) depends on the disorder as demonstrated by Figure 5.4. It seems reasonable that $\xi_2 \cong \lambda\xi(\omega)$ for $\omega \to 0$ with a positive parameter λ, independent on ω and the disorder. Eqs.(5.11) and (5.33), together with this hypothesis, imply:

$$c_2 = 8\lambda \frac{\langle K^{-1} \rangle}{\langle K^{-2} \rangle - \langle K^{-1} \rangle^2} \tag{5.45}$$

Again $m = 1$ and $a = 1$ has been used. For the uniform distribution $p(K)$, Eq. (5.17), (K^{-1}) and (K^{-2}) can easily be calculated. From this we obtain:

$$\begin{aligned} c_2(R) &= 8\lambda \frac{(R-1)R \ln R}{(R-1)^2 - R(\ln R)^2} \\ &\cong 72\lambda (R-1)^{-2}\left[1 + O(R-1)\right] \end{aligned} \tag{5.46}$$

Note, that $c_2(R)$ diverges in the no-disorder-limit $R \to 1^+$, as it should be since only extended states exist thereby. Accordingly, $\xi(\omega)$ should become infinite for all ω.

Introducing $c_2(R)$ from the first line of Eq. (5.46) and $(K^{-1})(R)=(\ln R)/(R-1)$ into the prefactor $C(R)$ of the power laws, Eqs. (5.37) and (5.40), leads to the R-dependence shown in Fig. 5.5 in case of a displacement and a momentum excitation, respectively. The unknown parameter λ has been adjusted in order to fit the numerical result for the prefactors. The latter are obtained from the numerical data in Figures 5.2 and 5.3 extrapolating $(e_n(t))|n-n_0|^{\eta}$ at large $|n-n_0|$.

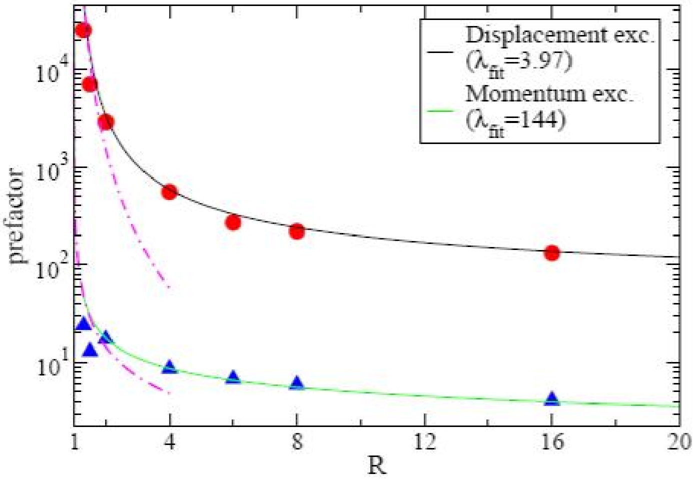

Fig. 5.5: (Color online) Dependence of the prefactors *C(R)* on the disorder strength *R* for a displacement ($A = 2$) and momentum ($B = 2$) excitation: numerical (full circles and triangles respectively) and analytical result Eqs. (5.37), (5.40) with formula (5.46) (solid lines). Dash-dotted lines are the expected asymptotic behaviors for $R \rightarrow 1^+$, $(R-1)^{-3}$ and $(R-1)^{-1}$, respectively. The fitting parameter λ_{fit} is given in the legend.

The numerical and analytical result for the prefactor in case of a displacement excitation agree satisfactorily, even for the smallest value of $R = 1.3$. Investigating the profile for even smaller values is hampered for our finite chain by the increase of the localization length with decreasing $(R - 1)$. The same agreement is also valid in case of the momentum excitation, except for the two smallest *R*-values at 1.3 and 1.5. Eq. (5.7) demonstrates that the weight of the low-lying Anderson modes for a momentum excitation is by a factor $1/\omega_\nu$ higher than for a displacement excitation. Since the localization length increases with decreasing ω_ν, this could be the reason for the "asymmetric" behavior of *C(R)* for both kind of excitations. Indeed, we have observed that $\langle e_n(t)\rangle |n-n_0|^{3/2}$ does not reach a stationary value, for e.g. $R = 1.3$. The strong deviation of the fit parameter λ for the displacement and momentum excitation may originate also from this fact.

5.3.3 Moments of the local energy

A customary way to describe wavepacket diffusion is to look at time evolution of moments of the energy distribution that are defined as

$$m_\nu(t) = \frac{\sum_n |n-n_0|^\nu e_n(t)}{\sum_n e_n} \tag{5.47}$$

(the denominator is clearly only a scale factor). Of particular interest for a statistical characterization are the disorder averaged moments $\langle m_v(t)\rangle$. Their numerical result is shown in Figure 5.6. If one uses the asymptotics Eqs. (5.37), (5.40) and introduces a cutoff of the sum in the numerator of Eq. (5.47) at the ballistic distance $|n - n_0| = ct$ one obtains

$$\langle m_v(t)\rangle \propto t^{\beta(v)}, \qquad \beta(v) = \begin{cases} v+1-\eta, & v > \eta - 1 \\ 0, & v < \eta - 1. \end{cases} \tag{5.48}$$

For $v = \eta - 1$ there is a logarithmic divergence of $\langle m_v(t)\rangle$ with time. As demonstrated in Fig. 5.7, the numerical values of $\beta(v)$ are in excellent agreement with Eq. (5.48). This also implies that the contribution of the traveling peaks is not relevant as implicitly assumed in the derivation of Eq. (5.48).

This result is consistent with the values that could be inferred by Datta and Kundu [103]. Indeed, they predict $\beta(2) = 1/2$ and $\beta(2) = 3/2$, respectively, for a displacement and momentum excitation. Notice that, if one looks only at $m_2(t)$ one would incorrectly conclude that the two cases would correspond to sub- and superdiffusive behavior respectively. A full analysis of the spectrum of moments and of the wavefront shape is necessary to assess the real nature of dynamics.

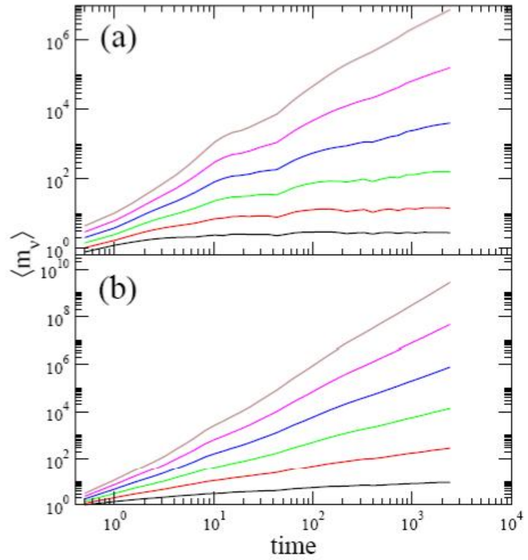

Fig. 6: (Color online) Evolution of moments $\langle m_v(t)\rangle$ for v = 0.5, 1, 1.5, 2, 2.5, 3 (bottom to top respectively) for the harmonic chain N = 8192, R = 6. Displacement (*a*) and momentum (*b*) excitation (A = 2 and B = 2 respectively). Averages are over 6×10^3 disorder realizations.

5.4 Energy profile: anharmonic case

In this section we will investigate numerically the n-dependence of the energy profile averaged over the disorder in the presence of anharmonicity. Particularly, we will check whether its tails can be described by those of the harmonic chain. As a model we have chosen the Fermi-Pasta-Ulam (FPU) chain with cubic nonlinear force

$$\begin{aligned} m\ddot{u}_n &= K_n(u_{n+1} - u_n) - K_{n-1}(u_n - u_{n-1}) \\ &+ G(u_{n+1} - u_n)^3 - G(u_{n-1} - u_n)^3 \end{aligned} \tag{5.49}$$

It reduces to the harmonic chain for $G = 0$. For simplicity, we considered the case of uniform nonlinear coupling G ($G = 1$ in the following).

The analysis of the previous section shows that the behavior of the harmonic chain follows all the expected features. Which influence of the anharmonicity do we expect? If the initially localized energy would spread completely it would be $e_n(t)$, $\to 0$ for $t \to \infty$, for all n. For incomplete spreading, however, $(e_n(t))$ for t large enough should decay byhe power laws Eqs. (5.37) or Eqs. (5.40), again, and the amplitudes of oscillations at sites far away from site n_0 of the initial excitation should become so small that the harmonic approximation applied to those tails should become valid.

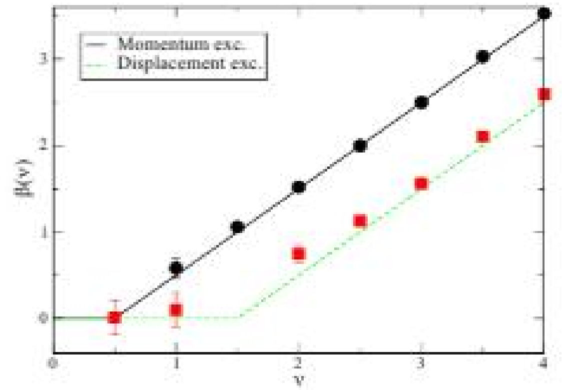

Fig. 5.7: (Color online) Comparison between the exponents measured numerically for momentum and displacement excitations (full circles and squares respectively) and the analytical result Eq. (5.48), same parameters as in Fig. 5.6. The exponents are evaluated by a power-law fit. Error bars are estimated from the fluctuations of the (discrete) logarithmic derivative $\Delta \log(m^{\nu}(t))/\Delta \log t$ and are reported only when larger than symbols' size.

A detailed analysis of the effects of nonlinearity goes beyond the scope of the present work. We thus limited ourselves to the case of FPU with initial displacement excitation with $A = 2$. We checked that the energy is about a factor of 2 larger with respect to the $G = 0$ case meaning that the nonlinear part of the potential is sizeable. We consible the usual definition of $e_n^{(pot)}$ where $K_i[u_{i+1} - u_i]$, $i = n-1, n$ Eq. (5.14) is replaced by $V_i'(u_{i+1} - u_i)$ with $V_i(x) = K_i x^2/2 + Gx^4/4$. As for the harmonic case, we performed the average over disorder at three different times.

The average energy profiles for three different disorder strengths are reported in Fig. 5.8. The profiles still show a pretty slow decay, reminiscent of the harmonic case. From Fig. 5.8 we first observe that the convergence of $(e_n(t))$ to a limiting profile at $t=\infty$ becomes slower for larger disorder strength R, i.e. for shorter localization lengths. Second, whereas the profile for $R=4$ and there larger time t=6000 can be satisfactorily fitted by the power law Eg. 5.37, this is less obvious for R=2 and R=8. For R=2 and $|n - n_0| > 1000$ the profile is practically time independent for $t \geq 2000$. But in contrast to the harmonic case (see Fig. 5.2) it does not reveal the asymptotic power law $|n - n_0|^{-5/2}$, although the data suggest that this may happen for $|n - n_0| \geq 3000$. For R=8 the profile follows that power law for $100 < |n - n_0| < 1000$, i.e. for about a decade, but deviates for $|n - n_0| > 1000$. However, comparing this profile for the three different values for t hints that the range of the power law decay may increase with increasing t. In addition, the profiles display some form of weak "broadening" of the tails indicating that some energy is indeed slowly propagating.

As a consequence, the disorder averaged moments $(m_v(t))$ do not display a convincing scaling with time. Even for statistically accurate data as the one in Fig. 5.8, the effective exponents (as measured for example by the logarithmic derivatives of $(m_v(t))$ display sizeable oscillations which are well outside the range of the statistical of the statistical fluctuations (see Fig 5.9). Similar results are obtained for momenta of different order (not reported).

We may thus argue that, at least in the considered parameter range, the nonlinear case has a core which remain almost localized (in a similar way as the harmonic case) but in addition there must be a small propagating component. The fraction of such propagating component increases upon increasing the energy and/or nonlinearity. As a consequence, with the data at hand it is impossible to draw definite conclusions on the nature of the spreading process.

5.5 Summary and conclusions

The relaxation of an initially localized excitation in a translationally invariant chain of particles has been studied for harmonic and anharmonic nearest neighbor couplings. The main focus has been on the energy profile $(e_n(t))$, the moments $(m_v(t))$, both averaged over the disorder, and the relation between the asymptotic t-dependence of $(m_\nu(t))$ with the asymptotic n-dependence of $\langle\overline{e_n(t)}\rangle$. As far as we know, this has neither been explored for the anharmonic nor for the harmonic case due to the lack of analytical knowledge of $\langle\overline{e_n(t)}\rangle$ for $|n - n_0| \to \infty$.

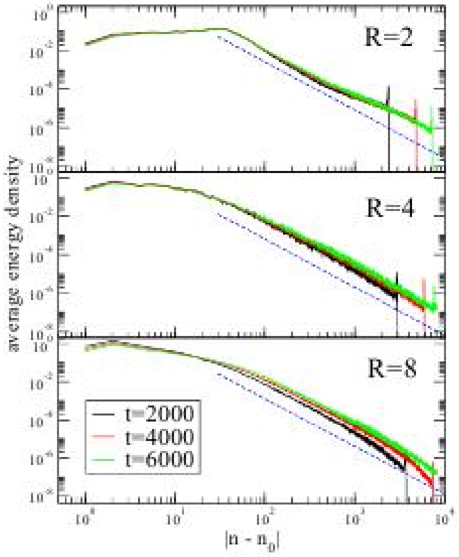

Fig. 5.8: (Color online) FPU model: Disordered-average energy profile at three different times averaged over 10^3 realizations of the disorder and for different disorder strengths R. Chain of $N = 8192$ particles with displacement excitation $A = 2$. For comparison, the predicted power law decay for the harmonic chain, Eq. (5.37), is also drawn (dashed lines).

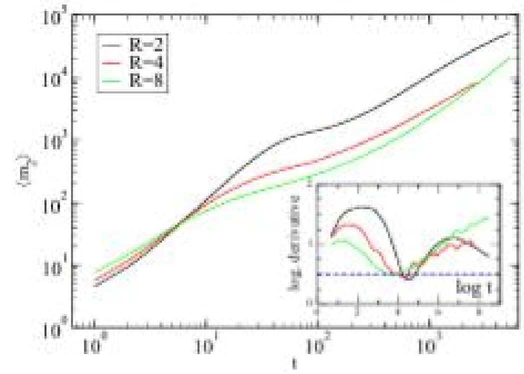

Fig. 5.9: (Color online) FPU model: Evolution of $(m_2(t))$ for $R = 2, 4, 8$ (top to bottom respectively) same parameters as in Fig. 5.8. The inset reports the (discrete) logarithmic derivative $\Delta\ log(m_2(t))\ /\Delta\ log$ t of the data versus $log\ t$. For comparison, the value for the harmonic chain $\beta(2) = 1/2$ is also drawn (dashed horizontal line).

For the harmonic model we succeeded to determine analytically the disorder and time averaged energy profile $\langle \overline{e_n(t)} \rangle$ displacement and a momentum excitation at site n0 and initial time t = 0. Whereas $e_n(t)$ is a quasiperiodic function which does not converg for $t \rightarrow \propto$ we have argued that $\langle \overline{e_n(t)} \rangle$ converges for $t \rightarrow \propto$. In that case $\langle \overline{e_n(t)} \rangle$ given the limiting profile averaged over the discorder. The analytical calculation yields a power law decay

$$(\overline{e_n(t)}) \cong C(R)|n - n_0|^{-\eta} \tag{5.50}$$

for $1 << |n - n_0| << N$, in case the system is finite. The exponent η and the prefactor $C(R)$ depend on the type of excitation. For a displacement and momentum excitation we have found $\eta = 5/2$ and $\eta = 3/2$, respectively, in good agreement with the numerical values. This agreement also holds for the analytical and numerical results for the R-dependence of $C(R)$, except for the two smallest values of R in case of a momentum excitation. Accordingly our assumption $\xi_2(\omega) \sim \xi(\omega)$ for $\omega \rightarrow 0$ is supported. From this proportionality it also follows that $C(R)$ diverges at $R = 1$, the no-disorder limit. The power law decay, Eq. (5.50), originates from the gapless excitation spectrum of the Anderson modes. . It is the consequence of the translational invariance of model (4). Destruction of this invariance by adding, e.g. an on-site potential like in the KG model generates an energy gap. The corresponding localization length at the lowest eigenfrequency will not diverge anymore, and therefore the energy profile will decay exponentially for $|n - n_0| \rightarrow \propto$. However, we stress that *any* lattice model without an external potential has to be invariant under arbitrary translations. This implies a gapless spectrum which is the origin of the power law decay of the profile.

The power law decay of $\langle \overline{e_n(t)} \rangle$ has remarkable consequences on the asymptotic t-dependence of the moments. If we use Eq. (5.50) to calculate the time and disorder averaged v-th moment we get for displacement and momentum excitation:

$$\langle \overline{m_v(t)} \rangle = \infty \tag{5.51}$$

for *all* $v \geq 2$; note that, for instance, $\langle \overline{m_1(t)} \rangle$ is finite for a displacement, but not for a momentum excitation. The result, Eq. (5.51), implies that the disorder averaged moment $(m_v(t))$ must diverge with time, although the initial local energy excitation does not spread completely. This power law divergence of $(m_v(t))$ with time is clearly supported by the numerical result for $v \geq 2$ and $v \geq 1$ for the displacement and momentum excitation, respectively. As a matter of fact, consideration of $m_2(t)$ alone is not sufficient to conclude that the energy diffuses. This is one of the main messages of the paper.

The analytically exact result for $\langle\overline{e_n(t)}\rangle$ in case of harmonic interactions also allows to check how far the tails of an anharmonic chain, where the average displacements become arbitrary small, can be described by the tails of the harmonic system Although no definite conclusion can be drawn, we have found evidence for a crossover of the energy profile of the anharmonic to that of the harmonic chain. However, for the weakest and strongest strength of disorder this crossover seems to occur for $|n - n_0| > 3000$ and for $t > 6000$, respectively. This may be explained as follows. The localization length $\xi_2(\omega)$ is large for weak disorder. Since $|n-n_0|/\xi_2(\omega)$ enters into the calculation of the disorder averaged profile (see Eq. (5.35)) the asymptotic power laws, Eqs. (5.37) and (5.40), occur at larger values of $|n - n_0|$. For large disorder, $\xi_2(\omega)$ is small. But the time scale for tunneling processes responsible for the energy propagation increases significantly due to an increase of the potential barriers. Therefore the convergence to a limiting profile is much slower which is exactly what we observed (see Fig. 5.7). The increase of the localization length for weak disorder and the increase of the relevant time scale of relaxation for strong disorder probably are also the reasons for the absence of a convincing scaling of the moments $(m_v\ (t))$. In order to test this, one has to increase both, the number of particles and the simulation time significantly. Requiring a similar good statistic of the data this has not been possible so far within the available CPU time. If it is true that the asymptotic energy profile agrees with that of the harmonic chain this would imply that the moments $(m_v\ (t))$ for the anharmonic model for $v \geq 2$ diverge with time, as well, although the energy does not spread completely.

From our results, it is nonetheless clear that the interplay of localized and almost-extended modes leads to a nontrivial decay of wavepackets amplitudes and this must be taken into account when dealing with the nonlinear case.

\

6 TRANSMISSION AND ANDERSON LOCALIZATION IN DISPERSIVE METAMATERIALS

Comprehensive theoretical and numerical studies of the effects of dispersion and absorption on the Anderson localization of classical waves in weakly disordered, one-dimensional stacks composed of dispersive metamaterials and normal materials are presented. An asymptotic analysis for studying the effects of dispersion and absorption is developed. It is shown that the localization of waves in random stacks composed entirely of either metamaterial or normal dielectric layers is completely suppressed at frequencies where the magnetic permeability or the dielectric permittivity is zero. In mixed stacks of alternating layers of normal and metamaterials with disorder present in either the dielectric permittivity or the magnetic permeability, localization is substantially suppressed not only at these frequencies but in essentially wider frequency ranges. When both the permittivity and the permeability are random, the localization behavior is similar to that in monotype stacks. At the transition from a double negative metamaterial to a single negative metamaterial, the transmission length drops dramatically in a manner that might be useful in optical switching. Polarization effects are also considered and it is shown that localization is suppressed at the Brewster angle, in a manner dependent on both the polarization and the nature of the disorder. Theoretical predictions are in excellent agreement with numerical calculations.

6.1 Introduction

Anderson localization is one of the most fundamental concepts in physics. Localization of light in random media has been investigated intensively during the last few decades, with one-dimensional (1D) strong localization receiving the most comprehensive study. Recently, the emergence of metamaterials - a new class of artificial materials with negative refractive index - has sparked considerable interest from researchers and engineers; see, for example, Refs.121-125. Metamaterials are also referred to as double-negative materials (DNMs), associated with permittivity and permeability whose real parts are both negative, in contrast with single-negative materials (SNMs), in which either the real part of the dielectric permeability or the real part of the magnetic permittivity is negative.

Since, today, all available metamaterials are manmade, they usually contain technological imperfections or faults. The first consideration of manufacturing defects in magnetic metamaterials showed that imperfections could have a strong impact on propagation. Further studies showed that Anderson localization in metamaterials is suppressed, either partially or completely, compared to localization in conventional materials. A rich vein of new phenomena related to such suppression has been revealed recently. In one-dimensional stacks comprising alternating layers of normal and metamaterials, with only thickness disorder, delocalization can occur at a single frequency at which the of layers match. Disorder in the dielectric permittivity of the layers (in the absence of thickness disorder) also gives rise to a startling suppression of localization at long wavelengths. This suppression is so strong that there is a change in the functional dependence $\mathrm{l}{\sim}\lambda^{K}$ of the localization length at long wavelengths. From the well-known, classical value of $\kappa = 2$, this exponent increases to a much larger value, estimated in Ref. 128 as $k \approx 6$, i.e., the λ^6 anomaly. In mixed stacks with weak, long correlated disorder of the layer thicknesses, the frequency regions corresponding to complete delocalization (pass bands) are essentially wider than those for conventional right-handed stacks. Complete delocalization occurs at special frequencies and special angles of incidence corresponding to the Brewster anomaly.

While further studies confirmed the λ^6 anomaly, more detailed numerical calculations for very long stacks showed that the exponent κ may increase to larger values, up to $k \approx 8.78$, for a stack of approximately 10^{12} layers. As is reported in Ref. 130, off-axis incidence, by a a small angle, can affect this functional dependence. However, the introduction of correlation in the disorder has little effect. The consideration of layers with different thicknesses, or the introduction of the layer thickness disorder, in addition to the material parameters disorder, strongly enhances localization. In Ref. 135 it is shown that because of specific, nonuniform phase distribution, in the second order of disorder, localization is completely destroyed for long waves, and that fourth-order calculations are required. Eventually, in a recent paper, the long-wave dependence of $l \sim \lambda^8$ was analytically established, showing that the anomaly which was discovered numerically in Refs. 128 and 133 was actually a λ^8 anomaly.

Localization in SNMs has also been considered, with it being shown that the localization length can be smaller than the decay length of the corresponding periodic structure. The suppression of localization has been reported also in one-dimensional metamaterial superlattices with thickness disorder.

All metamaterials inherently exhibit dispersion and absorption, and this has to be taken into account in any realistic study of localization. While the dispersive effects on localization in normal materials have been considered in Ref. 138, the corresponding study for metamaterials has only started. The first of these papers is devoted to light propagation through one-dimensional photonic disordered quasiperiodic superlattices, composed of alternating layers with random thicknesses of air and a dispersive metamaterial. In the second one, the effects of disorder correlations on light propagation and Anderson localization in one-dimensional dispersive metamaterials are studied.

Of particular interest are dispersive materials, in which real parts of the dielectric permittivity or magnetic permeability may vanish at some frequencies. Structures containing metamaterials with $\varepsilon \approx 0$ have been studied most intensively. It has been shown in particular that energy may propagate through ultranarrow waveguide channels in such structures. It is thus interesting and important to investigate localization in samples with ε-near-zero (ENZ), i.e., with $\varepsilon \approx 0$, and in μ-near-zero (MNZ) materials, with $\mu \approx 0$.

In this paper, we examine transport and localization in one-dimensional disordered systems with different types of dispersive metamaterials, and predict a new instance of delocalization. We prove theoretically, and through numerical simulations, that, in systems with $\varepsilon = 0$ or $\mu = 0$, the field is delocalized in the presence of either dielectric permittivity disorder, magnetic permeability disorder, or thickness disorder. This is in contrast to delocalization at the Brewster angle that occurs in the presence of solely thickness disorder.

In Sec. 6.2, we describe the theoretical model and present the asymptotic analysis based on the extension of the approach developed in Ref. 133. The analysis of delocalization in ENZ or MNZ disordered stacks and the study of polarization effects are presented in Secs. 6.2.3.1 and 6.2.3.2, respectively. Numerical simulations and comparisons with the asymptotic predictions are presented in Sec. 6.3, comprising the characterization of localization in monotype stacks (Secs. 6.3.1 and 6.3.2) and in mixed alternating stacks (Sec. 6.3.3).

6.2 Theoretical consideration

6.2.1 Description of the model

We consider a one-dimensional stack which consists of an even number N of layers. The stack may be either monotype, in which case each layer is either a metamaterial (A) layer or a normal material (B) layer, or mixed, comprising alternating A and B layers, as shown in Fig. 6.1. All layers have the same thickness $d = 0.003$ m, which is consistent with manufactured metamaterials.

The dielectric permittivity and the magnetic permeability of the metamaterial layers as functions of a circular frequency f are described by the Lorentz oscillator model

$$\varepsilon(f) = 1 - \frac{f^2 ep - f^2 e}{f^2 - f^2 e + i\gamma f}, \tag{6.1}$$

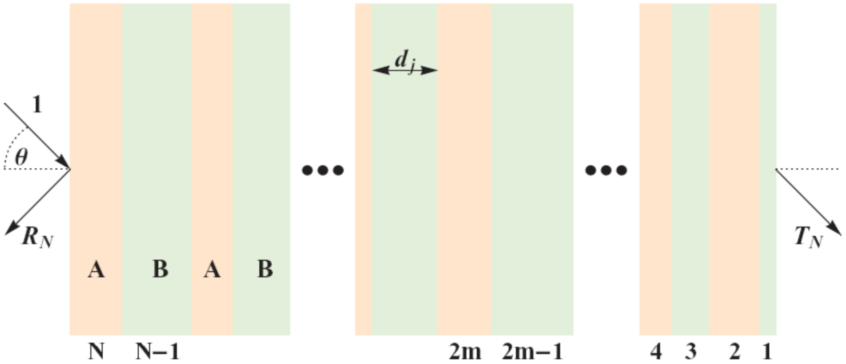

Fig. 6.1. (Color online) The geometry of the model. θ denotes the angle of incidence from free space.

$$\mu(f)=1-\frac{f^2mp-f^2m}{f^2-f^2em+i\gamma f}, \tag{6.2}$$

here f_m and f_e are the resonance frequencies and γ is the absorption parameter. In our model, disorder enters the problem through random resonance frequencies so that

$$f_e(1+\delta_e),\qquad f_m=\overline{f}m(1+\delta_m). \tag{6.3}$$

where $f_{e,m}$ = $(f_{e,m})$ are the mean resonance frequencies (with the angle brackets denoting ensemble averaging) and $\delta_{e,m}$ are independent random values distributed uniformly in the ranges [- $Q_{e,m}$,$Q_{e,m}$]. The characteristic frequencies f_{mp} and f_{ep} are nonrandom. Therefore, in lossless media (γ= 0), both the magnetic permeability and the dielectric permittivity vanish with their mean values, $\overline{\varepsilon}(f)=<(f)>$ and $\overline{\mu}(f)=<\mu(f)>$, at frequencies $f = f_{ep}$ and $f = f_{mp}$, respectively; i.e.,

$$\mu(f_{mp})=\overline{\mu}(f_{mp})=0,\quad \varepsilon(f_{ep})=\overline{\varepsilon}(f_{ep})=0\,. \tag{6.4}$$

Following Refs._144 and_145, in our numerical calculations we choose the values of characteristic frequencies f_{mp} = 10.95GHz, f_{m0} = = 10.05 GHz, f_{ep} = 12.8 GHz, $f_{e0} = f_e$ = 10.3 GHz, and γ = 10 MHz, which fit the experimental data given in Ref._144. That is, we are using a model based on experimentally measured values for the metamaterial parameters. Then we choose the maximal widths of the distributions of the random parameters $\delta_{e,m}$ as $Q_{e,m}$ < 5 x 10^{-3}, corresponding to weak disorder.

We focus our study on the frequency region 10.40 GHz < f < 11.00 GHz. In the absence of absorption and disorder, for these frequencies the dielectric permittivity and the magnetic permeability of the metamaterial layers vary over the intervals -26.9 < ε < -2.9 and -1.64 < μ < 0.055. The refractive index is negative in the frequency range 10.40 GHz < $f < f_{mp}$ = 10.95 GHz, as shown in the inset of Fig. 6.2. However, at f_{mp} = 10.95 GHz, the magnetic permeability changes sign and the metamaterial changes from being double negative (DNM) to single negative (SNM). As we show later, such changes have a profound effect on the localization properties.

In generic normal dielectric layers with a similar dispersion, the values of the dielectric permittivity and the magnetic permeability are set to be - $\varepsilon^*(f)$ and -$\mu^*(f)$, respectively, where $\varepsilon(f)$ and $\mu(f)$, are given by Eqs. (6.1) and (6.2) and the asterisk (*) denotes complex conjugation. In the region 10.40 GHz < f < 10.95 GHz, the refractive index is positive and at higher frequencies 10.95 GHz < f < 11.00 Ghz the magnetic permittivity becomes negative and so the material becomes a SNM.

In Sec. 6.3.B 2, we consider a specific model for which the dielectric permittivity coincides with that of normal material, -$\varepsilon^*(f)$, in the range of frequencies 10.40 GHz < f < 11.00 GHz, while the magnetic permeability coincides with -$\mu^*(f)$ only in the region 10.40 GHz < f < 10.95 GHz, and at higher frequencies, 10.95 GHz < f < 11.00 GHz, is equal to $\mu(f)$. As a consequence of this exotic choice, the refractive index is positive in the entirety of the studied frequency region, aside from f = 10.95 GHz at which it vanishes.

6.2.2 Analytical treatment

In what follows, we study the transmission of a plane wave incident on a random stack from free space, as shown in Fig. 6.1. The plane wave may be either s or *p* polarized where we adopt the conventional definition for polarization, in which s and *p* polarizations refer respectively to the cases where the electric and magnetic fields are perpendicular to the plane of incidence. Due to Anderson localization, the transmission coefficient T_N of a plane wave propagating through a sufficiently long stack exponentially decays with its length *Nd.* This decay is described by the transmission length l_T, measured in units of the mean thickness *d* of each layer (for details see Ref. 133), and which we define as

$$l_T(N) = -\frac{N}{\langle \ln|T_N| \rangle}. \tag{6.5}$$

In the limit $N \to \infty$, the transmission length l_T coincides with the localization length l:

$$l = \lim_{N\to\infty} l_T.$$

Accordingly, in numerical simulations for calculating the localization length, it is necessary to generate random realizations that are sufficiently long for the condition $N \gg l_T$ to hold.

In Refs. 128, 136 and 146 an effective method for studying the transport and localization in random stacks composed of the weakly reflecting layers has been developed. In the dispersive case considered in the present paper, the reflection from a layer located in free space is not necessarily weak, in which instance the method is inapplicable.

However, as localization properties of a random stack are intrinsic properties of the stack, they cannot, and must not, depend on the material properties of the exterior medium, i.e., free space in this case. Accordingly, the localization length can be calculated from

$$l = -\lim_{N\to\infty}\frac{2N}{\ln T_n^2} = -\lim_{N\to\infty}\frac{2N}{\ln T_N^2}, \tag{6.6}$$

where $\check{T}_N$ is the transmission coefficient of a stack embedded in an exterior medium with permittivity and permeability given by the mean values of and , respectively. The connection to the outside medium through the “leads” (a circuit theory term borrowed to describe thin coupling layers) can only change the coupling conditions to the random stack through the angle of incidence. The proof of this statement is given in the Appendix to this paper.

Therefore, instead of vacuum, we consider that the layers are embedded in an effective medium with the dielectric permittivity $\bar{\varepsilon}(f) = \langle \varepsilon(f) \rangle$ and magnetic permeability $\bar{\mu}(f) = \langle \mu(f) \rangle$. In such circumstances, the reflection coefficient is always small and we may apply the method derived in Refs._128, 133 and 146. It is important to note that while in the localized regime the input and output media are of no significance, they do play a crucial role when localization breaks down (see the following Sec.6.2.C).

Following Refs.128 and_133 we employ the exact recurrence relations for the total transmission *(T_n)* and reflection *(R_n)* coefficients

$$T_n = \frac{T_{n-1} t_n}{1 - R_{n-1} r_n}, \tag{6.7}$$

$$R_n = r_n + \frac{R_{n-1} t_n^2}{1 - R_{n-1} r_n}, \quad n \geq 2, \tag{6.8}$$

with the initial conditions $T_0 = 1$ and $R_0 = 0$. Here r_n and t_n are the reflection and the transmission coefficients of the single *n*th layer embedded in the effective medium with mean dielectric permittivity $\bar{\varepsilon}(f) = \langle \varepsilon(f) \rangle$ and magnetic permeability $\bar{\mu}(f) = \langle \mu(f) \rangle$. That is,

$$r_n = \frac{p_n\left(1-e^{2i\beta n}\right)}{1-p_n^2 e^{2i\beta n}}, \tag{6.9}$$

$$t_n = \frac{\left(1-p_n^2\right)e^{i\beta n}}{1-p_n^2 e^{2i\beta n}}. \tag{6.10}$$

In Eqs.(6.9) and (6.10), $\beta_n = kdv_n cos\theta_n$, $v_n = \sqrt{\varepsilon_n \mu_n}$ is the free-space wave number $k = 2\pi/\lambda_0$, and the interface Fresnel reflection coefficient ρ_n is given by

$$p_n = \frac{z_b \cos\theta_b - z_n \cos\theta_n}{z_b \cos\theta_b + z_n \cos\theta_n}, \tag{6.11}$$

The impedances Z_b and Z_n are

$$Z_b = \begin{cases} \sqrt{\overline{\mu}/\overline{\varepsilon}} & \rho \text{ polarization,} \\ \sqrt{\overline{\varepsilon}/\overline{\mu}} & s \text{ polarization,} \end{cases} \tag{6.12}$$

$$Z_n = \begin{cases} \sqrt{\mu_n/\varepsilon_m} & \rho \text{ polarization,} \\ \sqrt{\varepsilon_m/\mu_m} & s \text{ polarization,} \end{cases} \tag{6.13}$$

The angles θ_b and θ_n satisfy Snell`s law

$$v_n \sin\theta_n = \overline{v}\sin\theta_b = \sin\theta a, \qquad \overline{v} = \sqrt{\overline{\varepsilon}\overline{\mu}}, \tag{6.14}$$

$$\sin\theta_b = \frac{\sin\theta_a}{\sqrt{\overline{\varepsilon}(f)}\sqrt{\overline{\mu}(f)}}, \tag{6.15}$$

where θ_a is the external angle of incidence from free space. These expressions are equally applicable for both normal and metamaterial slabs with the corresponding choice of the square root branch. Note, however, that for a fixed angle of incidence θ_a [from free space (air)], it follows that the angle θ_b is will vary with frequency, due to dispersion (6.15).

In the limit of weak disorder ($|r_n| \ll 1$), Eqs. (6.7) and (6.8) can be linearized and written as

$$\ln T_n = \ln T_{n-1} + \ln t_n + R_{n-1} r_n, \tag{6.16}$$

$$R_n = r_n + R_{n-1} t_n^2, \quad n \geq 2. \tag{6.17}$$

For this case, the localization length has been calculated in Ref. 133 for monotype-stack (composed of either double-negative metamaterial layers or normal material layers) samples

$$\frac{1}{t} = -\operatorname{Re}\langle \ln t_n \rangle - \operatorname{Re}\frac{\langle r_n \rangle^2}{1-\langle t_n^2 \rangle}, \tag{6.18}$$

And for mixed stacks of alternating normal and metamaterial layers,

$$\frac{1}{l} = -\operatorname{Re}\langle \ln t_n \rangle - \frac{\left|\langle r_n \rangle^2\right| + \operatorname{Re}\left(\langle r_n \rangle^2 \langle t_n^2 \rangle^*\right)}{1-\left|\langle t_n^2 \rangle\right|^2}. \tag{6.19}$$

6.2.3 Suppression of localization in disordered stacks

Dispersion affects dramatically the transport properties of the disordered medium. In particular, the localization can be suppressed either at some angle of incidence or at a selected frequency, or even in a finite frequency range. The first two cases are studied below (Secs. 6.2.3.1 and 6.2.3.2 , while the third one is considered in Sec. 6.3.3.

1. *Power decay of the transmission coefficient at normal incidence in the vicinity of μ- or ε- near-zero points*

The localization length in *a lossless, nondispersive, monotype meta- or normal-material random stack* increases in the long-wave region as ~λ^2; see Ref. 133. In the presence of dispersion, the first term in Eq. (6.18) is dominant, and the long-wave asymptotic of the localization length manifests the same behavior according to

$$\frac{1}{l} = \frac{\pi^2 d^2}{2\lambda^2(f)}\left(\frac{\langle \mu^2 \rangle}{\langle \mu \rangle^2} + \frac{\langle \varepsilon^2 \rangle}{\langle \varepsilon \rangle^2} - 2\right), \tag{6.20}$$

in which we have omitted the subscript *n*.

The distinctive property of dispersive media is that the wavelength $\lambda(f)$ in the medium given by

$$\lambda(f) = \frac{\lambda_0(f)}{\sqrt{\varepsilon(f)\mu(f)}}, \tag{6.21}$$

is frequency dependent, and can be large even when the wavelength of the incident signal, $\lambda_0(f) = 2\pi/k = c/f$, is small.

Accordingly, the inverse localization length

$$l^{-1}af^{2}\varepsilon(f)\mu(f) \tag{6.22}$$

becomes small not only at low frequencies $f \longrightarrow 0$ but also in the vicinity of μ- or ε-zero points. For example, as the frequency approaches the μ-zero point from below, i.e., $f \longrightarrow f_{mp}$, in *a monotype stack of random metamaterial layers, $\mu(f)$,* for any realization, is proportional to the difference $(f_{mp}-f)$ and the expression for localization length diverges as $(f_{mp}-f)^{-1}$. Formally, this divergence can be treated as delocalization; however, the limiting value $1/l = 0$ means nothing but the absence of exponential. Moreover, when the localization length becomes larger than the size of the stack, ballistic transport occurs and the transmission coefficient is determined by transmission length, (6.5), rather than by the localization length.

To calculate the transmission coefficient for this case we consider, for the sake of simplicity, *a stack with only ε disorder*. Here the transfer matrix of the nth layer at $f = f_{mp}$ has the form

$$\mathrm{T}_n \equiv \mathrm{T}(\in_n) = \begin{pmatrix} 1+\in_n & \in_n \\ -\in_n & 1-\in_n \end{pmatrix}, \quad \in_n = \frac{ikd\varepsilon_n}{2}$$

As a consequence of the easily verified property

$$T(\in 1)T(\in 2) = T(\in 1 + \in 2), \tag{6.23}$$

it follows that the stack transfer metrix T is

$$\mathrm{T} = \Pi_n^N \mathrm{T}(\varepsilon_n) = \begin{bmatrix} 1+\varepsilon & \varepsilon \\ -\varepsilon & 1-\varepsilon \end{bmatrix},$$

where

$$\varepsilon = \frac{ikl}{2}\frac{1}{N}\sum\nolimits_{n=1}^{N}\varepsilon_n, \qquad \mathrm{L} = \mathrm{Nd}. \tag{6.24}$$

In a sufficiently long stack, $\varepsilon \approx \frac{1}{2} ikL\,\overline{\in}$ and the transmittance $T = |T_{11}|^{-2}$ is given by

$$T = \frac{1}{1+\left(\frac{kL\varepsilon(f)}{2}\right)^{2}}. \tag{6.25}$$

Thus, at the frequence f_{mp}, the transmittance of the sample is not an exponentially decreasing function of the length L (as is typical for 1D Anderson localization). It decreases much more slowly, namely, according to the power law $T \alpha L^{-2}$.

There are two physical explanations for the delocalization described above. First, at a μ-zero point $(f = f_{mp})$, the refractive index υ_n vanishes together with the phase terms $\beta_n = kd\upsilon_n cos\theta_n$ across the layer, thereby weakening the interference, which is the main cause of localization. Second, the effective wavelength inside the stack tends to infinity when $\mu \rightarrow 0$ and exceeds the stack length. Obviously, such a wave is insensitive to disorder and therefore cannot be localized.

In the limit as the frequency approaches the μ-zero frequency, from above, i.e., $f \rightarrow f^{+}_{mp}$, the medium is single negative and $\varepsilon\mu < 0$. For frequencies f not too close to f_{mp}, the radiation decays exponentially inside the sample due to tunneling, and in the absence of dissipation the decay rate is

$$l = \frac{1}{kd\sqrt{-\langle\mu\rangle\langle\eta\rangle}}. \tag{6.26}$$

Thus, as we approach the μ-zero frequency from the right, the formally calculated localization length diverges as $l \alpha (f - f_{\mathrm{mp}})^{-1/2}$, i.e., much more slowly than for the left-hand limit fr which $l \alpha (f_{\mathrm{mp}} - f)^{-1}$. The transport properties in the vicinity of the ε-zero frequency f_{ep} can be considered in a similar manner. Waves are also delocalized in the more exotic case when both dielectric permittivity and magnetic permeability vanish simultaneously. The vanishing of both μ and ε simultaneously can happen at Dirac points in photonic crystals.

The use of off-axis incidence from free space for frequencies for which μ or ε are zero is not an appropriate mechanism for probing the suppression of localization. In such circumstances, tunneling occurs and the localization properties of the stack are not “accessible” from free space. Nevertheless, suppression of localization can be revealed using an internal probe, e.g., by placing a plane-wave source inside the stack, or by studying the corresponding Lyapunov exponent. Both approaches show total suppression of localization at the frequencies at which dielectric permittivity or magnetic permeability vanish.

In such circumstances, each layer which is embedded in a homogeneous medium with material constants given by the average values of the dielectric permittivity and magnetic permeability is completely transparent, with this manifesting the complete suppression of localization. However the “delocalized” states at the zero-μ or zero-ε frequencies are in a sense trivial, corresponding to fields which do not change along the direction normal to the layers.

2. *Brewster anomaly*

We now consider another example of the suppression of localization, this time related to the Brewster anomaly. It has been shown in Ref. 146 that in a *one-dimensional nondispersive mixed stack with only thickness disorder,* delocalization of p-polarized radiation occurs at the Brewster angle of incidence. At this angle, the Fresnel coefficient ρ [Eq. (6.11)] and, therefore, the reflection coefficient [Eq. (6.9)] as well, vanish for any frequency, thus making each layer completely transparent.

In the presence of dispersion, the same condition $\rho = 0$ leads to more intriguing results. In this instance, frequency- dependent angles, at which a layer with the dielectric permittivity $\varepsilon(f)$ and magnetic permeability $\mu(f)$ embedded in the effective medium with mean dielectric permittivity $\overline{\varepsilon}(f)$ and magnetic permeability $\overline{\mu}(f)$ becomes transparent, exist not only for p polarization but also for an s-polarized wave. This means that the Brewster anomaly occurs for both polarizations, with the corresponding angles, θ_p and θ_s, being determined by the conditions

$$\tan^2\theta_p = \frac{\varepsilon(\varepsilon\overline{\mu} - \overline{\varepsilon}\mu)}{\overline{\varepsilon}(\varepsilon\mu - \overline{\varepsilon}\overline{\mu})}, \tag{6.27}$$

$$\tan^2\theta_s = \frac{\varepsilon(\varepsilon\overline{\mu} - \overline{\varepsilon}\mu)}{\overline{\varepsilon}(\varepsilon\mu - \overline{\varepsilon}\overline{\mu})}, \tag{6.28}$$

It can be shown that the right-hand sides of these equations (the Brewster conditions) always have opposite signs. From Eqs.(6.27) and (6.28) one can find either the Brewster angle for a given frequency or the Brewster frequency for a given angle of incidence.

While for a stack with only thickness disorder, the condition $\rho = 0$ can be satisfied for all layers simultaneously, when ε and/or μ fluctuate, the conditions (27) or (28) define the frequency-dependent Brewster angles which are slightly different for different layers. These angles occupy an interval within which *both homogeneous or mixed stacks* are not completely transparent, but have anomalously large transmission lengths.

When only the dielectric permittivity is disordered and $\mu = \overline{\mu}$, the Brewster conditions (27), (28) simplify to

$$\tan^2\theta_p = -1, \tag{6.29}$$

$$\tan^2\theta_s = \frac{\varepsilon}{\varepsilon} \approx 1, \tag{6.30}$$

Hence, in the presence of only permittivity disorder, the Brewster condition is satisfied only for *p* polarization. Since the disorder is weak, i.e., $\varepsilon \approx \bar{\varepsilon}$, the Brewster angle of incidence from the effective medium is $\theta_p \approx \pi/4$.. The corresponding angle from free space, θ_a is related to the Brewster angle θ_p hrough Snell's law, and for the given θ_a, the Brewster frequency f_p follows from

$$\sqrt{\bar{\varepsilon}(f_p)\bar{\mu}(f_p)} = \frac{\sin\theta_a}{\sin\theta_p} = \sqrt{2}\sin\theta_a \tag{6.31}$$

Note that this equation may be satisfied at multiple frequencies depending on the form of the dispersion.

In the case of only magnetic permeability disorder, $\varepsilon = \bar{\varepsilon}$, the Brewster conditions (6.27), (6.28) reduce to [compare with Eqs. (6.29) and (6.30)]

$$\tan^2\theta_s = \frac{\mu}{\mu} \approx 1, \tag{6.32}$$

$$\tan^2\theta_s = \frac{\mu}{\mu} \approx 1, \tag{6.33}$$

and the Brewster anomaly is observed for *s* polarization at the Brewster frequency f_s given by

$$\sqrt{\varepsilon(f_s)\mu(f_s)} = \frac{\sin\theta_a}{\sin\theta_s} = \sqrt{2}\sin\theta \tag{6.34}$$

For disorder in both the permeability and the permittivity, the existence of a Brewster anomaly angle depends, in accordance with Eqs. (6.27) and (6.28), on the sign of the quantity $\xi = (\bar{\varepsilon}\mu - \varepsilon\bar{\mu})/(\varepsilon\mu - \bar{\varepsilon}\bar{\mu})$. If $\xi > 0$, the Brewster angle exists for *s* polarization, while if $\xi < 0$, it exists for *p* polarization. In the case $\xi = 0$, the layer and the medium in which it is embedded are impedance matched, and thus the layer is completely transparent.

6.3 Nunerical results

6.3.1 Metamaterial stack

Along with the analytical calculations a comprehensive numerical study of the properties of the transmission length as a function of wavelength and angle of incidence has been carried out. We first consider the case of normal incidence on a stack of $N = 10^7$ layers, in which we randomize only the dielectric permittivity ($Q_m = 0$) with $Q_e = 0.5 \times 10^{-2}$. Figure 6.2 displays the transmission length l_T as a function of frequency *f*. The upper curves present the case in which absorption is neglected, while the lower curves show the effects of absorption.

The red solid curves and the blue dashed curves display results from numerical simulations and the theoretical prediction (6.18), respectively. The top curves represent the genuine localization length for all frequencies except those in the vicinity of f & f_{mp} = 10.95 GHz where the transmission length dramatically increases.

In the absence of absorption, for frequencies f *>10.95* GHz, the metamaterial transforms from being double negative to single negative (see inset in Fig. 6.2). The refractive index of the metamaterial layer changes from being real to being purely imaginary, the random stack becomes opaque, and the transmission length substantially decreases. Such a drastic change in the transmission length (by a factor of 10^5) might be able to be exploited in a frequency-controlled optical switch.

The theoretical result (6.18) is in excellent agreement with simulation based on the exact recurrence relations (6.7) and (6.8) across the frequency interval 10.4 GHz $< f <$ 11.0 GHz.

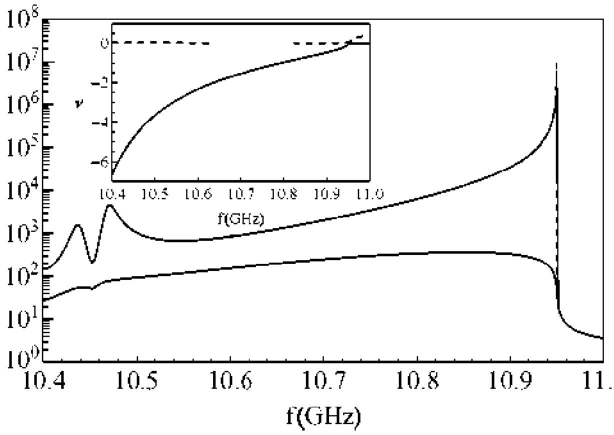

Fig. 6.2. (Color online) Transmission length l_T vs frequency f at normal incidence ($_a$ = 0) for a metamaterial stack without absorption (top curve) and in the presence of the absorption (bottom curves). Red solid curves display numerical simulations while blue dashed curves show the analytical predictions. Inset: The real (red solid line) and imaginary (green dashed line) part of the metamaterial layer refractive index.

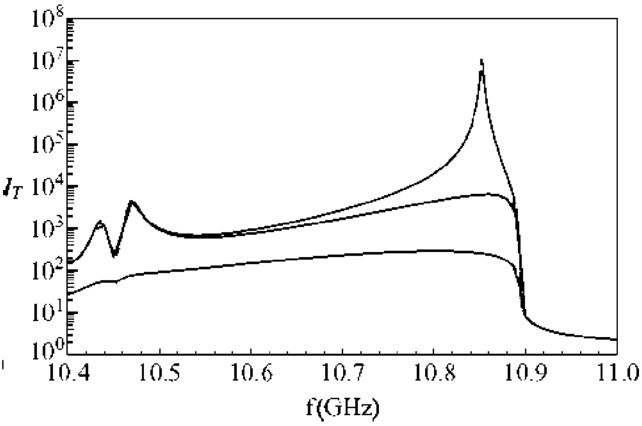

Fig. 6.3. (Color online) Transmission length l_T vs frequency f for $_a$ = 30° for a metamaterial stack: without absorption, *p* polarization (top curves), s polarization (middle curves); in the presence of absorption (bottom curves). Results for numerical simulations (red solid curves) and analytical predictions Eq. (6.18) (blue dashed curves) are shown.

Transmission length l_T vs frequency f at normal incidence (0_a = 0) for a metamaterial stack without absorption (top curve) and in the presence of the absorption (bottom curves). Red solid curves display numerical simulations while blue dashed curves show the analytical predictions. Inset: The real (red solid line) and imaginary (green dashed line) part of the metamaterial layer refractive index.

Moreover, the first term in Eq. (6.18), corresponding to the single-scattering approximation, dominates for all frequencies except in the region 10.4 GHz $< f <$ 10.5 GHz where both terms in Eq. (6.18) are necessary to describe the localization length. Quite surprisingly, the asymptotic equations (6.20) and (6.26) are in excellent agreement with the numerical results over the frequency range 10.9 GHz $< f <$ 11.0 GHz, including in the near vicinity of the frequency f_{mp} = 10.95 GHz at which μ vanishes.

Absorption substantially influences the transmission length (the lower curve in Fig. 6.2) and smooths the nonmonotonic behavior of the transmission length for $f <$ 10.5 GHz. The small dip at $f \approx$ 10.45 GHz correlates with the corresponding dip in the transmission length in the absence of absorption. The most prominent effect of absorption occurs for frequencies just below the μ-zero frequency f_{mp} = 10.95 GHz. While in the absence of absorption, the stack is nearly transparent in this region, turning on the absorption reduces the transmission length by a factor of 10^2-10^3 for $f >$ 10.7 GHz. In contrast, for frequencies $f >$ 10.95 GHz, the transmission lengths in the presence and absence of absorption are nearly identical because here the stack is already opaque and its transmittance is not much affected by an additional small amount of absorption. Again, the simulations and the theoretical predictions are in excellent agreement and show that the theoretical form (6.18) accounts accurately for dissipation.

The transmission length spectrum in the case where both disorders of the dielectric permittivity and magnetic permeability are present, i.e., $Q_e = Q_m = 0.5 \text{ x } 10^{-2}$, is qualitatively similar to that of the single-disorder case considered above, and so we do not present these results here.

In the case of *oblique incidence,* polarization effects become important. In Fig. 6.3, we display the transmission length frequency spectrum for a homogeneous metamaterial stack with only dielectric permittivity disorder for the angle of incidence Θ_a = 30°. For frequencies $f <$ 10.55 GHz, the transmission length is largely independent of the polarization.

Moreover it does not differ from that for normal incidence (compare with the top curve in Fig.6.2). This is due to the high values of the refractive indices at these frequencies ($| \nu_n | > 4$), resulting in almost zero refraction angles (6.14) for angles of incidence that are not too large.

As noted previously, true delocalization, such as in the presence of only thickness disorder, cannot occur for material disorder (i.e., permittivity or permeability disorder). Nevertheless, the transmission length manifests a sharp maximum at an angle close to the Brewster angle, as commented upon in Refs.146 and 149. This is indeed apparent in Fig. 6.3 for the frequency $f \approx$ 10.85 GHz. Because only ε fluctuates, the Brewster condition is satisfied only for p polarization (6.30) at a single frequency $f_p \approx$ 10.852 GHz. The introduction of additional permeability disorder (not shown) reduces the maximum value of the localization length by two orders of magnitude.

Comparison of Figs.6.2 and 6.3 shows that the frequency of the maximal suppression of localization decreases as the angle of incidence increases. At normal incidence it coincides with the μ-zero frequency f_{mp} while for oblique incidence at $\Theta_a = 30°$ it coincides with the Brewster frequency f_p for p polarization.

Absorption strongly diminishes the transmission length. In Fig.6.3, we display results of numerical simulations of the transmission length for p polarization (bottom red solid curve) and the corresponding theoretical prediction (6.18) (blue dashed curve). Both curves are almost identical, with absorption providing the main contribution to the transmission length, and with the permittivity disorder having little influence on the transmission length. The results for s polarization are therefore practically indistinguishable from those for p polarization.

The transmission properties of a stack *with only magnetic permeability disorder at oblique incidence* are similar to those for the case of only dielectric permittivity disorder. In Fig.6.4 we plot the transmission length as a function of frequency at the incidence angle $\Theta_a = 30°$. The key difference is that there is a Brewster anomaly for s polarization (top curves in Fig.6.4) while for p polarization (middle curves in Fig.6.4) the Brewster anomaly is absent. The effect of absorption (the bottom curves) is also similar to that of the preceding case.

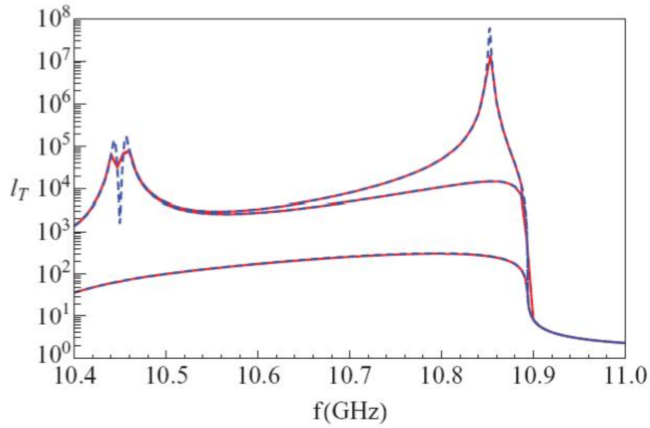

Fig. 6.4. (Color online) Transmission length l_T vs frequency f at $\Theta_a = 30°$ for a metamaterial stack with the magnetic permeability disorder: without absorbtion, s polarization (top curve), p polarization (middle curve); in the presence of the absorbtion (bottom curves). Red solid curves are simulation results while the blue dashed curves are analytical predictions, Eq. (6.18).

We finally consider the dependence of the transmission length on the angle of incidence at a fixed frequency. The results for both polarizations are displayed in Fig. 6.5. Here we have plotted the transmission length of the stack *with only dielectric permittivity disorder* with $Q_e = 0.5\text{x}10^{-2}$ at the frequency $f = 10.90$ GHz, as a function of the angle of incidence. The upper and middle curves correspond to the results for *p*- and *s*-polarized waves, respectively, in the absence of absorption. For *s*-polarized light, the transmission length decreases monotonically with increasing angle of incidence, while for *p*-polarized waves it increases with increasing angle of incidence. Such behavior reflects the existence of a Brewster angle for *p* polarization at the Brewster angle Θ_a = 15°. The red solid curve shows the results of simulations, while the blue dashed line is the analytic prediction based on Eq.(6.18).

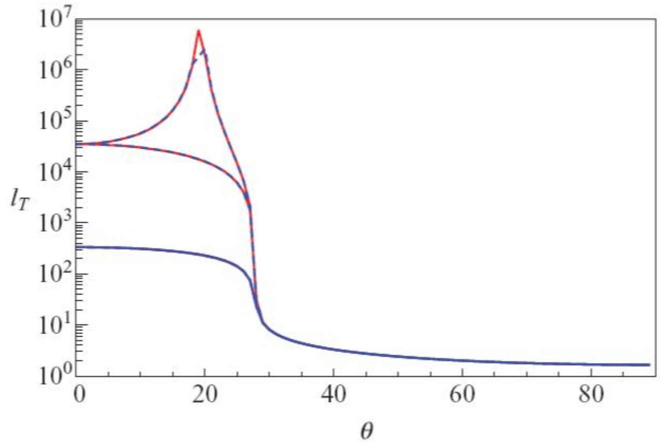

Fig. 6.5. (Color online) Transmission length l_T vs angle of incidence for a homogenous metamaterial stack at f = 10.7 GHz with permittivity disorder: in the absence of absorption—upper curve and for *p* polarization; middle curve is for *s* polarization and in the presence of absorption; and for both polarizations, lower curves. The solid red lines are the numerical simulations and the blue dashed lines are the theoretical predictions, Eq. (6.18).

As in the previous cases, in the presence of absorption, the results for both polarizations are almost identical (the lower curves in Fig 6.5). For angles $\Theta_a < 30°$, the transmission length is dominated by absorption, while for angles $\Theta_a > 30^\circ$ tunneling is the dominant mechanism. The results for permeability disorder (not presented) are very similar to those for permittivity disorder.

6.3.2 Normal-material stacks

1. Standard normal stacks

According to the definitions of Sec. 6.2.1, in a homogeneous normal layer the dielectric permittivity and the magnetic permeability are defined as $-\varepsilon^*(f)$ and $-\mu^*(f)$, respectively, with $\varepsilon(f)$ and $\mu(f)$ given by Eqs. (6.1) and (6.2). For such a layer the refractive index is positive in the region 10.40 GHz < f < 10.95 GHz. At higher frequencies 10.95 GHz < f < 11.00 GHz, the magnetic permittivity becomes negative and we now deal with a SNM. The transmission length in this case manifests exactly the same behavior as for stacks comprised of metamaterial layers that were considered in the previous Sec.6.3.1.

2. *Exotic normal stacks*

The most unusual features of the transmission length appear in the vicinities of the μ-zero and/or ε-zero frequencies and at the Brewster frequency. In this section, we consider a model, which although being rather artificial, offers extraordinary transport properties that could be useful for designing optical switching devices. Within this model, the dielectric permittivity coincides with that of the normal material, $-\varepsilon^*(f)$, over the entire frequency range 10.40 GHz < f < 11.00 GHz, while the magnetic permeability coincides with that of normal material, $-\mu^*(f)$, only in the region 10.40 GHz < $f < 10.95$ GHz, with its values at higher frequencies, 10.95 GHz < f < 11.00 GHz, being given by Eq.(6.2) (metamaterial). It is easy to see that the refractive index is always positive and is practically symmetric [$\mu(f)\ \alpha\ |f - f_{mp}|$] about the frequency $f_{mp} = 10.95$ GHz, at which it vanishes. As a consequence, when this frequency is crossed, the transmission length of a random stack of such layers manifests an abrupt switching from complete transparency (at normal incidence) to strong localization (i.e., strong reflection) at oblique incidence. Therefore, the transmission length, in the case of normal incidence, must manifest the same symmetry in the vicinity of this frequency. Note that qualitatively the transmission behavior would have been the same as observed here if the frequency model for μ behaved according to the form $\mu(f)\ \alpha\ (f - fmp)^2$ rather than $\mu(f)\ \alpha\ |f - f_{mp}|$. Note that the former does not violate the Kramers-Kronig condition and as a consequence the transmission characteristics depicted below are possible.

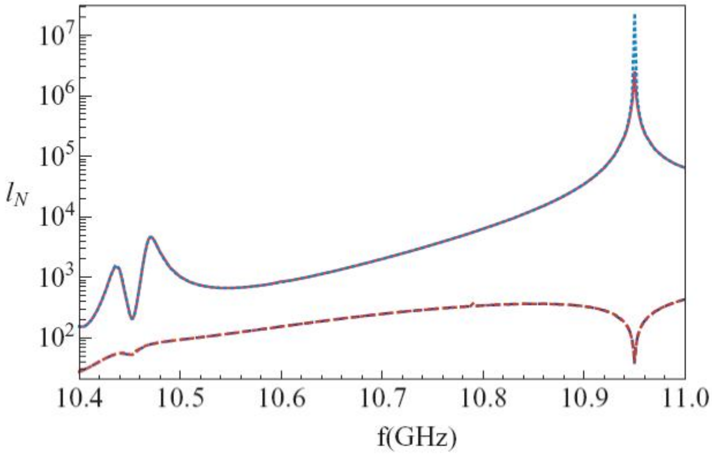

Fig. 6.6. (Color online) Transmission length l_T vs frequency f at normal incidence for a homogeneous stack: without absorption (upper curve), and in the presence of absorbtion (lower curves). The red solid curves are the numerical simulations and the blue dotted lines are Eq. (6.18).

The normal incidence transmission length, as a function of wavelength, is plotted in Fig.6.6 for stacks of $N=10^7$ layers with only dielectric permittivity disorder Q_e = 0.5 x 10^{-2}, Q_m = 0. The upper and lower curves display l_T (f) for lossless and absorbing stacks, respectively. The red solid curves and the dashed blue curves display, respectively, the results of numerical simulations and the theoretical prediction (6.18). The upper curves, corresponding to an absence of absorption, represent the genuine localization length for all frequencies except for the vicinity of $f \approx f_{mp}$ = 10.95 GHz, where the transmission length drastically increases. For frequencies $f < f_{mp}$ = 10.95 GHz, the transmission length coincides with that of the normal or metamaterial stack (see Fig.6.2), while for frequencies f slightly exceeding the characteristic frequency f_{mp} the symmetry mentioned above is clearly manifest. Absorption (lower curve in Fig.6.6) has a similar effect on the transmission length as that shown for metamaterial stacks.

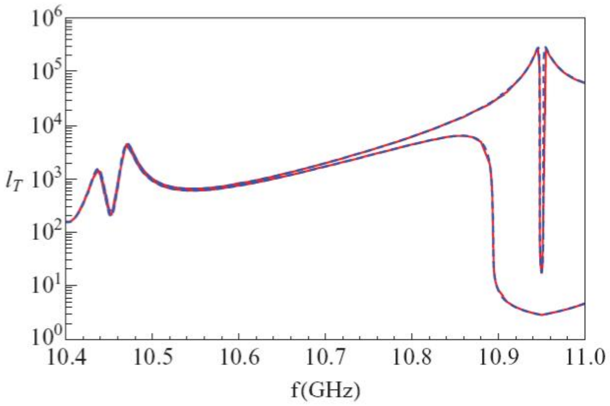

Fig. 6.7. (Color online) Transmission length l_T vs frequency f for s-polarized, off-axis incidence $_a$ = 5° top curve and for Θ_a = 30° bottom curve for a normal material stack in the absence of absorbtion. The red solid curves are numerics and the blue dashed curves are the theoretical predictions, Eq. (6.18).

We have plotted (see Fig.6.7 top curve) the same curve for an angle of incidence Θ_a = 5°. The corresponding curve demonstrate a deep dip (four orders of magnitude) in the transmission length over the narrow frequency range 10.93 GHz < f < 10.97 GHz. The origin of the dip is related to the tunneling nature of wave propagation at these frequencies.

The width of the strong localization region (where the transmission length becomes comparatively small) increases with increasing angle of incidence. For Θ_a = 30° and s polarization, this range is 10.85 GHz < f < 11 GHz (lower, dashed, blue line in Fig.6.7) and corresponds to the tunneling regime. For frequencies f < 10.85 GHz, the localization length coincides with the localization length for a metamaterial stack (see middle curve in Fig.6.2).

The results for p polarization are similar to those for s polarization (with the exception that the transmission length has its maximum at Θ=30° at $f \approx$ 10.85 GHz), and thus we do not present them here.

6.3.3 Mixed stacks

The case of mixed stacks without thickness disorder is very interesting. It is shown in Ref.128 that, for a nondispersive mixed stack with fluctuating refractive indices and constant layer widths, localization of long-wavelength radiation is strongly suppressed. This suppression manifests itself as the anomalous, $l \propto \lambda^6$, growth of the localization length in the long-wave region instead of the usual dependence $l \propto \lambda^2$. To study how dispersion influences this effect we consider transmission through mixed stacks with only dielectric permittivity disorder.

In Fig.6.8(a), we plot the transmission length spectrum in the case of normal incidence, for a small permittivity disorder of $Q_e = 0.5 \times 10^{-2}$, and observe significant (up to four orders of magnitude) suppression of localization in the frequency region 10.50 GHz $< f <$ 10.68 GHz. However, in this case the localization length grows with increasing frequency, while, in Ref.128 similar growth has been observed with increasing incident wavelength. This is shown in Fig.6.8(b) where the same transmission length spectrum is plotted as a function of free-space wavelength. Thus, the localization length decreases by four orders of magnitude, manifesting as an enhancement, rather than the suppression, of localization with increasing wavelength.

Although at first sight these findings are in sharp contrast, both are correct and physically meaningful. In the model studied in Ref.128 the wavelength of the incident radiation largely coincided with the wavelength inside each layer. In the problem that we consider here, these two wavelengths differ substantially. Accordingly, in Fig 6.8(c), we plot the transmission length as a function of wavelength within the stack and obtain results which are very similar to those in Ref.128. To emphasize the similarity with Fig.6.3 in Ref.128 we have plotted the transmission length spectrum for three different stack lengths: $N = 10^5, 10^6, 10^7$. It is easily seen that the suppression of localization in the dispersive media is qualitatively and quantitatively similar to that predicted in Ref.128 Indeed, the suppression observed there was described by a power law $l_T \propto \lambda^6$, with subsequent more detailed calculations correcting the estimate of this power from 6 to 8.78. The results in Fig.6.8(c) correspond to a power of 8.2. The lower curves in Figs.6.8(a)-6.8(c) correspond to samples with both types of disorder $Q_e = Q_m = 0.5 \times 10^{-2}$ and are very well described by the analytical prediction (6.19) with $l \propto \lambda^2$.

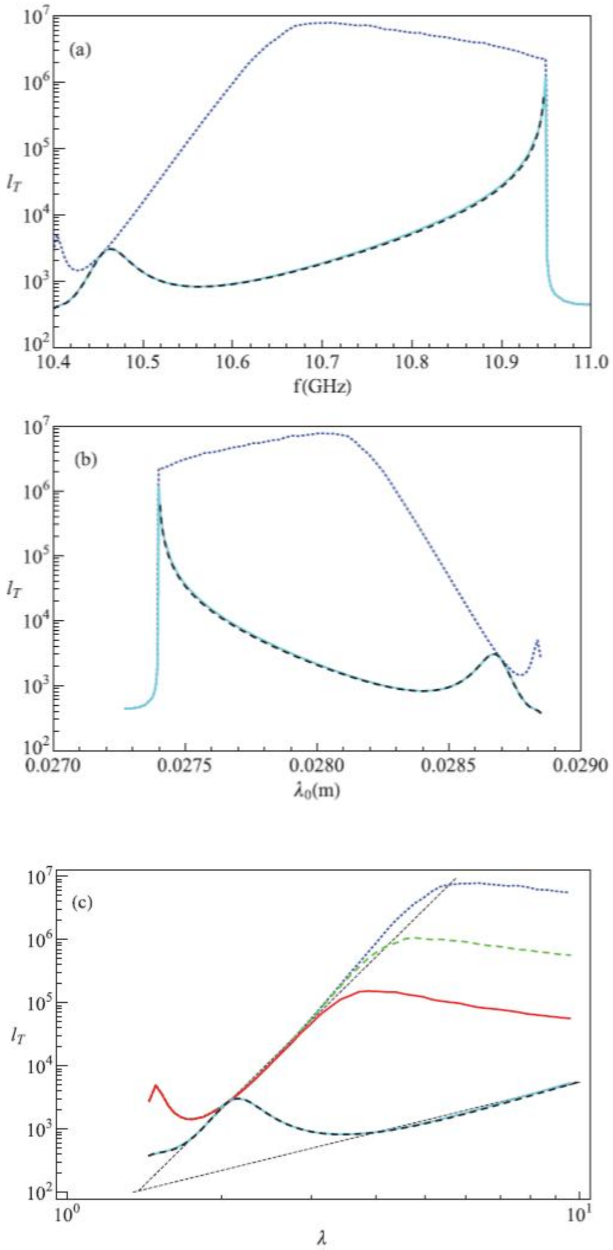

Fig. 6.8. (Color online) (a) Transmission length l_T vs frequency f for a mixed stack with $N = 10^7$ layers (top dotted blue curve), and only dielectric permittivity disorder. The bottom curves on all three panels are for a stack with $N = 10^7$ layers with both permittivity and permeability disorder (the cyan solid curve displays simulation results while the dashed black curve is for the analytic prediction, Eq. (6.19); (b) is the same as in (a) but plotted as a function of the free-space wavelength A_0 while on panel (c) we plot the transmission length as a function of the averaged wavelength inside the stack normalized to the thickness of the layer, for $N = 10^7$ layers (blue dotted top curve), $N = 10^6$ layers (dashed green curve), and for $N = 10^5$ layers (red solid curve).

Combining the results of this section with those obtained previously, we may conclude that dielectric permittivity disorder in mixed stacks having constant layer thickness is not sufficiently strong to localize low-frequency radiation. To obtain the "typical" long-wavelength behavior of the localization length, $\alpha\lambda^2$, one has to “switch on” additional disorder-either thickness disorder as in Refs.128 and_133 or magnetic permeability disorder as in the present work.

The transmission length obtained here remains very large up to the μ-zero frequency f_{mp} = 10.95 GHz [Fig. 6.8(a)]. This leads us to hypothesize that suppression of localization in the model considered here is related to the vanishing of the effective magnetic permeability at $f = f_{\mathrm{mp}}$. In this case, one should expect a substantial increase of the localization length with increasing frequency and a sharp peak of the localization length at $f = f_{\mathrm{mp}}$. However, the stack of $N = 10^7$ layers is too short for this to occur, and thus its localization regime is bounded from above by the frequency f = 10.65 GHz. Therefore, we do not observe the expected peak at f = 10.95 GHz. However, we do observe the abrupt drop of the localization length as we approach this frequency from the right. Thus, we conclude that we are dealing with the same effect of delocalization at д-zero frequency as was observed in monotype samples (see Fig. 6.2). However, in contrast to the latter case, the corresponding growth of the localization length begins essentially earlier and occurs substantially faster.

6.4 Conclusion

Transport and localization of classical waves in onedimensional disordered systems containing dispersive, lossy metamaterials have been studied analytically and numerically. It has been shown that the field can be delocalized in onedimensional μ-near-zero or ε-near-zero media – a new form of delocalization that occurs in one dimension in the presence of short-correlated disorder. We have also demonstrated disspersion-induced suppression of Anderson localization in mixed stacks with either dielectric permittivity or magnetic permeability disorder. The presence of both forms of disorder, however, enhances localization. The effects of polarization in the presence of different forms of disorder have been studied and Brewster anomalies have been demonstrated at angles (or frequencies) that depend not only on the polarization of the radiation, but also on the type of disorder. The theoretical predictions are in excellent agreement with the results of numerical simulations.

7 PHOTONIC CRYSTALS WITH ANOMALOUS DISPERSION: UNCONVENTIONAL PROPARGATING MODES IN THE PHOTONIC BAND GAP

We present an investigation of the optical properties of photonic crystals whose constituent materials exhibit anomalous dispersive behavior. In particular, the anomalous dispersion near resonances may lead to additional propagating modes in the gap of the undoped system for a localized region of wave-vector space. Such a system may be realized by infiltrating quantum dots in polymer suspensions into the pores of two-dimensional high-index photonic crystals. An evaluation of the absorption lengths associated with these unconventional modes and corresponding transmission calculations demonstrate that this effect can be observed in currently accessible structures.

7.1 Introduction

Progress in photonics is closely related to development of optical materials with tailor-made properties. Photonic crystals (PCs) [149-151] represent a novel class of man-made optical materials. The judicious design of these two-dimensional (2D) or three-dimensional (3D) periodic dielectric arrays allows one to tailor the photonic dispersion relation and the corresponding mode structure to almost any need. In particular, the flexibility associated with material composition, lattice periodicity, and symmetry together with the deliberate creation of defect structures makes PCs the optical analog of an electronic semiconductor.

The usefulness of PCs and defect structures embedded in them may be substantially enhanced if the structures exhibit one or more forms of tunability. This has led a number of authors to propose PC structures whose constituent materials exhibit tunable properties such as temperature-dependent refractive indices, [152] strongly dispersive behavior [153] as well as electro[152-154] and magnetrooptically [155]controllable anisotropies.

In this paper, we consider photonic band structures and absorption lengths of PCs whose constituent materials exhibit anomalous dispersion. By embedding these materials into a PC, one may expect to modify the photonic band structure considerably, if the resonance frequency is tuned to lie close to a photonic band edge. As we will show, the hybridization of the electromagnetic wave mode with the local dielectric modes leads to a splitting of the wave mode into three submodes in a limited region of wave-vector space. Of these three modes, two are stable and form a bubble shape in the band structure. However, as any frequency dependence of the effective dielectric constant is necessarily accompanied by a dissipative component, the question arises as to whether these bubble modes are overdamped. To answer this question, it requires a full treatment of the propagating and absorptive properties of the electromagnetic wave. As a consequence, we describe a highly efficient on-shell methodology based on photonic Wannier functions [156] which allows us to solve for the photonic band structure and absorption lengths associated with complex-valued and frequency-dependent dielectric constants. We present a careful study of this problem and conclude that the bubble modes should, indeed, be observable in currently accessible materials.

The paper is organized as follows. In Sec. 7.2, we define the model system used in the following sections. The numerical methods for band structure and attenuation length calculations of PCs with dispersive components are described and discussed in Sec. 7.3. In Sec. 7.4, we present results for the model system, discuss the effects of the anomalous dispersion of the constituent materials on the photonic band structure, and investigate the attenuation length resulting from the nonzero imaginary part of the dielectric constant. Finally, we summarize our results in Sec. 7.5.

7.2 Model system

In the following sections, we discuss in detail the case of TM-polarized radiation in 2D macroporous silicon PCs [157] (square lattice of pores with lattice constant α in silicon, dielectric constant of silicon εSi=12.0, and electric field polarized parallel to the pore axis), where the pores (radius $r/a = 0.475$) have been infiltrated with a polymer (typical dielectric constant εpolymer=2.56) that contains a (small) volume fraction of quantum dots. This is schematically depicted in Fig. 7.1, and we would like to note that similar systems have recently been realized [158-159], albeit for different purposes. However, we would like to emphasize that all our arguments are directly applicable to the case

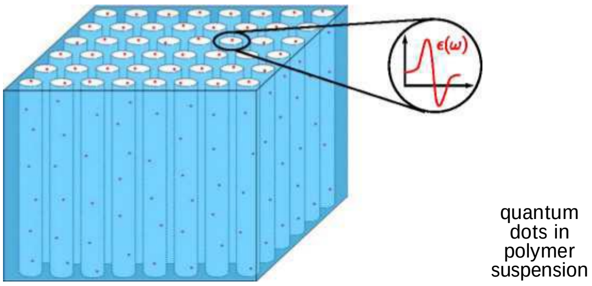

FIG. 7.1. (Color online) Model system of a 2D macroporous silicon PC infiltrated with quantum dots in a polymer suspension. This PC consists of a 2D macroporous silicon backbone (dielectric constant εSi=12.0) into which a square lattice of pores (radius r/a = 0.45) has been etched, which subsequently have been filled with a low-index polymer (dielectric constant εpolymer=2.56).

of TE-polarized radiation in 2D PCs as well as to the case of 3D PCs if only the constituent materials exhibit frequency ranges with anomalous dispersion.

In our simplified approach, the quantum dots are modeled through a (linear) two-level dielectric constant,

$$\varepsilon_{tl}(\omega) = 1 + \frac{\omega^2 p}{\omega_0^2 - \omega^2 - \imath\gamma\omega'} \tag{7. 1}$$

where ω0, ωp, and y denote, respectively, the resonance frequency, the oscillator strength, and the linewidth (damping constant). Owing to their small size of a few nanometers relative to the optical wavelength, we may treat the admixture of a certain concentration y of quantum dots to the polymer within a Maxwell-Garnett effective dielectric constant approach [160]. As a consequence, the effective dielectric constant of this doped polymer that fills the pores of the macroporous silicon PCs reads

$$\varepsilon_{porb}(\omega) = \varepsilon_m\left(1 + \frac{3\eta a(\omega)}{1 - \eta a(\omega)}\right) \tag{7.2}$$

In Fig.7.2, we depict the frequency dependence of the real and imaginary parts of this effective dielectric constant [Eq. (7.2)] for a resonance frequency $\omega_0 a/2\omega\pi c$ = 0.245, oscillator strength ω_p = 0.8ω_0, damping constant γ=0.01ω_0, and several realistic values of the concentration η. In fact, changing the concentration y of quantum dots allows a rather simple way of significantly tuning the pore dielectric constant in the vicinity of the quantum-dot resonance frequency. As a result of the hybridization of the quantum-dot modes with the background modes provided by the polymer, this

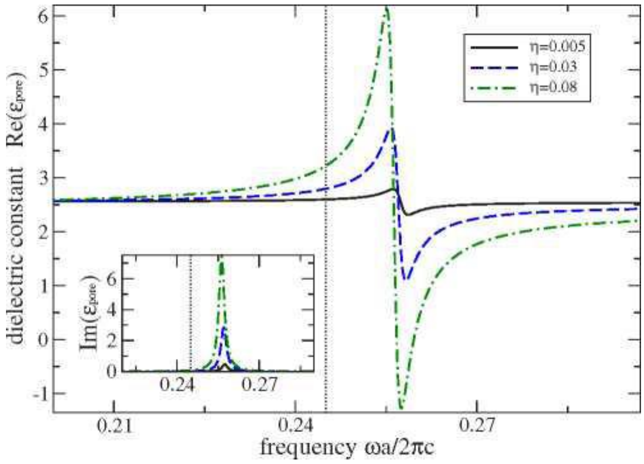

FIG. 7.2. (Color online) Effective dielectric constant of a typical polymer doped with quantum dots for three different concentrations y. The quantum-dot parameters are given in the text. The resonance of this Maxwell-Garnett effective dielectric constant is shifted relative to the resonance frequency of isolated quantum dots (vertical dotted line).

resonance is slightly shifted relative to the bare quantum-dot resonance frequency.

Before proceeding to photonicband structure computations of composite PC structures, we would like to make two observations. First, while we have derived the effective dielectric constant $\varepsilon_{porb}(\omega)$ of the pore material for a specific and easily realizable model system (see Ref. 160), it should be clear that its frequency-dependent behavior depicted in Fig. 7.2 is rather generic and can be obtained via many other routes such as the growth of polar semiconductor nanocrystals within the pores. Second, the value of the resonance frequency determines the PC's photonic bands which experience the effects of the anomalous dispersion depicted in Fig. 7.2 most strongly. Therefore, the undoped PC has to be carefully engineered in order to ensure that the corresponding Bloch functions sample the pores sufficiently well. Analogous considerations apply to other structures. We will return to this issue in Sec. 7.4.

7.3 Band structure and attenuation length computations

The Maxwell equations for time-harmonic TM-polarized light propagating in the *(x, y)* plane of a 2D PC can be reduced to a scalar wave equation for the *z*-component $E(\vec{r})$of the electric field.

$$\nabla^2 E(\vec{r}) + \left(\frac{\omega}{c}\right)^2 \varepsilon_{pc}(\omega,\vec{r})E(\vec{r}) = 0 \qquad (7.4)$$

Here, $\nabla^2 = \partial_x^2 + \partial_y^2$ and c denote the 2D Laplacian and the vacuum speed of light, respectively. The dielectric constant $\varepsilon_{pc}(\omega,\vec{r}) \equiv \varepsilon_{pc}(\omega,\vec{r}+\vec{R})$ contains all the information about the PC and is periodic with respect to the set $R = \{n_1\vec{a}_1 + n_2 k_2;$ *(n_1,n_2)* $\in Z^2$ of lattice vectors R that are generated by the primitive translations a_1 and a_2. For our model system, the PC dielectric constant reads as

$$\varepsilon_{pc}(\omega,\vec{r}) = \varepsilon_{si} + \left[\varepsilon_{porb}(\omega) - \varepsilon_{si}\right]\sum_{\vec{R}} \Theta\left(r - \left|\vec{r} - \vec{R}\right|\right), \qquad (7.5)$$

where we have introduced the Heaviside function Θ(x).

Equation (7.4) represents a differential equation with periodic coefficients and, therefore, its solutions obey the Bloch-Floquet theorem,

$$\varepsilon_{n\vec{k}}\left(\vec{r} + \vec{a}_j\right) = e^{i\vec{k}\vec{a}j} E_{n\vec{k}}\left(\vec{r}\right), \qquad j=1,2 \qquad (7.6)$$

In the reduced zone scheme,13 which we adopt here, the Bloch modes $E_{n\vec{k}}(\vec{r})$ are labeled with the composite index $(n\vec{k})$, where n and k, respectively, denote the band index and the wave vector in the first Brillouin zone (BZ).

In the case of a frequency-independent dielectric constant, $\varepsilon_{pc}(w,\vec{r}) = \varepsilon_{pc}(r)$, Eq. (7.4) can be solved as a standard eigenvalue problem using general purpose methodologies such as plane wave expansion (PWE) approaches,[14][15]finite-difference based multigrid methods [164] or advanced finite element techniques[165]. However, the situation becomes much more complicated for frequency-dependent dielectric constants which we study in this paper. In this case, Eq. (7.4) constitutes a nonlinear elliptic eigenvalue problem with Bloch-boundary conditions and, therefore, solving Eq. (7.4) either requires the usage of an on-shell methodology, [166-167] which—for a given frequency ω—allows one to compute the allowed wave vectors k (ω) or an extension of the standard band structure methods to nonlinear eigenvalue problems. For instance, the standard PWE approach has been adapted to treat specific forms of frequency-dependent dielectric constants, and, recently, it has been reformulated to facilitate on-shell computations[168] However, the Kramers-Kronig relations—which are a manifestation of causalite [169] — require that dispersive materials have to be described through a complex-valued dielectric constant such as those described in Eqs. (7.1) and (7.2). As a consequence and in order to ensure the viability of the results, absorption has to be taken into account by all methods of photonic band structure computations.

In general, there exist two distinct ways how to deal with absorption in photonic band structure theory. Within the first route, real-valued wave vectors are maintained so that absorption leads to complex eigenfrequencies [170,172] From a mathematical point of view, this has the advantage that the Bloch modes can be normalized. Physically, this corresponds to the situation where the Bloch modes acquire a finite lifetime, i.e., an initially excited Bloch mode decays as time progresses. The realization of a corresponding experiment appears to be rather challenging. The second option is to retain real-valued frequencies and to associate the effects of absorption with complex-valued wave vectors. As a result, the Bloch modes resist normalization. On the other hand, an imaginary part of the wave vector allows one to define a length scale that describes how waves at a given frequency are attenuated within a PC. This attenuation length accounts for both the effects of absorption and photonic band gaps. The latter are also present in the nonabsorbing case. An experimental realization of this situation would have to be based on studies of the transmission through finite but sufficiently large PC samples, so that effects related to the PC surfaces (for instance, in- and outcoupling efficiencies) can be separated from the attenuation in the bulk PC (Sec. 7.4).

The relation between the two approaches discussed above is nontrivial. For instance, in the case of complex eigenfre- quencies as functions of real wave vectors, it would be necessary to develop an analytical continuation of those frequencies to complex-valued wave vectors and to search for wave vectors for which the imaginary part of the frequency vanishes. Since the eigenfrequencies are, in general, only known numerically, this is a formidable task. Furthermore, even in the weakly absorbing case, simple perturbation techniques for the transition from complex frequencies to complex wave vectors fail, [170] although recent advances [171] suggest that more sophisticated approaches could improve the situation (see also Ref. 173).

In the following sections, we describe three independent and somewhat complementary methods that allow one to develop a complete physical picture of PCs with dispersive constituent materials and apply those methods to our model problem with anomalous dispersion. First, we present an efficient on-shell methodology based on photonic Wannier functions that allows one to carry out band structure and attenuation length calculations for general frequency-dependent and complex-valued dielectric constants. We then provide a brief summary of an extension of standard band structure calculation techniques (initially described in Ref. 173 and subsequently rediscovered in Ref. 175) that allows one to deal with frequency-dependent but real-valued dielectric constants. This extension may provide the basis for reasonable approximations in systems where absorption can be treated perturbatively. [176]Most importantly, this extension suggests a straightforward geometrical interpretation and additional intuitive insights into the results obtained from the more general Wannier function approach. Finally, we demonstrate how attenuation lengths can be extracted from transmission calculations through finite PC samples. These calculations are based on a rigorous coupled wave analysis (RCWA) approach with numerical scattering matrices and allow a direct comparison with the Wannier function results for infinite PCs.

7.3 A .Wannier function approach

In order to solve Eq. (7.4) within the Wannier function approach, we decompose the complex-valued PC dielectric constant $\varepsilon_{pc}(w,\vec{r})$ into a real-valued and nondispersive reference part $\varepsilon_{ref}(\vec{r})$ and a complex-valued frequency-dependent part $\Delta\varepsilon(w,\vec{r})=\varepsilon_{pc}(w,\vec{r})-\varepsilon_{ref}(\vec{r})$ that both retain the lattice periodicity of the PC. As alluded to above, for the reference system, we can easily solve the corresponding wave equation, via standard band structure computations. Moreover, we have a certain flexibility in choosing the reference dielectric constant $\varepsilon_{ref}(\vec{r})$.The actual choice of $\varepsilon_{ref}(\vec{r})$should be guided by physical considerations, such as the range of values, which the PC's different constituent material dielectric constants take on over the frequency range of interest so that the reference dielectric constant is (in some sense) not too far from the actual system that should be solved. For our model system, the natural choice for $\varepsilon_{ref}(\vec{r})$ is the 2D macroporous silicon PC whose pores have been infiltrated with the undoped polymer.

As a result, Eq. (7.7) provides us with a reference band structure and corresponding reference Bloch functions $E^{(0)}_{n\vec{k}}(\vec{r})$. These Bloch functions are then further processed to yield the reference PC's photonic Wannier functions,

$$W_{n\vec{k}}(\vec{r}) = \frac{v_{wsc}}{(2\pi)^2} \int_{BZ} d^2 k e^{-ik\vec{R}} \sum\nolimits_m U_{nm}(\vec{k}) E^{(0)}_{n\vec{k}}(\vec{r}). \tag{7.8}$$

Here, V_{WSC} denotes the volume of the PC's Wigner-Seitz cell. The unitary matrices $U_{nm}(\vec{k})$ have to be determined numerically and facilitate that the Wannier functions are maximally localized in the unit cell that corresponds to the lattice vector $\vec{R}$_. Owing to the fact that photonic Wannier functions are essentially the result of a lattice Fourier transform of Bloch functions, they have encoded into them the entire information of the reference PC's photonic band structure and exhibit very useful orthonormality and translational properties,

$$\int d^2 r W^*{}_{m\vec{R}}(\vec{r}) \varepsilon_{ref}(\vec{r}) W_{m\vec{R}}(\vec{r}) = \delta_{mm} \cdot \delta_{\vec{R}\vec{R}} \tag{7.9}$$

$$W_{m\vec{R}}(\vec{r}) = W_{m\vec{0}}(\vec{r} - \vec{R}) \tag{7.10}$$

In Eq. (7.9), the integration extends over all space and $\delta_{mm'}$ denotes the Kronecker symbol. For details on the actual constructionof photonic Wannier functions and their usage in the design of functional elements, we refer to Ref. 157. In Figs.7.3 and 7.4, we display, respectively, the photonic band structure (calculated with the multigrid methos [164] and a selection ofmaximally localized Wannier functions for the reference PCstructure. The band structure exhibits a photonic band gap in the frequency range $\omega a / 2\pi\varepsilon \in$ [0.233,0.249] located betweenbands 1 and 2. For the subsequent computations, weemploy the first 18 Wannier functions.These reference Wannier functions may now be utilizedfor solving the photonic band structure of the full system with anomalous dispersion,

$$V^2 E(\vec{r}) + \left(\frac{\omega}{c}\right)^2 \left[\varepsilon_{ref}(\vec{r}) + \Delta\varepsilon(\omega, \vec{r})\right] E(\vec{r}) = 0 \tag{7.11}$$

Upon inserting an expansion of the electric field into Wannier functions,

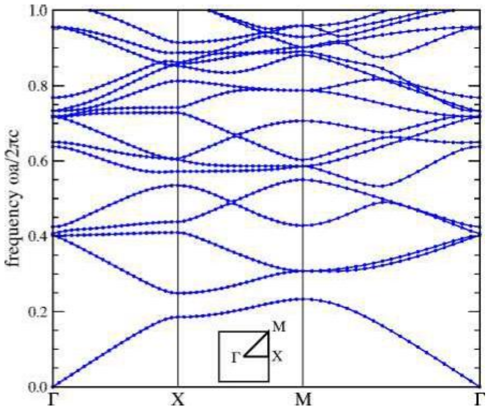

FIG. 7.3. (Color online) Photonic band structure for TM-polarized radiation propagating in the reference PC structure. The associated system parameters are listed in the caption of Fig. 7.1.

$$E(\vec{r}) = \sum\nolimits_{m'\vec{R}'} E_{m\vec{R}} W_{m\vec{R}}(R), \tag{7.12}$$

we obtain—via projecting onto the same basis—a matrix equation for the unknown amplitudes E_{mR} that in component form reads as

$$\sum\nolimits_{m',\vec{R}'} M^{mm'}_{\vec{R}\vec{R}'}(\omega) E_{m'\vec{R}'} = 0 \tag{7.13}$$

with the corresponding frequency-dependent system matrix,

$$M^{mm'}_{\vec{R}\vec{R}'}(\omega) = \delta_{mm'}\delta_{\vec{R}\vec{R}'} + D^{mm'}_{\vec{R}\vec{R}}(\omega) - \left(\frac{c}{\omega}\right)^2 A^{mm'}_{\vec{R}\vec{R}'} \tag{7.14}$$

Here, the entries are constructed from the overlap matrix elements of Wannier functions with respect to the operators appearing in Eq. (7.11), utilizing the orthonormality of the Wannier functions [Eq. (158)]. Explicitly, we have

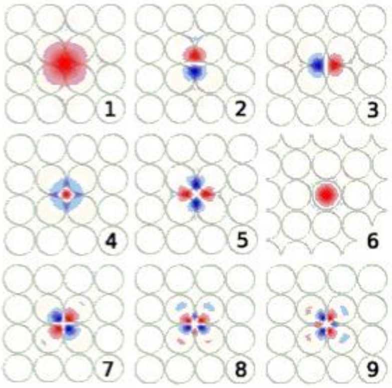

FIG. 7.4. (Color online) A selection of maximally localized Wannier functions for the reference PC structure. The corresponding photonic band structure is displayed in Fig. 7.3 and the associated system parameters are listed in the caption of Fig. 7.1

$$A_{\vec{R}\vec{R}'}^{mm'} = -\int d^2 r W_{m'\vec{R}'}^{*}(\vec{r}), \tag{7.15}$$

$$A_{\vec{R}\vec{R}'}^{mm'}(\omega) = \int d^2 r W_{mR'}^{*}(\vec{r})\Delta\varepsilon(w,\vec{r})W_{m'\vec{R}'}(\vec{r}) \tag{7.16}$$

With the help of the translational properties of both the Wannier functions [Eq. (7.10)] and _$\Delta\varepsilon(\omega,\vec{r})$ it is straightforward to show that the system matrix itself exhibits translational symmetries,

$$M_{\vec{R}-\vec{a}_i R'-\vec{a}_l}^{mm'}(\omega) = M_{\vec{R},\vec{R}'}^{mm'}(\omega) \tag{7.17}$$

with respect to both lattice vectors $\vec{a}_i$, where i=1,2. We are interested in the Bloch mode solutions of our model system including the material dispersion, i.e., the Bloch modes $E_{n\vec{k}}(\vec{r})$ of Eq. (7.11) or its representation within the Wannier function approach [Eq. (7.13)]. As alluded to above, this may be facilitated within an on-shell approach. Therefore, we fix the real frequency ω, choose a direction *k* ˆ in wave-vector space, and determine the allowed complex-valued magnitudes k of the full wave vector $\vec{k}$ -kkˆ so that their real parts lie within the first BZ.

This is realized through several steps. First, we determine suitable integer numbers α and β such that the reciprocal lattice vector $\vec{G} = a b_1 + \beta \vec{b}_2$ is parallel to k ˆ . As usual, the reciprocal basis vectors b_j, where j=1,2 are defined through their orthogonality condition $(\vec{a}_i \bullet b_j) = 2\pi\delta_{ij}$ relative to the real space lattice vectors $\vec{a}_i$, with i=1,2.

Second, we define the real space lattice vectors $\vec{s}_{\parallel} = a\vec{\alpha}_1 + \beta\vec{a}_2$ and $s_{\perp} = a\vec{\alpha}_2 - \beta\vec{a}_1$ that define the sides of the computational supercell employed in the on-shell computations. In addition, we define a set of M lattice vectors $\vec{p}_l$, which consists of the origin $\vec{p}_1 = \vec{0}$ and all the sites $\vec{p}_l$, with l =2, . . . ,M, inside the supercell formed by the vectors $\vec{s}_{\parallel}$ and $\vec{s}_{\perp}$. As a consequence, any lattice site $\vec{R}$ of the PC can uniquely be expressed as

$$\vec{R} \equiv \vec{R}_{ijl} = i \cdot \vec{s}_{\parallel} + j \cdot s_{\perp}^{\rightarrow} + \vec{p}_{l,} \tag{7.18}$$

such that the three integers i, j, and *l* determine a partitioning of the PC into supercells. This is illustrated in Fig. 7.5.

This partitioning facilitates a rewriting of Eq. (7.13) as

$$\sum\nolimits_{m',i',\hat{j},l'} M_{\vec{R}_{ijl}\vec{R}\hat{i}\hat{j}\hat{l}}^{mm'}(\omega) E_{m'\vec{R}_{\hat{i}\hat{j}\hat{l}}} = 0, \forall ij, m, l. \tag{7.19}$$

By construction, the Bloch-Floquet theorem [Eq. (7.6)] stipulates a periodic boundary condition on the supercell in the direction of $\vec{s}_\perp$; i.e., we have $E_{n\vec{k}}(\vec{r} + j \cdot \vec{s}_\perp) \equiv E_{n\vec{k}}(\vec{r})$. Therefore, we obtain that $E_{m\vec{R}_{ijl}} = E_{m\vec{R}_{|0|}}$ for all integers j.

Based on the above considerations and upon taking into account Eq. (7.17), we may rewrite Eq. (7.19) in a matrix form that is suitable for band structure computations,

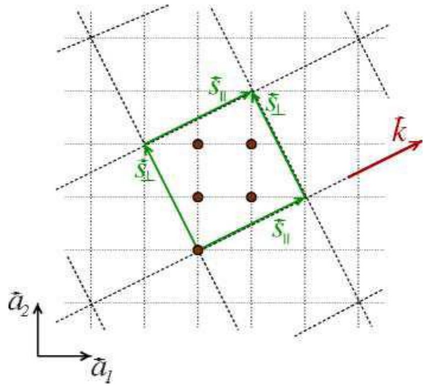

FIG. 7.5. (Color online) Illustration of the partitioning of real space in order to facilitate an on-shell band structure calculation. For a fixed frequency ω and direction $\hat{k}$ in reciprocal space, we partition the PC into identical rectangular supercells whose sides are given by $\vec{s}_\parallel = a\vec{\alpha}_1 + \beta\vec{a}_2$ and $s_\perp = a\vec{\alpha}_2 - \beta\vec{a}_1$, where α and β are integers such that $G = ab_1 + \beta b_2$ is parallel to $\hat{k}$. Periodic and Blochboundary conditions are, respectively, applied along $\vec{s}_\perp$ and $\vec{s}_\parallel$. For this illustration on a square lattice, we have chosen

a =2 and β =1, so that a supercell contains five unit cells of the PC.

$$\sum_{i' -\infty}^{\infty} M_{i-i'}(\omega)\vec{\varepsilon}_{r} = 0, \forall i. \tag{7.20}$$

Here, we have introduced the vectors $\vec{\varepsilon}_i$ and submatrices M_i according to

$$\vec{\varepsilon}_i = \{E_{m,\vec{R}|0|,} \forall m, l\} \tag{7.21}$$

$$M_i = \left\{\sum_{j -\infty}^{\infty} M^{mm}_{\vec{R}_{ijl}\vec{R}_{ijl'}}, \forall m, m', l, l'\right\} \tag{7.22}$$

In a numerical implementation, we have to truncate these infinite vectors $\vec{\varepsilon}_i$ and submatrices $\hat{M}_i$, by taking into account a finite number N_w of bands (or equivalently Wannier functions), i.e., m =1,... , N_w in Eqs. (7.20)-(7.22), and a finite number L of coupled supercells, i.e., replacing ∞ in Eqs. (7.20) and (7.22) by L.

Following the approach of Ref. 157—originally developed for calculations of waveguide dispersion relations in PC_S—we can now rewrite Eq. (7.20) in a transfer-matrix form by defining the composite vectors $\vec{F}_i = \{\vec{\varepsilon}_1, \vec{\varepsilon}_{i+1.....,} \vec{\varepsilon}_{i+2L-1}\}$. As a result, we obtain

$$\vec{F}_{i-1} = T(\omega)\vec{F}_i \tag{7.23}$$

where the transfer matrix $\hat{T}(\omega) = \{\hat{T}_{i,l}(w)\}$ has nonzero submatrix entries of size M * N_w X M * N_w only for

$$\hat{T}_{1,j}(\omega) = -\hat{M}_L^{-1}(\omega)M_{L-1}(\omega) \text{ for j=1,2..,2L-1} \tag{7.24}$$

$$\widetilde{T}_{j+Ij} = \hat{1} \text{ for j=1,2..,2L-1} \tag{7.25}$$

Here, we have denoted the M*N_w x M* N_w unit matrix by $\hat{1}$. Finally, the combination of Eq. 7.23 and the Bloch Floquet theorem [Eq. (7.6)] allows us— at the given frequency ω and for the given direction $\hat{k}$ — to identify the Bloch modes with wave vector $\vec{k} = k\hat{k}$ as the solutions $\vec{F}^{(n)}(\omega)$, where n =1, . . . ,*2L*M** N_w of the transfer-matrix eigenvalue problem,

$$\hat{T}(\omega)\vec{F}^{(n)}(\omega) = \exp\{i\vec{k}_n(\omega)\cdot\vec{s}_{\parallel}\}\vec{F}^{(n)}(\omega) \tag{7.26}$$

with the required wave vectors $\vec{k}_n(\omega) = k_n(\omega)\hat{k}\|\vec{G}$.

These solutions exist for all frequencies. In the presence of material absorption and/or for frequencies inside a stop band in the direction of $\hat{k}$, the wave vector $\vec{k}$ will be complex valued. Therefore, this complex dispersion relation $\vec{k}(\omega)$ contains the full band structure information, i.e., information on dispersion and attenuation or absorption inside the PCs. The accuracy of this Wannier function approach can easily be tested with the help of the reference band structure. In particular, a comparison of the results of Eq. (7.26) with ab initio computations of the reference band structure allows one to assess the number of Wannier functions NW and the maximal number of coupled supercells L required for obtaining accurate results for the full system with dispersive constituent materials [Eq. (7.11)]. For instance, for wave-vector directions lying along the Γ-X direction of the model PC, the computational supercell contains M=1 unit cells. In addition, we require NW=18 Wannier functions and L=4 coupled supercells, so that the resulting transfer matrices $\hat{T}$ to be diagonalized are only 144×144 in size in order to obtain converged results. This is considerably less than what is required with other on-shell methods.

7.3 B. Extension of standard band structure methods

Standard band structure techniques [162-164] that operate with fixed real-valued wave vectors $\vec{k}$ can be extended to deal with the nonlinear eigenvalue problem of Eq. (7.4) for frequency-dependent real-valued dielectric constants. This is facilitated by performing computations for a certain set of standard eigenvalue problems for frequency-independent dielectric constants and a subsequent postprocessing of the corresponding data in order to solve the nonlinear eigenvalue problem via an appropriate fix-point iteration. Specifically, for our model problem, we identify a frequency range of interest and determine the associated range of variation of the pore dielectric constant's real part over this range. Next, we perform standard band structure computations for a set of (fictitious) frequency- independent realvalued pore dielectric constants ε_{fict}, which covers this range. As a result, we obtain—for the fixed wave vector $\hat{k}$—a series of "frequency lines" $\omega_i(\varepsilon_{fict})$, which reflect the variation of eigenfrequencies of the individual bands (indexed through the integer i) when this (fictitious) pore dielectric constant ε_{fict} varies. Then, we obtain the physical eigenfrequencies we

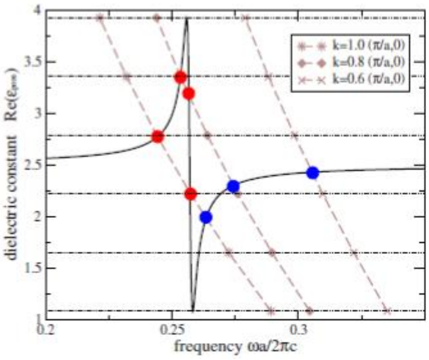

FIG. 7.6. (Color online) Geometric illustration of the iterative solution of the nonlinear eigenvalue problem associated with the band structure of a PC with dispersive constituent materials. The solid line depicts the frequency dependence of the real part of the model system's dielectric constant for a quantum-dot filling ratio of η =0.03.

The values of the other system parameters are given in the text. The dashed lines display the frequency line $\omega_1(\varepsilon_{fict})$, of the first band for three different but fixed wave vectors $\hat{k}$. The intersections of these frequency lines with the graph of the model system's dielectric constant (circles) correspond to the iterative solutions of the nonlinear eigenvalue problem of Eq. (7.4). are looking for by requiring consistency between these frequency lines and the true real part of the system's dielectric constant $\varepsilon_{pore}(\omega)$. This provides us with the solutions $\omega(\bar{k})$ of the nonlinear eigenvalue problem for fixed wave vector $\hat{k}$. We may then repeat the procedure for the next wave vector. We illustrate this fix-point iteration scheme [177] in Fig. 7.6. The dashed lines depict the variation of the first frequency line $\omega_1(\varepsilon_{fict})$ as a function of the fictitious pore dielectric constant ε_{fict} for three different wave vectors in the vicinity of the X point. Note that for a more transparent interpretation of the fix-point iteration, we have assigned the dependent variable ε_{fict} to the ordinate. Then, the intersections (filled circles) of these lines with the frequency-dependent real part of the pore dielectric constant $\varepsilon_{pore}(\omega)$ (solid line) fulfill the consistency condition alluded to above and, therefore, represent the physical eigenfrequencies of the system. While this fix-point iteration scheme appears to be somewhat inefficient relative to on-shell methodologies and does not directly allow one to address the issue of material absorption[imaginary part of $\varepsilon_{pc}(\omega,\vec{r},)$], it does provide an elegant geometric interpretation of the physics of PCs whose constituent materials exhibit anomalous dispersion. In particular, Fig. 7.6 suggests that over certain frequency ranges with sufficiently strong anomalous material dispersion, three distinct solutions $\omega_n(\vec{k})$, n=1,2,3 associated with a single frequency line $\omega_i(\varepsilon_{fict})$ may develop. This is in stark contrast to frequencies away from the resonance where only one solution is allowed. Owing to the facts that for finite damping, the resonance covers only a finite frequency range and that near a photonic band edge, only a finite region of wave-vector space is of relevance, these imply that near a photonic band edge and relative to the undoped reference system, additional propagating states may develop, which are limited to both a finite frequency and a finite wave-vector range. This will lead to the formation of a closed bubblelike object in the photonic band structure diagram of the undoped system [172] (see Fig. 7.9) and will be further elaborated in Sec. 7.4.

7.4 Finite samples: Scattering-matrix approach

An experimental investigation of PCs usually requires the measurement of reflectance and transmittance from finitesized samples. The analysis of such data may substantially benefit from a comparison with corresponding computations. For instance, reflectance and transmittance computations allow one to assess the fabricational tolerances of the structures and to assist in their design [174]. In the present case, we are interested in estimating the impact of material absorption and whether any effects derived from the photonic band structure computations alluded to above could be observed experimentally. In addition, we will demonstrate below that the careful analysis of the length dependence of the transmittance through finite-sized samples at fixed frequency allows an alternative route for determining the inverse attenuation length, i.e., the imaginary part of the wave vector. The computation of the reflectance and transmittance from periodic structure is a well-documented subject of diffractive optics [175-177], where it is often referred to as the RCWA. In the context of PCs, it is more often known as the scattering-matrix method [178]. For our subsequent computations, we utilize our own implementation of the scatteringmatrix method [178] enhanced with the correct Fourier factorization techniques [176, 179] that significantly improve the convergenceproperties of the approach.

In Fig. 7.7, we display the frequency dependence of the transmittance (at normal incidence) through a finite-sized PC (our model system with quantum-dot concentration η=0.03) or several values of the sample thickness (measured in terms of the number of unit cells N). The sample is oriented such that normal incidence corresponds to propagation along the crystallographic Γ-X direction. In addition, we have chosenthe surface termination such that we cut right through the middle of a row of pores of the infinite PC. Clearly, in ourtransmittance or reflectance computations, we have refrained from filling these slit open pores with the doped polymer. In addition, we display complementary reflectance calculations for the same structure in Fig. 7.8 (note, however, the different scalings of the ordinates in Figs. 7.7 and 7.8).

Taken together, Figs. 7.7 and 7.8 suggest that once the PC sample exceeds a certain length (about 20 unit cells in our example and considered frequency range), the in- and outcoupling processes to and from the sample have been decoupled such that for larger sample sizes, the transmittance is only affected by the total attenuation within an effectively bulk PC. Consequently, we may determine the total attenuation length l_ω of the corresponding bulk PC for a fixed frequency ω by fitting the corresponding length dependence of the transmittance $T_\omega(N)$ to an exponential of the form

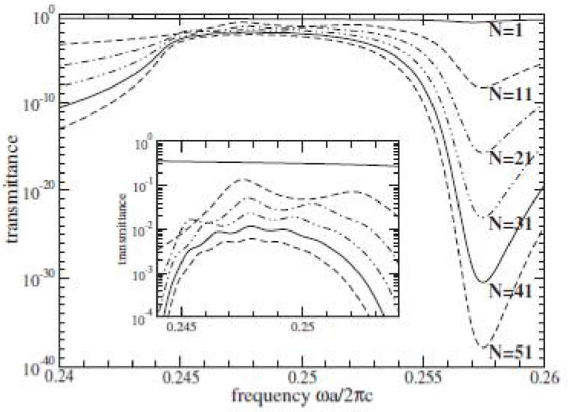

FIG. 7.7. Frequency dependence of the transmittance at normal incidence for finite-sized PC samples with different thicknesses (N=1,11,21,31,41,51 unit cells). The PC is oriented such that normal incidence corresponds to propagation along the Γ-X direction.

The inset demonstrates that once the sample thickness exceeds about 20 unit cells, the transmittance decays approximately exponentially with thickness. This behavior should be compared with the corresponding reflectance calculations displayed in Fig. 7.8. For actual calculations of the attenuation length, sample thicknesses in the range of N=1, . . . ,100 with a step size of N=1 have been analyzed. The PC parameters are given in the text/ $T_\omega(N) = C_\omega \exp(-Na/l_\omega)$. This total attenuation length is connected to the imaginary part of the complex wave vectors' modulus in the corresponding crystallographic $\hat{k} \parallel$ Γ-X via Im $[k(\omega)] = 1/(2l_\omega)$. For the actual calculations of the attenuation length via transmittance computations, we have analyzed the transmittance values for thicknesses ranging from 1 to 100 unit cells with a step size of 1.

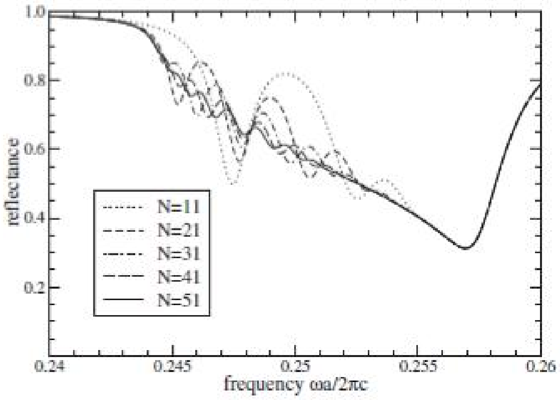

FIG. 7.8. Frequency dependence of the reflectance at normal incidence for finite-sized PC samples with different thicknesses (N=11,21,31,41,51 unit cells). The PC is oriented such that normal incidence corresponds to propagation along the Γ-X direction. Once the sample thickness exceeds about 20 unit cells, the reflectance values (approximately) become independent of the sample thickness. This behavior should be compared with the corresponding transmittance calculations displayed in Fig. 7.7. The PC parameters are given in the text.

ing from 1 to 100 unit cells with a step size of 1. More precisely, Fig. 8 shows that the reflectance does not change within a 1% margin for frequencies below $\omega\alpha / 2\pi c = 0.243$ and above $\omega\alpha / 2\pi c = 0.255$ for sample thicknesses of N >10 unit cells. This behavior originates in the absorptive behavior of the material, which strongly suppresses the Fabry-Perot oscillations that could be observed for absorption-free systems. Therefore, in these frequency ranges, the exponential could be fitted to the computed data with N>10. However, for frequencies in between, this damping out of the Fabry-Perot oscillations is less effective and the reflectance approaches saturation only for sample thicknesses of N>20 unit cells. As a consequence, the exponential fit should only be carried out for the corresponding range of N>20. In order to be consistent, we have computed the total attenuation length for all frequencies by fitting to the data for N>20. In addition, we have checked that in those cases for which we could fit to larger data sets, no discrepancies occur.

7.5 Results

We now apply the computational methods described in Sec. 7.3 to our model problem in Sec. 7.2. First, the extended band structure approach (Sec. 7.3 B) will be used to derive a physical interpretation of the results. This will be followed by a fully quantitative analysis through the Wannier function technique (Sec. 7.3 A) and the scattering-matrix method (Sec. 7.3 C). The latter also allows one to assess the feasibility of corresponding experiments. We have chosen the parameters of our model system such that the resonance of the pore dielectric constant [Eq. (7.2)] lies inside the photonic band gap of the undoped system, close to the upper band edge of the first band gap (see Figs. 7.2 and 7.3). This choice has been guided by the fact that the Bloch modes associated with the second band near the X point have a significant part of the field inside the pores. Therefore, these modes are rather sensitive to any modification of the pore properties. For the time being, we disregard the imaginary part in thepore dielectric constant and apply the extended band structure method to the problem with a quantum-dot concentration η=0.03. The resulting band structure is depicted in Fig. 7.9 and shows a significant splitting of the second band into one continuous band and a bubblelike structure of finite extent in wave-vector space located partly inside the photonic band gap of the undoped reference system. Despite the fact that these frequencies appear inside the photonic band gap of the undoped system, the associated modes represent—in the present case of ignored material absorption—bona fide extended Bloch modes, as they do obey the Bloch-Floquet theorem. The occurrence of this bubblelike structure is a direct consequence of the anomalous dispersion over a finite frequency range provided by the "energy-dependent" potential $\varepsilon_{pc}(\omega,\vec{r})$ which directly translates into both a finite extent in frequency and wave vector of the bubble. To the best of our knowledge, this does not have an analogy in electronic crystals, although a potential function with a nonmonotonic variation in energy would allow a similar effect to occur. Furthermore, the geometric interpretationof this effect in terms of a fix-point problem (Sec. 7.3 B) suggests that the effect can equally well be realized for TE-polarized radiation in 2D PCs as well as in onedimensional and 3D PCs. While these results of the extended band structure method provide a physical understanding of the interplay of anomalous material dispersion and photonic band structures, they do not contain any information

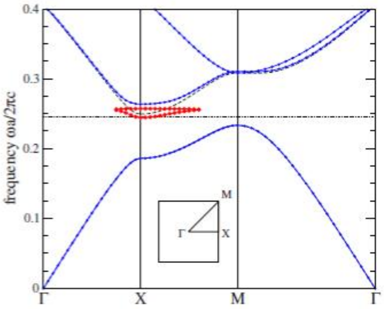

FIG. 7.9. (Color online) Photonic band structure for the model system with quantum-dot concentration η =0.03 and when material absorption is ignored (solid lines with symbols). The anomalous dispersion of the pore dielectric constant near the band edge of the second band leads to the formation of propagating modes (lines with diamonds) inside the photonic band gap of the undoped system. For reference, the photonic band structure of the undoped PC is indicated by dashed lines. The horizontal dotted line again depicts the resonance frequency of isolated quantum dots.

about the effect of the—by the Kramers-Kronig relations unavoidable—material absorption. In particular, it is not clear whether this effect could be observed for realistic experimental parameters. Therefore, we proceed to a complete analysis of the model system and discuss the frequency-dependent attenuation length. As alluded to in Sec. III, this may be facilitated both through the Wannier function method or the scatteringmatrix approach. In Fig. 7.10, we display and compare the results of all three methods applied to the model system with quantum-dot concentration $\eta = 0.03$ for wave vectors oriented along the crystallographic Γ-X direction. In the left panel of Fig. 7.10, we compare the real part of the wave vector's modulus of the Wannier function approach with the results of the extended band structure technique. Clearly, the extended band structure method cannot obtain a wave-vector solution for frequencies in the stop gap. For the frequencies of the propagating modes, the agreement is very good. Here, we would like to recall that, in contrast to the extended band structure method, the Wannier function approach fully includes material absorption. In the middle panel, we display the imaginary part of the wave vector's complex magnitude as obtained from the Wannier function method. In the undoped reference system, we would expect that this imaginary part is zero for frequencies in the bands, takes on small values for frequencies slightly inside the photonic stop band (weak attenuation) and, finally, takes on large values for frequencies near the center of the stop gap (strong attenuation). Material absorption would only modify the actual values but not the qualitative behavior. However, owing to the anomalous material dispersion, we find very low values of this imaginary part for frequencies near the bubble. Finally, in the right panel of Fig. 7.10, we convert these values into attenuation lengths and compare them with the results of corresponding scattering-matrix computations. Besides a very good agreement between the two methods, we find that the values of the attenuation length for

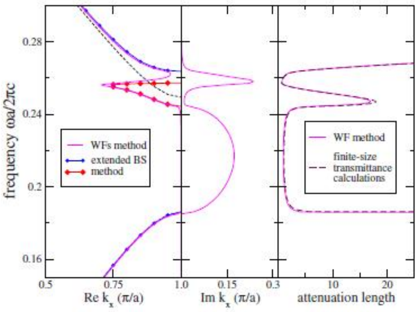

FIG. 7.10. Color online_ Band structure and attenuation length calculations for the model system with a quantum-dot concentration η =0.03. In the left panel, Wannier function (WF) calculations are compared to the extended band structure (extended BS) method. The Wannier function calculations yield both real and imaginary parts of the wave vector (middle panel). The latter can be converted into an attenuation length and can be compared with results from transmittance calculations through finite-sized PCs via the scattering-matrix method (right panel). The large values of the attenuation length for frequencies close to the bubble suggest that this effect can be observed experimentally.

frequencies near the bubble are in excess of ten lattice constants. This suggests that transmittance experiments on 2D macroporous silicon PCs [157] should be able to directly observe this (unique) signature of the bubble.

The shape of the bubblelike structure created inside the photonic band gap can be controlled through the parameters entering Eq. (7.2). For instance, different two-level systems with different resonance frequencies, oscillator strengths, and damping constants could be implanted into appropriate PC backbones. In these cases, considerations similar to our discussion above about the overlap of the targeted mode profile with the dopants' location would have to be carried out. In the experimental realization via colloidal quantum dots that we have envisaged, the easiest tuning parameter might be the concentration η of two-level systems. In Fig. 7.11, we depict the evolution of the bubblelike structure and the attenuation length of the corresponding modes as the concentration η increases. The extension of the bubble both in wave-vector space and in frequency is strongly modified.

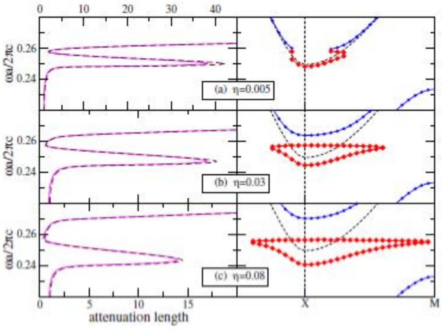

FIG. 7.11. (Color online) Right panel: evolution of the bubble (lines with diamonds) when the concentration η of quantum dots in the model system is increased. The dashed lines depict the band structure of the undoped PC. Left panel: Wannier function (solid lines) and scattering-matrix (dashed lines) calculations of the corresponding attenuation lengths.

Higher concentrations η allow a larger wave-vector and frequency range to be covered. Furthermore, these results suggest an alternative interpretation of the bubble formation. Starting from a very low concentration of quantum dots, we observe the onset of a "pinch-off" effect near the band edge. For higher concentration, the bubble is completely separated (completely pinched off) from the original band edge so that, effectively, a stop band is formed. Whether or not this stop band turns into a complete photonic band gap depends on the other regions of wave-vector space, which are less affected by the anomalous dispersion. This stop band is, however, somewhat ill defined. This stems from the fact that the top portion of the bubble, i.e., the flat part of the dispersion relation, corresponds to the unstable branch of the anomalous dispersion and, therefore, exhibits rather large values of the imaginary part of the wave vector. It thus becomes problematic to identify the lower frequency edge of the stop band. In addition, for other materials that exhibit a two-level resonance structure in their dielectric behavior such as systems for which interband transitions are of importance, there does not exist a simple analog to the change of quantum-dot concentration. Therefore, we prefer the first interpretation that anomalous dispersion may lead to additional propagating modes inside the photonic band gap of the undoped system. At any rate, the resulting tunability of the wave vector and frequency extent of the bubble structure may be beneficial for efficient realizations of superprism effects and other super-refractive phenomena [180].Specifically, it might be advantageous to avoid unwanted diffraction effects by limiting the available wave vectors, while simultaneously allowing only narrow frequency bands to couple into the PC. Equally well, one might conceive a modulator via tunable attenuation.

7.6 Summary

We have investigated photonic band structures for PCs whose constituent materials exhibit anomalous dispersion. In such systems, anomalous dispersion leads to the occurrence of unconventional propagating modes in the gap. The solution of the corresponding nonlinear eigenvalue problem through an iterative approach allows a simple geometric interpretation of the fact that the limited frequency range over which anomalous dispersion occurs confines these additional modes to a limited wave-vector range in the band diagrams. For the calculation of attenuation lengths associated with these modes, we have developed an efficient on-shell methodology based on photonic Wannier functions. The results of this approach agree very well with those from corresponding transmittance computations and suggest that these modes should be experimentally observable. PCs that exhibit such effects may be realized by infiltrating colloidal quantum dots in a polymer suspension suitably engineered into macroporous silicon PC structures. This technique has been demonstrated [158,159]. The resulting tunability of PC structures with dispersive components may lead to an enhanced flexibility in tailoring photonic dispersion relations and associated phenomenasuch as super-refractive effects.

8 RADIATIVE TRANSFER IN 1D AND CONNECTUIN TO THE O'DOHERTY-ANSTEY FORMULA

There is a growing interest in incorporating multiply scattered waves into modeling the Earth's interior using radiative transfer. We examine radiative transfer in a layered medium with general scattering and directional properties of the source. This allows us to demonstrate in detail the nature of energy propagation in the presence of strong scattering. At its most basic level, radiative transfer predicts that, after a distance known as the mean free path, the wavefield breaks into a coherent, or wave-like part and an incoherent, or diffusive flow. The dynamic properties of both aspects are linked.

For 1D point scatterers, or thin beds, we derive the equivalence of the exponential decay of the transmitted wave predicted by the O'Doherty-Anstey formula with the coherent, or direct, wave obtained from the radiative transfer equation. The equivalence shows an underlying relationship between mean field theory and radiative transfer.

Turning to the incoherent wave intensity, we make the well-known diffusion approximation to the late-time radiative transfer behavior. A finite-difference simulation of the wave equation with random scatterers corroborates the theoretical results for the incoherent energy.

8.1 Introduction

Radiative transfer has its origins in the kinetic theory of gases and is sometimes referred to as the Boltzmann transport equation in honor of its earliest proponent. In the earth sciences, it first appeared within the context of light propagation through the atmosphere [198]. Recently, geophysicists have begun to address the applicability of radiative transfer to multiply-scattered seismic waves [191, 188, 202].

By squaring a wavefield and averaging over many realizations of random disorder, the phase information of the underlying wavefield is, for the most part, lost. What remains is the average intensity, or squared am-plitude. Radiative transfer is a phenomenological theory for the spatial and temporal evolution of a wavefield's average intensity. The theory's strengths lie in the abil-ity to provide statistical information about the structure of a medium at scales less than a wavelength and the description of the decoupling of scattering and absorption effects for incoherent wave energy.

Here, we give the complete solution of the radia-tive transfer equation in one dimension (1D) for general directional sources and general scattering. Such generality is relevant for plane wave propagation in layered media, and recently became important for describing physical experiments of surface wave propagation through 1D disordered grooves with a directional source [202]. We derive results from radiative transfer that agree with results from mean field theory, namely the O'Doherty-Anstey formula. Such an equiva-lence suggests that radiative transfer is a proper exten-sion of mean field theory (a "variance field" theory) for the fluctuating, multiply-scattered waves.

At late times, we demonstrate that radiative trans-fer can be simplified even further by approximating its behavior as the solution to a diffusion equation. Results of finite-difference simulations of the 1D wave equation with random scatterers are presented to support the accuracy of this approximation. Using correct values for the parameters needed to describe the scattering, the average intensity of the numerical simulations is seen to approach the diffusive limit with time.

8.2 The radiative transfer equation

The radiative transfer equation can be derived from energy balance considerations [194, 192, 201]. Heuristically, the equation takes the form:

$$[\partial_t + \mathrm{v} \bullet \nabla]\, \mathit{Intensity} = \mathit{source} - \mathit{loss} + \mathit{gain}. \tag{8.1}$$

The left-hand side of equation (8.1) is the total time derivative of the intensity. On the right-hand side, loss and gain mechanisms in addition to sources determine the dynamic behavior. In the absence of loss or gain, this equation becomes the advection, or one-way wave, equation. Scattering and absorption show up as loss mech anisms since both remove energy from the forward di rection. Only scattering can put energy back into the original direction of propagation. Hence, scattering and absorption enter equation (8.1) in fundamentally differ ent ways. This fact leads to the ability to separate their effects within radiative transfer theory.

Using the same form as equation (8.1), here is a general radiative transfer equation valid for any dimension:

$$\begin{aligned}&\frac{\partial I(\vec{r},\Omega,t)}{\partial t} + v\hat{n}(\Omega)\cdot\nabla I(\vec{r},\Omega,t) = S(\vec{r},\Omega,t) - \frac{1}{\tau_n} I(\vec{r},\Omega,t) - \frac{1}{\tau_a} I(\vec{r},\Omega,t) - \\ &\frac{1}{\tau_S}\int \frac{1}{\sigma_S}\frac{\partial\sigma_s}{\partial\Omega'} I(\vec{r},\Omega',t)\,d\Omega'\end{aligned} \tag{8.2}$$

where $I(r, \Omega, t)$ is the intensity, or average squared wavefield, at position r propagating in direction Ω, v is the group velocity of the average (coherent) wavefield, $n^{\wedge}$ is the unit vector in the direction of propagation, and $S(r, \Omega, t)$ is the angle-resolved source function. The differential scattering cross section, $\partial\sigma s/\partial\Omega'$, describes the exchange of energy traveling from direction Ω into direction Ω'. The characteristic time between these exchanges is τ_s, the scattering mean free time. The total scattering cross section, σ_s, is the energy exchanged into all directions:

$$\sigma_s = \int \frac{\partial \sigma_s}{\partial \Omega'} d\Omega' \tag{8.3}$$

We have allowed for attenuation by including the char-acteristic absorption time τ_a.

Using terminology originally coined by Clausius in 1858, it is common to define mean free paths for scattering and absorption, l_s and l_a, according to the relations $l_s = v\tau_s$ and $l_{s=}$ $_{v\tau a.}$ The scattering mean free path, l_s, can be thought of as the typical distance a wave travels between scatterings. Under most circumstances, l_s is inversely proportional to the number density of scatterers, ρ, and their scattering cross section:

$$\ell_S = \frac{1}{\rho\sigma_S} \tag{8.4}$$

This equation is called the independent scattering approximation (ISA) and it holds when the scatterers are separated by more than a wavelength. It can be obtained from a stationary phase argument applied to the average wavefield in random media [192]. From equation (8.4), ℓ_S contains information about the product of ρ and σ_s in a way analogous to a wave reflected from an interface containing information about the acoustic impedance.

8.3 Radiative transfer in 1D

Since in 1D only two directions of propagation exist, a general expression for the differential scattering cross section, appearing under the integral in equation (8.2), is:

$$\frac{\partial \sigma_S(\Omega, \Omega')}{\partial \Omega'} = E_f \delta(\Omega' - \Omega) + E_b \delta(\Omega' - \Omega - 180^\circ), \tag{8.5}$$

where E_b and E_f represent amounts of energy back scattered and forward-scattered divided by the energy of the incident wave. Their sum is equal to the total scattering cross section:

$$\sigma_S = E_b + E_f \tag{8.6}$$

Hence, in equation (8.2), the differential scattering cross section divided by the total scattering cross section becomes:

$$\frac{1}{\sigma_S}\frac{\partial\sigma_S(\Omega,\Omega')}{\partial\Omega'}=\frac{E_f}{E_b+E_f}\delta(\Omega'-\Omega)+\frac{E_b}{E_b+E_f}\delta(\Omega'-\Omega-180^\circ) \qquad (8.7)$$

For the rest of this paper, we denote the ratios $E_f/(E_b+E_f)$ and $E_b/(E_b+E_f)$ by F and B respectively. These ratios satisfy $B + F = 1$. In the case of isotropic scattering, $B = F = 1/2$ [196].

For a general 1D scatterer, B and F can be related to the total transmission and reflection coefficients of a thin bed, T_t and R_t [202]

$$\begin{aligned} B &= \frac{|R_t|^2}{|R_t|^2+|T_t-1|^2} \\ F &= \frac{|T_t-1|^2}{|R_t|^2+|T_t-1|^2} \end{aligned} \qquad (8.9)$$

Note that a thin bed consists of two interfaces, and hence R_t and T_t are not simple reflection and transmission coefficients. The quantities R_t and T_t can be related to a geometric summation of the interface reflection and transmission coefficients via generalized rays [182].

Inserting equation (8.7) into equation (8.2), we obtain:

$$\begin{aligned} &\frac{\partial I(x,\Omega,t)}{\partial t}+u\hat{n}(\Omega)\frac{\partial I(x,\Omega,t)}{\partial x}=S(x,\Omega,t)-\frac{1}{\tau_S}I(x,\Omega,t)-\frac{1}{\tau_a}I(x,\Omega,t)+ \\ &\frac{1}{\tau_S}\int\left[F\delta(\Omega'-\Omega)+B\delta(\Omega'-\Omega-180^\circ)\right]I(\vec{r},\Omega',t)d\Omega' \\ &=\frac{B}{\tau_S}I(x,\Omega+180^\circ,t)-\frac{B}{\tau_S}I(x,\Omega,t)-\frac{1}{\tau_a}I(x,\Omega,t)+S(x,\Omega,t), \end{aligned} \qquad (8.9)$$

where we have used the fact that $B + F = 1$. Equation (8.9) can be evaluated for the two possible directions in 1D, $\Omega = 0^\circ$ or 180°. In this paper, we will referto these directions as right and left, respectively. For simplicity, the total intensity propagating in direction $\Omega = 0^\circ$, $I(r, 0^\circ, t)$, will be represented by I_r, $I(r, 180^\circ, t)$ will be I_l, and the source function will be split into S_r and S_l. The coordinate system is defined such that $\hat{n}(0^\circ) = 1$ and $\hat{n}(180^\circ) = -1$. The two equations that describe the propagation of right-going and left-going intensities are:

$$\frac{\partial I_r}{\partial t}+u\frac{\partial I_r}{\partial x}=\frac{B}{\tau_S}(I_l-I_r)-\frac{I_r}{\tau_a}+S_r \qquad (8.10)$$

$$\frac{\partial I_l}{\partial t}-u\frac{\partial I_l}{\partial x}=\frac{B}{\tau_S}(I_r-I_l)-\frac{I_l}{\tau_a}+S_l \qquad (8.11)$$

This system of partial differential equations comprises radiative transfer in 1D and has been derived by other methods [189]. In Appendix A, the system of partial differential equations is solved for both I_r and I_l. For now, we solve for the total intensity, $I_t = I_r + I_l$, since this is commonly measured in practice.

Two new quantities emerge from adding and sub-tracting equations (8.10) and (8.11). In addition to the total intensity, I_t, the net right-going intensity, $I_n = I_r - I_l$, appears. Similarly, the source function can be expressed as its total and net right-going components: $S_t = S_r + S_l$ and $S_n = S_r - S_l$. The result of adding equations (8.10) and (8.11) is:

$$\frac{\partial I_t}{\partial t} + u\frac{\partial I_n}{\partial x} = -\frac{I_t}{\tau_a} + S_t, \tag{8.12}$$

Subtracting equations (8.10) and (8.11) yields:

$$\frac{\partial I_n}{\partial t} + u\frac{\partial It}{\partial x} = -\frac{2B}{\tau_S} I_n - \frac{I_r}{\tau_a} + S_n \tag{8.13}$$

From these two equations, we derive a single partial differential equation in terms of what we measure, I_t, by taking the spatial derivative of equation (8.13):

$$\frac{\partial}{\partial t}\frac{\partial I_n}{\partial x} + u\frac{\partial^2 I_t}{\partial x^2} = \left[-\frac{2B}{\tau_S} - \frac{1}{\tau_a}\right]\frac{\partial I_n}{\partial x} + \frac{\partial S_n}{\partial x} \tag{8.14}$$

But we know from equation (8.12) that:

$$\frac{\partial I_n}{\partial x} = \frac{1}{u}\left[-\frac{I_t}{\tau_a} - \frac{\partial I_t}{\partial t} + S_t\right] \tag{8.15}$$

Substituting equation (8.15) into equation (8.14) yields a single partial differential equation in I_t. Omitting some algebraic manipulation, we obtain:

$$\begin{aligned} \frac{\partial^2 I_t}{\partial x^2} = \frac{1}{v^2}\frac{\partial^2 I_t}{\partial t^2} + \left[\frac{2B}{v\ell_S} + \frac{2}{v\ell_a}\right]\frac{\partial I_t}{\partial t} + \frac{1}{\ell_a}\left[\frac{2B}{\ell_S} + \frac{1}{\ell_a}\right] I_t - \\ \left[\frac{2B}{v\ell_S} + \frac{1}{v\ell_a}\right] S_t - \frac{1}{v^2}\frac{\partial S_t}{\partial t} + \frac{1}{v}\frac{\partial S_n}{\partial x}, \end{aligned} \tag{8.16}$$

Equation (8.16) encapsulates a wealth of information. First of all, in the absence of a source, the scattering and attenuation show up in both the first and zeroth order time derivatives of the total intensity. For a medium with no scattering or attenuation, $\ell_S^{-1} = \ell_a^{-1} = 0$, we are left with the 1D wave equation.

Also, in order to solve for the Green's function of the total intensity, we cannot simply insert a δ-source into the homogeneous form of equation (8.16). Instead, a more complicated combination of the source and its time and spatial derivatives must be inserted.

8.4 The green's function of the total intensity

To solve for the Green's function of the total intensity, we find the Green's function of the homogeneous form of equation (8.16) and construct the total intensity Green's function from it. First, take an impulsive total source function:

$$S_t = \delta(x)\delta(t), \tag{8.17}$$

and a general form for its net right-going component:

$$S_n = cS_{t,} \tag{8.18}$$

where $c \in [-1,1]$. The parameter c allows the radiation pattern of the impulsive source function to directionally vary from left-going ($c = -1$), to isotropic ($c = 0$), to right-going ($c = 1$), and to any combination in between.

After inserting this source into equation (8.16), we find that the "effective source", denoted S_e, is a combination of a δ-function in time, its time derivative, and its x-derivative:

$$S_e = \left[\frac{2B}{v\ell_S} + \frac{1}{v\ell_a}\right]\delta(x)\delta(t) + \frac{1}{v^2}\delta(x)\delta'(t) - \frac{c}{v}\delta'(x)\delta(t.) \tag{8.19}$$

This effective source can be constructed from the knowledge of the Green's function, P of the homogeneous form of equation (8.16):

$$\frac{\partial^2 P}{\partial x^2} = \frac{1}{v^2}\frac{\partial^2 P}{\partial t^2} + \left[\frac{2B}{v\ell_S} + \frac{1}{v\ell_a}\right]\frac{\partial P}{\partial t} + \frac{1}{\ell_a}\left[\frac{2B}{\ell_S} + \frac{1}{\ell_a}\right]P - \delta(x)\delta(t) \tag{8.20}$$

Note that P is not the Green's function for the total intensity. This equation is a variation of the telegraph equation, there being a zeroth order derivative appear-ing due to the presence of attenuation. In Morse and Feshbach (1953), the Green's function of the telegraph equation is solved via a spatial Fourier transform and a Laplace transform over time. Applying the same tech-nique, the Green's function of equation (8.20) can be read-ily obtained by generalizing the solution stated in Morse and Feshbach (1953):

$$P(x,t)=\frac{v}{2}\exp\left(-Bvt/\ell_s-vt/\ell_a\right)\times J_0\left(\frac{B}{\ell_S}\sqrt{x^2-v^2t^2}\right)u\left(ut-|x|\right) \tag{8.21}$$

where $u(vt - |x|)$ is the unit step-function, guaranteeing causality. This Green's function only differs from the one for the telegraph equation by the exponential damping factor due to attenuation. The Green's function for the total intensity, denoted I_t, can be expressed in terms of the above Green's function through equation (8.19):

$$I_t=\left[\frac{2B}{v\ell_S}+\frac{1}{v\ell_a}\right]P+\frac{1}{v^2}\frac{\partial P}{\partial t}-\frac{c}{v}\frac{\partial P}{\partial x} \tag{8.22}$$

Taking the necessary derivatives of P , we obtain for $B \in [0, 1]$ and $c \in [-1, 1]$:

$$\begin{gathered}I_t(x,t)=\frac{1}{2}\exp\left(-Bvt/\ell_S-vt/\ell_a\right)\times\\ \left[\begin{array}{l}(1-c)\delta(vt+x)+(1+c)\delta(vt-x)+\\ \frac{B}{\ell_S}u\left(ut-|x|\right)\left[I_0\left(\frac{B}{\ell_S}\sqrt{v^2t^2-x^2}\right)+\frac{vt+cx}{\sqrt{v^2t^2-x^2}}I\left(\frac{B}{\ell_S}\sqrt{v^2t^2-x^2}\right)_1\right]\end{array}\right]\end{gathered} \tag{8.23}$$

where I_0 and I_1 are the modified Bessel functions of the zeroth and first orders. These should not be confused with the symbols used for the various intensities (I_t, I_r, I_l, and In). A previous result by Hemmer (1961) is obtained from equation (8.23) for the case of an isotropic source ($c = 0$) and isotropic scattering, $B=1/2$.

The Green's function for the total intensity can be broken up into two parts. The term with the δ-function propagates like a wave and is called the *coherent* intensity. The rest of the total intensity is referred to as the *incoherent* intensity. It does not propagate ballistically, and, in later sections of this paper, we show that at late times it propagates diffusively. Also, in Appendix A we show that each Bessel function represents a different direction of propagation for the incoherent energy.

An interesting result in equation (8.23) is that the decay of coherent intensity due to scattering, described by the first exponential term, goes with distance by the factor l_s/B and not l_s. This new length scale, determining the decay of the coherent energy, is called the extinction mean free path, l_{ext}. The fact that $l_{ext} \neq l_s$ is unique to 1D [196].

8.5 The coherent intensity and the O'Doherty - Anstey formula

In the field of exploration geophysics, a well known result for waves multiply scattered by a 1D layering is that obtained by O'Doherty and Anstey [195]. The O'Doherty-Anstey formula has subsequently been derived from mean field theory [183]. One outcome of O'Doherty-Anstey is that the amplitude of a wave transmitted through a stack of layers decays exponentially with distance as [199] :

$$|T| \sim \exp\left(-\tilde{R}(k)x\right) \tag{8.24}$$

where $\tilde{R}(k)$ represents the power spectrum of the average reflection coefficient series normalized by two-way travel distance [183]. From the solution for the total intensity obtained in the last section, equation (8.23), radiative transfer also predicts an exponential decay for the transmitted, or coherent, wave with distance:

$$|T| \sim \exp\left(-\tilde{B}x/2\ell_S\right) \tag{8.25}$$

where the distance x has replaced vt in equation (8.23) since the δ-function is only non-zero at $x = vt$ The factor of 1/2 in the exponent of this equation shows up since radiative transfer predicts decay of the transmitted intensity - the square of the true transmission oefficient. We investigate the equivalence of these two theories for the transmission of normally incident waves through assemblages of weak 1D point scatterers (thin beds). The two theories are equivalent if:

$$\tilde{R}(k) = B/2\ell_S \tag{8.26}$$

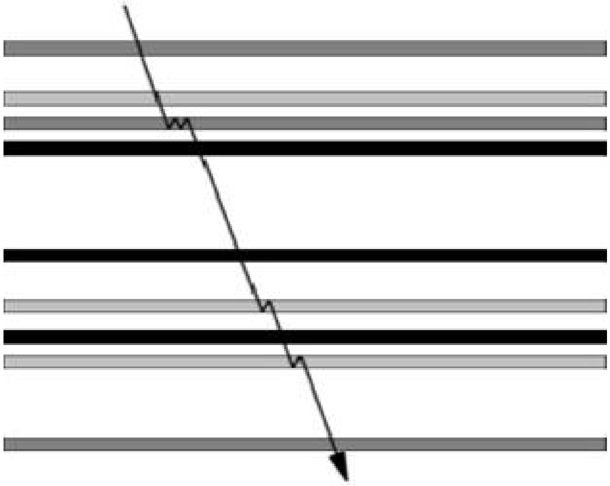

Fig. 8.1. A wave transmitted through a random sequence of thin beds of varying strength. The thin beds are embedded in a constant background medium.

Depicted in Fig. 8.1 is the random medium we will consider: a series of thin layers of varying strength are embedded in a constant velocity background medium. In the parlance of O'Doherty-Anstey, this would be called a "cyclic" sequence. It happens to be the type of medium that radiative transfer, and scattering theory, are geared for. The reflection coefficient series, *RC(x),* for such a medium would be a series of delta functions of oscillating plus and minus sign:

$$RC(x)=\sum_{j=1}^{N} R_j\left[\delta\left(x-d_j\right)-\delta\left(x-h-d_j\right)\right] \tag{8.27}$$

where *h* is the thickness of the beds, R_j and d_j represent the reflection coefficient and location of the *j*-th bed, respectively, and *N* is the number of beds.

To calculate *R(k)*, we take the Fourier transform of equation (8.26), square its magnitude to get the power spectrum, and divide by the two-way travel distance:

$$\tilde{R}(k)=\frac{\left|\int_{-\infty}^{\infty} RC(x)e^{-i2kx}dx\right|^2}{2L} \tag{8.28}$$

Note that the Fourier transform is with respect to *2k* and not *k*, similar to a Born inversion formula in 1D [184]. This is evident from standard references in the literature [183, 199].

Inserting equation (8.27) into equation (8.28) results in:

$$\tilde{R}(k)=\frac{1}{2L}\left|\sum_{j=1}^{N} R_j e^{i2kd_j}(1-e^{i2kh})\right|^2 \tag{8.29}$$

For thin layers, *kh* << 1 and a first order Taylor series expansion in h leads to $1-e^{2ikh}\approx -2ikh$. Pulling it out of the summation yields:

$$\tilde{R}(k)=\frac{1}{2L}4k^2h^2\left|\sum_{j=1}^{N} R_j e^{i2kd_j}\right|^2 \tag{8.30}$$

We now use a standard argument from the theory of multiple scattering: if d_j , the spacing of the thin beds, is a random variable, the cross terms in the square of the summation in equation (8.30) cancel in the *average* and the squaring can be brought inside the summation:

$$\tilde{R}(k)=\frac{1}{2L}4k^2h^2\sum_{j=1}^{N}\left|R_j e^{i2kd_j}\right|^2 \tag{8.31}$$

Now, inside the summation, the exponential does not contribute to the magnitude and we are left with:

$$\tilde{R}(k) = \frac{1}{2L}4k^2h^2\sum_{j=1}^{N}\left|R_j\right|^2 = \frac{1}{L}2k^2h^2N\left\langle\left|R_j\right|^2\right\rangle \tag{8.32}$$

where $\left\langle\left|R_j\right|^2\right\rangle$ is the mean-square of the interface reflection coefficients.

Returning to equation (8.26), to prove that radiative transfer and the O'Doherty-Anstey formula predict the same exponential decay for the transmitted wave, we (8.28) set equation (8.32) to:

$$\frac{B}{2\ell_S} = \frac{1}{L}2k^2h^2N\left\langle\left|R_j{}^2\right|\right\rangle \tag{8.33}$$

For (Rayleigh) point scatterers in 1D, the radiation is isotropic. Hence, B = 1/2. Rearranging equation (8.33):

$$\ell_S = \frac{1}{8k^2h^2\left\langle\left|R_j{}^2\right|\right\rangle\frac{N}{L}} \tag{8.34}$$

The quantity *N/L* is simply the number density of the thin beds, ρ. In the limit of weak scatterers (such that $R_j << 1$) $8k^2h^2\left\langle\left|R_j\right|^2\right\rangle = \sigma_s$, the scattering cross section [200]. The presence of weak reflection coefficients is an underlying assumption in the O'Doherty-Anstey result [183], so that equation (8.34) can now be rewritten in a familiar form:

$$\ell_S = \frac{1}{\rho\delta_S} \tag{8.35}$$

This is recognized as equation (8.4), the independent scattering approximation. Previously, we stated that for this relation to hold, the scatterers (thin beds) had to be separated by at least a wavelength. Hence, in this model, no reflections from below the recording depth interfere with the transmitted wave. All the interference resulting in the exponential decay of the direct wave originates from peg-leg multiples within the thin beds, not between them (Fig. 8.1). Equation (8.35) demonstrates that, for this model, the exponential decay of the transmitted wave from O'Doherty-Anstey, or mean-field theory, is equivalent to that predicted by radiative transfer.

A conceptual diagram of this equivalence is shown in Fig. 8.2. From mean field theory, both the phase and the amplitude of the transmitted wave can be obtained; however, the incoherent energy, for which the mean is zero, falls out.

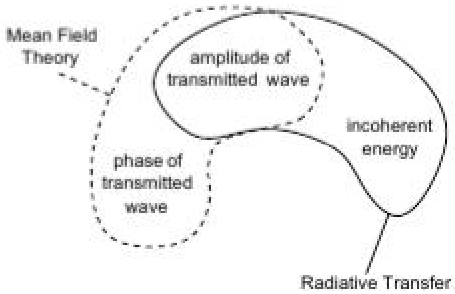

Figure 8.2. A diagram representing the overlap of mean field theory and radiative transfer for the amplitude of the trans-mitted wave through a medium like that depicted in Fig. 8.1.

Similarly, 1D radiative transfer can address the amplitude of the transmitted wave and the behavior of the incoherent intensity, but phase information is lost. Both theories agree in their region of overlap, as demonstrated by the case of random layering we considered here.

8.6 The diffusion approximation in unfinite 1D media

In addition to the coherent intensity, physical insight can be gained on the incoherent part of the total intensity. The general expression for the Green's function for radiative transfer in 1D, equation (8.23), shows that for late times the coherent term is zero and the incoherent field, defined by a combination of Bessel functions, approximates the solution to the diffusion equation [192]. Especially in optics, where it is hard to obtain phase information, inferences on the statistical properties of the medium are often based on this late-time diffusive behavior [184]. In elastic wave-scattering, the incoherent field is used to decipher the different mechanisms of attenuation [193]. To derive the diffusion approximation from equation (8.23), all we need is that *vt* >> *x*. Noting that the zeroth and first modified Bessel functions have the asymptotic forms:

$$I_0(z) \approx I_1(z) \approx (2\pi z)^{-\frac{1}{2}} \exp(z) \qquad \textit{for } z >> 1 \tag{8.36}$$

we can write equation (8.23) in the late-time limit as:

$$I_t(x,t) = \exp(-Bvt/\ell_S - vt/\ell_a) \times \frac{B}{\ell_S}\left[\frac{\exp\left(\frac{B}{\ell_S}\sqrt{v^2t^2 - x^2}\right)}{\sqrt{2\pi\frac{B}{\ell_S}\sqrt{v^2t^2 - x^2}}}\right] \tag{8.37}$$

In this expression, the delta functions from equation (8.23) have fallen out.

Organizing terms in equation (8.37), expanding the square root in the exponential as a Taylor series in the small parameter *x/vt*, and keeping the lowest order in *x/vt*, we get:

$$I_t(x,t) = \exp\left(-Bvt/\ell_s - vt/\ell_a\right)\frac{\exp\left(\dfrac{Bvt}{\ell_a}\left(1-\dfrac{1}{2}\left(x/vt\right)^2\right)\right)}{\sqrt{2\pi\dfrac{\ell_S}{B}vt}} \tag{8.38}$$

Two of the exponentials cancel in equation (8.38) and, after isolating the term $\ell_i = B$, the late-time limit of the radiative transfer equation can finally be written:

$$I_t(x,t) = \frac{\exp\left(-\dfrac{x^2}{4\left(\dfrac{\ell_S}{2B}\right)vt} - \dfrac{vt}{\ell_a}\right)}{\sqrt{4\pi\left(\dfrac{\ell_S}{2B}\right)vt}} \tag{8.39}$$

In the case of no attenuation $\left(\ell_a \to \infty\right)$, equation (8.39) can be identified as the Green's function for the 1D diffusion equation with the diffusion constant $D = \left(\ell_s/2B\right)v$. This implies that the movement of energy at late times has an effective mean free path different from ℓ_s or ℓ_{ext}. This effective mean free path is called the *transport* mean free path, $\ell_{tr} = \ell_s/2B$. In 1D, $\ell_{tr} = \frac{1}{2}\ell_{ext}$, since $\ell_{ext} = \ell_s/B$. Note that the transport mean free path can be determined from the extinction mean free path without knowledge of the underlying details of the scattering.

It is common to relate ℓ_{tr} to ℓ_s via:

$$\ell_{tr} = \frac{\ell_S}{1-\langle\cos\theta\rangle} \tag{8.40}$$

where $\langle\cos\theta\rangle$ represents the average scattered energy in all directions weighted by the cosine of that direction. For isotropic scattering, $\langle\cos\theta\rangle$=0 and the two mean free paths are identical. However, using the general relation $\langle\cos\theta\rangle$=F-B [191] and the fact that $F + B = 1$, equation (40) can be rewritten:

$$\ell_{tr} = \frac{\ell_S}{1-F+B} = \frac{\ell_S}{2B} \tag{8.41}$$

which is exactly the relationship we have derived from the diffusion approximation.

8.7 The diffusion appromaximation in finite 1D media

The above derivation of the diffusion approximation showed how the solution of the radiative transfer equation approaches that of the diffusion equation at late times. In this section, we prove that the underlying governing equation for the total intensity at late times also becomes the diffusion equation. While the radiative transfer equation cannot be analytically solved for in a finite geometry, its late time equivalent - the diffusion equation - can be solved with boundary conditions.

Neglecting absorption $(\ell_a \to \infty)$, we can rearrange equation (8.13) as:

$$\frac{\partial I_n}{\partial t} + \frac{2B}{\tau_S} I_n = -v \frac{\partial I_t}{\partial x} \tag{8.42}$$

In the diffusive regime, we assume that [194]:

$$\frac{2B}{\tau_S} I_n >> \frac{\partial I_n}{\partial t} \tag{8.43}$$

meaning that the time rate of change of the right and left-going intensities is relatively small. Under this condition, equation (8.42) becomes:

$$\frac{2B}{\tau_S} I_n = -v \frac{\partial I_t}{\partial x} \tag{8.44}$$

Substituting equation (8.44) into equation (8.12) for I_n yields:

$$\frac{\partial I_t}{\partial t} + v \frac{\partial}{\partial x}\left[-\frac{\tau_s v}{2B} \frac{\partial I_t}{\partial x} \right] = 0 \tag{8.45}$$

Under the assumption that v and τs do not depend on position, equation (8.45) takes the form:

$$\frac{\partial I_t}{\partial t} = v\left(\frac{\ell_s}{2B} \right) \frac{\partial^2 I_t}{\partial x^2} \tag{8.46}$$

which we recognize as the 1D diffusion equation with the same diffusion constant $D = v\left(\frac{\ell_s}{2B} \right) = v\ell_{tr}$ we obtained in the previous section.

Now assume there is a boundary at x = 0 where scattering occurs to the right (positive values of x), but not to the left (negative values of x). Then, at x = 0, there is no intensity coming into the scattering region, i.e. the right-going intensity is zero. We can express the right-going intensity as the sum of the total intensity and the net right-going intensity (flux) and set it to zero at $x = 0$:

$$I_r = \frac{1}{2} I_t + \frac{1}{2} I_n = 0 \qquad at\, x{=}0 \tag{8.47}$$

Using the approximation we derived in equation (8.44), the In-term can be replaced by a spatial derivative of I_t:

$$\frac{1}{2} I_t + \frac{1}{2}\left(-\frac{\ell_S}{2B}\frac{\partial I_t}{\partial x} \right) = 0 \tag{8.48}$$

From this equation, we learn that:

$$I_t = \frac{\ell_S}{2B}\frac{\partial I_t}{\partial x} = \ell_{tr}\frac{\partial I_t}{\partial x} \tag{8.49}$$

The solution to equation (8.49) states that, near $x = 0$, I_t has the form:

$$I_t \sim x + \ell_{tr} \tag{8.50}$$

Extrapolating away from the boundary according to equation (8.50), $I_t=0$ *at* $x = -\ell_{tr}$. Hence, the presence of a boundary that radiates energy out of a finite scattering region can be approximated by a Dirichlet boundary condition a distance ℓ_{tr} *outside* the scattering region.

Suppose there is a region of length L extending from $x = 0$ to $x = L$. Then, at late times, the Green's function for the total intensity should obey the boundary value problem:

$$\frac{\partial I_t}{\partial t} = D\frac{\partial^2 I_t}{\partial x^2} + \partial(x - x')\delta(t)$$

$$I_t = 0 \quad at \quad x = -\ell_{tr} \quad and \qquad x = \ell_{tr} + L \tag{8.51}$$

where $D = v\ell_{tr}$. In 1D, this PDE can be solved by expanding over the modes of the Laplacian:

$$I_t(x, x', t) = \sum_{m=1}^{\infty} \exp\left(-\frac{m^2\pi^2 Dt}{(L + 2\ell_{tr})^2} \right) \times \sin\left(\frac{m\pi(x + \ell_{tr})}{L + 2\ell_{tr}} \right) \sin\left(\frac{m\pi(x' + \ell_{tr})}{L + 2\ell_{tr}} \right) \tag{8.52}$$

The PDE could have equivalently been solved by the method of images.

8.8 Numerical simulations

These late-time solutions of the total intensity have been tested with finite-difference simulations of the wave equation in the presence of random discrete scatterers. The setup of the numerical experiment is shown in Fig. 8.3. A source S is excited in the center of a finite 1D random medium, of size L, containing identical low velocity (1 km/s) thin beds. By "thin" in this experiment, we mean that their thickness is approximately one-tenth of the dominant wavelength. The background medium in which they are embedded has a velocity of 2 km/s. A receiver *R* is placed just outside the scattering region. The experiment is repeated for L = 80m, 120m, 160m, 200m, and 240m.

The number of scatterers per unit length is constant for each size of the scattering region and the number of scatterers per dominant wavelength is 2. All interfaces are numerically put into welded contact [186] and there is no intrinsic absorption ($\ell a \rightarrow \infty$). For each of the five sizes of the scattering region, the average intensity was obtained by performing the experiment for 20 realizations of the randomness, squaring each of the 20 wavefields, and adding them. Of course, in practice we only have one realization of the model, the Earth. By assuming the Earth to be ergodic at some scale, we can obtain ensemble averages from earthquake data, seismic exploration, or rock physics [198].

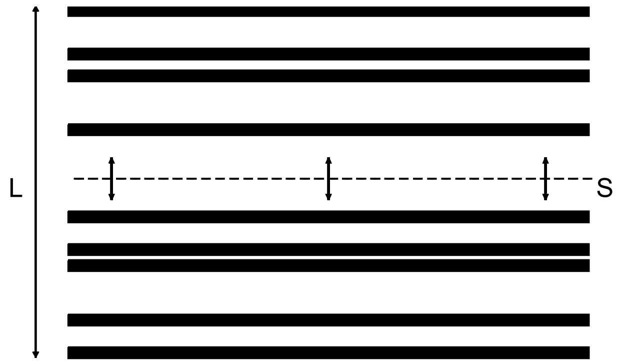

Fig. 8.3. The geometry of the 1D numerical scattering experiments. The source was at the center of a region with thin random layers and a receiver was positioned above the layers for each experiment. The size L of the scattering region varied between experiments with the values 80m, 120m, 160m, 200m, and 240m.

The results are plotted in Fig. 8.4. The average intensities contain a large direct wave traveling at nearly the background velocity (2 km/s). This is the coherent intensity. Following the coherent intensity is the incoherent multiply scattered energy. If, in the averaging process, the wavefields were added (stacked) before they were squared, the incoherent energy would cancel out and leave only the coherent intensity. From the moveout of the direct wave, we know that the group velocity entering the radiative transfer equation, v, is the background velocity (2 km/s).

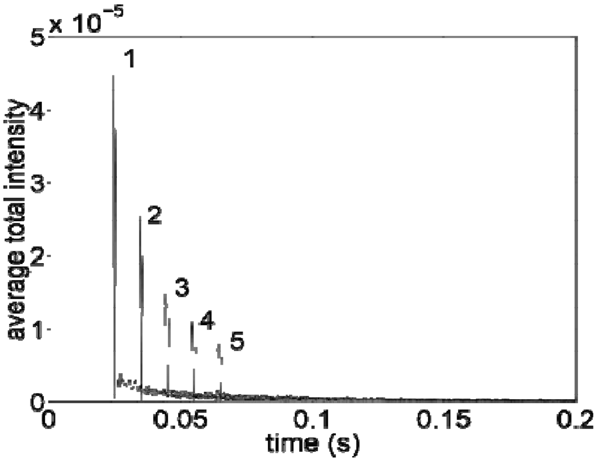

Fig. 8.4 The average intensity measured as a function of time for the 5 experiments. Note how the direct wave decays due to the scattering with offset.

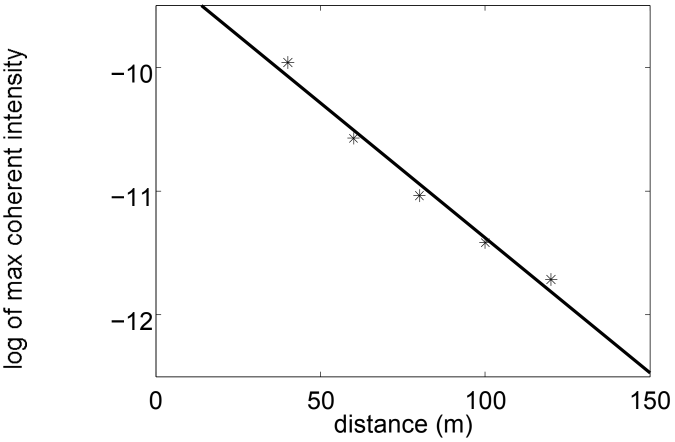

Fig. 8.5. The maximum of the direct wave (coherent intensity) as a function of offset for the 5 experiments. Note that this is a log-linear plot. A linear fit to the data gives the characteristic exponential decay due to scattering - the extinction mean free path, L_{ext}. We estimate L_{ext} =45.9m.

To fully characterize the scattering in the radiative transfer model, the extinction mean free path, ext, must be measured. This parameter describes the exponential decay of the maximum of the coherent intensity with distance. The decay is depicted in Fig. 8.5. By doing a linear regression on a logarithmic plot, the characteristic distance over which the direct wave decays exponentially can be estimated. For this model, $\ell_{ext} = 45.9 \pm 2.1$. In the previous sections, we showed that $\frac{1}{2}\ell_{ext} = \ell_{tr}$. Therefore $\ell_{tr} = 22.9 \pm 1.0m.$ Getting an estimate of s would require knowledge of the degree of back-scattering the individual scatterers radiated relative to their forward-scattering [203].

With v and l_{tr} estimated from the numerical results, the theoretical prediction of equation (8.52) can be compared to the simulated total intensities.

In Fig. 8.6, the solution of the diffusion equation asymptotically approaches the numerical intensities with time, as it should. Note that the approximation fails severely for early times since it is acausal. The late time exponential decay is correctly predicted by the diffusion approximation. Such behavior verifies our radiative transfer model for late times and hints at the fact that, in 1D systems, there is an intermediate range of distances where the incoherent intensity can be described by diffusion instead of localization [201].

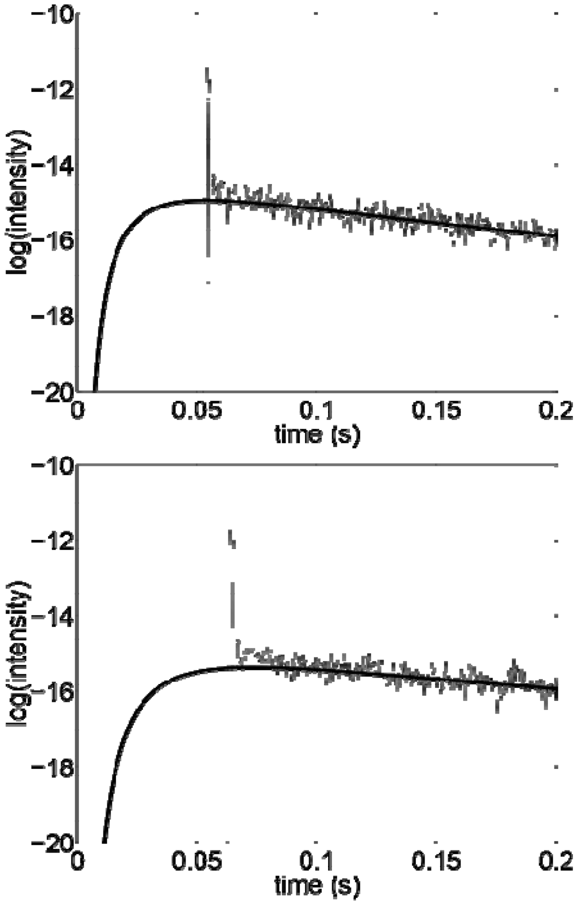

Fig. 8.6. A logarithmic plot of the total intensity of experiment 4, at an offset of 100m (top) and 120m (bottom) compared with the diffusion approximation, equation (52). At early times, the analytic solution to the diffusion equation (thick line) differs from the numerical observations, because the diffusion solution is acausal, and does not account for the coherent field.

8.9 Discussion

In higher dimensions, the radiative transfer equation becomes considerably more difficult since there are an infinite number of directions to scatter into, as compared to 2 in 1D [196]. However, even in 1D, the rich character of radiative transfer is evident. Exponential decay is experienced by the direct wave due to scattering and absorption. Aspects of both wave and diffusive behavior emerge in the average total intensity, and, in the presence of both, a “mesoscopic” picture of the scattering medium can be formed.

The theory of radiative transfer has its limitations. The most severe is that it does not include wave interference. As a result of this, there exists a distance between source and receiver, known as the localization length, past which radiative transfer is incorrect. Sheng (1995) estimates that in 1D the localization length is approximately 4 mean free paths. This offers the possibility of an intermediate range (1 to 4 mean free paths) when radiative transfer holds. Future work should attempt to find good bounds on this range in practice.

8.10 Conclusions

Radiative transfer is a relative newcomer to the field of exploration seismology. By formulating the theory in 1D, we have attempted to make the connection with familiar concepts such as reflection/transmission coefficients, thin beds, and the O’Doherty-Anstey formula. In the process, new features have emerged, such as the diffusion approximation and incoherent intensity.

The link between radiative transfer and the O’Doherty-Anstey formula can be extended beyond the 1D point scatterer approximation we made in this paper. To do so implies moving into the more complicated Mie scattering regime, where the wavelength is on the order of the size of the scatterer. Additionally, we considered a “cyclic” sequence, which radiative transfer and scattering theory are designed for. It remains to be seen what radiative transfer can do for “transitional” sequences when the interfaces cannot be grouped into pairs that define scatterers.

9 SCATTERING OF WAVES BY IMPURITIES IN PRECOMPRESSED GRANULAR CHAINS

We study scattering of waves by impurities in strongly precompressed granular chains. We explore the linear scattering of plane waves and identify a closed-form expression for the reflection and transmission coefficients for the scattering of the waves from both a single impurity and a double impurity. For single-impurity chains, we show that, within the transmission band of the host granular chain, high-frequency waves are strongly attenuated (such that the transmission coefficient vanishes as the wavenumber $k \to \pm\pi$), whereas low-frequency waves are well-transmitted through the impurity. For double-impurity chains, we identify a resonance — enabling full transmission at a particular frequency — in a manner that is analogous to the Ramsauer–Townsend (RT) resonance from quantum physics. We also demonstrate that one can tune the frequency of the RT resonance to any value in the pass band of the host chain. We corroborate our theoretical predictions both numerically and experimentally, and we directly observe complete transmission for frequencies close to the RT resonance frequency. Finally, we show how this RT resonance can lead to the existence of reflectionless modes even in granular chains (including disordered ones) with multiple double impurities.

9.1 Introduction

One-dimensional (1D) granular crystals (i.e., granular chains) consist of closely packed chains of elastically colliding particles. This setup has been used as a testbed for the investigation of wave phenomena in chains of strongly nonlinear oscillators, and the interplay between nonlinearity and discreteness in granular chains has inspired the exploration of a diverse set of coherent structures, including traveling waves, breathers, and dispersive shock waves [204–206]. Granular crystals can be constructed from a wide variety materials of different types and sizes, so their properties are very tunable, and they thus provide a versatile type of metamaterial for both fundamental physical phenomena and applications [204, 205, 207, 208].

Granular crystals have been used for the investigation of numerous structural and material heterogeneities on nonlinear wave dynamics. This includes the role of defects [209–212] (including in experimental settings [213, 214]); the scattering from interfaces between two different types of particles [215 –217]; and wave propagation in decorated and/or tapered chains [218, 219], chains of diatomic and triatomic units [220–227], and quasiperiodic and random configurations [228–234]; and much more. One can model strongly compressed granular chains as a type of Fermi–Pasta–Ulam (FPU) lattice, and granular chains have been employed in studies of phenomena such as equipartition (see, e.g., [235, 236]).

Granular chains also provide prototypes for numerous potential engineering applications [228]. A few examples include shock and energy absorbing layers [216, 230, 238], sound-focusing devices and delay lines [339], actuators [240], vibration absorption layers [222], sound scramblers [215, 241], and acoustic switches and logic gates [243].

The study of disordered granular crystals is also becoming increasingly popular. Important themes in such studies have been transport properties of wavepackets and solitary waves and the interplay between disorder (especially in the context of Anderson localization), discreteness, and nonlinearity [231–234]. These themes are also relevant to a wide variety of other nonlinear lattice models [243, 244].

To get a handle on disordered granular chains, it is useful to start with a simpler setting in which one or a few defects occur within an otherwise homogeneous ("host") lattice [212]. In this context, scattering due to inhomogenities is a fundamental consideration when studying wave propagation in complex media [245, 246]. This is especially important when the scales of the waves and those of the inhomogeneities (i.e., impurities or defects) are comparable, as interactions in such situations can lead to very rich dynamics. Pertinent phenomena include the formation of localized modes [247, 248], Fano resonances [249, 250], cloaking [251, 252], and many other examples of broad interest across numerous branches of physics.

In the present paper, we use theory, numerical computations, and experiments in the linearized and weakly nonlinear regimes to explore the scattering of a plane wave from a single impurity and a double impurity in a granular chain. A key finding is that an analog of the well-known Ramsauer–Townsend (RT) effect can occur in granular chains. An RT resonance is a prototypical mechanism that enables scattering transparency in quantum mechanics [253]. In its most recognizable form, it consists of the presence of a sharp minimum in the electron scattering cross-section at low energies for scattering with rare gases. The RT effect has been observed experimentally in many scenarios involving quantum tunneling, including e−–Ar scattering [254] and positron–Ar scattering [255], e−–methane scattering [256], and others. When used in mechanical systems, the implication of the RT effect is equally significant. One possible application is embedding foreign objects, such as sensors, in systems so that they induce minimal interference with the existing structures. This has the potential to be very useful for applications in structural health monitoring.

The remainder of our paper is organized as follows. In Sec. 9.2, we introduce the fundamental equations that govern the dynamics of driven granular crystals. In Sec. 9.3, we solve, in closed form, the linear scattering problems of a single impurity and a double impurity embedded in a homogeneous ("host") granular chain. For double impurities, we demonstrate that an effect analogous to an RT resonance occurs in a well-defined region of parameter space. We use both numerical simulations and laboratory experiments to corroborate our theoretical results. In Sec. 9.4, we discuss and compare the results from our theory, computations, and experiments. In Sec. 9.5, we use numerical simulations to explore disordered granular chains, which include a large number of impurities. We demonstrate numerically that strongly precompressed chains with multiple impurities can admit solutions that consist of reflectionless modes (i.e., generalizations of the RT resonances). Finally, in Sec 9.4, we conclude and offer some directions for future work.

9.2 Driven granular crystals

One can describe a 1D crystal of *2N* +1 spherical particles as a chain of nonlinearly coupled oscillators with Hertzian interactions between each pair of particles [203–206]. The system is thus modeled using the following equations of motion:

$$\ddot{u}_n = \frac{A_n}{m_n}\left[\Delta_n + u_{n-1} - u_n\right]_+^{2/3} - \frac{A_{n+1}}{m_n}\left[\Delta_{n+1} + u_n - u_{n+1}\right]_+^{2/3} \tag{9.1}$$

where mn is the mass of the nth particle, particle (n ∈ {−N,−N +1, . . ., N}) un is the displacement of the nth particle measured from its equilibrium position, the pairwise interaction parameter A_n depends on the geometry and elasticity of particles in the *n*th and ($n-1$)th positions [203],

$$\Delta_n = \left(\frac{F_0}{A_n}\right)^{2/3} \tag{9.2}$$

is the change in displacement between centers of neighboring particles due to the static load F_0, and the bracket $[\cdot]_+$ is defined as

$$[\chi]_+ = \begin{cases} \chi, & if \chi > 0 \\ 0, & if \chi < 0 \end{cases} \tag{9.3}$$

We consider a chain that is compressed initially by two plates placed at the boundaries. This yields the following boundary conditions:

$$\begin{aligned} u_{-(N+1)} &= \psi_r(t), \\ u_{(N+1)} &= \psi_r(t), \end{aligned} \tag{9.4}$$

We focus on a situation in which the chain is driven periodically from one side and the other side is at rest. That is, $\psi_r(t) = 0$ and $\psi_l(t) = d\ sin(2\pi ft)$, where d and f, respectively, are the amplitude and frequency of the external driving.

We are interested in chains that are homogeneous except for a few particles (i.e., impurities) in the bulk. We consider two cases: (i) a single impurity and (ii) a double impurity (in which the impurities are adjacent particles). The interaction parameter A_n can take one of four possible values (depending on the type of spheres that are in contact). These values are

$$A_n = \begin{cases} A_{11} \equiv \dfrac{E_1(2r_1)^{1/2}}{3(1-v_1^2)}, & (type-1, type-1) \\ A_{12} \equiv \dfrac{4E_1E_2\left(\dfrac{r_1r_2}{r_1+r_2}\right)^{1/2}}{3\left[E_1(1-v_2^2)+E_2(1-v_1^2)\right]}, & (type-1, type-2) \\ A_{22} \equiv \dfrac{E_2(2r_1)^{1/2}}{3(1-v_2^2)}, & (type-2, type-2) \\ A_{1\omega} \equiv \dfrac{2E_1r_1^{1/2}}{3(1-v_1^2)}, & (type-1, wall) \end{cases} \tag{9.5}$$

where $E_{1,2}$, $v_{1,2}$, and $r_{1,2}$ are, respectively, the elastic modulus, the Poisson ratio, and the radii of the type-1 and type-2 particles. The particle masses are m_1 and m_2. We assume that the mechanical properties of the elastic plates at the boundaries are the same as for type-1 particles. The radius of an impurity particle is $r_2 = \alpha r_1$, where $\alpha > 0$ is the ratio between the radii of the two types of spheres. If we assume that type-1 and type 2 particles have identical densities (i.e., $\rho_1 = \rho_2$), then $\alpha < 1$ implies that the impurities are lighter than the particles in the host homogeneous chain, whereas $\alpha > 1$ implies that the impurities are heavier.

9.3 Scattering between liner waves and impurities

Depending on the relative magnitudes of Δn and $|u_n - u_{n+1}|$, the effective nonlinearity in Eq. (9.1) can be either strong or weak. In particular, for sufficiently strong static precompression or sufficiently small-amplitude vibrations in the crystal, $\Delta n >> |u_{n-1} - u_n|$, so the nonlinearity is very weak. If one ignores the nonlinearity entirely, there is a harmonic interaction between the particles, so the dynamics can be described by the equation

$$m_n u_n = B_n u_{n-1} + B_{n+2} u_{n+1} - (B_n + B_{n+1}) u_n, \tag{9.6}$$

which corresponds to Eq. (9.1) linearized about the equilibrium state. Consequently,

$$B_n = \frac{3}{2} A_n \Delta_n{}^{1\backslash 2} = \frac{3}{2} A_n{}^{2\backslash 3} F_0{}^{1\backslash 3} \tag{9.7}$$

One can express solutions of Eq. (9.6) in terms of a complete set of eigenfunctions of the form $u_n = v_n e^{i\omega t}$, where ω is the eigenfrequency. It is well-known that without impurities – i.e., for a completely homogeneous crystal with $m_n = m$ and $B_n = B$ – that $v_n = e^{ikn}$, so there is a single acoustic branch of solutions with eigenfrequency

$$\omega = \sqrt{\frac{2B}{m}[1 - \cos(k)]} \in [0, \Omega] \tag{9.8}$$

where m is the mass, k is the wave number, and $\Omega = \sqrt{\frac{4B}{m}}$. When impurities are introduced into a host chain, localized or resonant linear modes can arise (depending on the characteristics of the impurities [212].) For light impurities (i.e., $\alpha < 1$), one expects localized modes whose frequencies are larger than the upper bound Ω of the linear spectrum. For heavy impurities (i.e., $\alpha > 1$), by contrast, one expects impurity modes with frequencies in the linear spectrum, and one thus expects resonant modes with extended linear eigenmodes.

9.3.1 Theory

We are interested in studying scattering processes between a plane wave $e^{i(kn - \omega t)}$ and both single impurities and double impurities in the linear regime. In Fig. 9.1, we show schematics for chains with single and double impurities. We

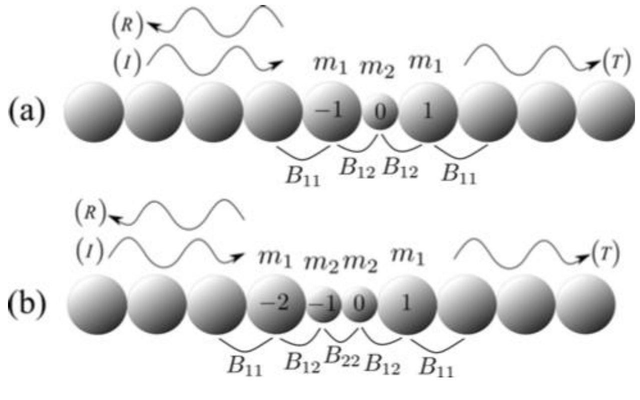

Fig. 9.1 Schematic of a homogeneous granular chain with (a) one impurity and (b) two contiguous impurities (i.e., a double impurity). The incident wave is characterized by I , the reflected wave is characterized by R, and the transmitted wave is characterized by T . We label the identities of the particles with integers. We calculate the parameters $\mathrm{B}_{\mathrm{ij}} = \frac{3}{2} A_{ij}^{2/3} F_0^{1/3}$ from the static precompression and the interactions between consecutive particles.

treat an impurity particle as a perturbation of a host particle: an impurity particle has radius $r_2 = \alpha r_1$, where r_1 is the radius of a host particle in the chain. We focus on $\alpha \in (0, 2]$. The value of the parameter α determines the mass of an impurity and the values of the interaction coefficients A_n between neighboring particles. For double impurities, we only consider the "symmetric" case in which both impurities are the same type of particle (and hence have the same radius).

To solve the scattering problem in the linear regime, it is convenient to use complex quantities rather than real ones. We write [246]

$$u_n = \begin{cases} e^{i(kn-\omega t)} + \mathrm{R}e^{-i(kn+\omega t)}, & if n < 0 \\ Te^{i(kn-\omega t)}, & if n > 0 \end{cases} \tag{9.10}$$

which represents an incident plane wave producing reflected and transmitted waves due to the interaction with the impurity. We thereby define a transmission coefficient $|T|^2$ and a reflection coefficient $|R|^2$. Note that $|R|^2 + |T|^2$ need not equal 1 because both $|T|^2$ and $|R|^2$ are based on the norm of the displacement, which is not a conserved quantity of either Eq. (9.1) or Eq. (9.6). Intuitively, $|T|^2$ and $|R|^2$ are still "complementary" quantities, as a decrease in one is accompanied by an increase in the other (and vice versa). To have $|R|^2 + |T|^2 = 1$ for all parameter values, one would need to instead define $|R|^2$ and $|T|^2$ in terms of the energy density. The total energy is conserved by the dynamics, though it is much harder to measure experimentally than other quantities (e.g., velocity). Given Eq. (9.9), the velocity is $u^{\cdot}_n = -\omega u_n$. Therefore, if we defined $|T|^2$ and $|R|^2$ in terms of $u^{\cdot}_n$ rather than u_n, we would obtain the same results because $u^{\cdot}_n$ and un differ only by the constant factor $-\omega$. We therefore define reflection and transmission coefficients in terms of displacement, which allows us to compare analytical results directly with not only computations but also laboratory experiments, for which we compute the coefficients in terms of velocity (see Secs. 9.3.2 and 9.3.3).

We substitute the ansatz (9.10) into Eq. (9.6) near the impurities and do a straightforward calculation to obtain the following linear system of equations for *T* and *R*:

$$\begin{pmatrix} \beta_{(i),(ii)} \delta_{(i),(ii)} \\ \eta_{(i),(i,i)} \gamma_{(i),(ii)} \end{pmatrix} \begin{pmatrix} T_{(i),(ii)} \\ R_{(i),(ii)} \end{pmatrix} = \begin{pmatrix} \in_{(i),(ii)} \\ \zeta_{(i),(ii)} \end{pmatrix} \tag{9.11}$$

where the subscripts (i) and (ii), respectively, indicate chains with single and double impurities.

For a single-impurity chain, the parameters in Eq. (9.10) are

$$\begin{aligned}
&\beta_{(i)} = \overline{\Omega} + B_{12}\left(2 - e^{ik}\right),\\
&\delta_{(i)} = B_{12}e^{-ik},\\
&\eta_{(i)} = B_{12},\\
&\gamma_{(i)} = -\mathbf{B}_{12}e^{ik},\\
&\epsilon_{(i)} = B_{11}e^{2ik} - (B_{11} + B_{12} + \overline{\Omega})e^{ik},\\
&\xi_{(i)} = -B_{11}e^{-2ik} + (B_{11} + B_{12} + \overline{\Omega})e^{-ik},
\end{aligned}$$

Where $\overline{\Omega} = -\dfrac{2B_{11}m_2}{m_1}\left[1 - \cos(k)\right]$. Solving Eq. (9.10) yields the reflection and transmission coefficients:

$$\begin{aligned}
\left|R_{(i)}\right|^2 &= \left|\frac{B_{11}\left(B_{11} - B_{12}\right)m_2 - \left(2B_{11} - B_{12}\right)\left(B_{11}m_2 - B_{12}m_1\right)e^{ik} + B_{11}\left(B_{11}m_2 - B_{12}m_1\right)e^{ik}}{B^2{}_{11}m_2e^{ik} + \left(B_{11} - B_{12}\right)\left(B_{11}m_2 - B_{12}m_1\right)e^{3ik} - B_{11}\left(2B_{11}m_2 - 2B_{12}m_1 - B_{12}m_2\right)e^{2ik}}\right|^2\\
\left|T_{(i)}\right|^2 &= \left|\frac{B_{11}B_{12}m_1\left(1 + e^{ik}\right)}{B^2{}_{11}m_2 + \left(B_{11} - B_{12}\right)\left(B_{11}m_2 - B_{12}m_1\right)e^{2ik} - B_{11}\left(2B_{11}m_2 - 2B_{12}m_1 - B_{12}m_2\right)e^{2ik}}\right|^2
\end{aligned} \tag{9.11}$$

For a double-impurity chain, we follow the same procedure and use the parameters

$$\begin{aligned}
&\beta_{(ii)} = \overline{\Omega} + B_{12}\left(1 - e^{ik}\right) + B_{22}, \quad \delta_{(ii)} = B_{22}e^{ik}, \quad \eta_{(ii)} = B_{22}, \quad \gamma_{(ii)} = -B_{22}e^{ik}.\\
&\epsilon_{(ii)} = B_{12}e^{2ik} - \left(B_{12} + B_{22} + \overline{\Omega}\right)e^{ik}, \quad \xi_{(ii)} = -B_{12}e^{-2ik} + \left(B_{12} + B_{22} + \overline{\Omega}\right)e^{-ik},
\end{aligned}$$

in Eq. (9.10). Note that $\overline{\Omega}$ has exactly the same expression as before. We obtain

$$\begin{aligned}
\left|R_{(ii)}\right|^2 &= \left|\frac{4B_{12}\left(B_{12} - B_{22}\right)m_1^2 - 2B_{11}\left(B_{12} + B_{22}\right)m_1\, m_2 + 2B_{11}^2m_2^2 + 2B_{11}m_2\left(B_{12}m_1 - B_{11}m_2\right)\cos(k))\sin^2(k/2)e^{-2ik}}{\left(B_{12}m_1(e^{ik} - 1) + 2B_{11}m_2 - 2B_{11}m_2\cos(k)\right)\left(B_{12}m_1(e^{ik} - 1) - 2B_{22}m_2 + 2B_{11}m_2 - 2B_{11}m_2\cos(k)\right)}\right|^2\\
\left|T_{(ii)}\right|^2 &= \left|\frac{B_{12}B_{22}m_1^2\left(1 - e^{-2ik}\right)}{\left(B_{12}m_1(e^{ik} - 1) + 2B_{11}m_2 - 2B_{11}m_2\cos(k)\right)\left(B_{12}m_1(e^{ik} - 1) - 2B_{22}m_2 + 2B_{11}m_2 - 2B_{11}m_2\cos(k)\right)}\right|^2
\end{aligned} \tag{9.12}$$

In Fig. 9.2, we show the reflection and transmission coefficients as functions of *k* and *α*. Observe in Figs. 9.2(b) and 9.2(d) that there is a black region of *reflectionless* modes that can traverse either a single impurity or a double impurity almost without modification. For single impurities, the reflection coefficient $|R|^2$ vanishes only when either $\alpha = 1$ or $k = 0$. By contrast, for a double impurity, $|R|^2$ vanishes not only when $\alpha = 1$ and $k = 0$ but also when $k = \pm k_r \neq 0$ for *α* larger than some critical value α_c. At these resonant values, a wave can be transmitted completely through the impurities (i.e., there is no scattering), and it experiences only a phase shift. Granular crystals thereby admit an analog of the well-known Ramsauer–Townsend (RT) effect [253], which in its traditional form consists of the presence of a sharp minimum in the electron scattering cross-section at low energies for scattering with rare gases (such as Xe, Kr, and Ar). Hereafter, we use the term “RT resonance” to describe the resonance at $k = \pm k_r$. In our case, one can explicitly write k_r in terms of the physical parameters of the system as

$$k_r = \arccos(\phi), \tag{9.13}$$

where

$$\phi = \frac{B_{12}B_{22}m_1^2 - 2B_{11}B_{22}m_1m_2}{2B_{11}m_2\left[B_{11}m_2 - B_{12}m_1\right]} + \frac{B_{11}\left[m_1^2 - 2m_1m_2 + 2m_2^2\right]}{2m_2\left[B_{11}m_2 - B_{12}m_1\right]}$$

In Fig. 9.3, we show k_r and the other relevant values of the reflection coefficient for a double impurity in terms of the parameter α. To ensure that $k_r \in R$, we need $\varphi \in [-1, 1]$. In terms of α, this implies that the resonant wavenumber k_r exists when $\alpha_c \leq \alpha < \infty$. An interesting feature of k_r is that it can be tuned as a function of α to any value in the interval $[0, \pi]$. In particular, we find that $k_r = \pi$ at $\alpha = \alpha_c$ and $k_r \to 0$ as $\alpha \to \infty$. Consequently, one can tune the frequency of the RT resonance to any value in the transmission band [0, Ω] of the host granular chain.

In the following subsections, we discuss our computational and experimental results on transmission, and we compare them with our analytical predictions (obtained using a linear approximation, as we discussed above) for transmission from Fig. 9.2.

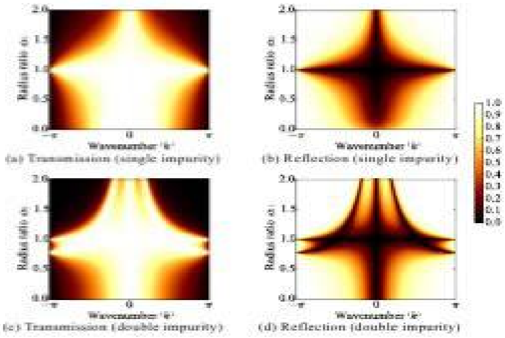

(a) Transmission (single impurity)
(b) Reflection (single impurity)
(c) Transmission (double impurity)
(d) Reflection (double impurity)

Fig. 9.2: (Color online) (Left) Transmission and (right) reflection coefficients for the scattering of a plane wave in a chain with impurities as a function of the wavenumber k and the radius ratio α. We show examples for (top) a single impurity and (bottom) a double impurity. We describe the physical arameters of the particles in the chain in Table I.

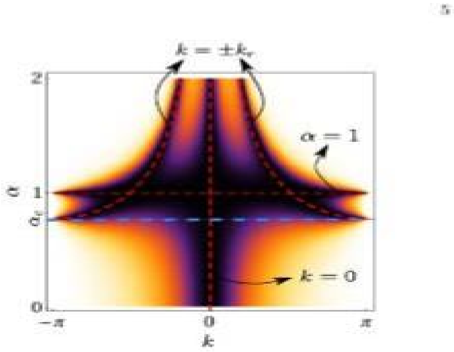

Fig. 9.3: (Color online) Reflection coefficient |R(ii)|^2 for the double impurity. The red dashed curves indicate the points at which the reflection coefficient is exactly 0. The resonant wavenumber kr is given by Eq. (13). The blue dashed line highlights the critical value αc; the system has a Ramsauer Townsend (RT) resonance at wavenumber k = ±kr for α > αc.

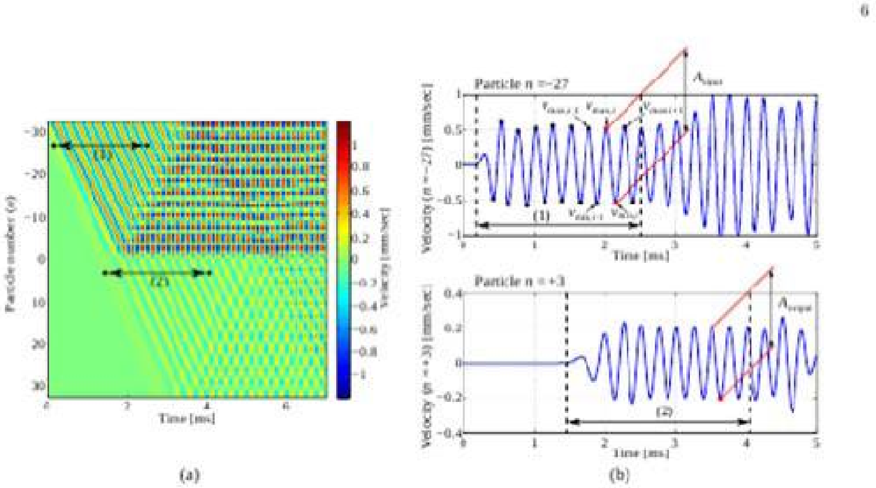

Fig. 9.4 (a) Space-time contour plot of particle velocity profiles in a host 63-particle chain in which a double impurity has been inserted between particles −2 and +1. We use α = 1.5 and the parameters in Table I for this numerical simulation. Arrows (1) and (2) indicate the regions that we consider for the calculation of the transmission coefficient. These regions are not affected by the plane waves that reflect from the left or right walls. We also show velocity profiles for particles (b) n = −27 and (c) n = +3. The dots indicate the maximum and minimum peaks of oscillatory velocity profiles, and the domains of (1) and (2) correspond to the temporal regions marked with (1) and (2) in panel (a).

9.3.2. Numerical simulations

For our numerical computations, we solve Eq. (9.1) directly via a Runge–Kutta method (using the ode45 function in Matlab). To quantify the transmission efficiency of the impurity-bearing chains, we analyze velocity profiles of propagating waves under harmonic excitations, as discussed earlier. In Fig. 9.4(a), we show a space-time contour plot of particle velocities from numerical simulations. In this case, we consider a double impurity (with α = 1.5) embedded between particles −2 and +1 [see Fig. 9.1(b)] of a 63-particle chain.

The sinusoidal perturbation that we apply to the left end of the chain has a frequency of 4 kHz and an amplitude of 0.35 N. In this scenario, we calculate the magnitude of the particles' maximum displacements to be less than 4.59 $\times 10^{-8}$ m. The associated oscillations are two orders-of-magnitude smaller than the static precompression $\Delta_n \approx 1.02\times10^{-6}$ from $F_0 = 10$ N, so it is reasonable to assume that the system is operating near the linear regime.

To quantify transmission efficiency, we measure the velocity profiles at specific particles: n = −27 for incident waves and n = +3 for transmitted waves. We choose these particle locations to allow a sufficiently long spatial interval between the two nodes in Fig. 9.4(a). The two-sided arrows (1) and (2) indicate regions over which the motion is not affected by the presence of reflections by the chain boundaries. In Fig. 9.4(b), we show the velocity profiles of particles n = −27 (top panel) and $n = +3$ (bottom panel). The arrows (1) and (2) again correspond to the temporal domains without interference from wave reflection.

In the temporal plots of velocity profiles, we denote the maxima by $v_{\mathrm{max,i}}$ and the minima by vmin,i, where i ∈ {1, 2, . . . } is the index of the wave peaks in the oscillation. As indicated by the dots in Fig. 9.4(b), the values of these peaks are not constant even in the designated region before the arrival of the reflected waves. Therefore, we need to extract the steady-state component from the propagating plane waves. To do this, we calculate the relative error between a pair of adjacent peaks:

$$Error_i = \frac{v_{\max,i+1} - v_{\max,i}}{v_{\max,i+1}} \tag{9.14}$$

We identify the steady-state component of the waves by finding a wave packet with a minimal error. The amplitude $\tilde{A}_i$ of the steady-state velocity component is then

$$\overline{A}_i = v_{\max,i} - v_{\min,i} \tag{9.15}$$

By calculating $\tilde{A}_i$ for each peak i, we measure the incident wave amplitude Ainput and transmitted wave amplitude A_{output} [see Fig. 9.4(b)]. Finally, we quantify the transmission coefficient by calculating the ratio of the transmitted wave's velocity amplitude to that of the in cident wave:

$$\overline{T}_{(i),(ii)} = \frac{A_{output(i),(ii)}}{A_{input(i),(ii)}}, \tag{9.16}$$

where (as mentioned in Sec. 9.3.A) the subscripts (i) and (ii), respectively, indicate cases with a single impurity and a double impurity. The transmission coefficient $\widetilde{T}$, which is written in terms of velocity amplitudes, should be equivalent to the displacement ratios introduced in Eq. (9.10) in the ideal situation of harmonic responses of the particles. In the next subsection, we will present our numerical and experimental calculations of $\widetilde{T}_{(i),(ii)}$.

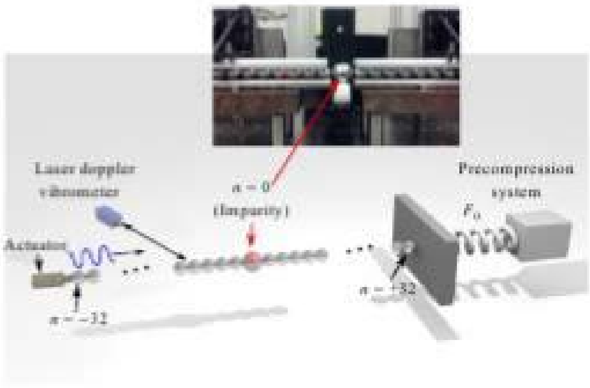

Fig. 9.5. (Color online). Schematic of the experimental setup for a granular chain with a single impurity. In the inset, we show an image of the experimental setup.

9.3.3 Experimental setup and diagnostics

We now discuss the results of experiments in granular chains with a single impurity and a double impurity. In Fig. 9.5, we show a schematic to illustrate our experimental setup. We consider a granular chain with 65 spheres: there are 64 type-1 spheres and one impurity in the single-impurity chain, and there are 63 type-1 spheres and 2 impurities in the double-impurity chain. Because of availability limitations, we use distinct materials for type-1 and type-2 particles. However, their material properties are sufficiently similar (see Table I) so that it is permissible to treat them as identical materials. As we show in the inset of Fig. 9.5, we align the type-1 particles by using four stainless steel rods, and the impurity particle is held in place by an external holder that ensures that its center is aligned with the other particles in the chain.

To excite the granular chain, we position a piezoelectric actuator on the left side of the chain in direct contact with particle $n = -32$. To generate plane waves in the granular system, we use harmonic excitations with a frequency range from 1.0 to 7.0 kHz with a 200 Hz increment. The right end of the chain is compressed by the wall with a static precompression of F_0 using a spring and linear-stage system. We visualize the propagation of stress waves by measuring the velocity profiles of particles via a non-contact laser Doppler vibrometer

Polytec, OFV-534). See Refs. [257, 258] for the details of this full- field visualization technique.

Table 9.1 Properties of type-1 and type-2 particles.

	Type-1	Type-2
Material	440 C	AISI 52100
Elastic modulus	E_1 = 204 GPa	E_2 = 210 GPa
Poisson ratio	v_1 = 0.28	v_2 = 0.30
Density	ρ_1 = 7.80 g/cm^2	ρ_2 = 7.81 g/cm^2
Radius	r_1 = 9.525 mm	$r_2 = \alpha r_1$

Similar to our numerical approach, we measure the transmission coefficient by estimating the amplitude of the incident (A_{input}) and transmitted (A_{output}) waves. Unlike our numerical simulations, however, the experimental results are susceptible to noticeable attenuation because of dissipation and slight particle misalignment. Therefore, we calibrate our experimental results by normalizing them with respect to the measurement results obtained from a homogeneous particle chain. The calibrated transmission coefficient is

$$\overline{T}^{cal}_{(i),(ii)} = \frac{\overline{T}_{(i),(ii)}}{\overline{T}_{\alpha=1}} = \frac{A_{output\$(i),(ii)}}{A_{oytput\$\alpha=1}}, \tag{9.17}$$

Where $\overline{T}_{(i),(ii)}$ is the transmission coefficient for singleimpurity and double-impurity chains based on Eq. (9.16), and $\overline{T}_{\alpha=1}$ is the transmission coefficient for a homogeneous chain (i.e., for α = 1).

9.4 Comparison between analytic, numerical, and experimental results

We now compare our analytical results with numerical simulations and experimental data for the radius ratios α = 0.7 and α = 1.5. In Figs. 6(a) and 6(b), we show our results for the transmission coefficients for a single-impurity chain. In Figs. 9.6(c) and 9.6(d),we present our results for a double-impurity chain. In these plots, black solid curves indicate the analytical predictions from Eqs. (9.11) and (9.12), blue dots indicate the results of simulations obtained by solving Eq. (9.1), and red squares give the experimental results after calibration using Eq. (9.17).

For a single-impurity chain, the transmission coefficient has a decreasing trend as we increase the excitation frequency. This supports our prediction from Fig. 9.2(a). The slope of the decrease depends on the mass ratio. When $\alpha = 0.7$, the decreasing trend is slow at first, but there is a rapid drop near the cutoff frequency of 7.25 kHz that we obtained analytically from the formula $\Omega = \sqrt{\frac{4B}{m}}$. For α = 1.5, the decrease has a near-linear trend throughout the frequency pass band. In Figs. 9.6(a) and 9.6(b), we observe these trends in both numeric and experiments. However, as we will discuss shortly, there are some differences in the experiments as compared to the simulations and theoretical predictions.

For a double-impurity chain, we obtain more interesting behavior. When α = 0.7, we observe, broadly speaking, a decrease of transmission efficiency as the frequency increases; this is reminiscent of the single-impurity chain. However, for the mass ratio α = 1.5, the transmission coefficient has a pronounced double-peak shape in the frequency pass band. In particular, our analytical results for transmission predict a resonant mode at an excitation frequency of about 3.0 kHz. This leads to complete transmission of plane waves despite the existence of impeding double impurities. This “cloaking” mode is notable, and we observe it in both experiments and numerical simulations [see Fig. 9.6(d)]. However, we again note that quantitative differences exist despite the numerical corroboration and the accurate qualitative description of the experiments.

As we have just discussed, our analytical predictions match reasonably well with the results of our numerical simulations and experimental findings, especially for frequencies between 1.0 and 4.0 kHz. By comparing analytical predictions and experimental results around 3.0 and 4.0 kHz, however, we observe some discrepancies that are not noticeable when comparing analytical and numerical calculations. They probably stem from experimental errors, such as a potential slight misalignment of the external holder and, perhaps more notably, an intrinsic frequency response of a piezo actuator.

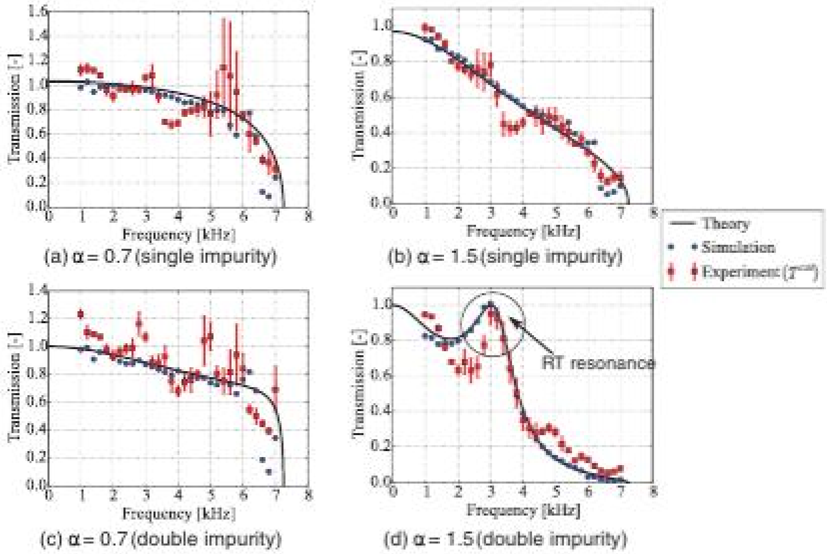

(a) α = 0.7 (single impurity)
(b) α = 1.5 (single impurity)
(c) α = 0.7 (double impurity)
(d) α = 1.5 (double impurity)

Fig. 9.6. Transmission of plane waves in a granular chain with impurities. The ratio of the impurity radius to the host-particle radius is (left) α = 0.7 and (right) α = 1.5. We show results for chains with (top) a single impurity and (bottom) a double impurity.

For higher frequencies, especially between 6.0 and 7.0 kHz, we observe an especially noticeable discrepancy when comparing the theoretical predictions to the numerical and experimental results. [For example, see Figs. 9.6(b,c).] We believe that this arises due to transient waveforms – and specifically due to wave localization – in the vicinity of the excitation particle (i.e., at the left end of the chain). If one excites a granular chain from a stationary state, the propagating waves include a wide range of frequencies near the excitation frequency. If the excitation frequency is close to the cutoff frequency, then incident waves whose frequencies are larger than the cutoff frequency will not propagate but will instead be localized at the excitation particle in the form of evanescent waves. Such perturbations result in transient behavior in the form of propagating waves, often in modulated waveforms in the time domain. This, in turn, affects the calculation of transmission coefficients in numerical simulations and experiments. In both cases, we examine the dynamics in subsets of the chains for small propagation times to avoid the effects of reflection from the right boundary. See the Appendix for further details.

9.5 Multiple impurities

An interesting application of the RT resonance, which we discussed in Sec. 9.3.A for scattering with a double impurity, is its extension to systems with multiple double impurities. In particular, it is interesting to examine systems in which multiple impurities are either periodically or randomly distributed within a host homogeneous chain. A fascinating question arises: can reflectionless modes still occur?

When considering multiple impurities in a host granular chain, the formalism of transfer matrices provides a useful framework to study transmission of waves through the entire system [259]. Following recent work by Zakeri et al. [260], we assume stationary plane waves un(t) = wneiωt as in Sec. 9.3.A. Equation (9.7) then leads to

$$\omega_{n+1} = \frac{\left\lfloor (B_n + B_{n+1}) - m_n \omega^2 \right\rfloor}{B_{n+1}} \omega_n - \frac{B_n}{B_{n+1}} \omega_{n-1}, \tag{9.18}$$

which generates the modes given a seed $\{w_{-N}, w_{-N+1}\}$. For $\omega = 0$, Eq. (9.19) reduces to

$$\omega_{n+1} = \frac{B_n}{B_{n+1}} (\omega_n - \omega_{n-1}) + \omega_n \tag{9.19}$$

Thus, for any distribution of particles in the chain, the seed $w_{-N} = w_{-N+1}$ implies that $w_n = w_{-N}$ for all n. This explains why the reflection coefficients are exactly 0 at ω = k = 0 for both single and double impurities (see Fig. 9.2).

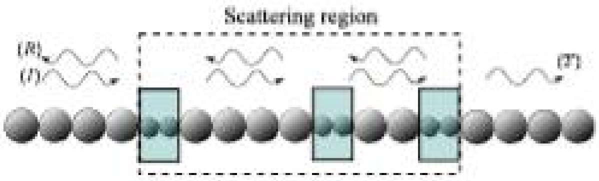

Fig. 9.7. Schematic of a host homogeneous granular chain with multiple double impurities. The incident wave is (*I*), the reflected wave is (*R*), and the transmitted wave is (*T*). We highlight impurities in solid turquoise boxes, and we indicate the scattering region with the dashed box.

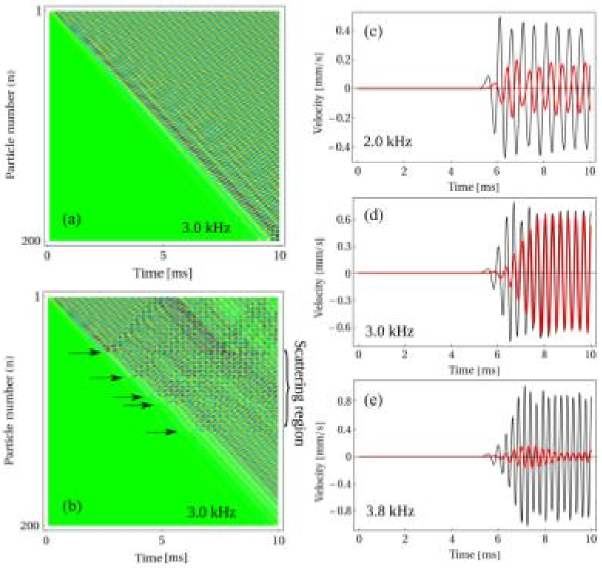

FIG. 9.8. (a) Space-time contour plot of the normalized velocity for a homogeneous hain with N = 200 particles and an excitation frequency of 3.0 kHz. (b) The same plot as in panel (a), but with five double impurities located at positions $n = 50$,n= 72,n= 90,n= 96, and n = 118. The radius ratio is $\alpha = 1.5$, and arrows indicate the position of the impurities. Panels (c)–(e) show the velocity at particle $n = 130$ for excitation frequencies of (c) 2.0kHz,(d)3.0kHz,and(e)3.8 kHz. The black (large-amplitude) curves are associated with the homogeneous chain [panel (a)], and the red (smaller-amplitude) curves are associated with the chain with the impurities [panel (b)].

In the absence of impurities, Eq. (9.18) generates propagating waves for any $\omega \in [0, \Omega]$; this is, at least true in the infinite domain, while for a finite domain, only the wavenumbers conforming to the specific boundary conditions, and the associated frequencies get selected. Once we add impurities, the iterative process to generate such propagating waves is the same until we reach what we call a "scattering region" (see Fig. 9.7). In this region, multiple scatterings occur because the presence of impurities has broken discrete translation symmetry, and successive interferences can then lead to complicated dynamics that depend on the distribution of impurities. A particular example of this phenomenon was investigated recently in the context of disordered granular chains [232].

When the distribution of impurities is such that impurities are well separated from each other, one can reformulate the transmission problem [given by Eq. (9.18)] through the entire scattering region as a sequence of transfer problems from each segment of a granular chain through an impurity to the next segment. Thus, an incident plane wave $w_{\text{n}} = Ie^{ikrn}$ with wavenumber $k = k_r$ and amplitude I transforms into $T^{(1)}\text{e}^{\text{ikrn}}$ after a scattering event because no reflected waves are generated during the scattering at $k = k_r$. By considering each impurity, we obtain the sequence $Ie^{\text{ikrn}} \rightarrow T^{(1)}e^{\text{ikrn}} \rightarrow T^{(2)}e^{\text{ikrn}} \rightarrow \cdot \cdot \cdot \rightarrow T^{(\text{L})}\text{e}^{\text{ikrn}}$, where arrows denote the transmission of the wave through the impurities and T(j), with j ∈ {1, 2, . . . , L}, denotes the transmitted-wave amplitudes, which are are given by Eq. (9.12). Consequently, reflectionless modes can be supported by the chain in the form

$$\omega_n = \begin{cases} Ie^{ik_r n}, & \mathit{if} n \le n_1 \\ T^{(1)}e^{ik_r n}, & \mathit{if} n_1 < n \le n_2 \\ \vdots & , \\ T^{(L)}e^{ik_r n}, & \mathit{if} n_L < n \end{cases} \qquad (9.20)$$

where n_{j} (with j ∈ {1, 2, . . . , L}) represents the position (of the first particle) of the j th impurity in the host homogeneous chain. For other modes, transmission through the scattering region depends on the frequency ω. Based on our analysisin Sec. 9.2 , we expect that transmission decays rapidly as one approaches the upper band edge Ω. By contrast, plane waves slowly attenuate for frequencies near 0.

To corroborate that these effects arise in strongly precompressed granular crystals, we numerically integrate Eq. (9.1) using the same parameters as in Sec. 9.3 B, but this time we randomly place double impurities within a scattering region near the middle of a chain. One can calculate the frequency of the RT resonance using Eq. (9.13), which in this case gives $f_{\text{r}} \approx 3.0$ kHz. As we predicted, when the system is driven at this frequency, waves experience a phase shift due to the scattering, but the amplitude is consistently transmitted almost without modification through the scattering region of the random chains. However, when we move away from the frequency of the RT resonance, the transmission decays. We observe this directly by measuring the velocity of a particle located just after the scattering region. To illustrate this, we compare (see Fig. 9.8) the temporal evolution of particle velocities in a homogeneous chain to that in a chain with five randomly-distributed double impurities. In Figs. 9.8(c) and 9.8(e), we observe attenuation in the magnitude of the velocity due to the presence of impurities in the chain. In Fig.9.8(d), when the system is driven at 3.0 kHz, the wave is clearly delayed in the perturbed chain compared with the homogeneous one, although the magnitude of the velocity is about the same for both chains. As predicted, we observe the RT resonance even in granular chains with multiple double impurities.

9.6 Conclusions

In the presentwork,we examined the scattering ofwaves by single impurities and double impurities in granular chains.We started by exploring the linear scattering problem motivated by the context of strongly precompressed granular chains with either a single impurity or a double impurity. We derived analytical formulas to show that the scattering is markedly different in the two scenarios. For single-impurity chains, we showed that the transmission coefficient $|T|^2$ decays monotonically with k (and hence with the frequency ω).We also found that $|T|^2 \rightarrow 0$ as one approaches the band-edge frequency of the host homogeneous chain. By contrast, for a doubleimpurity chain, we showed that an effect analogous to the Ramsauer–Townsend resonance takes

place at $k = k_r \in [0,\pi]$ in a specific region of parameter space. We demonstrated

that one can tune the frequency of this RT resonance to any value within the transmission band of the host homogeneous chain.

We compared our analytical results to numerical computations and laboratory experiments, and we obtained good agreement. In our experiments, we used noncontact laser Doppler vibrometry to obtain a full-field visualization of plane waves propagating in a granular chain. This allowed us to observe the RT resonance for double impurities in a granular chain by directly measuring a transmission coefficient associated with the scattering. We also discussed how this RT resonance can be responsible for the emergence of reflectionless modes in systems with multiple (either ordered or disordered) double impurities. We demonstrated this reflectionless transmission using numerical simulations.

Our study paves the way for a systematic study of the properties of Ramsauer–Townsend resonances in granular crystals. It is worthwhile to study such resonances when there are more impurities and for various (ordered or disordered) distributions of impurities. One possible application of RT resonances in granular crystals is embedding foreign objects, such as sensors, in systems so that they induceminimal interference with existing structures. It is also of considerable interest to explore disordered granular crystals, rather than merely placing a disordered segment in otherwise homogeneous chains. In 1D disordered granular crystals, the recent numerical predictions of superdiffusive transport and other features [29,30] are especially interesting to explore further. Such efforts are currently in progress.

10 TRANSPORT OF LOCALIZED WAVES VIA MODES AND CHANNELS

10.1 Introduction

Suppressed transport and enhanced fluctuations of conductance and transmission are prominent features of random mesoscopic systems in which the wave is temporally coherent within the sample [261–264]. The associated breakdowns of particle diffusion and of self-averaging of flux were first considered in the context of electronic conduction and for many years thought to be an exclusively quantum phenomena [261, 264–272]. Independently, however, wave localization was demonstrated theoretically for radio waves in a statistically inhomogeneous waveguide [273]. Over time, it became increasingly apparent that localization and mesoscopic fluctuations reflected general wave properties and might therefore be observed for classical waves as well [263, 273–288]. In particular, the level and transmission eigenchannel descriptions proposed,respectively, by Thouless [266, 267] and Dorokhov [270, 271] to describe the scaling of conductance in electronic wires at zero temperature, are essentially wave descriptions involving the character of quasi-normal modes of excitation within the sample and speckle patterns of the incident and transmitted field. Quasi-normal modes, which we will refer to as modes, are resonances of an open system. These modes decay at a constant rate due to the combined effects of leakage from the sample and dissipative processes. Eigenchannels of the transmission matrix, are obtained by finding the singular values of the field transmission matrix and represent linked field speckle patterns at the input and output of the sample surfaces. Eigenchannels are linear combinations of phase coherent channels impinging upon and emerging from the sample. Examples of such channels may be propagating transverse modes of an empty waveguide, or transverse momentum states in the leads attached to a resistor. In measurements, input and output channels are often combinations of source and detectors at positions on the incident and output planes, respectively. Whereas modes are biorthogonal field speckle patterns over the volume of an open sample [299, 300], eigenchannels are orthogonal field speckle patterns at the input and output planes of the sample. When there is no risk of confusion, we will refer to eigenchannels as channels. Though levels and channels have not been observed directly in electronic systems, these approaches have served as powerful conceptual guides for calculating the statistics and scaling of conductance [261].

Recent measurements of spectra of transmitted field patterns and of the transmission matrix of microwave radiation propagating through random multimode waveguides have made it possible to determine the eigenvalues of modes and channels as well as their speckle patterns in transmission in mesoscopic samples [301, 302]. These experiments were carried out in a multimode copper tube filled with randomly positioned dielectric elements, which is directly analogous to a resistive wire in the zero-temperature limit, in which dephasing vanishes. The study of modes and channels promises to provide a comprehensive description of transport and to clarify long-standing puzzles regarding steady state and pulsed propagation.

In this chapter, we will discuss studies of wave localization and strong fluctuations of the electromagnetic (EM) field, intensity, total transmission and transmittance, also known as the "optical" conductance from the per-spectives of modes and channels. These approaches are useful in numerous applications. The mode picture is of particular use in considering emission, random lasing, and absorption, while the channel framework is indispensable in optical focusing, imaging and transmission fluctuations. We will describe lasing in disordered liquid crystals [303] and in random stacks of glass cover slips [304] in which the mode width falls below the typical spacing between modes. The lasing threshold is then suppressed by the enhancement of the pump intensity and by the lengthening of the dwell time of emitted light within the sample. Measuring the transmission matrix allows us to study the fluctuations of transmittance over a random ensemble. The statistics of transmittance can be described using an intuitive "Coulomb charge" model Measurements of the transmission matrix make it possible to obtain the statistics of transmission in single samples at a particular incident frequency [306], which are crucial for focusing and imaging applications [306, 309]. These statistics, as well as the contrast in focusing, are given in terms of the par-ticipation number of transmission eigenvalues and the size of the measured transmission matrix [306, 309].

In the next section (section 10.2), we discuss instructive analogies between the transport of electrons and classical waves. Spectra of intensity, total transmission and transmittance are presented based on measurements of field transmission coefficients. A modal analysis of spectra of field speckle patterns on the output surface of a multimode waveguide and along the length of a single mode waveguide is described in section 10.3. Pulse propagation in mesoscopic samples is discussed in terms of the distribution of mode decay rates and the correlation between modal speckle patterns in transmission. The role of modes in lasing in nearly periodic liquid crystals and in random slabs is described in section 10.4. In section 10.5, we describe the statistics of transmission eigenvalues and their impact on the statistics of transmission for ensembles of random samples and in single instances of the transmission matrix. The manipulation of transmission eigenchannels to focus radiation is described in section 10.6. We conclude in section 10.7 with a discussion of the prospects for a complete description of transport in terms of modes and channels.

10.2 Analogies between transport of electrons and classical waves

Anderson [265] showed over 50 years ago that the electron wave function would not spread throughout a disordered three dimensional crystal once the ratio of the width of distribution of the random potential at different sites relative to the coupling between sites passes a threshold value. At lower levels of disorder, electrons diffuse in the band center but are localized in the tail of the band. Ioffe and Regel [310] pointed out shortly thereafter that an electron wave function could not be considered to be properly propagating if it were scattered after traveling less than a fraction of a wavelength so that for traveling waves, $\ell > \lambda / 2\pi$ where ℓ is the mean free path. This gives the criterion for localization in three dimensions, $\kappa\ell < 1$, where k is the wave number. Though not explicitly noted at the time, this criterion for localization applies equally to classical and quantum waves. In subsequent work, Thouless [266] considered the electronic state in the system as a whole rather than the strength of scattering within the medium. He argued that in bounded samples, the weight of electron states at the boundaries of the sample relative to points in the interior would be a useful measure of the extension of electron states within the sample. Since localized states would be peaked within the sample remote from the boundaries, their energies could be expected to be insensitive even to substantial changes at the boundary such as are engendered in a periodic system when the boundary conditions for repeated sections of a random system are changed from periodic to antiperiodic [266]. When the energy shift is less than the typical spacing between states, the state is localized within the sample. An associated measure of electron localization, which relates to the properties of the states and not to the impact of some hypothetical manipulation of the sample, is the typical width of an electron level relative to the average spacing between levels. When the electron wave function is exponentially peaked within the sample, electrons are remote from the boundary and their escape from the sample is slow. The linewidth of the level is then smaller than the spacing between neighboring levels, which is the inverse of the density of states of the sample as a whole. This indicates that electron localization is achieved when the dimensionless ratio of the level width to level spacing, the Thouless number, $\delta = \delta E / \Delta \mathrm{E}$, falls below unity. Pendry [311] has described the electron localization process as one in which “electrons can be forced to abandon their predilection for momentum” in favor of space as the defining characteristic. The inhibition in transport manifested in localization in space then leads to a lengthened escape from the sample and narrow linewidth manifested in terms of sharp spikes in energy “one per electron” [311] as opposed to a continuous spectrum. For diffusing electrons, the wave function extends throughout the sample. Energy then readily leaks out of the sample and levels are consequently short lived with line widths greater than the typical spacing between levels. Thus the electron localization threshold lies at $\delta = 1$The Thouless number may equally well be defined for classical waves as the ratio of the typical frequency width to the spacing of quasinormal modes, $\delta = \delta\omega / \Delta\omega$ where ω where where is the angular frequency. The level width is the inverse of the Thouless time τ_{Th} in which a mode leaks out of the sample. Wave localization is signaled by exponentially long dwell times for the wave. Such long decay times contribute little to the average linewidth which could be dominated by spectrally broad modes peaked near the sample boundary with short decay times. To most meaningfully capture the dynamics of a mode, it is therefore natural to identify $\delta\omega$ with the average of the inverse Thouless time, $\delta\omega \equiv \left\langle \tau_{Th}^{-1} \right\rangle = \left\langle 1/\Gamma'^{0}_{n} \right\rangle^{-1}$ where $\langle ... \rangle$ indicates an average taken over modes for an ensemble of samples and Γ_n^0 is the leakage rate of energy in the n^{th} mode of the sample [266, 301]. $\delta > 1$ is a universal criterion for localization in any dimension for any type of wave.

Thouless [266, 267] was concerned with the coupling between adjacent regions in finite samples and so with the scaling of δ as an indicator of the changing character of the electron states with sample size. However δ cannot be easily measured in electronic systems and has been measured only recently for classical waves [301]. Using the Einstein relation, which gives the conductivity in terms of a product of the electron diffusion coeffcient D and the density of states, which is $1/\Delta$ E divided by the sample volume, Thouless [267] showed that _ was equal to the conductance G in units of the quantum of conductance, $\delta = G/\left(e^2/h\right) = g$. Thouless [267] argued therefore that the dimensionless conductance would scale exponentially for localized waves as would be expected for δ. He showed that the resistance of a wire at $T = 0$ behaves ohmically [267], with the resistance increasing linearly with length L and the dimensionless conductance varying as $g = N\ell/L$, only up to a length $\xi = N\ell$, at which $\delta = 1$. Here, N is the number of independent channels that couple to the resistor, $N \sim Ak_F^2/2\pi$ where A is the cross sectional area of the sample, k_F is the electron wave number at the Fermi level, ℓ is the electron mean free path, and ξ is the localization length. For $L < \xi$ electrons di_use with residence time within the conductor of $\tau_{Th} \sim L^2/$D [266, 267]. The level width would then be δE~ $\hbar/\tau_{Th} \sim \hbar$D/ L^2, while the level spacing ΔE would scale inversely with volume of the wire as $1/L$. As a result, for $L < \xi$, δ scales as $1/L$. For $L > \xi$, electrons would be localized and δ and g would fall exponentially while the resistance would increase exponentially with L. Abrahams *et al.* [268] showed that only above two dimensions is it possible for transport to be diffive at all length scales. For lower dimensions, localization always sets in as the size of the sample increases, independent of the scattering strength, so that a transition between diffive and localized transport can only occur above two dimension [268].

The scaling of average conductance and fluctuctuation in conductance may also be calculated within the framework of random matrix theory [270, 271, 205, 312, 313]. The field in outgoing channel b is related to the field in all possible incident channels a via the field transmission matrix t, $E_b = \sum_{a=1}^{N} t_{ba} E_a$. Taking the two independent polarization states into account, the number of propagating modes in the empty waveguide leading to the sample is N=2πA/λ^2 where A is the illumination area and λ is the wavelength of the incident wave. Summing over all possible incoming and transmitted channels yields the transmittance $T = \sum_{a,b=1}^{n} \left| t_{ab} \right|^2 = \sum_{n=1}^{N} \tau_n$ [54], where the τ_n are the eigenvalues of the matrix product tt. The transmission eigenvalues can be found using the singular value decomposition of the transmission matrix t=UΛV. Here, U and V are unitary matrices and Λ is a diagonal matrix with elements $\lambda_n = \sqrt{\tau_n}$. The ensemble average of T is equal to the dimensionless conductance, $\langle T \rangle = g$. [315] Random matrix theory predicts that, for di_usive waves, the transmission eigenvalue follow the bimodal distribution, $\rho(\tau) = \frac{g}{2r\sqrt{1-r}}$ [271, 305, 312, 316]. Most of the contributions to T comes from approximately g eigenvalues that are larger than 1/e, while most of the transmission eigenvalues are close to zero. The characteristics of these "open" [317] and "closed" channels were first discussed by Dorokhov [270, 271]. He considered the scaling of each of the transmission eigenvalues which he expressed in terms of the auxiliary localization length ξn. He found that the average spacing between inverse auxiliary localization lengths of adjacent eigenchannels in a sample made up of N parallel chains with weak ransverse coupling to neighboring chains was constant and equal to the inverse of the localization length 1/ξ [270, 271].

Localization of quantum and classical waves in quasi-one-dimensional (Q1D) samples with lengths much greater than the transverse dimensions occurs at a length at which even the highest transmission eigenvalue τ_1 falls below 1/e. Thus localization will always be achieved as the sample length is increased in Q1D samples [277]. It is di_cult, however, to localize EM waves in three-dimensional dielectric materials. As opposed to s-wave scattering prevalent in electronic systems, EM waves experience p-wave scattering and cannot be trapped by a confining potential. The scattering cross section only becomes appreciable once the size of the scattering element becomes comparable to the wavelength. But once the scattering length is comparable to the wavelength, the mean free path cannot fall significantly below the scatterer size and so it is hard to satisfy the Io_e-Regel condition for localization in three dimensions, kℓ < 1. For smaller scattering elements such as spheres of radius a, the Rayleigh scattering cross section is proportional to a^6 while the density of spheres is proportional to $1/a^3$. As a result, the inverse mean free path for _xed volume fraction of particles is proportional to a^3. For high particle density and $a \ll \lambda$, the sample acts as an effective medium with mean free path $\ell \sim 1/a^3$.It is therefore not possible to achieve strong scattering with $k\ell < 1$ by crowding together small scattering elements [297]. In ordered structures, however, EM bands appear and a photonic band gap (PBG) with vanishing density of states can be created in appropriate structures with su_ciently strong contrast in dielectric constant. John [318] has pointed out that disturbing the order in such structures would create localized states within the frequency range of the band gap in analogy with the Urbach tail at the edge of the electronic band gap in semiconductors.

Though it has proven to be more diffcult to localize EM radiation than electrons in three dimensions, transport of EM radiation can be probed in ways that are often closer to the theoretical paradigm of Anderson localization than is the case for electronics. The particles of classical waves do not mutually interact as do electrons, dephasing is negligible even at room temperature and ensembles of statistically equivalent random samples can be created. For classical waves, localization is most easily achieved in low dimensional systems such as masses on a string [319], single mode optical fibers [320], single- [321] and multi-mode waveguides [296], surfaces [286], layered structures [322, 323] and highly anisotropic samples [324–326], particularly samples in which the longitudinal structure along the direction of wave propagation is uniform. Anderson localization can be expected to occur for EM radiation at the edge of the conduction or pass band in nearly periodic three dimen-sional systems. Transport near the Anderson threshold has been observed for ultrasound in a slab of brazed aluminum beads [327].

An experimentally important difference between classical and quantum transport is that coherent propagation is the rule for classical waves such as sound, light and microwave radiation in granular or imperfectly fabricated structures, whereas electrons are only coherent at ultralow temperatures in micron-sized samples. For classical waves in static samples, the wave is not inelastically scattered by the sample so that the wave remains tempo- rally coherent throughout the sample even as its phase is random in space. In contrast, mesoscopic features of transport arise in disordered electronic systems only in samples with dimensions of several microns at ultralow temperatures. Mesoscopic electronic samples are intermediate in size between the microscopic atomic scale and the macroscopic scale. Electrons are typically multiply scattered within conducting samples so their dimensions are larger than the electron mean free path, which is on the scale of or larger than the microscopic atomic spacing and electron wavelength. At the same time, electronic samples are typically smaller than the macroscopic scale on which the wave function is no longer coherent. In contrast, monochromatic classical waves are generally temporally coherent over the average dwell time of the wave within large samples. It is therefore possible to explore the statistics of mesoscopic phenomena with classical waves. Such studies may also be instructive regarding the statistics of transport in electronic mesoscopic samples. Measurements can also be made in both the frequency and time domains. The impact of weak localization can be investigated in the time domain by measuring transmission following an excitation pulse or by Fourier transforming spectra of field multiplied by the spectrum of the exciting pulse.

The connection between electronic and classical transport emerges as well from the equivalence proposed by Landauer [314, 315] of the dimensionless con-ductance g and the transmittance T, known as the "optical" conductance. The transmittance is the sum over all incident and outgoing channels of the transmission coefficient of flux. The phase of electrons arriving from a reservoir in different channels is randomized over the time of the measurement and the conductance is related to the incoherent sum of transmission coefficients over all channels, $g = \langle T \rangle = \left\langle \sum_{a,b=1}^{N} T_{ba} \right\rangle = \left\langle \sum_{a=1}^{N} T_a \right\rangle$. Measurements have been made of the statistics of transmission coefficients of the field, t_{ba}, intensity, $I_{ba} = |t_{ba}|^2$, and total transmission, $T_a = \sum_{b-1}^{N} T_{ba}$ for a single incident channel, a and for the transmittance, T.

The experimental setup for measurements of microwave transmission in the Q1D geometry described in this chapter is shown in Fig. 10.1. Measurements

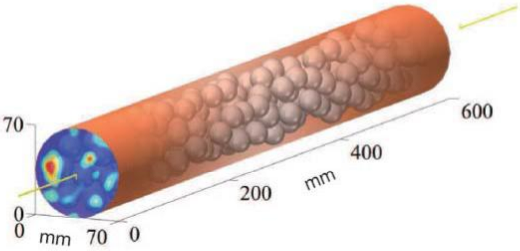

Figure 10.1 Copper sample tube containing a random medium with microwave source and detector antennas. Intensity speckle pattern is produced with a single source location.

are carried out in ensembles of random samples contained in a copper tube. The samples are random mixtures of alumina spheres with diameter of 0.95cm and index of refraction of $n = 3.14$ at a volume fraction of 0.068. Source and detector antennas may be translated over a square grid of points covering the incident and output surfaces of the sample and rotated between two perpendicular orientations in the planes of the sample boundaries. Spectra of the field transmission coefficient polarized along the length of a short antenna are obtained from the measurement of the in- and out-of-phase components of the field with use of a vector network analyzer. The intensity for a single polarization of the wave is the sum of the squares of the in- and out-of-phase components of the field. The sum of intensity across the output face for two perpendicular orientations of the detector antenna gives the total transmission. The field speckle pattern for each antenna position on the sample input is obtained by translating the detection antenna over the output surface. An example of an intensity speckle pattern formed in transmission is shown at the output of the sample tube in Fig. 10.1. The tube is rotated and vibrated momentarily after measurements are completed for each sample configuration to create a new and stable arrangement of scattering elements. In this way, measurements are made over a random ensemble of realizations of the sample. Field spectra can be Fourier transformed to yield the temporal response to pulsed excitation.

Spectra of intensity, total transmission and transmittance normalized by the ensemble average values $s_{ba} = T_{ba}/\langle T_{ba}\rangle, s_a = T_a/\langle T_a\rangle$, and $s = T/\langle T\rangle$ in a single random configuration in two different frequency ranges are shown in Fig. 10.2. Fluctuations of relative intensity are noticeably suppressed in the higher frequency range as the degree of spatial averaging increases. For the ensemble represented in Fig. 10.2, var (s_a) = 0.13 in the high frequency range and 3.88 in the low frequency range. Since waves are localized for var (s_a) >2/3 [296], this indicates that the wave is localized in the low frequency range.

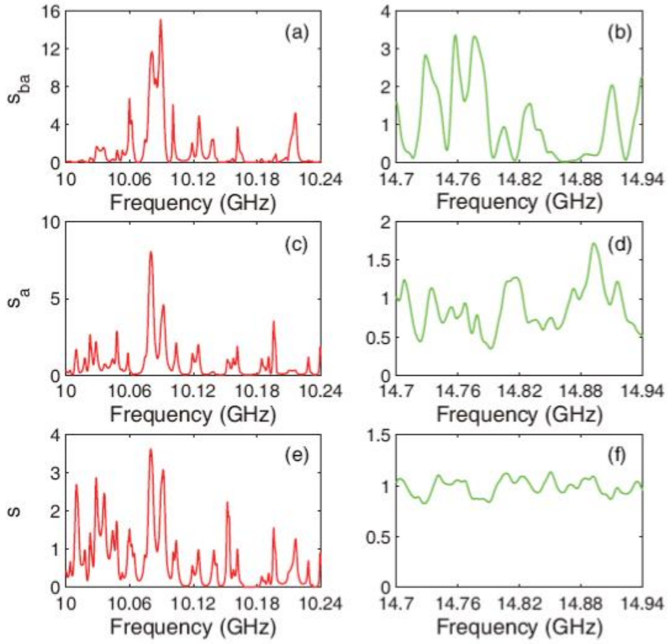

Fig.10.2 Spectra of transmitted microwave intensity, total transmission, and transmittance relative to the ensemble average value for each in a single random configuration. The wave is localized in (*a*), (*c*),and (*e*) and diffusive in (*b*), (*d*),and (*f*).

It is instructive to consider the spectra in Fig. 10.2 from both the mode and channel perspectives. When the wave is localized, distinct peaks appear when the incident radiation is on resonance with a mode. The resonance condition holds for all source and detector positions and therefore sharp peaks remain even when transmission is integrated over space. When the wave is diffusive, many modes contribute to transmission at all frequencies and for all source and detector positions. The relative coupling strengths of a single polarization component of the intensity into and out of each of these modes has a negative exponential distribution and phases of the field transmission coefficient are random so that relative fluctuations will be suppressed with increased spatial averaging. From the channel perspective, many orthogonal transmission channels contribute to transmission for diffusive waves and the coupling to channels varies with source and detector positions. Fluctuations in the incoherent sum of this random jumble of orthogonal eigenchannels are therefore suppressed upon averaging over space.

This suppresses the variance of transmission by a degree related to the number of channels that contribute substantially to transmission. This may be expressed quantitatively in term of the participation number of eigenvalue of the transmission matrix, $M \equiv \left(\sum_{n=1}^{N} \tau_n \right)^2 / \sum_{n=1}^{N} \tau_n^2$. For diffusive waves, var (s_a) ~ $1/M$ and relative fluctuations are enhanced since the number of effective channels M is smaller than the number of independent channels N. We will see below that for diffusive waves the spectrum of transmission eigenvalues is rigid so that the number of transmission eigenvalues above $1/e$ fluctuates by approximately unity and fluctuations of conductance T are of order unity [261,26 4, 317, 329–331]. This results in universal conductance fluctuations which are independent of the sample size for Q1D sample [261, 264].

The localization transition may be charted in terms of a variety of related localization parameters, all of which can be measured for classical waves. In addition to δ and the average over a random collection of samples of the dimensionless conductance, $g = \langle T \rangle$, measurements of fractional fluctuations of intensity or total transmission characterize the nature of the wave in random systems. In the diffusive limit, the variance of total transmission relative to the average value of total transmission over a random ensemble of statistically equivalent samples is inversely proportional to g, var (s_a) = $2/3g$ [263, 290–292, 296]. Since the wave is localized for $g < 1$, localization occurs when var (s_a) > 2/3. Perhaps the most easily accessible experimental localization parameter is the variance of fractional intensity, which can be expressed as var (s_{ab}) = 1 + 4/3g [31]. The localization threshold at $g = 1$ corresponds to var (s_{ab})=7/3. var (s_a) and var(sab) remains useful localization parameters even for localized waves. Fluctuations are relatively insensitive to absorption as compared to measurements of absolute transmission [296]. Mesoscopic fluctuations are directly tied to intensity correlation within the sample [280–282, 284, 322, 323]. The fractional correlation of intensity at two points on the output surface or between two transmission channels, *b* and b$'$, is equal to the variance of relative total transmission, $\kappa = \langle \delta s_{ba} \delta s_{b'a} \rangle = \text{var}\,(s_a)$. It is equal to $\langle M^{-1} \rangle$ in the diffusive limit, which is enhanced over the value of *1/N* that would be expected if mesoscopic correlation were not present.

The relationships between key localization parameters mentioned above arise since the nature of propagation in disordered Q1D samples, in which the wave is thoroughly mixed in the transverse directions, depends only on asingle dimensionless parameter [268]. For diffusive waves, $\delta = g = 2/3\ \text{var}\,(s_a) = 2/3\kappa = 2/3\ \langle M^{-1} \rangle$ The relationships $\text{var}\,(s_a) = \kappa$ and $\text{var}\,(s_{ab}) = 2\text{var}(s_a)+1$ hold through the localization transition, but the relationship between the other variable does not. However, we anticipate these relationships will change in a manner that can be described in terms of a single parameter. Other classical wave measurements that indicate the closeness to the localization threshold are coherent backscattering and the transverse spread of intensity in steady state or in the time domain. The width of the coherent backscattering peak gives the transverse spread of the wave on the incident surface and hence the transport mean free path ℓ, from which the value of $k\ell$ can be found.

10.3 Modes

We find that the fields at any point in the sample may be expressed as a superposition of the field associated with the excitation of all the modes in the sample. This superposition is a sum of products for each mode of the *j* polarization component of the spatial variation of the mode, $a_{n,j}(\mathbf{r})$, and the frequency variation of the mode, which depends only upon the central frequency of the mode ω_n and its linewidth, Γ_n,

$$E_j(r,\omega) = \sum_n a_{nj}(r) \frac{\Gamma_n/2}{\Gamma_n/2 + i(\omega - \omega_n)} = \sum_n a_{nj}(r)\varphi_n(\omega), \tag{10.1}$$

The frequency variation of the n^{th} mode $\varphi_n(\omega)$ is given by the Fourier transform of $\exp(-\Gamma_n t/2)\ \cos \omega_n t$ for $t > 0$. Equation (1) can be fit simultaneously to the field at a large number of points on the output speckle patterns in a single configuration since all spectra share a common set of ω_n and Γ_n. Armed with the values of ω_n and Γ_n, we find $a_{n,j}(\mathbf{r})$ and hence the speckle pattern for each of the modes.

The transmission spectrum is determined by the variation with position of the field amplitudes $|a_{n,j}(\mathbf{r})|$ and phases over the transmitted speckle patterns for the modes. The contribution of individual modes to transmission can be seen in the spectrum of total transmission near the single strong peak at 10.15 GHz shown in Fig. 10.3 (a) in a random sample of length L = 61 cm. The asymmetrical shape for the line in both intensity and total transmission indicates that more than a single mode contributes to the peak. The modal analysis of the field spectra shows that three modes contribute substantially to transmission over this frequency range. Spectra of the total transmission for the three modes closest to 10.15 GHz acting independently are plotted in Fig. 10.3(a). The integrated transmission for the 28th and 29th mode found in the spectrum starting at 10 GHz are each greater than for the measured peak indicating that these modes interfere destructively. The intensity and phase patterns for these two modes are shown in Figs. 10.3b-e. Aside from a difference in the average value of transmission, the intensity speckle patterns of the two modes are nearly the same. The distributions of phase shift at 10.15 GHz for the two modes are also similar except for a constant phase difference between them of $\Delta\varphi = 1.02\pi$ rad. The similarity between the speckle patterns for these overlapping modes suggests that these modes are formed from coupled resonances within the sample which overlap spatially and spectrally. We expect that such resonances peaked at different locations will hybridize to form modes of the system. Such modes may be close to symmetric and antisymmetric combinations of the two local resonances. This would produce similar intensity speckle patterns at the output with a phase shift of ~ π rad between the modes. The similarity in the intensity speckle patterns of these adjacent modes and the uniformity of the phase shift across the patterns of these modes allows for interference between modes across the entire speckle pattern. The similarity between modes is most evident in a sample configuration such that a pair of nearest neighbor modes are particularly close in frequency. This is a point of anticrossing which arises because of level repulsion inside the sample [335, 336]. The magnitude of the field inside a 1D sample is seen to be the same throughout the sample. Modes are orthogonal by virtue of a change of phase of π rad along the length of the sample. At the anticrossing, the fields at the sample output for the two modes are the same except for a change in phase close to π rad. The Thouless number, which equals the dimensionless conductance for diffusive waves, provides a key measure of the dependence of transmission on the underlying characteristics of modes. The modal decomposition of transmission spectra for the ensemble from which the configuration is analyzed in Fig. 10.3 is drawn gives $\delta = 0.17$ [331].

The statistics of level spacing was first considered by Wigner [337] in the context of nuclear levels probed in neutron scattering. He conjectured the eigenvalues of the Hamiltonian matrix would have the same statistics as the spacing of eigenvalues of a large random matrix with Gaussian elements. Agreement was found between the spacing between peaks in the scattering cross section and Wigner’s surmise for the spacing of eigenvalues of random Hamiltonian matrices. However, the analysis of spectra of nuclear scattering cross sections was done in samples with relatively sharp spectral lines. We have seen above that even when $\delta < 1$, a number of lines may coalesce into a single peak. A comparison of level spacing statistics in samples with different values of modal overlap δ in which the phase of the scattered wave can be measured

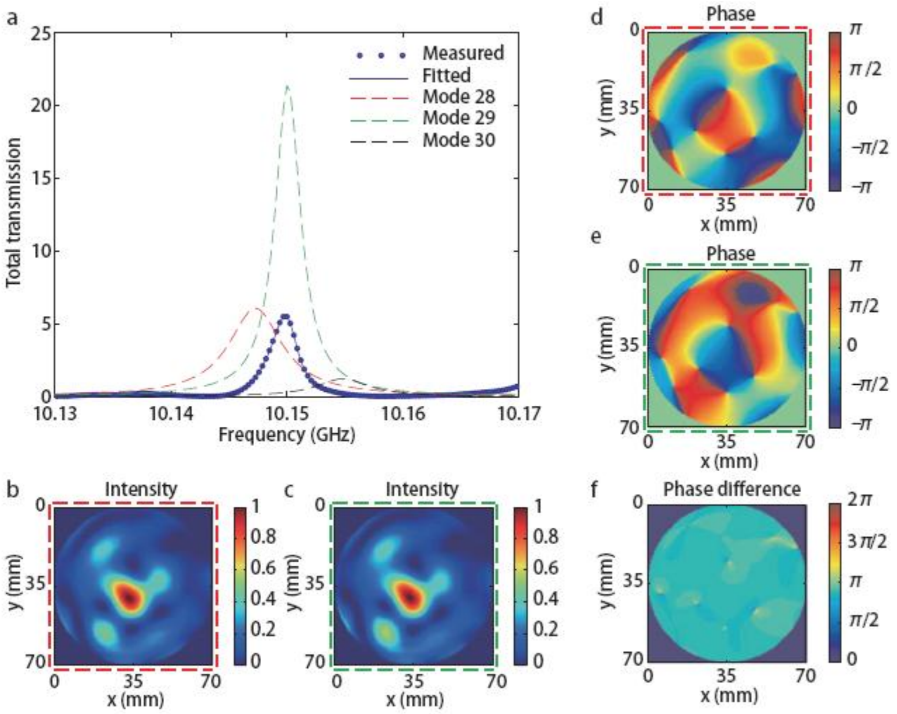

Fig. 10.3 (a) Three modes contribute to the asymmetric peak in the total transmission spectrum. Modes 28, 29 and 30 are in order of increasing frequency. Intensity speckle patterns for modes 28 and 29 are shown in (*b*) and (*c*) and the corresponding phase patterns are shown in (*d*) and (*e*). (*f*) The phase in mode 29 is shifted by nearly a constant of 1.02π rad relative to mode 28. (Ref. [41])

is therefore of interest in forming a picture of the statistics of transmission. Progressively stronger deviations from the Wigner surmise are found for decreasing values of δ.

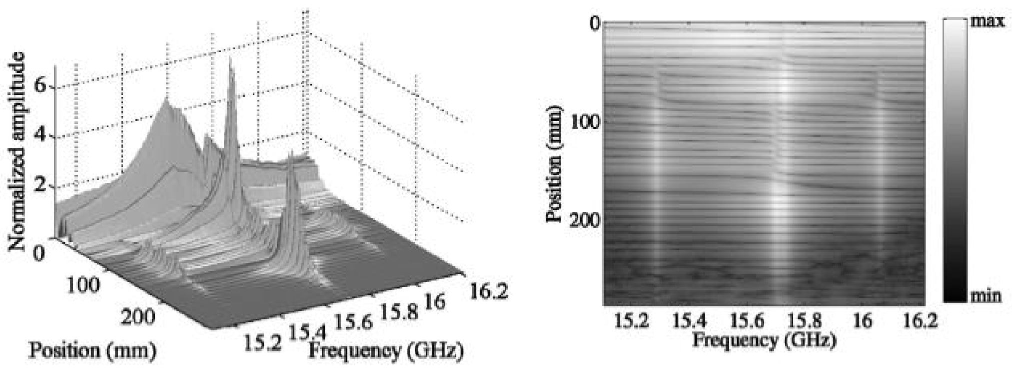

Fig. 10.4 (a) Spectra of the field amplitude at each point along a random sample with spectrally overlapping peaks normalized to the amplitude of the incident field. (*b*) Top view of (*a*) in logarithmic presentation. (Ref. [61])

It has not been possible to access the field distribution within the interior of multiply scattering three-dimensional samples, but spatial distributes can be examined in one- and two-dimensional samples [319, 321, 335]. The presence if both isolated and overlapping modes within the same frequency range has been observed in measurements of field spectra along the length of slotted single-mode random waveguides. The waveguides contained randomly positioned binary dielectric elements and a smaller number of low index Styrofoam elements. Measurements were carried out in the frequency range of a pseudogap associated with the first stop band of a periodic structure of consecutive binary elements. The density of states is particularly low in the frequency range of the band gap so that $\delta< 1$. When spectrally isolated lines are found, they are strongly peaked in space and their intensity spectra at each point in the sample is Lorentzian with the same width at all points within the sample. When modes overlap spectrally, however, spectral peaks have complex shapes which vary with position within the sample and the spatial intensity distribution is multiply peaked. Mott [338] argued that interactions between closely spaced levels in some range of energy in which $\delta < 1$ would be associated with two or more centers of localization within the sample. Pendry [339] showed that the occasional overlap of electronic states would dominate transport since regions in which the value of the electron wave function is high would not be far from both the input and output boundaries. Since the wave can then find a ready path through the sample, such modes are relatively short-lived and spectrally broad. This enhances the contribution of coupled resonances to transport. Such multiply peaked and spectrally overlapping excitations within the sample, termed "necklace states" by Pendry, are important in transmission since they arise in the localized regime and transport through isolated modes is typically small and over a narrow linewidth.

The variation in space and frequency of the amplitude of the waves within the pseudogap in a single random configuration is shown in Fig. 10.4. An additional ripple is observed in Fig. 10.4(b) in the intensity variation through the sample, corresponding to a phase shift of π rad, each time the frequency is tuned though a mode. The decomposition of field spectra inside the waveguide within the pseudogap into the modes and a background which varies slowly in frequency is shown in Fig. 10.5. The slowly varying background shown in Fig. 10.5(a) is the fit of a polynomial in the difference in frequency from a point in the middle of the spectral range considered. This background is presumably related to off-resonance excitation of many modes on either side of the band gap. The mode structure within the single-mode waveguide sample changes when a spacing is introduced between two parts of the sample and is increased gradually. A succession of mode hybridizations is observed with increasing spacing as a single mode tends to shift in frequency until it encounters the next mode. As the spacing is increased, the mode that had been moving becomes stationary and the next mode begins to move [336]. Simulations have shown that changing the index of a single scatterer leads to mode hybridization in 2D random systems, in which a single peak may be transformed to multiple peaks [335].

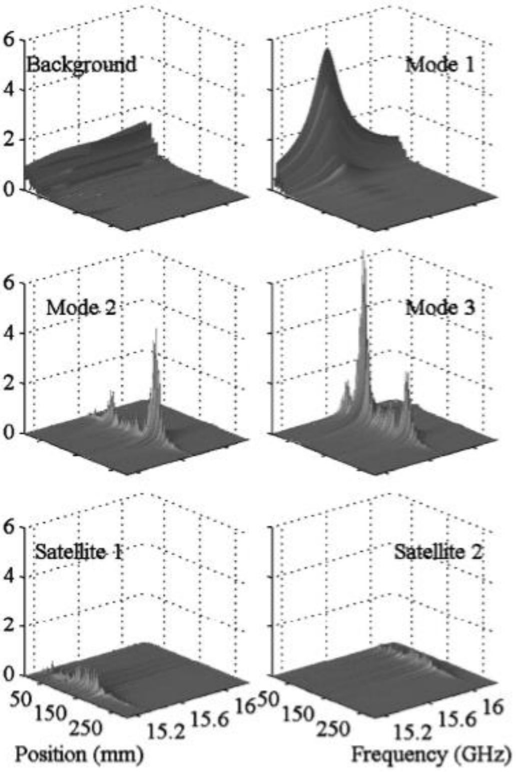

Fig. 10.5 Decomposition of field pattern in Fig. 4 into a slowly varying polynomial term and five modes. (Ref. [61])

One-dimensional localization has also been observed in optical measurements in single-mode optical fibers [320] and in single-mode channels that guide light within photonic crystals [340-342]. When the structure bracketing the channel is periodic, the velocity of the wave propagating down the channel experiences a periodic modulation so that a stop band is created. When disorder is introduced into the lattice, modes with spatially varying amplitude along the channel are created. Modes near the edge of the band gap are long lived and readily localized by disorder. An example of spectra of vertically scattered light versus frequency for light launched down a channel through a tapered optical fiber is shown in Fig.10.6. The inset shows the disordered sample of holes with random departure from circularity in silicon-on-insulator substrates at a hole filling fraction of $f \sim 0.30$.

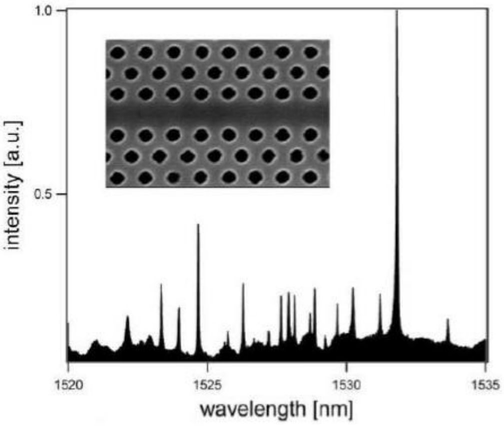

Fig. 10.6 Spectrum of wave transmitted to a region within a single-mode photonic crystal waveguide near the short wavelength edge of the first stop band at ~ 1520 nm. The channel surrounded by irregular holes is shown in the inset. (Ref. [80])

The modal decomposition method described above can be applied to localized waves for which modal overlap is relatively small. The impact of modes can be seen in the changing decay rate of transmission following pulsed excitation, even for diffusive waves. The slowing down of the decay rate with time will become more pronounced in samples in which the wave is more strongly localized [343, 345]. In the diffusive limit, the transverse extent of the modes is large and the wave is coupled to its surroundings through a large number of speckle spots. One expects therefore that the decay rate of all modes will approach the decay rate of the lowest diffusion mode [346, 347], $1/\tau_1 = \pi^2 D/(L + 2_{z0})^2$ after a time τ_1 in which higher order modes with decay rates $1/\tau_n = n^2\pi^2 D/(L + 2_{z0})^2$ have largely decayed. Here, n is the order of the diffusion mode and z_0 is the length beyond the boundary of the sample at which the intensity inside the sample extrapolates to zero. We find that pulsed transmission deviates increasingly from the diffusion model in nominally diffusive samples with $g > 1$ as the value of g decreases and the measured value of κ increases. Strong deviations from pulsed transmission in diffusing samples far from the localization threshold are observed for microwave radiation, light and ultrasound [327, 334, 348].

Measurements of pulsed transmission through a random sample of alumina spheres at low-density in samples of different length and absorption with values of κ = 0.09, 0.13, 0.25, and 0.125 are shown in Fig. 10.7 in samples A-D, respectively [348]. The decay rate of intensity is seen to deviate from the constant rate of the diffusive limit and is seen in Fig. 10.7 (b) to decreases at a nearly constant rate. A linear falloff of the decay rate would be associated with a Gaussian distribution of decay rates for the modes of the medium [343].

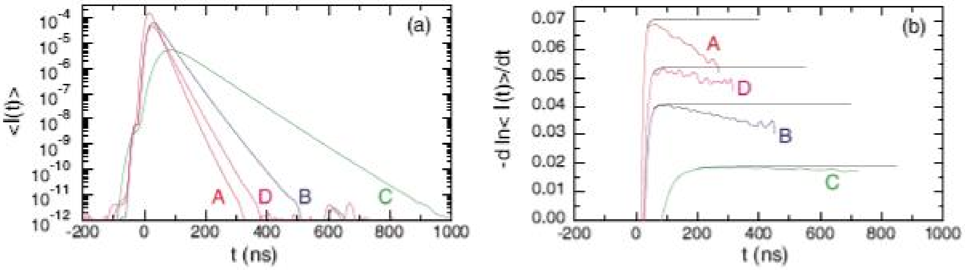

Fig. 10.7 (a) Average pulsed transmitted intensity in samples of alumina spheres with lengths, $L = 61$ cm (A), 90 cm (B and D), and 183 cm (C). Sample D is the same as sample B except for the insertion of a titanium foil inserted along the length of the sample tube D to increase absorption. (b) Temporal derivative of the intensity logarithm gives the rate γ of the intensity decay due to both leakage out of the sample and absorption. (Ref. [88])

A slightly more rapid decrease of the decay rate is associated with a slower than Gaussian falloff of the distribution of mode decay rates. The slowing down of the decay rate at long times reflects the survival of more slowly decaying modes [343, 348]. The distribution of modal decay rates is related to the Laplace transform of the transmitted pulse intensity.

Sample D is the same as sample B except for the increased absorption due to a titanium foil inserted along the length of the sample tube. The variation with time of the decay rate in sample D is the same as that in sample B except for an additional constant decay rate in sample D due to absorption. This shows that, at the low level of absorption in these samples, scattering rates are not affected by absorption and that the effect of absorption simply introduces a multiplicative exponential decay, which is the same for all trajectories at a given time. Thus the degree of renormalization of transport due to weak localization involving the interference of waves following time-reversed trajectories that return to a point in the medium is not affected by absorption. We note that the fractional reduction of the decay rate is greater at a given time delay in shorter samples with higher values of *g*. This is because the length of trajectories of partial waves within the medium is the same for all samples at a given delay but the number of crossings of trajectories is greater when the paths are congined within a smaller volume.

The temporal variation of transmission can also be described in terms of the growing impact of weak localization on the dynamic behavior of waves, which can be expressed via the renormalization of a time-dependent diffusion constant or mean free path [349]. The decreasing decay rate has also been explained using a self-consistent local diffusion theory for localization in open media [350, 351]. The theory uses a one loop self-consistent calculation of an effective diffusion coefficient that falls with increasing depth inside the sample. The spatial variation of the local diffusion coefficient reflects the increasing fraction of returns of wave trajectories to a point with greater depth due to the lengthened dwell time in the sample. This theory gives excellent agreement with recent measurements of non-diffusive decay of pulsed ultrasound transmission through a sample of aluminum spheres as seen in Fig. 10.8 [327]. The value of *g* is just beyond the localization threshold as deter mined from measurements of

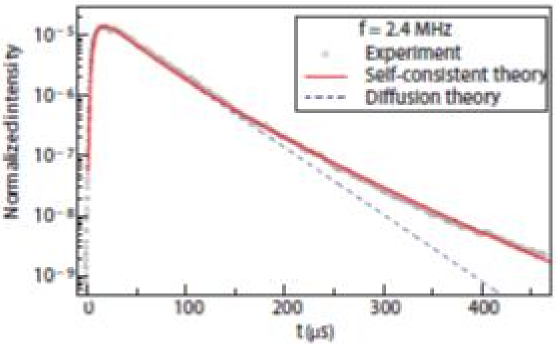

Fig. 10.8 Averaged time-dependent transmitted intensity *I(t)* normalized so that the peak of the input pulse is unity and centered on $t = 0$, at representative frequencies in the localized regimes. The data are fit by the self-consistent theory (solid curve). For comparison, the dashed line shows the long-time behavior predicted by diffusion theory. (Ref. [67])

var(s_{ba}), which is slightly above the value of 7/3 predicted as the localization threshold. The intensity distribution on the output face of the sample is found to be multifractal as predicted near the threshold for Anderson localization [343, 352]. However, the value of kl in this sample is ~ 1.5, which would indicate the wave is diffusive. Measurements of the spread of intensity on the sample output with increasing time delay show a trend towards an exponential decay of intensity on the output plane at later times supporting the localization of the wave. A similar approach to an exponential decay of intensity with transverse displacement on the sample output from the point of injection of the pulse on the incident surface has been observed by Sperling et *al.* [324] in optical measurements through a slab of titania particles. When $kl < 4.5$, the variance of the spatial intensity distribution reaches a peak value and then actually falls. This is taken as support of localization of the wave at $kl > 1$. However, this criterion for localization is directly tied to the Thouless criterion for localization $\delta = 1$.

It might also be that at later times, longer lived modes, which are more confined in space are more heavily represented and dominate the spatial distribution. Though each of these modes will not spread in time, the modes that survive with increasing time delay would be the more strongly confined modes and would lead to a falling variance of the spatial intensity distribution in time. Such states may be prelocalized with a slower falloff in space than exponential but still faster than for diffusive waves [353, 354].

The slowing of the spread of the transmitted wave in the transverse direction can also be seen in transverse localization in samples which are uniform in the longitudinal direction. This has been observed in a 2D periodic hexagonal lattice with superimposed random fluctuations [325]. The structured sample is created by first illuminating the photorefractive sample with a hexagonal optical pattern and then with a random speckle pattern of varying strength. A transition from a diffusive to a localized wave in the transverse plane is seen in the output plane with the ensemble average of the spatial intensity distribution changing from a Gaussian to an exponential function centered on the input beam as the thickness of the sample increases. Since the wave incident upon the sample, which is uniform along its length, is paraxial, it is not scattered in the longitudinal direction and travel time through the sample is proportional to the sample thickness. Transverse localization is also observed in an array of disordered waveguides lattices [326]. Measurements of pulsed microwave transmission of more deeply localized waves transmitted through a Q1D sample of random alumina spheres of thickness approximately 2.5 times the localization length, are shown in Fig. 10.9 [355]. The impact of absorption was removed statistically by multiplying

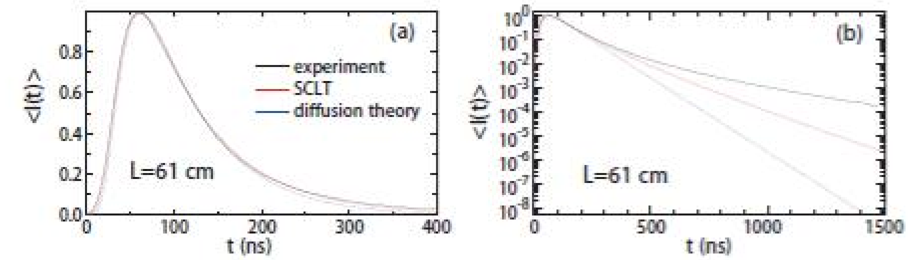

Fig. 10.9 (a) Fit of self-consistent localization theory (SCLT) (dashed curve) at early times to the average intensity response (solid curve) to a Gaussian pulse with σν = 15 MHz in a sample of length L = 61 cm and the result of classical diffusion theory (dotted curve); (b) semilogarithmic plot of hI(t)i reaching to longer times; In (a) and (b), the curves are normalized to the peak value. (Ref. [95])

the average measured intensity distribution by exp (t/τ_a) [296, 356]. For times near the peak of the transmitted pulse, diffusion theory corresponds well with the measurements of $\langle I(t)\rangle$. For times up to 4 times $\tau_D = L^2/\pi^2 D$, the decay rate of the lowest diffusion mode, pulsed transmission is in accord with self-consistent localization theory, but transmission decays more slowly for longer times. This indicates the inability of this modified diffusion theory to capture the decay of long-lived localized states. Such states are included in a position-dependent diffusion theory [357] that is in accord with simulations of the steady-state intensity profile within random systems [358]. The difference between self-consistent localization theory and the theory for position-dependent diffusion is seen to be precisely in the ability of the latter to include the impact of long-lived resonant states [357, 358].

Destructive interference between neighboring modes together with the distribution of mode transmission strengths and decay rates can explain the dynamics of transmission. The average temporal variation of total transmission due to an incident Gaussian pulse is found from the Fourier transform of the product of the field spectrum and the Gaussian pulse. The progressive suppression of transmission in time by absorption may be removed by multiplying $\langle Ta(t)\rangle$ by exp (t/τ_a) to give, $\langle T^0{}_a(t)\rangle = \langle Ta(t)\rangle \exp(t/\tau a)$ [296, 356]. With the influence of absorption upon average transmission removed, decay is due solely to leakage from the sample. The measured pulsed transmission corrected for absorption is shown as the solid curve in Fig. 10.10 and is compared to the incoherent sum of transmission for all modes in the random ensemble corrected for absorption, $\sum nT^0_{an}(t)$ shown as the dashed curve in the Fig. 10.10 $\sum nT^0_{an}(t)$ is substantially larger than $\langle T^0{}_a\ (t)\rangle$ at early times, but converges to $\langle T^0{}_a\ (t)\rangle$ soon after the peak. Though transmission associated with individual modes rises with the incident pulse, transmission at early times is strongly suppressed by the destructive interference of modes with strongly correlated field speckle patterns such as those shown in Fig. 10.3. At later times, random frequency differences between modes leads to additional random phasing between modes and averaged pulsed transmission approaches the incoherent sum of decaying modes. The decay of $\langle T^0{}_a\ (t)\rangle$, shown as the solid curve in Fig. 10.10, is seen to slow considerably with time delay reflecting a broad range of modal decay rates.

Measurements by Bertolotti *et al.* [322] of pulsed infrared transmission through random layers of porous silicon with different porosity produced by controlled electrochemical etching of silicon show that the pulse profiles depend on the degree of spectral overlap of excited modes. As the number of layers increases, spectra become sharper since propagation of a paraxial beam in the structure is essentially one dimensional and δ falls with sample thickness. When the pulse excites an isolated resonance peak, the decay rate of the falling edge of

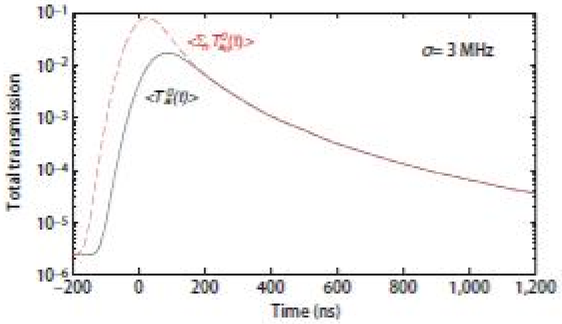

Fig. 10.10 Semilogarithmic plot of the ensemble average of pulsed transmission and the incoherent sum of transmission due to all modes in the random ensemble. (Ref. [41])

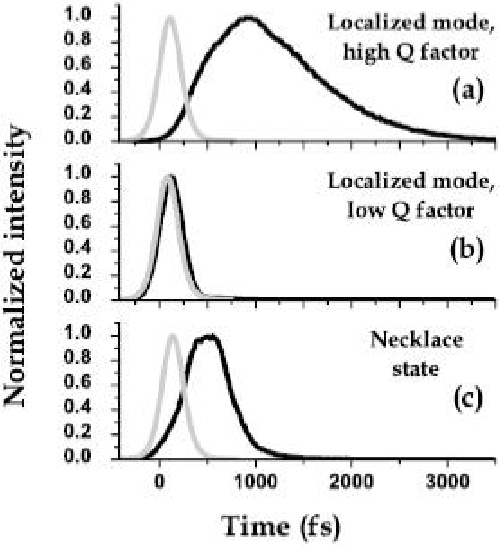

Fig.10.11 Time-resolved transmission data. In (*a*) and (*b*) the sample is excited on resonance with a sharp transmission peak, with small and large linewidths. In (*c*) a nearly symmetric pulse shape is observed that exhibits a fast decay time and a relatively large delay, typical for multiple-resonance necklace states. Sample thickness: 250 layers. Gray curves: instrumental response (cross correlation between probe and gate), corrected for the delay introduced by the effective refractive index of the sample. (Ref. [322])

the transmitted pulse is seen in Figs. 11(*a*) and (b) to be larger for the narrower spectral peak. The delayed rise in transmission seen in Fig. 10.11(a) suggests, however, that more than a single mode is involved since the interaction of a pulse with a single mode would lead to a prompt rof the falling edge of the transmitted pulse is seen in Figs. 11(a) and (b) to be larger for the narrower spectral peak. The delayed rise in transmission seen in Fig. 11(a) suggests, however, that more than a single mode is involved since the interaction of a pulse with a single mode would lead to a prompt rise in transmission as the pulse enters the sample, after which intensity decays at a constant rate. When the spectrum of the exciting pulse overlaps severalise in transmission as the pulse enters the sample, after which intensity decays at a constant rate. When the spectrum of the exciting pulse overlaps several spectral lines, a symmetrical profile for the transmitted pulse is observed, as seen in Fig. 10.11(c). These spectrally overlapping states form necklace states with a series of intensity peaks along the sample which provide a path for the wave through the medium. Such states would be expected to be short-lived.

The relationship of pulsed transmission to the transmission spectrum of microwave radiation through a sample of random dielectric spheres with $\delta = 0.43$ is shown in Fig. 10.12 [355]. The decay is slow when the spectrum of the pulse overlaps a single narrow mode and fast when two peaks fall within the spectrum of the incident pulse. In the latter case, the transmitted intensity is significantly modulated at the frequency difference between the modes.

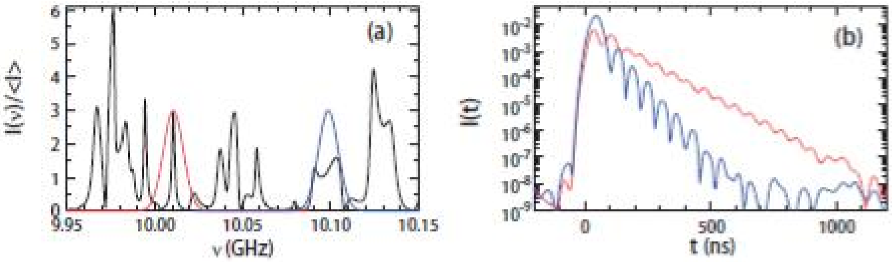

Fig. 10.12 (a) Transmitted intensity spectrum in a random sample of L = 40 cm and Gaussian spectra of incident pulses peaked at the center of the isolated line and overlapping lines. (*b*) Intensity responses to the Gaussian incident pulses with spectral functions shown in (*a*). (Ref. [95])

In addition to the reduction of the leakage rate with increasing delay observed in diffusive samples, the variance of relative intensity fluctuations and the degree of intensity correlation also increase with time delay [359–361]. The field correlation function with displacement and polarization rotation in pulsed transmission is the same as in steady state [359]. This reflects the Gaussian statistics within the speckle pattern of a given sample configuration and time delay. The intensity correlation function at a given time delay depends on the square of the field correlation function and the degree of intensity correlation in the same way as in steady state, but the degree of extended range correlation $k_\sigma(t)$ depends on delay time and on the spectral bandwidth of the pulse σ. The probability distribution functions of intensity at various delay times have the same form as for steady state propagation and depend upon a single parameter, which is the variance of the total transmission relative to its average over the ensemble, which equals the degree of intensity correlation at that time, $\mathrm{var}(s_a(t))=\kappa_\sigma(t)$. The time variation of $\kappa_\sigma(t)$ reflects the number of modes and the degree of correlation in the speckle pattern of the modes. Since strong correlation in the speckle patterns of a number of modes tends to produce a single transmission channel formed from these modes while correlation at any time is directly related to the number of channels contributing to transmission at that time, modal speckle correlation tends to increase the degree of intensity correlation.

For narrowband excitation, $\kappa_\sigma(t)$ first falls before increasing at later times since transmission at early times is dominated by a subset of short-lived modes among all the modes overlapping the spectrum of the pulse that promptly convey energy to the output [361]. At later times, only the longlived modes contribute to transmission and so the degree of correlation increases with time. But at intermediate times, when both short- and longlived modes contribute to transmission, the number of modes and hence the number of channels contributing is relatively high. This is inversely proportional to the degree of correlation so that $\kappa_\sigma(t)$ reaches a minimum.

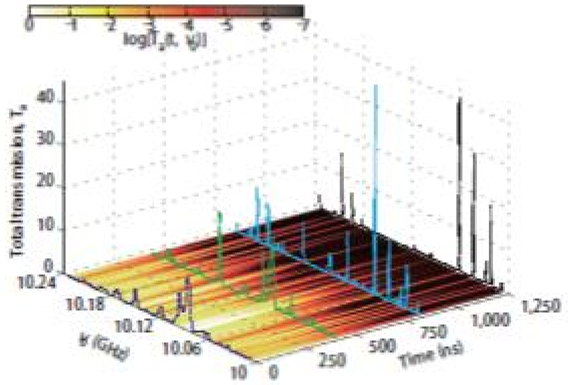

Fig. 10.13 Logarithm of time-frequency spectrogram of total transmission plotted in the x-y plane following the color bar. The central frequency v_0 of the incident Gaussian pulse of linewidth σ =50.85 MHz is scanned. Each of the four spectra of total transmission at different delay times are normalized to the total transmission at that time.

The changing distribution of modes contributing to transmission is seen in the time-frequency spectrogram for a sample with L = 61 cm and δ = 0.17 in Fig. 10.13. The spectrogram is formed from measurements of transmission at the output of a sample for an incident Gaussian pulse with width σ of its Gaussian spectrum as the central frequency of the pulse is tuned. The decay rate of the peak intensity of the mode at long times when isolated modes emerge in the time-frequency spectrogram is equal to the linewidth of the mode Γ_n to within experimental error of 10%.

10.4 Lasing in localized modes

The nature of propagation divides according to the character of the modes of the medium. For $\delta > 1$, transport can be described in terms of diffusing particles of the wave with transmission falling inversely with sample thickness, while for $\delta < 1$ transport is via tunneling through localized or multipeaked modes with average transmission falling exponentially. Since the location and intensity of pump excitation within the sample and the lifetime of emitted photons within the gain region in which stimulated emission occurs depend upon the character of modes, lasing characteristics depends crucially upon the value of δ.

For δ » 1 in random amplifying samples, nonresonant random lasing occurs. This can be described in terms of the densities of diffusing pump and emission photons and their coupling to energy levels whose occupation are described in terms of rate equations [362–364]. Very different behavior arises in the regime δ ~1, which can arise in strongly scattering but still diffusive samples which are not more than a few wavelengths thick [105, 106] and in 2D samples [367], in which the laser beam is tightly focused to create a small excitation volume [368, 369]. A small number of spectral peaks may then be observed in emission. These peaks sharpen up in the presence of gain due to enhanced stimulated emission in longer lived, spectrally narrow modes [365].

Letokhov [360] considered the lasing threshold in a spherical sample with uniform gain which is directly analogous to the critical condition for a nuclear chain reaction. Lasing occurs when on average more than one new photon is created for each photon that escapes the medium. Lasing was subsequently considered in granular media and in colloidal samples composed of dielectric particles in dye solution. Lasing in amplifying colloids reported by Lawandy *et al.* [361] is of particular interest since the strength of scattering and amplification can be controlled independently. A narrowing of emission and a shortening of the emitted pulse was observed above a threshold in pump power. A comparison of the emission spectrum in a neat dye solution and in colloidal solutions is shown in Fig. 10.14. The original studies were carried out in weakly scattering samples excited over transverse dimensions much greater than the sample thickness, which itself was not much thicker than the mean free path. Wiersma *et al.* [362] suggested that the observations reported could be due to scattering of light into transverse directions and its subsequent redirection out of the sample by another scattering event.

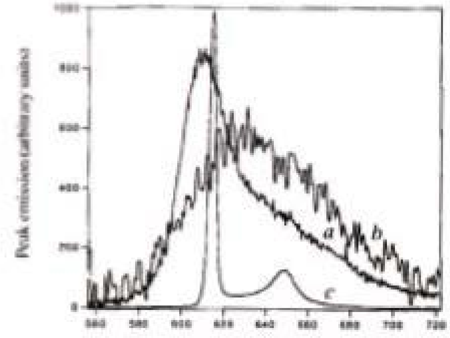

Fig. 10.14 (a) Emission spectrum of a 2.5 × 10^{-3} M solution of R640 perchlorate in methanol pumped by a 3-mJ (7 ns) pulses at 532 nm. (b) and (c) Emission spectra of the TiO_2 particles (2.8 × 1010 cm^{-3} colloidal dye solution pumped by 2.2 μJ and 3.3 mJ pulses, respectively. Emission: (b) scaled up 10 times, (c) scaled down 20 times. (Ref. [361])

The lasing threshold is typically not suppressed substantially below the threshold for amplified stimulated emission in a neat dye solution. Light penetrates a depth into the sample equal to the absorption length of the pump radiation $L_a = \sqrt{D\tau_a} = \sqrt{\ell\ell/3}$ which is the same as the exponential falloff with thickness of transmission in diffusing systems with loss [363]. Here $1/\tau_a$ is the absorption rate, ℓ the transport mean free path, $\ell_a = v\tau_a$ the length of the trajectory in which the intensity falls to 1/e due to absorption, and v is the transport velocity [364]. The excitation region illustrated in Fig. 10.15 is near the boundary so that the typical length of the paths of emitted photons would be comparable to those of the pump photons of ~ ℓ_a [365]. But this is the length over which stimulated emission occurs in a neat solution. So the lasing threshold may not be lowered below the value at which appreciable amplified spontaneous emission occurs in a neat dye solution. The lasing threshold could be lowered by increasing the residence time inside the medium in samples with a shorter mean free path at the emission frequency than at the pump frequency or by internal reflection at the boundary. Above threshold, the optical transition pumped may be saturated so that absorption is suppressed and the wave can penetrate deeper into the sample.

The lasing threshold can be dramatically suppressed, however, for localized waves. When $\delta < 1$, the intensity within the sample may grow exponentially when on resonance with a localized state far from the boundary. The excited region may then be in the middle of the sample and so emission will be into modes that overlap the excited mode and are similarly peaked in the middle of the sample and so are long lived. This was demonstrated in low-threshold lasing excited by a beam incident normally upon stacks of glass cover slips with

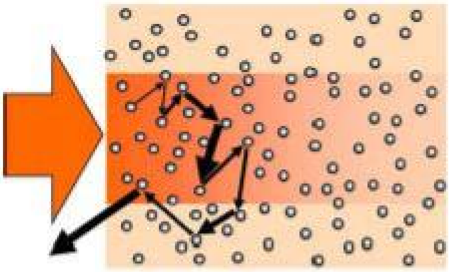

Fig. 10.15 Possible path for a photon emitted and amplified within a dye medium containing random scatterers. The lighter region indicates the volume pumped by the laser. (Ref. [365])

thickness of approximately 100 μm and intervening air layers of random thickness and with Rhodamine 6G dye solution between some of the slides . A plane wave incident upon parallel layers of random thickness is a one-dimensional medium and will be localized in the medium. In the present circumstance, the layers are not perfectly parallel and so light is scattered off the normal. This leads to a delocalization transition with a crossover at a thickness at which the transverse spread of an incident ray is equal to the size of the speckle spots formed. Beyond this thickness, the sample becomes three dimensional with regard to propagation of the initially normally incident beam. The spread of the beam is abetted by the thick layers used and could be reduced dramatically if layers with thickness ~ λ/4 were used.

Emission spectra excited by a pulsed Nd:YAG laser at 532 nm in a stack of cover slides with intervening dye solution recorded with a 0.07-nm-resolution grating spectrometer are shown in Fig. 10.16. The broad emission spectrum of the neat dye solution in Fig. 10.16(a) is compared with the emission spectrum from the random stack with interspersed dye layers slightly below and above the lasing threshold. Below threshold, the spectrum shows resolution-limited peaks of the electromagnetic modes of the system. Above threshold, a collimated emitted beam perpendicular to the sample layers was observed. The lasing spectrum with baseline shifted up for clarity is shown in Fig. 10.16 (b). An abrupt change in the output power with increasing pump energy occurs at the lasing transition seen in the inset in Fig. 10.16(b). Just above threshold, lasing occurs in a single narrow line (Fig. 10.16(b)), while at higher energies, multimode lasing was observed (Fig. 10.16(c)) with wavelength and intensity that vary randomly with the position of the pump beam on the sample surface. The lasing threshold was low enough so that lasing could be observed with a chopped continuous wave Argon-ion laser beam at 3W at 514.5 nm.

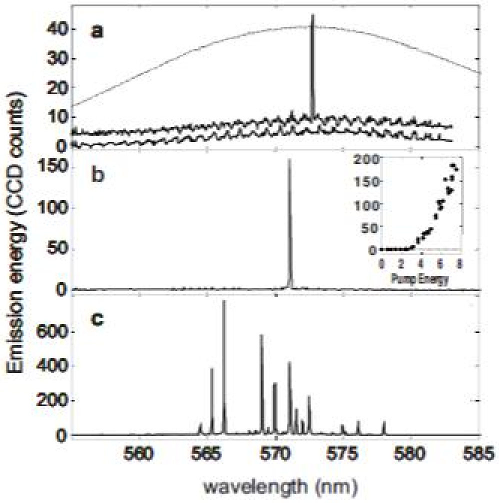

Fig. 10.16 (a) Spectra of spontaneous emission in neat solution and of spontaneous emission and near threshold lasing from Rhodamine 6G placed between layers of a glass slide stack at different laser pump energies.(b) Lasing in a single line above threshold and (c) in multiple lines well above threshold. The inset in (b) shows the sharp onset of lasing above threshold for excitation at a particular portion of the glass stack.

The role of resonance with localized modes at both the pump and emission wavelengths is seen in the strong correlation of pump transmission and output laser power. Such strong correlation is opposite to what would be expected for a nonresonant random laser in which peak emission would correspond to maximal absorption and so with reduced transmission.

Low-threshold lasing via emission into long-lived modes excited by a pump laser which penetrates deeply into a sample can be realized in periodic and nearly periodic structures. For 1D samples or for layered structures in which the dielectric function is modulated only along a single direction, stop band are seen in the transmission spectrum perpendicular to layers. This is the case even when the layers are anisotropic with an orientation that varies with depth. The states at the edge of the band are long lived and can be excited via emission from excited states of dopants in the periodic structure or of the structure itself when pumped by an external beam falling within the frequency range of the pass band. A coherent beam perpendicular to the layers then emerges without special alignment.

In an infinite structure, the group velocity vanishes as the band edge is approached. This leads to the expectation of a lowered lasing threshold at the edge of a photonic band gap [366]. But in periodic structures of finite thickness, states at the band edge are standing Bloch waves with a low number n of anti-nodes in the medium rather than traveling waves [367]. The intensity of the wave in each of these states is modulated by an envelope function $sin^2\ n\pi x/L$, where x is the depth into the sample of thickness L. Lasing properties are determined by the modes with increasingly narrow linewidths and intensity as the band edge is approached. The width of modes increases as n^2 away from the band gap.

Band edge lasing was demonstrated in dye-doped cholesteric liquid crystals (CLCs) [313]. Lasing from dye-dope CLCs was observed earlier and attributed to lasing at defect sites in the liquid crystal [368]. Roughly parallel rod-shaped molecules in CLCs with average local orientation of the long molecular axis in a direction called the director rotate with increasing depth into the sample. This periodic helical structure can be either right- or lefthanded. The indices for light polarized parallel and perpendicular to the director are the extraordinary and ordinary refractive indices, n_e and n_o, respectively. For sufficiently thick films, the reflectance of normally incident, circularly polarized light with the same sign of rotation as the CLC structure is nearly complete within a band centered at vacuum wavelength $\lambda_c = nP$ where $n = (n_e + n_o)/2$ and P is the pitch of the helix equal to twice the structure period. The reflected light has the same sign of rotation as the incident beam. The bandwidth is $\Delta\lambda = \lambda_c \Delta n/n$, where $\Delta n = n_e - n_o$. For circularly polarized light of opposite circular polarization, the wave is freely transmitted. In measurements on dye-doped cholesteric liquid crystal (CLC) films, spontaneous emission is inhibited within

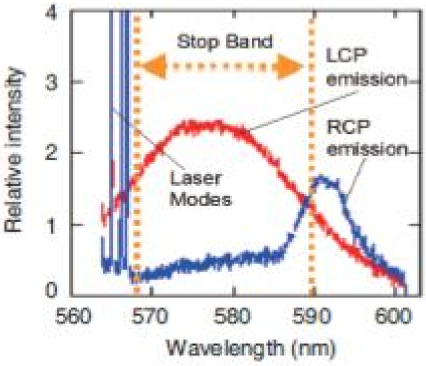

Fig. 10.17 Left and right circularly polarized emission spectra from a right handed dye-doped CLC sample as well as lasing emission at the shortwavelength edge of the reflection band. The height of the lasing lines is ~50 units. (Ref. [43])

the band and the density of states is enhanced at the band edge for light polarized with the same handedness as the chiral structure. Light of opposite chirality is unaffected by the periodic structure. This makes it possible to make a direct measurement of the density of photon states by comparing the emission spectra of oppositely polarized radiation. The observed suppression of the density of states within the band and the sharp rise at the band edge are shown in Fig. 10.17 and seen to be in good agreement with the calculated density of states in a 1D structure. The left circularly polarized (LCP) emission spectrum in this right handed structure is due to the spontaneous emission of the PM-597 dye. RCP emission is suppressed in the stop band and peaked at the band edges. The RCP light seen within the reflection band does not vanish because the emitted LCP light is converted to RCP light in Fresnel reflection from the surfaces of the glass sample holder. Multiple lasing lines are seen at the short-wavelength band edge.

The lasing peaks in Fig. 10.17 do not correspond precisely to the modes of a perfectly periodic CLC structure. These modes are seen in transmission spectra in Fig. 10.18 in a dye doped CLC sample which was carefully prepared and allowed to equilibrate. A comparison between transmission measured with a tunable narrowband dye laser in a 37-μm thick CLC sample with moderate absorption and simulations for a periodic system is shown below. The simulated spectrum is displaced vertically for visibility. In a nondissipative sample, the resonance transmission of all modes modes reaches unity. In Fig. 10.18, transmission through modes closest to the band edge is most suppressed by absorption since these modes are longest lived. Since the modes closest to the band edge are longest lived in nearly periodic systems, these states are most susceptible to being localized by disorder. Such localized states are often longer lived than the corresponding states of a periodic system and so disorder can help as well as hinder lasing.

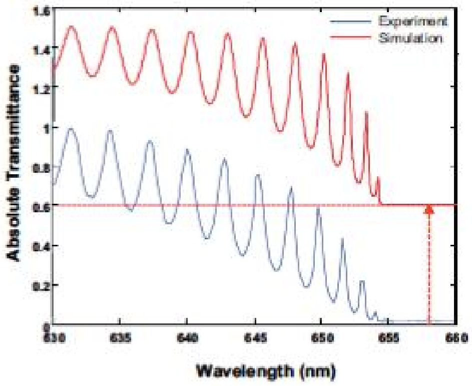

Fig.10.18 Comparison of measurements of transmission spectra in dyedoped CLC taken by Valery Milner in the lower curve with simulations in the upper curve. The linewidth narrows as the index *n* of the mode away from the band edge decreases. Differences between the frequencies of laser lines seen in Fig. 10.17 and frequencies of lines in high quality CLC samples in this figure are due to disorder in the sample of Fig. 10.17.

Simulations in random amplifying systems show that it is possible to maximize the lasing intensity at a particular frequency in the spectrum of a random laser by iteratively feeding back the intensity at a selected frequency to vary the intensity distribution of the pump beam [369]. The modes of the sample are not substantially modified in the lasing transition, but the spectral properties of the modes excited by the pump beam are selected by the spatial profile of the pump beam. T¨ureci et al. have shown that modes of passive diffusive systems interact via the gain medium to create a uniform spacing in the laser spectrum [370]. In contrast, isolated modes of localized lasers interact weakly and emit at a frequencies pegged to the modes of the passive systems [371]

10.5 Channels

Transmission through a disordered medium is fully determined by the transmission matrix t .The optical transmission matrix was measured by Popoff et al. [307] with use of a spatial light modulator (SLM) and an interference technique to find the amplitude and phase of the optical field. Measuring the transmission matrix allows one to focus the transmitted light at a desired channel at the output surface by phase conjugating the transmission matrix [307, 309]. In this way, the transmitted field from different input channels arrives in phase at the focal spot and interferes constructively. The presence of a random medium can increase the number of independent channels that illuminate a point so that the focused intensity and resolution are enhanced [362–364]. Because of the enormous number of channels in optical experiments, only a small portion of the transmission matrix is typically measured. The distribution of the singular values of the transmission matrix may then follow the quarter circle law which is characteristic of uncorrelated Gaussian fluctuations of the elements of the transmission matrix [375, 376]. Measurements of microwave radiation propagation through random media confined in a waveguide allow us to measure the field on a grid of points for the source and detector [302]. The closest spacing between points is approximately the distance at which the field correlation function vanishes so that the fields at different points on the gird are only weakly correlated.

The number of independent channels N supported in the empty waveguide is ~ 66 in the frequency range of 14.7-14.94 GHz in which the wave is diffusive and ~ 30 from 10-10.24 GHz in which the wave is localized within the sample. To construct the transmission matrix, *N/2* points are selected from each of two orthogonal polarizations. A representation of intensity patterns in typical transmission matrices for both diffusive and localized waves at a given frequency is presented in Fig. 10.19. Each column presents the variation of intensity across the output surface at points b for a source at points a with two orthogonal polarizations. The intensity in each column shown in Fig. 10.19 is normalized by its maximum value. For localized waves, intensity patterns in each column are similar indicating that transmission is dominated by a single channel. In contrast, no clear pattern is seen for diffusive waves since many channels contribute to the intensity at each point.

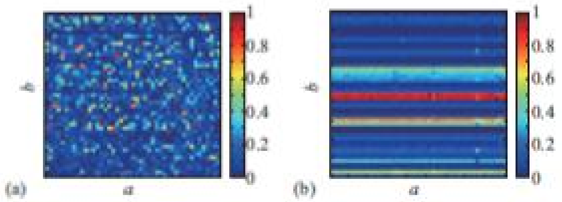

Fig. 10.19 Intensity normalized to the peak value in each speckle pattern generated by sources at positions a are represented in the columns with index of detector position and polarization *b* for (*a*) diffusive and (*b*) localized waves. (Ref. [46])

In Fig. 10.20, we show a spectrum of the optical transmittance and the underlying transmission eigenvalues from a single random realization for both localized and diffusive waves. This confirms that the highest transmission channel dominates the transmittance for localized waves while several channels contribute to transmission for diffusive waves. Thus for localized waves, the incident wave from different channels couples to the same eigenchannel and excites the same pattern in transmission as seen in Fig. 10.19(b). In contrast, the transmission patterns for incident waves for different incident channels are the sums of many orthogonal eigenchannels so that the transmitted patterns are weakly correlated.

Dorokhov [270, 271] showed that, the spacing between the inverse of the localization length for adjacent eigenchannels is equal to the inverse of the localization length of the sample, $\frac{1}{\xi_{n+1}}-\frac{1}{\xi_{n+1}}=\frac{1}{\xi}$. For localized waves, this is equivalent to $\langle \ln \tau_n \rangle - \langle \ln \tau_{n+1} \rangle = L/\xi = 1/g_0$, where g_0 is the bare conductance that one would obtain in the absence of wave interference and the transport can be described in terms of diffusion of particles. In Fig.10.21,

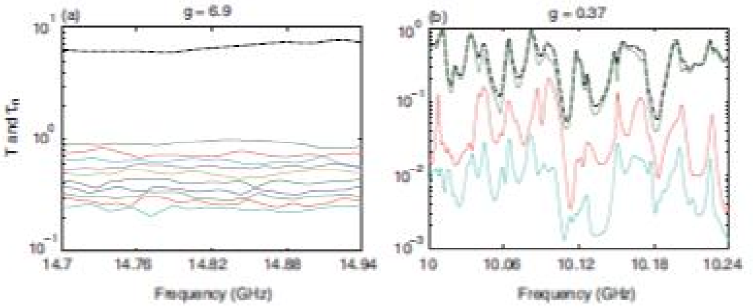

Fig. 10.20 Spectra of the transmittance *T* and transmission eigenvalues τ_n for (a) diffusive sample of L = 23 cm with g=6.9 and (b) localized sample of L = 40 cm with g=0.37. The black dashed line gives *T* and the solid lines are spectra of τ_n. (Ref. [302])

we show that $\langle \ln \tau_n \rangle$ falls linearly with respect to the channel index n for both diffusive and localized waves. We denote the constant spacing between adjacent values of $\langle \ln \tau_n \rangle$ as $1/g^n$, $\langle \ln \tau_n \rangle - \langle \ln \tau_{n+1} \rangle = 1/g''$. This supports the conjecture that g^n is the bare conductance.

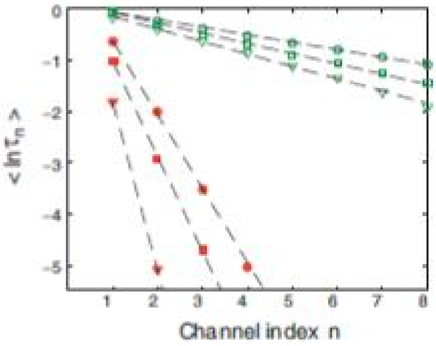

Fig. 10.21 Variation of hln τni with channel index n for sample lengths $L = 23$ (circle), 40 (square) and 61 (triangle) cm for both diffusive (green open symbols) and localized (red solid symbols) waves fitted, respectively, with black dashed lines.

We expect that the bare conductance should be influenced by the wave interaction at the sample interface . The wave interaction at the sample boundary can be described by a diffusion model [329] in which the incident wave is replaced by an isotropic source at a distance z_p from the interface in which the wave direction is randomized and with a length z_0, which is the length beyond the sample boundary at which the intensity inside the sample extrapolates to zero. z_0 was found by fitting the time of flight distribution of wave through random media [318, 320]. Once the surface effect is taken into account, the bare conductance is given as: $g = \eta\xi/L_{eff}$, where η is a constant of order of unity and $L_{eff} = L + 2z_0$ is the effective sample length. The constant value of $g'' L_{eff}$ seen in Fig. 10.22 is consistent with g 00 being the bare conductance and gives the localization length for the samples at two frequency ranges. The absolute values of the transmittance T and of the underlying transmission eigenvalues τn are obtained by equating $\langle T \rangle = Cg''$ for the most diffusive sample of length $L = 23$cm, at which the renormalization of dimensionless conductance due to wave localization is negligible. The normalization factor C is used to determine the values of g for other samples.

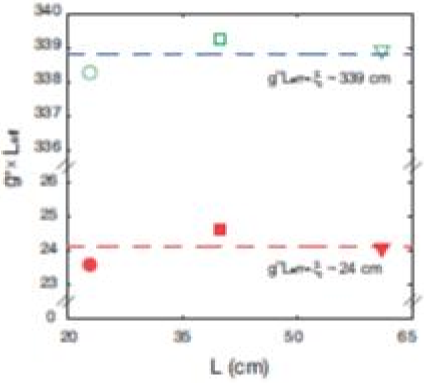

Fig. 10.22 The constant products of $g'' L_{eff}$ for three different lengths for both diffusive and localized samples give the localization length ξ in the two frequency ranges. (Ref. [42])

The probability density of ln τ_n of the first few eigenchannels and their contribution to the overall density ln τ is shown in Fig. 10.23 for the most diffusive sample with $g = 6.9$. Aside from the fall of the probability distribution P (ln τ) near ln τ ~ 0, which reflects the restriction $\tau_1 \leq 1$, P(ln τ) is nearly constant with ripples spaced by 1/g''. The nearly uniform density P(ln τ) of corresponds to a probability density $P(\tau) = P(\ln\tau)\ \frac{d\ln\tau}{d\tau} = g/\tau\ = g/\tau$. This distribution has a single peak at low values of τ , in contrast to the predicted bimodal distribution, which has a second peak nearly unity [271, 305, 312, 361]. This may reflect the fundamental difference of measuring the transmission matrix based on scattering between independent discrete points instead of waveguide modes. In theoretical calculation in which scattering between waveguide modes is treated, all the transmitted energy can be captured. However, only a fraction of energy transmitted through the disordered medium is captured when the TM is measured on a grid of points. As a result, full information is not available and the measured distribution of transmission eigenvalues does not accurately represent the actual distribution in the medium. In particular the bimodal

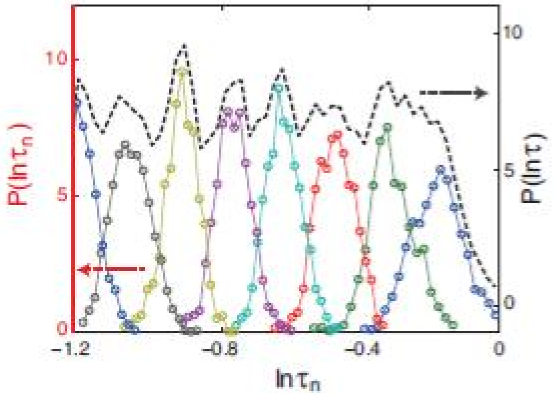

Fig. 10.23 Probability density of ln τ_n (lower curves) and the density of ln τ (top dashed curve), P(ln τ) = $\Sigma_n P(\ln\tau_n)$ for the diffusive sample with g=6.9.

distribution of transmission eigenvalues is not observed. This has been suggested in recent simulation of a scalar wave propagation in Q1D samples based on recursive Greens function method. Goetschy and Stone [372] have recently calculated the impact of degree of control of the transmission channels on the density of transmission eigenvalues. The matrix t is mapped to $t' = P_2tP_1$, where P_1, P_2 are $N \times M_1$ and $M_2 \times N$ matrices which eliminate $N - M_1$ columns and $N - M_2$ rows, respectively, of the original random matrix t. Therefore, only $M_1(M_2)$ channels are under control on the input (output) surface, respectively, and the degree of control on the input and output surfaces is measured by M_1/N (M_2/N). As a result, the density of transmission eigenvalues for diffusive samples changes from a bimodal distribution to a distribution characteristic of uncorrelated Gaussian random matrices, when the degree of control is reduced [302, 307]. Nevertheless, key aspects of the statistics of wave propagation and the limits of control of the transmitted wave can be explored using measurements of the transmission matrix.

Measuring the transmission matrix allows us to explore the statistics of transmittance, the most spatially averaged mesoscopic quantity. The importance of sample-to-sample fluctuation of conductance in disordered conductors was first recognized in conduction mediated by localized states, but fluctuations in transmission were first observed in the constant variance of fluctuations of conductance in diffusive samples known as universal conductance fluctuations . For diffusive waves, for which a number of transmission eigenchannels contribute substantially to the transmittance, the probability distribution of T is Gaussian with variance independent of the mean value of T and of sample dimensions. In the localization limit, $L/\xi \gg 1$, in which transmittance T is dominated by the largest transmission eigenvalues, $T \sim \tau_1$, the single parameter scaling (SPS) theory of localization predicts that the probability distribution of the logarithm of transmittance in 1D samples is a Gaussian function with a variance equal to the average of its magnitude, $\mathrm{var}(\ln T) = -\langle \ln T \rangle$. Therefore, the scaling of average of conductance and the entire distribution of conductance is determined by the single parameter $|\langle \ln T \rangle|/L = 1/\xi$. In recent work, the ratio $R \equiv -var(ln\ T)/\ \langle \ln T \rangle$, is found to approach unity in Q1D samples showing that propagation in Q1D in this limit is one-dimensional .

In the Q1D geometry, there is no phase transition between localization and diffusion as L increases for samples with equivalent local disorder. Instead, there exists a crossover from the diffusive to localized regime. For samples just beyond the localization threshold, in which only a few transmission eigenchannels contribute appreciably to the transmittance, numerical simulation [385–389] and random matrix theory calculation . by Muttalib and W¨olfle found a one-sided log-normal distribution for the transmittance. The source of this unusual probability distribution of conductance can be understood with the aid of the charge model proposed by Stone, Mello, Muttalib, and Pichard [405]. The charge model was first introduced by Dyson [391] to visualize the repulsion between eigenvalues of the large random Hamiltonian. In this model, transmission eigenvalues τn are associated with positions of parallel line charges at x_n and their images at $-x_n$ embedded in a compensating continuous charge distribution. The transmission eigenvalues are related to the x_n via the relation, $\tau_n = 1/\cosh^2 x_n$. The repulsion between two parallel lines of charges of the same sign with potential $\ln |x_i - x_j|$ mimics the interaction between eigenvalues of the random matrix. The oppositely charged jellium background provides an overall attractive potential that holds the structure together. The repulsion between charges for diffusive waves is the origin of universal conductance fluctuation. For localized waves, the charges are separated by a distance greater than the screening length due to the background charges so that the “Coulomb” interaction is screened. The repulsion between the first charge at x1 associated with the highest transmission eigenvalues τ_1 and its image placed at $-x_1$ provides ceiling of unity.

We have recently reported microwave measurements of the probability distribution of the“optical” transmittance T in the crossover from diffusive to localized waves . A Gaussian distribution is found for diffusive waves and a nearly log-normal distribution for deeply localized waves. Just beyond the localization threshold, a one-sided log-normal distribution is observed for an ensemble with g=0.37. In this ensemble, an exponential decay of $P(T)$ is found for high values of transmittance as was found in simulations and calculations [402]. The rapid falloff of $P(T)$ for $T > 1$ is due to the requirement that two eigenvalues need to be high in this case. This requires that two charges as well as their images be close to the origin. The probability for high values of T is therefore greatly suppressed due to the repulsion between these charges.

Measurements of the transmission matrix provide the opportunity to investigate the statistics in single disordered samples as opposed to the statistics of ensembles of random sample. Such statistics are essential in applications such as imaging and focusing through a random medium. In the Q1D geometry, in which the wave is completely mixed within the sample, the statistics of the intensity relative to the average over the transmitted speckle pattern, $T_{ba}/\left(\sum_{b=1}^{N} T_{ba}/N\right) = NT_{ba}/T_a$, is independent of source or detector positions [403, 404]. Because of the Gaussian distribution of the field in any single speckle pattern, the probability distribution of relative intensity is $P(NT_{ba}/T_a) = \exp(-NT_{ba}/T_a)$. Since the statistics of relative intensity are universal, the statistics of the transmission in a sample with transmittance T would be completely specified by the statistics of total transmission T_a relative to its average (T/N) within the sample.

We find in random matrix calculations that the variance of normalized total transmission within a single instance of a large transmission matrix is equal to the inverse eigenchannel participation number [306],

$$var(NT_a/T) = M^{-1}\ . \tag{10.2}$$

These results can be compared to measurements in samples of small N by grouping together measurements in collections of samples with similar values of M. We show in Fig. 10.24 that the average of var(NT_a/T) in subsets of samples with given M^{-1} is in excellent agreement with Eq. 10.2. var[var(NT_a/T)/M^{-1}] is seen in the insert of Fig. 10.24 to be proportional to $1/N$ indicating that fluctuations in the variance over different subsets are Gaussian with a variance that vanishes as N increases.

The central role played by M can be appreciated from the plots shown in Fig. 10.25 of the statistics for subsets of samples with identical values of M but drawn from ensembles with different values of g. The distributions $P(NT_a/T)$ obtained for samples with M^{-1} in the range 0.17 ± 0.01 selected from ensembles with g=3.9 and 0.17 are seen to coincide in Fig. 10.25(a) and thus to depend only on M^{-1}. The curve in Fig. 10.25(a) is obtained from an expression for P(sa) for diffusive waves given in Refs. [290, 291], in terms of a single parameter g=2/3var(sa) but with the substitution of 2/3M−1 for g. The dependence of $P(NT_a/T)$ on M^{-1} alone and its independence of T is also demonstrated in Fig. 10.25(b) for M^{-1} over the range 0.995 ± 0.005 from measurements in samples of

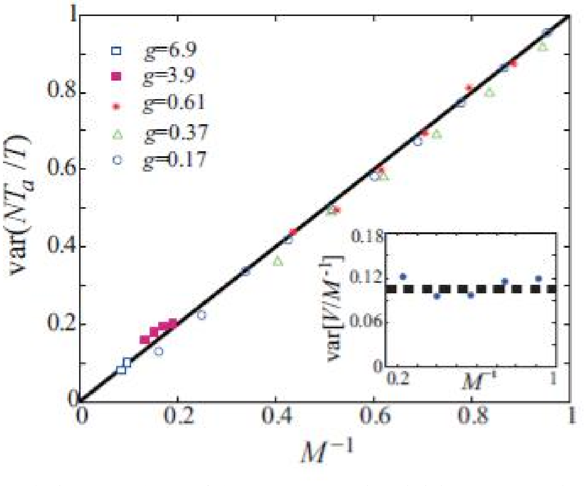

Fig. 10.24 Plot of the var(NT_a/T) computed within transmission matrices over a subset of transmission matrices with specified value of M^{-1} drawn from random ensembles with different values of g. The straight line is a plot of var(NT_a/T) = M^{-1} . In the inset, the variance of V/M^{-1} is plotted vs. M^{-1} , where V = $var(NT_a/T)$. (Ref. [296])

different length with g=0.37 and 0.17. Since a single channel dominates transmission in the limit, $M^{-1} \rightarrow 1$, we have $NT_a/T = |v_{1a}|$, where v1a is the element of the unitary matrix V which couples the incident channel a to the highest transmission channel. The Gaussian distribution of the elements of V leads to a negative exponential distribution for the square amplitude of these elements and similarly to $P(NT_a/T)$ = exp($-NT_a/T$), which is the curve plotted in Fig. 10.25. In Fig. 10.25, we plot the relative intensity distributions $P(N^2T_{ba}/T)$

corresponding to the same collection of samples as in Fig. 10.25, respectively. The curves plotted are the intensity distributions obtained by mixing the distributions for $P(NT_a/T)$ shown in Fig. 10.25 with the universal negative exponential function for the intensity of a single component of polarization.

In addition, we find in microwave measurements in Q1D samples that the SPS ratio *R* is equal to average of *M* weighted by *T*, ⟨MT⟩/⟨T⟩, which approaches unity for L/ξ » 1. The statistics of relative transmission within a single transmission matrix depends only upon the single parameter *M* while the transmittance *T* serves as an overall normalization factor. Therefore, the statistics of intensity and total transmission over random ensemble is given by the joint probability distribution of *T* and *M*.

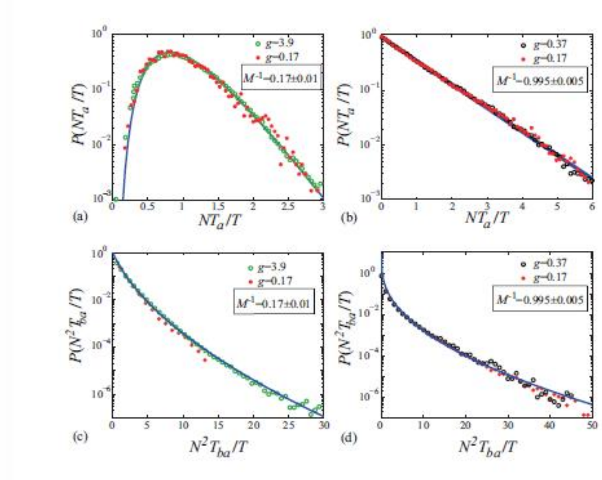

Fig. 10.25 (a) *P(NTa/T)* for subsets of transmission matrices with M^{-1} = 0.17 ± 0.01 drawn from ensembles of samples with L = 61 cm in two frequency ranges in which the wave is diffusive (green circles) and localized (red filled circles). The curve is the theoretical probability distribution of $P(s_a)$ in which var(s_a) is replaced by M^{-1} in the expression for $P(NT_a/T)$ in Ref. [30, 31]. (b) $P(NT_a/T)$ for M^{-1} in the range 0.995±0.005 computed for localized waves in samples of two lengths: L = 40 cm (black circles) and L = 61 cm (red filled circles). The straight line represents the exponential distribution, $\exp(-NT_a/T)$. (c,d) The intensity distributions $P(N_2T_{ba}/T)$ are plotted under the corresponding distributions of total transmission in (a) and (b).

10.6 Focusing

Focusing waves through random media was first demonstrated in acoustics by means of time reversal [405]. The amplitude and phase of the transmitted signal in time for an incident pulse from a source is picked up by arrays of transducers. The recorded signal is then played back in time and a pulse emerges at the location of the source. Recently, Vellekoop and Mosk [406] focused monochromatic light through opaque media by shaping the incident wavefront. Employing a genetic algorithm with a feedback from the intensity at the target point to adjust the phase of the incident wavefront, the intensity at the focus was enhanced by three orders of magnitude. The wavefront shaping method has been extended to focus optical pulses through random media at a spatial target at selected time delay [407, 408].

In order to focus a wave at a target channel β once the field transmission matrix has been measured, one simply conjugates the phase of the incident field relative to the transmitted field at β, yielding $t^*_{\beta a}\big/\sqrt{T_\beta}$ for the normalized incident field. Here, the incident field is normalized by $T_\beta = \sum_{a=1}^{N} \left|t_{\beta a}\right|^2$ so that the incident power is set to be unity. In this way, the field from different incident channels a arrives at the target in phase and interfere constructively. Random matrix calculations confirmed by microwave measurements show that the contrast between the average intensity at the focal spot $\langle I_\beta \rangle$ and the background intensity $\langle I_{b\neq\beta} \rangle$, $\mu = \langle I_\beta \rangle / \langle I_{b\neq\beta} \rangle$, depends upon the eigenchannel participation number M and size of the measured transmission matrix N,

$$\mu = \frac{1}{1/M - 1/N} \tag{10.3}$$

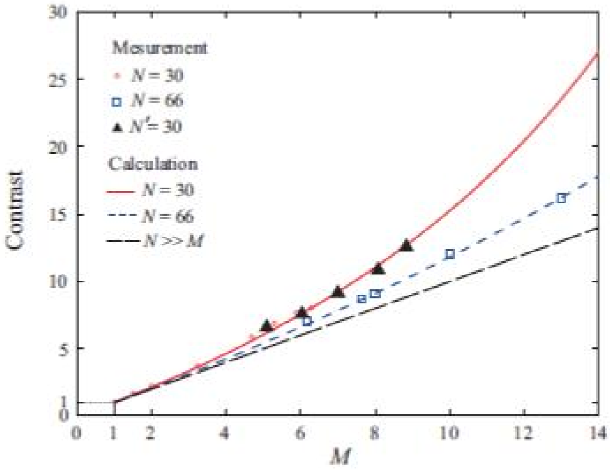

Fig. 10.26 Contrast in maximal focusing vs. eigenchannel participation number M. The open circles and squares represent measurements from transmission matrices $N = 30$ and 66 channels, respectively. The filled triangles give results for $N' \times N'$ matrices with $N' = 30$ for points selected from a larger matrix with size $N = 66$. Phase conjugation is applied within the reduced matrix to achieve maximal focusing. Equation (10.3) is represented by the solid red and dashed blue curves for $N = 30$ and 66, respectively. In the limit of $N \gg M$, the contrast given by Eq. (10.3) is equal to M, which is shown in long-dashed black line.

This expression for the contrast is confirmed in measurements shown in Fig. 10.26. This expression is still valid when the size of measured transmission matrix N' is smaller than N and the corresponding M' is correspondingly smaller than M. This is demonstrated by constructing a matrix of size $N' = 30$ from the measured transmission matrix of size $N = 66$ and calculating the contrast by phase conjugating the transmission matrix of size *N'* . The contrast computed falls on the curve for $N = 30$ for different values of *M'* . These results may be applied to measurements of the optical transmission matrix in which the size of the measured matrix *N'* is generally much smaller than *N*. In the limit $N \gg M$, the contrast approaches *M*.

These results indicate that localized waves cannot be focused via phase conjugation because the value of *M* is close to one. This is shown in Fig. 10.27 in which phase conjugation has been applied to focus the transmitted wave at the center of output surface for both diffusive and localized waves. Only for diffusive waves does a focal spot emerge from the background. We have recently demonstrated the use of phase conjugation to focus pulsed transmission through random media. By phase conjugating a time-dependent transmission matrix at a selected time delay, a pulse can be focused in space and time [409].

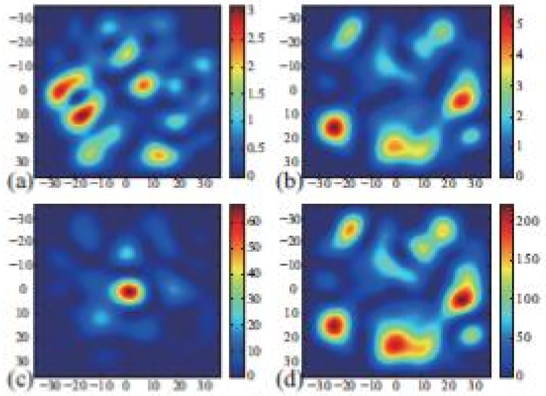

Fig. 10.27 Intensity speckle pattern generated for $L = 23$ cm for diffusive waves (a) and for $L = 61$ cm for localized waves (b) normalized to the average intensity in the respective patterns. Focusing at the central point at the same frequency as in (a) and (b) via phase conjugation is displayed in (c) and (d) with 66 and 30 input points, respectively. (Ref. [309])

10.7 Conclusion

In this chapter, we have explored the mode and channel approaches to waves in random media. We believe that each of these approaches has the potential to provide a full description of transmission and its relation to the wave within the sample and that this will be of use in a wide variety of applications.

In recent work, we have considered four statistical characteristics of modes that have proven to be particularly promising for explaining steady-state and pulsed transmission and will be reported elsewhere. These characteristics are the statistics of the spacing and widths of modes, the degree of correlation in the speckle patterns of modes, and the mode transmittance. Correlation between speckle patterns includes correlation between the intensity patterns of modes as well as the average phase difference and the standard deviation of phase shift between these patterns. The mode transmittance represents the transmittance integrated over frequency for a particular mode and is obtained from a modal decomposition of the transmission matrix based on measurements of field transmission spectra between sets of points on the incident and output surfaces. The analysis of waves into modes is of particular interest in emission and lasing since it gives the density of states which is a key factor in the emission cross section as well as the lifetimes of modes. The relationship between modes and transmission eigenchannels can be elucidated by expressing the transmission eigenchannels at each frequency as the sum of projections of the eigenchannels of the transmission matrix for the individual modes upon the transmission eigenchannel [410]. Precisely exciting a particular mode with a desired spatial distribution provides promise for control over energy deposition and collection within random media.

The relationship between modes and transmission eigenchannels can be seen from the equality of the density of states obtained from the sum of the contributions of modes and of eigenchannels. The density of quasi-normal modes or resonances of a region per unit angular frequency, is the sum over Lorentzian lines, $\rho(\omega) = \frac{1}{\pi}\sum n \frac{\Gamma_n/2}{(\Gamma_n/2)^2 + (\omega - \omega_n)^2}$. This is found from the central frequencies and linewidths determined from a modal decomposition of fields at any points in the medium. The density of states can also be obtained from the sum of the contributions of each transmission eigenchannel, which are the derivatives with angular frequency of the composite phase shift of the eigenchannel, $\rho(\omega) = \frac{1}{\pi} n \frac{d\Theta_n}{d\omega}$ The phase derivative is the intensity weighted phase derivative between all channels on the incident and output surfaces [411]. $\frac{d\Theta_n}{d\omega}$ is the transmission delay time for the n^{th} transmission eigenchannel. When a complete measurement of the transmission matrix is made, $\frac{d\Theta_n}{d\omega}$ is the integral of intensity inside the sample for the corresponding eigenchannel. The eigenchannel delay time and the associated intensity integral inside the sample increases with the transmission eigenvalue τ_n. The density of states may be accurately measured from the transmission matrix as long as $N' \gg M$.

We have also explored the distribution of transmission eigenvalues and seen that in a particular transmission matrix, the statistics of relative transmission depend only upon M. The absolute distribution within a single matrix then depends upon these two parameters M and T. Thus the distribution over a random ensemble of all transmission quantities depends only upon the joint distribution of M and T. This represents a considerable simplification from the joint distribution of the full set of transmission eigenvalues τ_n. Manipulation of the incident beam with knowledge of the transmission matrix makes it possible to achieve maximal focusing in a single transmission matrix with the peak intensity depending only upon T and the contrast depending upon the value of M in the measured matrix and the dimension of this matrix. Knowledge of the spectrum of both modes and channels may advance control over the wave projected within and through opaque samples for applications in imaging, and energy collection and delivery.

6. APEENDIX: DERIVATION OF EQ. (6.6)

Here we provide an outline of the derivation of Eq.(6.6) and assume that the disordered stack with *N* layers is embedded in a homogeneous infinitesimal medium with material parameters given by $\overline{\varepsilon} = \langle \varepsilon \rangle$ and $\overline{\mu} = \langle \mu \rangle$, where ε and μ are given by Eqs. (6.1) and (6.2), respectively. The impedance and refractive index of the medium are $Z_b = \sqrt{\overline{\mu}/\overline{\varepsilon}}$ and $\nu_b = \sqrt{\overline{\mu}}\sqrt{\overline{\varepsilon}}$ respectively.

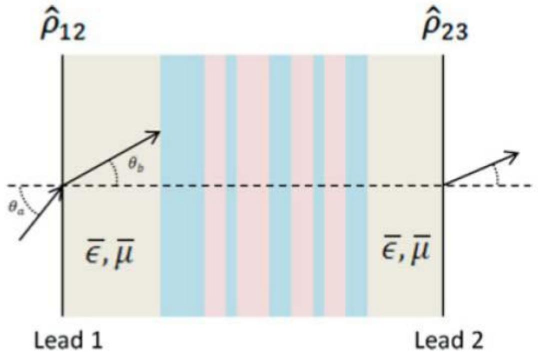

Fig. 6.9. (Color online) The disordered stack is embedded in a homogeneous medium with averaged material parameters , .

This random stack is sandwiched between two leads connecting the outside free space and the homogeneous medium $(\overline{\varepsilon}, \overline{\mu})$ (see Fig. 6.9). The right lead reflection coefficient for left-hand incidence is

$$\hat{\rho}_{23} = \frac{\mathcal{Z}_b \cos\theta_b - \mathcal{Z}_a \cos\theta_a}{\mathcal{Z}_b \cos\theta_b + \mathcal{Z}_a \cos\theta_a}, \tag{A1}$$

and

$$\cos\theta_b = \sqrt{1 - \frac{\sin^2\theta_a}{\nu_b^2}} \tag{A2}$$

while the transmission coefficient is given by $\hat{\tau}_{23} = 1 + \hat{\rho}_{23}$. The front (left) "lead" reflection and transmission coefficients for incidence from the left side are given by $\hat{\rho}_{12} = -\hat{\rho}_{23}$ and $\hat{\tau}_{12} = 1 + \hat{\rho}_{12}$, respectively.

The total transmission coefficient T_N (${}_{\text{a}}$) through such a structure with both Fresnel "leads" in place can be calculated from

$$T_N(\theta_a) = \frac{\hat{\tau}_{23}\hat{T}_N(\theta_b)\hat{\tau}_{12}}{(1 - \hat{R}_N\hat{\rho}_{21})(1 - \hat{R}'_N\hat{\rho}_{23}) - \hat{\rho}_{21}\hat{T}_N\hat{\rho}_{23}\hat{T}'_N} \tag{A3}$$

where $\hat{T}_N(\theta_b)$ is the transmission of a random stack with *N* layers embedded in homogeneous medium with and, for plane-wave incidence from the left with incident angle , and with $\hat{\rho}_{21} = \hat{\rho}_{23}$. The terms $\hat{R}_N$ and $\hat{R}'_N$ are reflection coefficients for the random stack for plane-wave incidence from the left/right sides, while the $\hat{T}'_N$ is the transmission coefficient for incidence from the right.

In the localized regime as $N \to \infty$, the transmission coefficient $T_N(\theta_a) = \hat{T}'_N(\theta_b) \to 0$ and therefore the final term in the denominator of Eq. (A3) vanishes. Accordingly,

$$\ln T_N(\theta_a) = \ln \hat{T}_N(\theta_b) + \ln \hat{\tau}_{23} + \ln \hat{\tau}_{12} \\ - \ln(1 - \hat{R}_N \hat{\rho}_{21}) - \ln(1 - \hat{R}'_N \hat{\rho}_{23}). \tag{A4}$$

As N, the last four terms in Eq. (A4) are bounded and we deduce

$$\lim_{N\to\infty} \frac{\ln T_N(\theta_a)}{N} = \lim_{N\to\infty} \frac{\ln \hat{T}_N(\theta_b)}{N}. \tag{A5}$$

Thus, the localization length for a stack embedded in free space for plane-wave incidence at an angle θ_a is equivalent to calculating the localization length for a stack of N layers embedded in a medium with the refractive index v_b with plane - wave incidence at an angle θ_b. The angles θ_a and θ_b are related by Snell's law [Eq. (6.14)]. From Eq. (A5), we thus deduce the relation in Eq. (6.6).

8. APPENDIX A: THE GREEN'S FUNCTION FOR THE DIRECTIONAL INTENSITY

Expressions (8.10) and (8.11) show that the 1D radiative transfer equation can be split into a system of PDEs in terms of the left and right-going intensities. So far, only the reduced PDE governing the total intensity has been studied. This is due to the fact that measuring either the left or right-going intensity entails splitting the wavefield into left and right-going waves. Such a decomposition requires dense spatial sampling to perform the type of filtering routinely done in Vertical Seismic Profiling: separating up from down-going waves. Here, we show that knowledge of the individual left and rightgoing energies can give us more detailed insight into the incoherent energy.

Assuming that the wavefield has been decomposed into left and right-going waves, we now solve the system of 2 partial differential equations that comprise the full radiative transfer equation. To begin, we write equations (8.10) and (8.11) in matrix form:

$$\frac{\partial I}{\partial t} + M\frac{\partial I}{\partial x} = N\vec{I} + S \tag{A1}$$

where $\vec{I}$, M, N, and $\vec{S}$ are:

$$\vec{I} = \begin{bmatrix} I_r \\ I_l \end{bmatrix}, M = \begin{bmatrix} v & 0 \\ 0 & -v \end{bmatrix},$$

$$N = \begin{bmatrix} -\frac{B}{T_s} - \frac{1}{T_a} & \frac{B}{T_s} \\ \frac{B}{T_s} & -\frac{B}{T_s} - \frac{1}{T_a} \end{bmatrix} \tag{A2}$$

$$\vec{S} = \begin{bmatrix} S_r \\ S_l \end{bmatrix}$$

There exists no general theory for solving systems of PDEs as there is for systems of ODEs. Hence, we proceed by Fourier transforming equation (A1) over space, solving the system of ODEs, and inverse Fourier transforming back to spatial coordinates. With the Fourier conventions:

$$\vec{I}(\chi) = \int_{-\infty}^{\infty} \tilde{I}(k) e^{-kx} dk \qquad \tilde{I}(k) = \frac{1}{2\pi}\int_{-\infty}^{\infty} \tilde{I}(\chi) e^{ikx} dx \tag{A3}$$

equation (A1) becomes a system of 2 ODEs:

$$\frac{\partial I}{\partial t} = (N + ikM)\tilde{I} + \tilde{S}. \tag{A4}$$

For the source function, we again take a general directional point source with right and left-going components S_r and S_l. Allowing the parameter c to govern the directivity of the source as we did previously, the source vector is:

$$\vec{S} = \begin{bmatrix} 1 + c \\ 1 - c \end{bmatrix} \frac{\delta(x)\delta(t)}{2} \tag{A5}$$

The solution of the system of ODEs follows that given in standard texts on differential equations [187]. Here we give the solution in the k domain:

$$I_x(k,t)=\frac{1}{4\pi}e^{-Bvt/l_s}e^{-vt/l_a}\left((1-c)\frac{B}{T_s}+i(1+c)Kv\right)\frac{\sinh\left(t\sqrt{\frac{B^2}{T_s^2}-k^2v^2}\right)}{\sqrt{\frac{B^2}{T_s^2}-k^2v^2}}+ \tag{A6}$$
$$(1+c)\cosh\left(t\sqrt{\frac{B^2}{T_s^2}-k^2v^2}\right)$$

$$I_l(k,t)=\frac{1}{4\pi}e^{-Bvt/l_s}e^{-vt/l_a}\left((1-c)\frac{B}{T_s}+i(1+c)Kv\right)\frac{\sinh\left(t\sqrt{\frac{B^2}{T_s^2}-k^2v^2}\right)}{\sqrt{\frac{B^2}{T_s^2}-k^2v^2}}+ \tag{A7}$$
$$(1+c)\cosh\left(t\sqrt{\frac{B^2}{T_s^2}-k^2v^2}\right)$$

To get the directional intensities in the spatial domain, we must inverse Fourier transform equations (A6) and (A7). Two identities are needed for this inversion:

$$ix\int_{-\infty}^{\infty}\vec{I}(k)e^{-ilx}dk=\int_{-\infty}^{\infty}\frac{\partial\tilde{I}(k)}{\partial k}e^{-ikx}dk, \tag{A8}$$

and from the theory of Bessel functions [187]:

$$\int_{-\infty}^{\infty}\cos(kx)\frac{\sin\left(t\sqrt{k^2v^2-\frac{B^2}{T_s^2}}\right)}{\sqrt{k^2v^2-\frac{B^2}{T_s^2}}}dk=\frac{\pi}{v}I_0\left[\frac{B}{l_s}\sqrt{k^2v^2-x^2}\right]u(vt-|x|) \tag{A9}$$

After inverting the Fourier transform, we obtain for the right-going intensity:

$$I_r(x,t)=\frac{1}{4}e^{-\frac{Bvt}{l_s}}e^{-\frac{vt}{l_a}}\left[\;2(1+c)\delta(vt-x)+\frac{B}{l_s}u(vt-|x|)\left[\;(1-c)I_o\left(\frac{B}{l_s}\sqrt{v^2t^2-x^2}\right)+\right.\right.$$

$$\left.\left.+(1+c)\sqrt{\frac{vt+x}{vt-x}}I_1\left(\frac{B}{l_s\sqrt{v^2t^2-x^2}}\right)\;\right]\right] \tag{A10}$$

and for the left-going intensity:

$$I_l(x,t)=\frac{1}{4}e^{-\frac{Bvt}{l_s}}e^{-\frac{vt}{l_a}}\left[\;2(1+c)\delta(vt-x)+\frac{B}{l_s}u(vt-|x|)\left[\;(1-c)I_o\left(\frac{B}{l_s}\sqrt{v^2t^2-x^2}\right)+\right.\right.$$

$$\left.\left.+(1+c)\sqrt{\frac{vt+x}{vt-x}}I_1\left(\frac{B}{l_s\sqrt{v^2t^2-x^2}}\right)\;\right]\right] \tag{A11}$$

These equations for the two intensities show that the two Bessel functions that make up the incoherent intensity are sensitive to different aspects of the source radiation pattern. For instance, if the source were unidirectional, $c = -1$ or $c = 1$ and the zero order Bessel function would come from one direction and the first order Bessel from the other. It can also be verified that adding equations (A10) and (A11) gives the total intensity, equation (8.23). In the absence of phase information, perhaps the directional intensities can yield important information about spatial variations in the material properties.

9. APPENDIX: EXPERIMENTAL VERIFICATIONS OF WAVE LOCALIZATION

To examine the wave localization that we mentioned in Sec. 9.4, we perform experiments to visualize full-field velocity profiles of all particles in a chain. In Fig. 9, we show space-time contour plots of velocity profiles for (top row) a single-impurity chain with $\alpha = 1.5$ and (bottom row) a double-impurity chain with $\alpha = 0.7$. We use excitation frequencies of (left panel) 2.0 kHz and (right panel) 6.0 kHz. The experimental results in Fig. 9.9 require measurements of the motion of individual particles followed by synchronization of all measured data, because the laser Doppler vibrometer scopes only a single particle's motion at a time. In each case, after we collect all data, we normalize the measured values of particles' velocities with respect to the maximum velocity component.

As we indicate with the arrows in the right panels of Fig. 9.9, we observe localization in our single-impurity and double-impurity experiments when the excitation frequency is 6.0 kHz. We do not find such a distinctive localization for the 2.0 kHz excitation [see Figs. 9.9(a) and 9.9(c)]. Again, as explained in Sec. 9.4, this is due to the inevitable perturbation of "beyond-cutoff frequency" components of stress waves in experiments when we excite the system near the cutoff frequency. Incident waves whose frequencies are close to the cutoff frequency cause this perturbation even when the static load F_0 is large enough or the excitation amplitude is small enough to remain near the linear regime of the granular chain. This wave localization contributes to the discrepancy between experiment and theory near 6.0 kHz in Fig.9.6. In our numerical simulations, we also observe wave localization at the edge of the chain, and we thereby obtain a dip in our transmission data near 6.0 kHz that appears systematically for different values of α and different chain lengths.

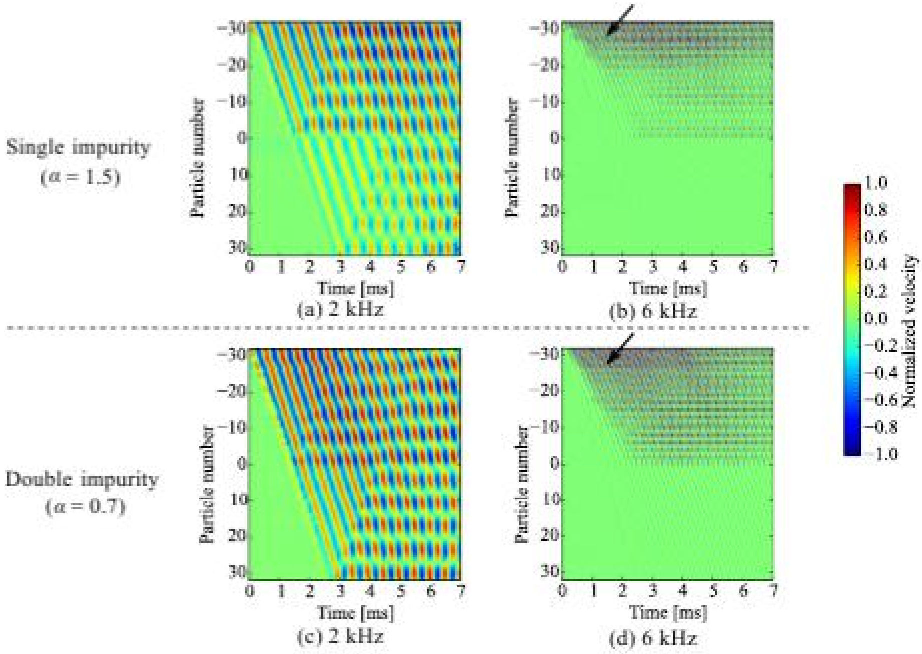

Fig. 9.9: (Color online) Space-time contour plot of normalized velocity for experiments with (top) a single-impurity chain with α = 1.5 and (bottom) a double-impurity chain with α = 0.7. In each case, we normalize the measured velocities with respect to the maximum velocity. We use excitation frequencies of (left) 2 kHz and (right) 6 kHz. The arrows point to incidents of wave localization.

REFERENCES

1. Bass, F. and L. Resnick, “Spatial and temporal rotation of the polarization plane of electromagnetic waves reflected from and transmitted through a gyrotropic plate,” J. of Electromagn. Waves and Appl., Vol. 17, 1131–1137, 2003.

2. Brekhovskikh, L. M., Waves in Layered Media, Academia, New York, 1980; Tsang, L., J. A. Kong, and R. T. Shin, Theory of Microwave Remote Sensing, Wiley-Interscience, New York, 1985.

3. Bilotti, F., A. Toscano, and V. Vegni, “Design of inhomogeneous slabs for filtering applications via closed form solutions of the reflection coefficient,” J. of Electromagn. Waves and Appl., Vol. 16, 1233–1254, 2002.

4. Hashish, E. A., “Forward and inverse scattering from an inhomogeneous dielectric slab,” J. of Electromagn. Waves and Appl., Vol. 17, 719–736, 2003.

5. Landau, L. D. and E. M. Lifshits, Electrodynamics of Continuous Media, Pergamon Press, Oxford, 1984.

6. Cheng, P. (ed.), Scattering and Localization of Classical Waves in Random Media, World Scientific, Singapore, 1990.

7. Belinskii, A. V., “Regular and quasiregular spectra of disordered layer structures,” Physics - Uspekhi, Vol. 38, 653–664, 1995.

8. Achenbach, J. D.: Wave Propagation in Elastic Solids. North-Holland, Amsterdam (1973)

9. Bale, D. S., LeVeque, R. J., Mitran, S., Rossmanith, J.A.: A wave propagation method for conservation laws and balance laws with spatially varying flux functions. SIAM J. Sci. Comp. 24, 955–978 (2003)

10. Bedford, A., Drumheller, D. S.: Introduction to Elastic Wave Propagation. Wiley, New York (1994)

11. Berezovski, A., Berezovski, M., Engelbrecht, J.: Numerical simulation of nonlinear elastic wave propagation in piecewise homogeneous media. Mater. Sci. Eng. A418, 364–369 (2006)

12. Berezovski A., Berezovski, M., Engelbrecht, J., Maugin, G. A.: Numerical simulation of waves and fronts in inhomogeneous solids. In: Nowacki, W. K., Zhao, H. (eds.) Multi-Phase and Multi-Component Materials under Dynamic Loading, pp. 71-80. Inst. Fundam. Technol. Research, Warsaw (2007)

13. Berezovski, A., Maugin, G. A.: Simulation of thermoelastic wave propagation by means of a composite wave-propagation algorithm. J. Comp. Physics 168, 249–264 (2001)

14. Berezovski, A., Maugin, G. A.: Thermoelastic wave and front propagation. J. Thermal Stresses 25, 719–743 (2002)

15. Berezovski, A., Maugin, G. A.: Stress-induced phase-transition front propagation in thermoelastic solids. Eur. J. Mech. A/Solids 24, 1–21 (2005)

16. Billingham, J., King, A. C.: Wave Motion. Cambridge University Press (2000)

17. Chakraborty, A., Gopalakrishnan, S.: Various numerical techniques for analysis of longitudinal wave propagation in inhomogeneous one-dimensional waveguides. Acta Mech. 162, 1–27 (2003)

18. Chakraborty, A., Gopalakrishnan, S.: Wave propagation in inhomogeneous layered media: solution of forward and inverse problems. Acta Mech. 169, 153–185 (2004)

19. Chen, X., Chandra, N.: The effect of heterogeneity on plane wave propagation through layered composites. Comp. Sci. Technol. 64, 1477–1493 (2004)

20. Chen, X., Chandra, N., Rajendran, A. M.: Analytical solution to the plate impact problem of layered heterogeneous material systems. Int. J. Solids Struct. 41, 4635–4659 (2004)

21. Chiu, T.-C., Erdogan, F.: One-dimensional wave propagation in a functionally graded elastic medium. J. Sound Vibr. 222, 453–487 (1999)

22. Engelbrecht, J., Berezovski, A., Pastrone, F., Braun, M.: Waves in microstructured materials and dispersion. Phil. Mag. 85, 4127–4141 (2005)

23. Fogarthy, T., LeVeque, R. J.: High-resolution finite-volume methods for acoustics in periodic and random media. J. Acoust. Soc. Am. 106, 261–297 (1999)

24. Godlewski, E., Raviart, P.-A.: Numerical Approximation of Hyperbolic Systems of Conservation Laws. New York, Springer (1996)

25. Grady, D.: Scattering as a mechanism for structured shock waves in metals. J. Mech. Phys. Solids 46, 2017–2032 (1998)

26. Graff, K. F.: Wave Motion in Elastic Solids. Oxford University Press (1975)

27. Guinot, V.: Godunov-type Schemes: An Introduction for Engineers. Elsevier, Amsterdam (2003)

28. Hirai, T.: Functionally graded materials. In: Processing of Ceramics. Vol. 17B, Part 2, pp. 292-341. VCH Verlagsgesellschaft, Weinheim (1996)

29. Hoffmann, K. H., Burzler, J. M., Schubert, S.: Endoreversible thermodynamics. J. Non-Equil. Thermodyn. 22, 311–355 (1997)

30. Langseth, J. O., LeVeque, R.J.: A wave propagation method for three-dimensional hyperbolic conservation laws. J. Comp. Physics 165, 126–166 (2000)

31. LeVeque, R.J.: Wave propagation algorithms for multidimensional hyperbolic systems. J. Comp. Physics 131, 327–353 (1997)

32. LeVeque, R. J.: Balancing source terms and flux gradients in high-resolution Godunov methods: the quasi-steady wave-propagation algorithm. J. Comp. Physics 148, 346–365 (1998)

33. LeVeque, R. J.: Finite volume methods for nonlinear elasticity in heterogeneous media. Int. J. Numer. Methods in Fluids 40, 93–104 (2002)

34. LeVeque, R.J.: Finite Volume Methods for Hyperbolic Problems. Cambridge University Press (2002)

35. LeVeque, R. J., Yong, D.H.: Solitary waves in layered nonlinear media. SIAM J. Appl. Math. 63, 1539–1560 (2003)

36. Liska, R., Wendroff, B.: Composite schemes for conservation laws. SIAM J. Numer. Anal. 35, 2250–2271 (1998)

37. Markworth, A.J., Ramesh, K. S., Parks, W. P.: Modelling studies applied to functionally graded materials. J. Mater. Sci. 30, 2183–2193 (1995)

38. Meurer, T., Qu, J., Jacobs, L. J.: Wave propagation in nonlinear and hysteretic media – a numerical study. Int. J. Solids Struct. 39, 5585–5614 (2002)

39. Muschik, W., Berezovski, A.: Thermodynamic interaction between two discrete systems in non-equilibrium. J. Non-Equilib. Thermodyn. 29, 237–255 (2004)

40. Rokhlin, S.I., Wang, L.: Ultrasonic waves in layered anisotropic media: characterization of multidirectional composites. Int. J. Solids Struct. 39, 5529–5545 (2002)

41. Santosa, F., Symes, W. W.: A dispersive effective medium for wave propagation in periodic composites. SIAM J. Appl. Math. 51, 984–1005 (1991)

42. Suresh, S., Mortensen, A.: Fundamentals of Functionally Graded Materials. The Institute of Materials, IOM Communications, London (1998)

43. Toro, E. F.: Riemann Solvers and Numerical Methods for Fluid Dynamics. Springer, Berlin (1997)

44. Toro, E. F. (ed.): Godunov Methods: Theory and Applications. Kluwer, New York (2001)

45. Wang, L., Rokhlin, S. I.: Recursive geometric integrators for wave propagation in a functionally graded multilayered elastic medium. J. Mech. Phys. Solids 52, 2473–2506 (2004)

46. Zhuang, S., Ravichandran, G., Grady, D.: An experimental investigation of shock wave propagation in periodically layered composites. J. Mech. Phys. Solids 51, 245–265 (2003)

47. F. Fogolari, A. Brigo and H. Molinari, J. Mol. Recognit. 15, 377 (2002).

48. M. H. Andrews, A. H. Marshak and R. Shrivastava, J. Appl. Phys. 52, 6783 (1981).

49. M. V. Basilevsky, F. V. Grigoriev, E. A. Nikitina and J. Leszczynski, J. Phys. Chem. B, 114, 2457 (2010).

50. H. Nymeyer and H.-X. Zhou, Biophysical Journal, 94, 1185 (2008).

51. G. Le and J. Zhang, Langmuir, 27, 5366 (2011).

52. F. Fogolari, P. Zuccato, G. Esposito, P. Viglino, Biophysical Journal 76, 1 (1999).

53. I. Borukhov, D. Andelman, H. Orland, Electrochimica Acta, 46, 221 (2000).

54. M. F.-Guasti, A. G.Villegas and R. Diamant, Rev. Mex. Fis. 46, 530 (2000).

55. R. Diamant and M. F.-Guasti, Proc. SPIE 8011, 22nd Congress of the International Commission for Optics: Light for the Development of the World, 80115U (November 02, 2011).

56. R. Diamant, Proc. SPIE 8011, 22nd Congress of the International Commission for Optics: Light for the Development of the World, 801163 (November 02, 2011).

57. R. Diamant and M. F.-Guasti, J. Opt. A: Pure Appl. Opt. 11, 045712 (2009).

58. R. Diamant and M. F.-Guasti, Communications 294, 64 (2013).

59. G. B. Arfken and H. J. Weber, Mathemathical Methods for Physics, Harcourt Academic Press, Fifth Edition (2001).

60. L. Dekar, L. Chetouani, and T. F. Hammann, J. Math. Phys. 39, 2551 (1998).

61. J. D. Jackson, Classical Electrodynamics, John Wiley & Sons, Third Edition, (1999).

62. NIST Digital Library of Mathematical Functions, http://dlmf.nist.gov/15.5.

63. A. Ronveaux, Heun's Differential Equations, Oxford Science Publications, (1995).

64. Yablonovitch E 1987 Inhibited spontaneous emission in solid-state physics and electronics *Phys. Rev. Lett.* **58** 2059

65. John S 1987 Strong localization of photons in certain disordered dielectric superlattices *Phys. Rev. Lett.* **58** 2486

66. Joannopoulos J D, Meade R D and Winn J N 1995 *Photonic Crystals: Molding the Flow of Light* (Princeton, NJ: Princeton University Press)

67. Johnson S G and Joannopoulos J D 2002 *Photonic Crystals: The Road from Theory to Practice* (Dordrecht: Kluwer)

68. Bayindir M, Temelkuran B and Ozbay E 2000 Propagation of photons by hopping: a waveguiding mechanism through localized coupled cavities in three-dimensional photonic crystals *Phys. Rev.* B **61** R11855

69. Xu-Sheng L, Chong H, Yan-Dong O and Sheng L 2004 Tolerance of photonic crystal impurity bands to disorder of defects in coupled cavity waveguides *Chin. Phys. Lett.* **21** 863

70. Qi M, Lidorikis E, Rakich P T, Johnson S G, Joannopoulos J D, Ippen E P and Smith H I 2004 A threedimensional optical photonic crystal with designed point defects *Nature* **429** 538

71. Chan D L C, Lidorikis E and Joannopolous J D 2005 Point defect geometries in inverted opal photonic crystals

Phys. Rev. E **71** 056602

72. Johnson S G and Joannopoulos J D 2001 Block-iterative frequency-domain methods for Maxwell's equations in a planewave basis *Opt. Express* **8** 173

73. Kunz K S and Luebbers R J 1993 *The Finite Difference Time Domain Method for Electromagnetics* (Boca Raton, FL: CRC Press)

74. Elson J M and Tran P 1996 Coupled-mode calculation with the *R*-matrix propagator for the dispersion of surface waves on a truncated photonic crystal *Phys. Rev.* B **54** 1711

75. Pendry J B and MacKinnon A 1992 Calculation of photon dispersion relations *Phys. Rev. Lett.* **69** 2772

76. Khazhinsky M G and McGurn A R 1998 Green's function method for waveguide and single impurity modes in 2D photonic crystals: H-polarization *Phys. Lett.* A **237** 175

77. Sakoda K 2001 *Optical Properties of Photonic Crystals* (New York: Springer)

78. Kittel C and Mitchell A H 1954 Theory of donor and acceptor states in silicon and germanium *Phys. Rev.* **96** 1488

79. Luttinger J M and Kohn W 1955 Motions of electrons and holes in perturbed periodic fields *Phys. Rev.* **97** 869

80. Nozaki H and Itoh S 2000 Energy correction for isolated impurities under periodic boundary conditions *Phys. Rev.* E **62** 1390

81. Menchero J G, Capaz R B, Koiler B and Chacham H 1999 Tight-binding scheme for impurity states in semiconductors *Phys. Rev.* B **59** 2722

82. Pradhan R D and Watson G H 1999 Impurity effects in coaxial-connector photonic crystals: a quasi-onedimensional periodic system *Phys. Rev.* B **60** 2410

83. McCall S L, Platzman P M, Dalichaouch R, Smith D R and Schultz S 1991 Microwave propagation in twodimensional dielectric lattices *Phys. Rev. Lett.* **67** 2017

84. Kouwenhoven L P, Hekking F W J, van Wees B J, Harmans C J P M, Timmering C E and Foxon C T 1990 Transport through a finite one-dimensional crystal *Phys. Rev. Lett.* **65** 361

85. Kuhl U and Stöckmann H-J 1998 Microwave realization of the Hofstadter butterfly *Phys. Rev. Lett.* **80** 3232

86. Kuhl U, Izrailev F M, Krokhin A A and Stöckmann H-J 2000 Experimental observation of the mobility edge in a waveguide with correlated disorder *Appl. Phys. Lett.* **77** 633

87. Griffiths D J and Steinke C A 2001 Waves in locally periodic media *Am. J. Phys.* **69** 137

88. Luna-Acosta G A, Schanze H, Kuhl U and Stöckmann H-J to be published

89. Sprung D W L, Wu H and Martorell J 1993 Scattering by a finite periodic potential *Am. J. Phys.* **61** 1118

90. Barra F and Gaspard P 1999 Scattering in periodic systems: from resonances to band structure *J. Phys. A:Math. Gen.* **32** 3357

91. Gumen L, Feldman E, Yurchenko V, Krokhin A and Pereyra P 2003 Topological defects in 1D potential and superlattices *Physica* E **17** 264

92. Morales A, Méndez-Sánchez R A and Flores J 2003 Topological defects in 1D elastic waves *Physica* E **19** 289

93. Yablonovitch E, Gmitter T J, Meade R D, Rappe A M, Brommer K D and Joannopoulos J D 1991 Donor and acceptor modes in photonic band structure *Phys. Rev. Lett.* **67** 3380

94. D.L. Shepelyansky, Phys. Rev. Lett., 70 , 1787 (1993).

95. M.I. Molina, Phys. Rev. B 58 12547 (1998).

96. A. S. Pikovsky and D. L. Shepelyansky, Phys. Rev. Lett. 100 094101 (2008).

97. G. Kopidakis, S. Komineas, S. Flach, and S. Aubry, Phys. Rev. Lett. 100 084103 (2008).

98. R. Bourbonnais and R. Maynard, Phys. Rev. Lett., 64 1397 (1990).

99. G. S. Zavt, M. Wagner, A. L¨utze, Phys. Rev. E 47 4108 (1993).

100. D.M. Leitner, Phys. Rev. B 64, 94201 (2001).

101. K.A. Snyder, T.R. Kirkpatrick, Phys. Rev. B 73 134204 (2006).

102. S. Flach, D.O. Krimer, and Ch. Skokos, Phys. Rev. Lett. 102, 024101 (2009).

103. P.K. Datta, K. Kundu, Phys. Rev. B 51, 6287 (1995).

104. S. Alexander, J. Bernasconi, W.R. Schneider, and R. Orbach, Rev. Mod. Phys., 53, 175 (1981).

105. S. Alexander and T. Holstein, Phys. Rev. B 108, 301 (1978).

106. S. Alexander and J. Bernasconi, J. Phys. C12, L1, (1979)

107. P.M. Richards and R.L. Renken, Phys. Rev. B21, 3740 (1980)

108. T. Burke and J.L. Lebowitz, J. Math. Phys. 9, 1526 (1968)

109. H. Matsuda and K. Ishii, Suppl. Prog. Phys. 45, 56 (1970)

110. K. Ishii, Suppl. Prog. Theor. Phys. 53, 77 (1973)

111. D. H. Dunlap, K. Kundu and P. Phillips, Phys. Rev. B 40, 10999 (1989)

112. S. Lepri, R. Livi, and A. Politi, Phys. Rep. 377, 1 (2003).

113. R.I. McLachlan and P. Atela, Nonlinearity 5, 541 (1992).

114. L.D. Landau and E.M. Lifshitz, Mechanics I (Butterworth Heinemann, Oxford, 1982)

115. F. Wegner, Z. Phys. B22, 273 (1975).

116. M. Kappus and F. Wegner, Z. Phys. B45, 15 (1981)

117. A. Mielke and F. Wegner, Z. Phys. B62, 1 (1985).

118. E.A. Bredikhina Almost Periodic Functions in M. Hazewinkel (ed.) Encyclopedia of Mathematics, Kluwer Academic Publishers (2001).

119. P. W. Anderson, Phys. Rev. 109, 1492 (1958).

120. E. Abrahams (ed.), *50 Years of Anderson Localization* (World Scientific, Singapore, (2010).

121. P. Marcos and C. M. Soukoulis, *Wave Propagation from Electrons to Photonic Crystals and Left-Handed Materials* (Princeton University Press, Princeton, 2008).

122. V. G. Veselago, Sov. Phys. Usp. 10, 509 (1968).

123. J.B. Pendry, Phys. Rev. Lett. 85, 3966 (2000)

124. K. Yu. Bliokh and Yu. P. Bliokh, Phys. Usp. 47, 393 (2004); Usp. Fiz. Nauk 174, 439 (2004).

125. T. Terao, Phys. Rev. E 82, 026702 (2010).

126. M. V. Gorkunov, S. A. Gredeskul, I. V. Shadrivov, and Yu. S. Kivshar, Phys. Rev. E 73, 056605 (2006).

127. Y. Dong and Z. Zhang, Phys. Lett. A 359, 542 (2006).

128. A. A. Asatryan, L. C. Botten, M. A. Byrne, V. D. Freilikher, S. A. Gredeskul, I. V. Shadrivov, R. C. McPhedran, and Yu. S. Kivshar, Phys. Rev. Lett. 99, 193902 (2007).

129. F. M. Izrailev and N. M. Makarov, Phys. Rev. Lett. 102, 203901 (2009)

130. D. Mogilevtsev, F. A. Pinheiro, R. R. dos Santos, S. B. Cavalcanti, and L. E. Oliveira, Phys. Rev. B 82, 081105(R) (2010)

131. E. Reyes-Gomez, A. Bruno-Alfonso, S. B. Cavalcanti, and L. E.Oliveira, Phys. Rev. E 84, 036604 (2011).

132. D. Mogilevtsev, F. A. Pinheiro, R. R. dos Santos, S. B. Cavalcanti, and L. E. Oliveira, Phys. Rev. B 84, 094204 (2011).

133. A. A. Asatryan, S. A. Gredeskul, L. C. Botten, M. A. Byrne, V. D. Freilikher, I. V. Shadrivov, R. C. McPhedran, and Yu. S. Kivshar, Phys. Rev. B 81, 075124 (2010).

134. F. M. Israilev, N. M. Makarov, and E. J. Torres-Herrera, Physica B 405, 3022 (2010).

135. E. J. Torres-Herrera, F. M. Israilev, and N. M. Makarov, Low Temp. Phys. 37, 1201 (2011).

136. E. J. Torres-Herrera, F. M. Israilev, and N. M. Makarov, e-print arXiv:1111.3397.

137. P. Han, C. T. Chan, and Z. Q. Zhang, Phys. Rev. B 77, 115332 (2008).

138. A. A. Asatryan, N. A. Nicorovici, L. C. Botten, C. M. de Sterke, P. A. Robinson, and R. C. McPhedran, Phys. Rev. B 57, 13535 (1998).

139. M. G. Silveirinha and N. Engheta, Phys. Rev. Lett. 97, 157403 (2006).

140. A. Alu, M. G. Silveirinha, A. Salandrino, and N. Engheta, Phys. Rev. B 75, 155410 (2007).

141. E. Liznev, A. Dorofeenko, L. Huizhe, A. Vinogradov, and S. Zouhdi, Appl. Phys. A 100, 321 (2010).

142. L. Liu, C. Hu, Z. Zhao, and X. Luo, Opt. Express 17, 12183 (2009).

143. B. Edwards, A. Alu, M. E. Young, M. Silveirinha, and N. Engheta, Phys. Rev. Lett. 100, 033903 (2008).

144. R. A. Shelby, D. R. Smith, and S. Schultz, Science 292, 77 (2001).

145. D. R. Smith, Phys. Rev. E 81, 036605 (2010).

146. A. A. Asatryan, L. C. Botten, M. A. Byrne, V. D. Freilikher, S. A. Gredeskul, I. V. Shadrivov, R. C. McPhedran, and Y. S. Kivshar, Phys. Rev. B 82, 205124 (2010).

147. P. W. Milonni, *Fast Light, Slow Light, and Left-Handed Light* (Dirac House, Bristol, 2005).

148. X. Huang, Y. Lai, Z. H. Hang, H. Zeng, and C. T. Chan, Nature Mater. 10,582 (2011).

149. J. E. Sipe, P. Sheng, B. S. White, and M. H. Cohen, Phys. Rev. Lett. 60, 108 (1988).

150. E. Yablonovitch, Phys. Rev. Lett. 58, 2059 (1987).

151. S. John, Phys. Rev. Lett. 58, 2486 (1987).

152. K. Busch, G. von Freymann, S. Linden, S. F. Mingaleev, L. Tkeshelashvili, and M. Wegener, Phys. Rep. 444, 101 _2007_.

153. P. Halevi and F. Ramos-Mendieta, Phys. Rev. Lett. 85, 1875 (2000).

154. V. Kuzmiak, A. A. Maradudin, and F. Pincemin, Phys. Rev. B 50, 16835 _1994

155. K. Busch and S. John, Phys. Rev. Lett. 83, 967 _1999_.

156. J. B. González-Díaz, A. García-Martín, G. Armelles, D. Navas, M. Vázquez, K. Nielsch, R. B. Wehrspohn, and U. Gösele, Adv. Mater. _Weinheim, Ger._ 19, 2643 (2007).

157. K. Busch, S. F. Mingaleev, A. García-Martín, M. Schillinger, and D. Hermann, J. Phys.: Condens. Matter 15, R1233 (2003).

158. A. Birner, R. B. Wehrspohn, U. Gösele, and K. Busch, Adv. Mater. (Weinheim, Ger.) 13, 377 (2001).

159. M. Steinhart, J. H. Wendorff, A. Greiner, R. B. Wehrspohn, K. Nielsch, J. Schilling, J. Choi, and U. Gösele, Science 296, 1997 (2002).

160. S. Richter, M. Steinhart, H. Hofmeister, M. Zacharias, U. Gösele, N. Gaponik, A. Eychmüller, A. L. Rogach, J. H. Wendorff, S. L. Schweizer, A. von Rhein, and R. B. Wehrspohn, Appl. Phys. Lett. 87, 142107 (2005).

161. C. F. Bohren and D. R. Huffman, Absorption and Scattering of Light by Small Particles (Wiley, New York, 1983).

162. N. W. Ashcroft and N. D. Mermin, Solid State Physics (Saunders Philadelphia, 1976).

163. K. M. Ho, C. T. Chan, and C. M. Soukoulis, Phys. Rev. Lett. 65, 3152 (1990).

164. R. D. Meade, A. M. Rappe, K. D. Brommer, J. D. Joannopoulos, and O. L. Alerhand, Phys. Rev. B 48, 8434 (1993).

165. D. Hermann, M. Frank, K. Busch, and P. Wölfle, Opt. Express 8, 167 (2001).

167. S. Burger, R. Klose, A. Schädle, F. Schmidt, and L. Zschiedrich, Proc. SPIE 5728, 164 (2005).

168. J. B. Pendry and A. MacKinnon, Phys. Rev. Lett. 69, 2772

(1992) Stefanou, V. Karathanos, and A. Modinos, J. Phys.: Condens. Matter 4, 7389 (1992).

169. E. Istrate, A. A. Green, and E. H. Sargent, Phys. Rev. B 71, 195122 (2005).

170. J. D. Jackson, Classical Electrodynamics, 3rd ed. (Wiley, New York, 1998).

171. A. A. Krokhin and P. Halevi, Phys. Rev. B 53, 1205 (1996).

172. A. Tip, A. Moroz, and J. M. Combes, J. Phys. A 33, 6223 (2000).

173. K. Busch, A. García-Martín, D. Hermann, L. Tkeshelashvili, M Frank, and P. Wölfle, Adv. Solid State Phys. 42, 41 (2002).

174. O. Toader and S. John, Phys. Rev. E 70, 046605 (2004).

175. D. C. Meisel, M. Diem, M. Deubel, F. Pérez-Willard, S. Linden, D. Gerthsen, K. Busch, and M. Wegener, Adv. Mater. (Weinheim, Ger.) 18, 2964 (2006).

176. M. G. Moharam, E. B. Grann, D. A. Pommet, and T. K. Gaylord, J. Opt. Soc. Am. A 12, 1068 (1995).

177. P. Lalanne and G. M. Morris, J. Opt. Soc. Am. A 13, 779 (1996).

178. G. Granet and B. Guizal, J. Opt. Soc. Am. A 13, 1019 (1996).

179. D. M. Whittaker and I. S. Culshaw, Phys. Rev. B 60, 2610 (1999).

180. L. Li, J. Opt. Soc. Am. A 13, 1870 (1996).

181. H. Kosaka, T. Kawashima, A. Tomita, M. Notomi, T. Tamamura, T. Sato, and S. Kawakami, Phys. Rev. B 58, R10096 (1998).

182. Aki, K., & Richards, P. 1980. Quantitative Seismology. San Francisco: W. H. Freeman and Company.

183. Banik, N. C., Lerche, I., & Shuey, R. T. 1985. Stratigraphic filtering, Part I: Derivation of the O'Doherty-Anstey formula. Geophysics, 50, 2768–2774.

184. Bleistein, N., Cohen, J. K., & Jr., J. W. Stockwell. 2001. Mathematics of multidimensional seismic imaging, migration and inversion. New York: Springer-Verlag.

185. Boas, D. A., Campbell, L. E., & Yodh, A. G. 1995. Scattering and imaging with diffusing temporal field correlations. Physical Review Letters, 75, 1855–1858.

186. Boore, D. M. 1970. Finite-difference solutions to the equations of elastic wave propagation, with applications to Love waves over dipping interfaces. Ph.D. thesis, MIT.

187. Boyce, W. E., & DiPrima, R. C. 1997. Elementary Differential Equations. New York: Wiley.

188. Campillo, M., & Paul, A. 2003. Long-range correlations in the diffuse seismic coda. Science, 299, 547–549.

189. Goedecke, G. H. 1977. Radiative transfer in closely packed media. Journ. Opt. Soc. Am., 67, 1339–1348.

190. Hemmer, P. C. 1961. On a generalization of Smoluchowski's Diffusion equation. Physica, 27, 79–82.

191. Hendrich, A., Martinez, A. S., Maynard, R., & van Tiggelen, B. A. 1994. The role of the step length distribution in wave-diffusion. Physics Letters A, 185, 110–112.

192. Hennino, R., Tr´egour`es, N., Shapiro, N. M., L. Margerin, L., Campillo, M., Tiggelen, B. A. Van, & Weaver, R. L. 2001. Observation of equipartition of seismic waves. Physical Review Letters, 86(15), 3447–3450.

193. Ishimaru, A. 1978. Wave Propagation and Scattering in Random Media. New York: Academic Press.

194. Margerin, L., Campillo, M., Shapiro, N. M., & van Tiggelen, B. 1999. Residence time of diffusive waves in the crust as a physical interpretation of coda Q: application to seismograms recorded in Mexico. Geoph. J. Int., 138, 343–352.

195. Morse, P., & Feshbach, H. 1953. Methods of Theoretical Physics. New York: McGraw-Hill.

196. O'Doherty, R. F., & Anstey, N. A. 1970. Reflections on Amplitudes. Geophysical Prospecting, 19, 430–458.

197. Paaschens, J. C. J. 1997. Solution of the time dependent Boltzmann equation. Phys. Rev. E, 56, 1135–1145.

198. Scales, J. A., & Malcolm, A. 2003. Laser characterization of ultrasonic wave propagation in random media. accepted for publication in Phys. Rev. E.

199. Schuster, A. 1905. Radiation through a foggy atmosphere. J. Astrophys., 21, 1–22.

200. Shapiro, S., & Zien, H. 1993. The O'Doherty-Anstey formula and localization of seismic waves. Geophysics, 58, 736– 740.

201. Sheng, P. 1995. Introduction to wave scattering, localization, and mesoscopic phenomena. San Diego: Academic Press.

202. Turner, J. 1994. Radiative transfer of ultrasound. Ph.D. thesis, University of Illinois.

203. Wijk, K., Haney, M., & Scales, J. A. 2003. Elastic energy propagation in a strongly scattering 1D laboratory model. submitted to Physical Review Letters.

204. V. F. Nesterenko. Dynamics of Heterogeneous Materials. Springer-Verlag, New York, NY, 2001.

205. S. Sen, J. Hong, J. Bang, E. Avalos, , and R. Doney. Solitary waves in the granular chain. Phys. Rep., 462:21, 2008.

206. P.G. Kevrekidis. Non-linear waves in lattices: Past, present, future. IMA J. Appl. Math., 76:389, 2011.

207. C. Daraio, V. F. Nesterenko, E. B. Herbold, and S. Jin. Tunability of solitary wave properties in one-dimensional strongly nonlinear photonic crystals. Phys. Rev. E, 73:026610, 2006.

208. C. Coste, E. Falcon, and S. Fauve. Solitary waves in a chain of beads under hertz contact. Phys. Rev. E, 56:6104, 1997.

209. Surajit Sen, Marian Manciu, and James D. Wright. Solitonlike pulses in perturbed and driven Hertzian chains and their possible applications in detecting buried impurities. Phys. Rev. E, 57:2386, 1998.

210. E. Hascoet and H. J. Herrmann. Shocks in non-loaded bead chains with impurities. Eur. Phys. J. B, 14:183, 2000.

211. J. Hong and A. Xu. Nondestructive identification of impurities in granular medium. Appl. Phys. Lett., 81:4868, 2002.

212. G. Theocharis, M. Kavousanakis, P. G. Kevrekidis, C. Daraio, M. A. Porter, and I. G. Kevrekidis. Localized breathing modes in granular crystals with defects. Phys. Rev. E, 80:066601, 2009.

213. S. Job, F. Santibanez, F. Tapia, and F. Melo. Wave localization in strongly nonlinear hertzian chains with mass defect. Phys. Rev. E, 80:025602(R), 2009.

214. Y. Man, N. Boechler, G. Theocharis, P. G. Kevrekidis, and C. Daraio. Defect modes in one-dimensional granular crystals. Phys. Rev. E, 85:037601, 2012.

215. V. F. Nesterenko, C. Daraio, E. B. Herbold, and S. Jin. Anomalous wave reflection at the interface of two strongly nonlinear granular media. Phys. Rev. Lett., 95:158702, 2005.

216. C. Daraio, V. F. Nesterenko, E. B. Herbold, and S. Jin. Energy trapping and shock disintegration in a composite granular medium. Phys. Rev. Lett., 96:058002, 2006.

217. C. Hoogeboom, G. Theocharis, and P. G. Kevrekidis. Discrete breathers at the interface between a diatomic and a monoatomic granular chain. Phys. Rev. E, 82:061303, 2010.

218. R. Doney and S. Sen. Decorated, tapered, and highly nonlinear granular chain. Phys. Rev. Lett., 97:155502, 2006.

219. U. Harbola, A. Rosas, A. H. Romero, M. Esposito, and K. Lindenberg. Pulse propagation in decorated granular chains: An analytical approach. Phys. Rev. E, 80:051302, 2009.

220. M. A. Porter, C. Daraio, E. B. Herbold, I. Szelengowicz, and P. G. Kevrekidis. Highly nonlinear solitary waves in periodic dimer granular chains. Phys. Rev. E, 77:015601(R), 2008.

221. M. A. Porter, C. Daraio, I. Szelengowicz, E. B. Herbold, and P. G. Kevrekidis. Highly nonlinear solitary waves in heterogeneous periodic granular media. Physica D, 238:666, 2009.

222. E. B. Herbold, J. Kim, V. F. Nesterenko, S. Y. Wang, and C. Daraio. Pulse propagation in a linear and nonlinear diatomic periodic chain: Effects of acoustic frequency band-gap. Acta Mech., 205:85, 2009.

223. A. Molinari and C. Daraio. Stationary shocks in periodic highly nonlinear granular chains. Phys. Rev. E, 80:056602, 2009.

224. K. R. Jayaprakash, Yuli Starosvetsky, and Alexander F. Vakakis. New family of solitary waves in granular dimer chains with no precompression. Phys. Rev. E, 83:036606, 2011.

225. K. R. Jayaprakash, Alexander F. Vakakis, and Yuli Starosvetsky. Solitary waves in a general class of granular dimer chains. J. App. Phys., 112(3):034908, 2012.

226. K. R. Jayaprakash, Y. Starosvetsky, A. F. Vakakis, and O. V. Gendelman. Nonlinear resonances leading to strong pulse attenuation in granular dimer chains. Journal of Nonlinear Science, 23(3):363–392, 2013.

227. N. Boechler, J. Yang, G. Theocharis, P. G. Kevrekidis, and C. Daraio. Tunable vibrational band gaps in one-dimensional diatomic granular crystals with three particle unit cells. J. App. Phys., 109(7):074906, 2011.

228. A. Sokolow and S. Sen. Exact solution to the problem of nonlinear pulse propagation through random layered media and its connection with number triangles. Ann. Phys., 322:2104, 2007.

229. A.-L. Chen and Y.-S. Wang. Study on band gaps of elastic waves propagating in one-dimensional disordered phononic crystals. Physica B, 392:369, 2007.

230. F. Fraternali, M. A. Porter, and C. Daraio. Optimal design of composite granular protectors. Mech. Adv. Mat. Struct., 17(1):1, 2010.

231. L. Ponson, N. Boechler, Y. M. Lai, M. A. Porter, P. G. Kevrekidis, and C. Daraio. Nonlinear waves in disordered diatomic granular chains. Phys. Rev. E, 82:021301, 2010.

232. A. J. Martınez, P. G. Kevrekidis, and M. A. Porter. Superdiffusive transport and energy localization in disordered granular crystals. Phys. Rev. E, 93:022902, 2016.

233. V. Achilleos, G. Theocharis, and Ch. Skokos. Energy transport in one-dimensional disordered granular solids. Phys. Rev. E, 93:022903, 2016.

234. B. Yousefzadeh and A. S. Phani. Supratransmission in a disordered nonlinear periodic structure. arXiv, 1510:00058v1, 2015.

235. I. Szelengowicz, M. A. Hasan, Y. Starosvetsky, A. Vakakis, and C. Daraio. Energy equipartition in two dimensional granular systems with spherical intruders. Phys. Rev. E, 87:032204, 2013.

236. Y. Zhang, M. A. Hasan, Y. Starosvetsky, D. M. McFarland, and A. F. Vakakis. Nonlinear mixed solitary—shear waves and pulse equi-partition in a granular network. Physica D: Nonlinear Phenomena, 291(0):45–61, 2015.

237. M. A. Porter, P. G. Kevrekidis, and C. Daraio. Granular crystals: Nonlinear dynamics meets materials engineering. Physics Today, 68(11):44, 2015.

238. J. Hong. Universal power-law decay of the impulse energyin granular protectors. Phys. Rev. Lett., 94:108001, 2005.

239. A. Spadoni and C. Daraio. Generation and control of sound bullets with a nonlinear acoustic lens. Proc. Nat. Acad. Sci. USA, 107(16):7230, 2010.

240. D. Khatri, P. Rizzo, and C. Daraio. Highly nonlinear waves' sensor technology for highway infrastructures. SPIE, 6934:69340U, 2008.

241. C. Daraio, V. F. Nesterenko, and S. Jin. Strongly nonlinear waves in a chain of Teflon beads. Phys. Rev. E, 72:016603, 2005.

242. F. Li, P. Anzel, J. Yang, P. G. Kevrekidis, and C. Daraio. Granular acoustic switches and logic elements. Nat. Comm., 5:5311, 2014.

243. S. Flach. Nonlinear lattice waves in random potentials. In C. Besse and J. C. Garreau, editors, Nonlinear Optical and Atomic Systems, volume 2146 of Lecture Notes in Mathematics, pages 1–48. Springer, 2015.

244. T. V. Laptyeva, M. V. Ivanchenko, and S. Flach. Nonlinear lattice waves in heterogeneous media. J. Phys. A: Math. Theor., 47:493001, 2014.

245. Roger G. Newton. Scattering Theory of Waves and Particles, 2nd ed. Dover Piblications Inc., USA, 2013.

246. A. E. Miroshnichenko, S. Flach, and Yu. S. Kivshar. Fano resonances in nanoscale structures. Rev. Mod. Phys., 82:2257–2298, 2010.

247. S. Flach and A. Gorbach. Discrete breathers: advances in theory and applications. Phys. Rep., 467:1–116, 2008.

248. F. Lederer, G. I. Stegeman, D. N. Christodoulides, G. Assanto, M. Segev, and Y. Silberberg. Discrete solitons in optics. Phys. Rep., 463:1–126, 2008.

249. B. Luk'yanchuk, N. I. Zheludev, S. A. Maier, N. J. Halas, P. Nordlander, H. Giessen, and C. T. Chong. The Fano resonance in plasmonic nanostructures and metamaterials. Nat. Mater., 9:707–715, 2010.

250. A. E. Miroshnichenko and Y. S. Kivshar. Fano resonances in all-dielectric oligoners. Nano Lett., 12:6459–6463, 2012.

251. W. Cai, U. K. Chettiar, A. V. Kildishev, and V. M. Shalaev. Optical cloaking with metamaterials. Nat. Photon., 1:224, 2007.

252. H. Chen and C. T. Chan. Acoustic cloaking in three dimensions using acoustic metamaterials. Appl. Phys. Lett., 91:183518, 2007.

253. J. J. Sakurai. Modern Quantum Mechanics. Addison Wesley, 1994.

254. D. E. Golden and H. W. Bandel. Low-energy e–-ar total scattering cross sections: The ramsauer-townsend effect. Phys. Rev., 149:58, 1966.

255. W. E. Kauppila, T. S. Stein, and G. Jesion. Direct observation of a ramsauer-townsend effect in positron-argon collisions. Phys. Rev. Lett., 36:580, 1976.

256. F. A. Gianturco and D. G. Thompson. The ramsauertownsend effect in methane. J. Phys. B: Atom. Molec. Phys., 9:L383, 1976.

257. F. Li, L. Zhao, Z. Tian, L. Yu, and J. Yang. Visualization of solitary waves via laser doppler vibrometry for heavy impurity identification in a granular chain. Smart Mater. Struc., 22:035016, 2013.

258. C. Chong, F. Li, J. Yang, M. O. Williams, I. G. Kevrekidis, P. G. Kevrekidis, and C. Daraio. Dampeddriven granular chains: An ideal playground for dark breathers and multibreathers. Phys. Rev. E, 89:032924, 2014.

259. A. Crisanti, G. Paladin, and A. Vulpiani. Products of random matrices. Springer, 1993.

260. S. S. Zakeri, S. Lepri, and D. S. Wiersma. Localization in one-dimensional chains with Lervy-type disorder. Phys. Rev. E, 91:032112, 2015.

261. Altshuler, B. L., Lee, P. A., and Webb, R. A. (eds), 1991. Mesoscopic phenomena in solids. Elsevier, Amsterdam.

262. Akkermans, E., and Montambaux, G. 2007. Mesoscopic physics of electrons and photons. Cambridge university press.

263. van Rossum, M. C. W., and Nieuwenhuizen, T. M. 1999. Multiple scattering of classical waves: microscopy, mesoscopy, and diffusion. Rev. Mod. Phys., 71, 313-371.

264. Webb, R. A., Washburn, S., Umbach, C. P., and Laibowitz, R. B. 1985. Observations of h/e Aharonov-Bohm oscillations in normal-metal rings. Phys. Rev. Lett., 54, 2696-2699.

265. Anderson, P. W. 1958. Absence of diffusion in certain random lattices. Phys. Rev., 109, 1492-1505.

266. Thouless, D. J. 1974. Electrons in disordered systems and the theory of localization. Phys. Rep., 13, 93.

267. Thouless, D. J. 1977. Maximum metallic resistance in thin wires. Phys. Rev. Lett., 39, 1167-1169.

268. Abrahams, E., Anderson, P. W., Licciardello, D., and Ramakrishnan, T. V. 1979. Scaling theory of localization: absence of quantum diffusion in two dimensions. Phys. Rev. Lett., 42, 673.

269. Anderson, P. W., Thouless, D. J., Abrahams, E., and Fisher, D. S. 1980. New method for a scaling theory of localization. Phys. Rev. B, 22, 3519-3526.

270. Dorokhov, O. N. 1982. Transmission coefficient and the localization length of an electron in N bond disorder chains. Pisma Zh. Eksp. Teor. Fiz., 36, 259 [JETP Lett., 36, 318].

271. Dorokhov, O. N. 1984. On the coexistence of localized and extended electronic states in the metallic phase. Solid State Commun., 51 381.

272. Abrahams, E. (eds), 2010. 50 years of Anderson localization. World Scientific Publishing Co. Pte. Ltd.

273. Gertsenshtein, M. E., and Vasil’ev, V. B. 1959. Waveguides with random inhomogeneities and brownian motion in the Lobachevsky plane. Theory of probability and its applications., 4, 391-398.

274. Azbel, M. Ya. 1983. Eigenstates and properties of random systems in one dimension at zero temperature. Phys. Rev. B, 28, 4106.

275. John, S., Sompolinsky, H., and Stephen, M. J. 1983. Localization in a disordered elastic medium near two dimensions. Phys. Rev. B, 27, 5592.

276. John, S. 1984. Electromagnetic absorption in a disordered medium near a photon mobility edge. Phys. Rev. Lett., 53, 2169.

277. van Albada, M., and Lagendijk, A. 1985. Observation of weak localization of light in a random medium. Phys. Rev. Lett., 55, 2692.

278. Wolf, P. E., and Maret, G. 1985. Weak localization and coherent backscattering of photons in disordered media. Phys. Rev. Lett., 55, 2696.

279. Akkermans, E., Wolf, P. E., and Maynard, R. 1986. Coherent backscattering of light by disordered media: analysis of the peak lineshape. Phys. Rev. Lett., 56, 1471.

280. Stephen, M. J., and Cwilich, G. 1987. Intensity correlation functions and fluctuations in light scattered from a random medium. Phys. Rev. Lett., 59, 285.

281. Mello, P. A., Akkermans, E., and Shapiro, B. 1988. Macroscopic approach to correlations in the electronic transmission and reflection from disordered conductors. Phys. Rev. Lett., 61, 459-462.

282. Feng, S., Kane, C., Lee, P. A., and Stone, A. D. 1988. Correlations and fluctuations of coherent wave transmission through disordered media. Phys. Rev. Lett., 61, 834-837.

283. Garcia, N., and Genack, A. Z. 1989. Crossover to strong correlation for microwave radiation. Phys. Rev. Lett., 63, 1678.

284. Genack, A. Z., Garcia, N., and Polkosnik, W. 1990. Long-range intensity correlation in random media. Phys. Rev. Lett., 65, 2129.

285. van Albada, M. P., De Boer, J. F., and Lagendijk, A. 1990. Observation of long-range intensity correlation in the transport of coherent light through a random medium. Phys. Rev. Lett., 64, 2787.

286. Dalichaouch, R., Armstrong, J. P., Schultz, S., Platzman, P. M., and McCall, S. L. 1991. Microwave localization by two-dimensional random scattering. Nature, 354, 53.

287. Garcia, N., and Genack, A. Z. 1991. Anomalous photon diffusion at the threshold of the Anderson localization transition. Phys. Rev. Lett., 66, 1850.

288. De Boer, J. F., van Rossum, M. C. W., van Albada, M. P., Nieuwenhuizen, T. M., and Lagendijk, A. 1994. Probability distribution of multiple scattered light measured in total transmission. Phys. Rev. Lett., 73, 2567-2570.

289. Wiersma, D. S., van Albada, M. P., van Tiggelen, B. A., and Lagendijk, A. 1995. Experimental evidence for recurrent multiple scattering events of light in disordered media. Phys. Rev. Lett., 74, 4193-4196.

290. Nieuwenhuizen, Th. M., and van Rossum, M. C. 1995. Intensity distribution of waves transmitted through a multiple scattering medium. Phys. Rev. Lett., 74, 2674.

291. Kogan, E., and Kaveh, M. 1995. Random-matrix-theory approach to the intensity distributions of waves propagating in a random medium. Phys. Rev. B, 52, R3813.

292. Stoytchev, M., and Genack, A. Z. 1997. Measurement of the probability distribution of total transmission in random waveguides. Phys. Rev. Lett., 79, 309.

293. Wiersma, D. S., Bartolini, P., Lagendijk, A., and Righini, R. 1997. Localization of light in a disordered medium. Nature, 390, 671.

294. Scheffold, F., and Maret, G. 1998. Universal conductance fluctuations of light. Phys. Rev. Lett., 81, 5800.

295. Gr´esillon, S., Aigouy, L., Boccara, A. C., Rivoal, J. C., Quelin, X., Desmarest, C., Gadenne, P., Shubin, V. A., Sarychev, A. K., and Shalaev, V. M. 1999. Experimental observation of localized optical excitations in random metaldielectric films. Phys. Rev. Lett., 82, 4520-4523.

296. Chabanov, A. A., Stoytchev, M., and Genack, A. Z. 2000. Statistical approach to photon localization, Nature, 404, 850-853.

297. John, S. 1991. Localization of light. Phys. Today, 44, 32.

298. Lagendijk, A., van Tiggelen, B., and Wiersma, D. S. 2009. Fifty years of Anderson localization. Phys. Today, 62, 24-29.

299. Leung, P. T., Liu, S. Y., and Young, K. 1994. Completeness and orthogonality of quasinormal modes in leaky cavities. Phys. Rev. A, 49, 3057.

300. Ching, E. S. C., Leung, P. T., Suen, W. M., Tong, S. S., and Young, K. 1998. Waves in open systems: eigenfunction expansions. Rev. Mod. Phys., 70, 15451554.

301. Wang, J., and Genack, A. Z. 2011. Transport through modes in random media. Nature, 471, 345.

302. Shi, Z., and Genack, A. Z. 2012. Transmission eigenvalues and the bare conductance in the crossover to Anderson localization. Phys. Rev. Lett., 108, 043901.

303.Kopp, V. I., Fan, B., Vithana, H. K. M., and Genack, A. Z. 1998. Lowthreshold lasing at the edge of a photonic stop band in cholesteric liquid crystals. Opt. Lett., 23, 1707-1709.

304. Milner, V., and Genack, A. Z. 2005. Photon Localization Laser: Low-threshold lasing in a random amplifying layered medium via wave localization. Phys. Rev. Lett., 94, 073901 (2005).

305. Stone, A. D., Mello, P. A., Muttalib, K., and Pichard, J. L. 1991. Random matrix theory and maximum entropy models for disordered conductors.

Pages of 369-448 of: Altshuler, B. L., Lee, P. A., and Webb, R. A. (eds), Mesoscopic phenomena in solids. Elsevier, Amsterdam.

306. Davy, M., Shi, Z., Wang, J., and Genack, A. Z. 2013. Transmission statistics and focusing in single disordered samples. Opt. Express, 21, 10367-10375.

307. Popoff, S. M., Lerosey, G., Carminati, R., Fink, M., Boccara, A. C., and Gigan, S. 2010. Measuring the transmission matrix in optics: an approach to the study and control of light propagation in disordered media. Phys. Rev. Lett., 104, 100601.

308. Mosk, A. P., Lagendijk, A., Lerosey, G., and Fink, M. 2012. Controlling waves in space and time for imaging and focusing in complex media, Nat. Photon., 6, 283-292.

309. Davy, M., Shi, Z., and Genack, A. Z. 2012. Focusing through random media: eigenchannel participation number and intensity correlation. Phys. Rev. B, 85, 035105.

310. Ioffe, A. F., and Regel, A. R. 1960. Noncrystalline, amorphous and liquid electronic semiconductors. Prog. Semicond., 4, 237.

311. Pendry, J. B. 1991. Catching moonbeams. Nature, 351, 438-439.

312. Mello, P. A., Pereyra, P., and Kumar, N. 1988. Macroscopic approach to multichannel disordered conductors. Ann. Phys., (N.Y.) 181, 290.

313. Beenakker, C. W. J. 1997. Random-matrix theory of quantum transport. Rev. Mod. Phys., 69, 731-808.

314. Imry, Y., and Landauer, R. 1999. Conductance viewed as transmission. Rev. Mod. Phys., 71, S306.

315. Landauer, R. 1970. Electrical resistance of disordered one-dimensional lattices. Philos. Mag., 21, 863.

316. Pendry, J. B., Mackinnon, A., and Pretre, A. B. 1990. Maximal fluctuations - a new phenomenon in disordered systems. Physica A 168, 400-407.

317. Imry, Y. 1986. Active transmission channels and universal conductance fluctuations. Europhys. Lett., 1, 249-256.

318. John, S. 1987. Strong localization of photons in certain disordered dielectric superlattices. Phys. Rev. Lett., 58, 2486.

319. He, S., and Maynard, J. D. 1986. Detailed measurements of inelastic scattering in Anderson localization. Phys. Rev. Lett., 57, 3171-3174.

320. Shapira, O., and Fischer, B. 2005. Localization of light in a random grating array in a single mode fiber. J. Opt. Soc. of Am. B, 22, 2542-2552.

321. Sebbah, P., Hu, B., Klosner, J., and Genack, A. Z. 2006. Extended quasimodes within nominally localized random waveguides. Phys. Rev. Lett., 96, 183902.

322. Bertolotti, J., Gottardo, S., Wiersma, D. S., Ghulinyan, M., and Pavesi, L. 2005. Optical necklace states in Anderson localized 1D systems, Phys. Rev. Lett., 94, 113903.

323. Zhang, S., Park, J., Milner, V., and Genack, A. Z. 2008. Delocalization transition in dimensional crossover in random layered media. Phys. Rev. Lett., 101, 183901.

324. Raedt, H. D., Lagendijk, A., and de Vries, P. 1989. Transverse localization of light. Phys. Rev. Lett., 62, 47.

325. Schwartz, T., Bartal, G., Fishman, S., and Segev, M. 2007. Transport and Anderson localization in disordered two-dimensional photonic lattices. Nature, 446, 52.

326. Lahini, Y., Avidan, A., Pozzi, F., Sorel, M., Morandotti, R., Christodoulides, D. N., and Silberberg, Y. 2008. Anderson localization and nonlinearity in one-dimensional disordered photonic lattices. Phys. Rev. Lett., 100, 013906.

327. Hu, H., Strybulevych, A., Page, J. H., Skipetrov, S. E., and van Tiggelen, B. 2008. Localization of ultrasound in a three-dimensional elastic network. Nat. Phys., 4, 945-948 (2008).

328. Shi, Z., Wang, J., and Genack, A. Z. 2014. Microwave conductance in random waveguides in the cross-over to Anderson localization and single-parameter scaling. Proceedings of the National Academy of Sciences (PNAS) 111, 2926.

329. Altshuler, B. L. 1985. Fluctuations in the extrinsic conductivity of disordered conductors. Pis'ma Zh. Eksp. Teor. Fiz., 41, 530. [JETP Lett., 41, 648].

330. Lee, P. A., and Stone, A. D. 1985. Universal conductance fluctuations in metals. Phys. Rev. Lett., 55, 1622.

331. Castellanos-Beltran, M. A., Ngo, D. Q., Shanks, W. E., Jayich, A. B., and Harris, J. G. E. 2013. Measurement of the full distribution of persistent current in normal-metal rings. Phys. Rev. Lett., 110, 156801.

332. Sebbah, P., Hu, B., Genack, A. Z., Pnini, R., and Shapiro, B. 2002. Spatial field correlation: the building block of mesoscopic fluctuations. Phys. Rev. Lett., 88, 123901.

333. Sarma, R., Yamilov, A., Neupane, P., Shapiro, B., and Cao, H. 2014. Probing long-range intensity correlations inside disordered photonic nanostructures. arxiv.org/abs/1405.6339.

334. Sperling, T., Buhrer, W., Aegerter, C. M., and Maret, G. 2013. Direct determination of the transition to localization of light in three dimensions. Nat Photon., 7, 48-52.

335. Labont´e, L., Vanneste, C., and Sebbah, P. 2012. Localized mode hybridization by fine tuning of two-dimensional random media. Opt. Lett., 37, 1946.

336. Bliokh, K. Yu., Bliokh, Yu. P., Freilikher, V., Genack, A. Z., and Sebbah, P. 2008. Coupling and level repulsion in the localized regime: from isolated to quasiextended modes. Phys. Rev. Lett., 101, 133901.

337. Wigner, E. P. 1951. On the statistical distribution of the widths and spacing of nuclear resonance levels. Proc. Cambridge Phil. Soc., 47, 790.

338. Mott, N. F., 1970. Conduction in non-crystalline systems. IV. Anderson localization in a disordered lattice. Philos. Mag., 22, 7.

339. Pendry, J. B. 1987. Quasi-extended electron states in strongly disordered systems. J. Phys. C, 20, 733.

340. Topolancik, J., Ilic, B., and Vollmer, F. 2007. Experimental observation of strong photon localization in disordered photonic crystal waveguides. Phys. Rev. Lett., 99, 253901.

341. Lonˇcar, M., Nedeljkovi´c, D., Doll, T., Vuˇckvi´c, J., Scherer, A., and Pearsall, T. P. 2000. Waveguiding in planar photonic crystals. Appl. Phys. Lett., 77, 1937.

342. Smolka, S., Thyrrestrup, H., Sapienza, L., Lehmann, T. B., Rix, K. R., FroufeP´erez, L. S., Garc´ıa, P. D., and Lodahl, P. 2011. Probing the statistical properties of Anderson localization with quantum emitters. New J. Phys., 13, 063044.

343. Mirlin, A. D. 2000. Statistics of energy levels and eigenfunctions in disordered systems. Phys. Rep., 326, 259.

344. Starykh, O. A., Jacquod, P. R. J., Narimanov, E. E., and Stone, A. D. 2000. Signature of dynamical localization in the resonance width distribution of wave-chaotic dielectric cavities. Phys. Rev. E, 62, 2078.

345. Kottos, T. 2005. Statistics of resonances and delay times in random media: beyond random matrix theory. J. Phys. A, 38, 10761.

346. Watson, G. H., Fleury, P. A. and McCall, S. L. 1987. Searching for photon localization in the time domain. Phys. Rev. Lett., 58, 945.

387. Genack, A. Z., and Drake, J. M. 1990. Relationship between optical intensity fluctuations and pulse propagation in random media. Europhys. Lett., 11, 331.

348. Chabanov, A. A., Zhang, Z.Q., and Genack, A. Z. 2003. Breakdown of diffusion in dynamics of extended waves in mesoscopic media. Phys. Rev. Lett., 90, 203903.

349. Cheung, S. K., Zhang, X., Zhang, Z.Q., Chabanov, A. A., and Genack, A. Z. 2004. Impact of weak localization in the time domain. Phys. Rev. Lett., 92 173902.

350. Skipetrov, S. E., and van Tiggelen, B. A. 2004. Dynamics of weakly localized waves. Phys. Rev. Lett., 92, 113901.

351. Skipetrov, S. E., and van Tiggelen, B. A. 2006. Dynamics of Anderson localization in open 3D media. Phys. Rev. Lett., 96, 043902.

352. Faez, S., Strybulevych, A., Page, J. H., Lagendijk, A., and van Tiggelen, B. A., 2009. Observation of multifractality in Anderson localization of ultrasound. Phys. Rev. Lett., 103, 155703.

353. Muzykantskii, B. A., and Khmelnitskii, D. E. 1995. Nearly localized states in weakly disordered conductors. Phys. Rev. B, 51, 5480.

354. Apalkov, V. M., Raikh, M. E., and Shapiro, B. 2004. Anomalously localized states in the Anderson model. Phys. Rev. Lett., 92, 066601.

355. Zhang, Z.Q., Chabanov, A. A., Cheung, S.K., Wong, C.H., and Genack, A. Z. 2009. Dynamics of localized waves. Phys. Rev. B, 79, 144203.

356. Weaver, R. 1993. Anomalous diffusivity and localization of classical waves in disordered media: the effect of dissipation. Phys. Rev. B, 47, 1077.

357. Tian, C.S., Cheung, S.K., and Zhang, Z.Q. 2010. Local diffusion theory for localized waves in open media. Phys. Rev. Lett., 105, 263905.

358. Payne, B., Yamilov, A., and Skipetrov, S. E. 2010. Anderson localization as position-dependent diffusion in disordered waveguides. Phys. Rev. B, 82, 024205.

359. Chabanov, A. A., Hu, B., and Genack, A. Z. 2004. Dynamic correlation in wave propagation in random media. Phys. Rev. Lett., 93, 123901.

360. Cherroret, N., Pe˜na, A., Chabanov, A. A., and Skipetrov, S. E. 2009. Nonuniversal dynamic conductance fluctuations in disordered systems, Phys. Rev. B, 80, 045118.

361. Wang, J., Chabanov, A. A., Lu, D. Y., Zhang, Z.Q., and Genack, A. Z. 2010. Dynamics of fluctuations of localized waves. Phys. Rev. B, 81, 241101(R).

362. Wiersma, D. S., and Lagendijk, A. 1996. Light diffusion with gain and random lasers. Phys. Rev. E, 54, 4256.

363. Kempe, M., Berger, G. A., and Genack, A. Z. 1997. Stimulated emission from amplifying random media. Pages of 301-330 of: Hummel, R. E., and Wissmann, P. (eds) Handbook of Optical Properties. CRC Press, Boca Raton, FL.

364. Berger, G. A., Kempe, M., Genack, A. Z. 1997. Dynamics of stimulated emission from random media. Phys. Rev. E, 56, 6118.

365. Cao, H., Zhao, Y. G., Ho, S. T., Seelig, E. W., Wang, Q. H., and Chang, R. P. H. 1999. Random laser action in semiconductor powder. Phys. Rev. Lett., 82, 22782281.

366. Frolov, S. V., Vardeny, Z. V., and Yoshino, K. 1999. Cooperative and stimulated emission in poly(p-phenylene-vinylene) thin films and solutions. Phys. Rev. B, 57, 9141-9147.

367. Vanneste, C., Sebbah, P. and Cao, H. 2007. Lasing with resonant feedback in weakly scattering random systems. Phys. Rev. Lett., 98, 143902.

368. Yamilov, A., Wu, X., Cao, H., and Burin, A. L., 2005. Absorption-induced connement of lasing modes in diffusive random media. Opt. Lett., 30, 2430.

369. Andreasen, J., Asatryan, A.A., Botten, L. C., Byrne, M. A., Cao, H., Ge, L., Labont´e, L., Sebbah, P., Stone, A. D. T¨ureci, H. E., Vanneste, C., 2011. Modes of random lasers. Adv. Opt. Photonics, 3, 88.

370. Letokhov, V. V. 1968. Generation of light by a scattering medium with negative resonance. Sov. Phys. JETP, 26, 835840.

361. Lawandy, N. M., Balachandran, R. M., Gomes, A. S. L., and Sauvain, E. 1994. Laser action in strongly scattering media. Nature, 368, 436-438.

362. Wiersma, D. S., van ALbada, M. P., and Lagendijk, A. 1995. Random laser? Nature, 373, 203-204.

373. Genack, A. Z. 1987. Optical transmission in disordered media. Phys. Rev. Lett., 58, 2043-2046 (1987).

374. van Albada, M. P., van Tiggelen, B. A., Lagendijk, A., and Tip, A. 1991. Speed of propagation of classical waves in strongly scattering media. Phys. Rev. Lett., 66, 3132.

375. Genack, A. Z., and Drake, J. M. 1994. Scattering for super-radiation. Nature, 368, 400.

376. Dowling, J. P., Scalora, M., and Bloemer, M. J. 1994. The photonic band edge laser: a new approach to gain enhancement. Jour. Appl. Phys., 75, 1896-1899.

377. Kopp, V. I., Zhang, Z.-Q., and Genack, A. Z. 2003. Lasing in chiral photonic structures. Prog. In Quant. Electron., 27, 369.

378. Il'chishin, I. P., and Vakhnin, A. Yu. 1995. Detecting of the structure distortion of cholesteric liquid crystal using the generation characteristics of the distributed feedback laser based on it. Mol. Cryst. Liq. Cryst., 265, 687.

379. Bachelard, N., Andreasen, J., Gigan, S., and Sebbah, P. 2012. Taming random lasers through active spatial control of the pump. Phys. Rev. Lett., 109, 033903.

380.T¨ureci, H. E., Ge, L., Rotter, S., Stone, A. D. 2008. Strong interactions in multimode random lasers. Science, 320, 643.

381. Stano, P., and Jacquod, P. 2013. Suppression of interactions in multimode random lasers in the Anderson localized regime. Nature Photon., 7, 66.

382. Vellekoop, I. M., Lagendijk, A., and Mosk, A. P. 2010. Exploiting disorder for perfect focusing. Nat Photon., 4, 320-322.

383. van Putten, E. G., Akbulut, D., Bertolotti, J., Vos, W. L., Lagendijk, A., and Mosk, A. P. 2011. Scattering lens resolves sub-100 nm structures with visible light. Phys. Rev. Lett., 106, 193905.

384. Choi, Y., Yoon, C., Kim, M., Yang, T., Fang-Yen, C., Dasari, R. R., Lee, K., and Choi, W. 2012. Scanner-free and wide-field endoscopic imaging by using a single multimode optical fiber. Phys. Rev. Lett., 109, 203901.

385. van Putten, E. G., and Mosk, A. P. 2010. The information age in optics: measuring the transmission matrix. Physics, 3, 22.

386. Mehta, M. L. 2004. Random matrices, 3rd ed. Academic Press, New York.

387. Lagendijk, A., Vreeker, R., and de Vriesb, P. 1989. Influence of internal re- flection on diffusive transport in strongly scattering media. Phys. Lett. A., 136, 81.

388. Zhu, J. X., Pine, D. J., and Weitz, D. 1991. A. Internal reflection of diffusive light in random media. Phys. Rev. A, 44, 3948.

389. Li, J. H., Lisyansky, A. A., Cheung, T. D., Livdan, D., and Genack, A. Z. 1993. Transmission and surface intensity profiles in random media. Europhys. Lett., 22, 675.

390. Garcia, N., Genack, A. Z., and Lisyansky, A. A. 1992. Measurement of the transport mean free path of diffusing photons. Phys. Rev. B, 46, 14475.

391. Nazarov, Y. V., 1994. Limits of universality in disordered conductors. Phys. Rev. Lett., 73, 134.

392. Goetschy, A., and Stone, A. D. 2013. Filtering random matrices: the effect of imperfect channel control in multiple-scattering. arXiv:1304.5562.

393. Kim, M., Choi, Y. Yoon, C., Choi, W., Kim, J., Park, Q., and Choi, W. 2012. Maximal energy transport through disordered media with the implementation of transmission eigenchannels. Nat. Photon., 6, 581.

394. Abrikosov, A. A., and Ryzhkin, I. A. 1978. Conductivity of quasi-onedimensional metal systems. Adv. Phys., 27, 147.

395. Slevin, K., and Ohtsuki, T. 1997. The Anderson transition: time reversal symmetry and universality. Phys. Rev. Lett., 78, 4083.

396. Plerou, V., and Wang, Z. 1998. Conductances, conductance fluctuations, and level statistics on the surface of multilayer quantum Hall states. Phys. Rev. B, 58, 1967.

397. Soukoulis, C. M., Wang, X., Li, Q., and Sigalas, M. M. 1999. What is the right form of the probability distribution of the conductance at the mobility edge?. Phys. Rev. Lett., 82, 668.

398. Markoˇs, P. 1999. Probability distribution of the conductance at the mobility edge. Phys. Rev. Lett., 83, 588.

399. Garc´ıa-Mart´ın, A., and S´aenz, J. J. 2001. Universal conductance distributions in the crossover between diffusive and localization regimes. Phys. Rev. Lett., 87, 116603 (2001).

400. Muttalib, K. A., and W¨olfle, P. 1999. “One-sided” log-normal distribution of conductances for a disordered quantum wire. Phys. Rev. Lett., 83, 3013.

401. Dyson, F. J., and Mehta, M. L. 1962. Statistical theory of the energy levels of complex systems. I-V. J. Math. Phys., 3, 140.

402. Gopar, V. A., Muttalib, K. A., and W¨olfle, P. 2002. Conductance distribution in disordered quantum wires: crossover between the metallic and insulating regimes. Phys. Rev. B, 66, 174204.

403. Zhang, S., Lockerman, Y., and Genack, A. Z. 2010. Mesoscopic speckle. Phys. Rev. E, 82, 051114.

404. Chabanov, A. A., and Genack, A. Z. 2005. Statistics of the mesoscopic field. Phys. Rev. E, 72, 055602.

405. Fink, M. 1992. Time reversal of ultrasonic fields-part I: basic principles. IEEE, 39, 12.

406. Vellekoop, I. M., and Mosk, A. P. 2007. Focusing coherent light through opaque strongly scattering media. Opt. Lett., 32, 2309-2311.

407. Aulbach, J., Gjonaj, B., Johnson, P. M., Mosk, A. P., and Lagendijk, A. 2011. Control of light transmission through opaque scattering media in space and time. Phys. Rev. Lett., 106, 103901.

408. Katz, O., Small, E., Bromberg, Y., and Silberberg, Y. 2011. Focusing and compression of ultrashort pulses through scattering media. Nat Photon., 5, 372-377.

409. Shi, Z., Davy, M., Wang, J., and Genack, A. Z. 2013. Focusing through random media in space and time: a transmission matrix approach. Opt. Lett. 38, 2714.

410. Shi, Z., and Genack, A. Z. 2014. Modal makeup of transmission eigenchannels. arxiv.org/abs/1406.3673.

411. Davy, M., Shi, Z., Wang, J., and Genack, A. Z. 2014. Transmission eigenchannels and the densities of states of random media. arxiv.org/abs/1403.3811.